








EX LIBRIS  
UNIVERSITATIS  
ALBERTENSIS

The Bruce Peel  
Special Collections  
Library









Digitized by the Internet Archive  
in 2025 with funding from  
University of Alberta Library

<https://archive.org/details/0162012507040>







# University of Alberta

## Library Release Form

**Name of Author:** Michael James Ferguson

**Title of Thesis:** New Ternary Rare-Earth Antimonides with Low-Dimensional Structures

**Degree:** Doctor of Philosophy

**Year this Degree Granted:** 2000

Permission is hereby granted to the University of Alberta Library to reproduce single copies of this thesis and to lend or sell such copies for private, scholarly or scientific research purposes only.

The author reserves all other publication and other rights in association with the copyright in the thesis, and except as herein before provided, neither the thesis nor any substantial portion thereof may be printed or otherwise reproduced in any material form whatever without the author's prior written permission.







**University of Alberta**

New Ternary Rare-Earth Antimonides with Low-Dimensional Structures

by

Michael James Ferguson



A thesis submitted to the Faculty of Graduate Studies and Research in partial fulfillment  
of the requirements for the degree of Doctor of Philosophy

Department of Chemistry

Edmonton, Alberta

Spring 2000





**University of Alberta**

**Faculty of Graduate Studies and Research**

The undersigned certify that they have read, and recommend to the Faculty of Graduate Studies and Research for acceptance, a thesis entitled *New Ternary Rare-Earth Antimonides with Low-Dimensional Structures* submitted by Michael James Ferguson in partial fulfillment of the requirements for the degree of Doctor of Philosophy.





*To my family*





## Abstract

Four series of ternary rare-earth antimonides,  $RE_xM_ySb_z$  ( $M$  = transition metal or main-group metal), were synthesized through reactions of the elements and characterized by X-ray diffraction. These compounds possess low-dimensional structures that are based on weakly-bonded antimony networks, which are manifested as linear chains and square nets. The electronic and magnetic properties of several members were investigated. Extended Hückel band structure calculations were performed to quantify the nature of the bonding observed in these compounds.

A new family of nonstoichiometric rare-earth tin antimonides,  $RESn_xSb_2$  ( $RE$  = La–Nd, Sm), was discovered. The extent of the nonstoichiometry of Sn was investigated for the lanthanum series  $LaSn_xSb_2$  and was found to range from a minimum of  $x \approx 0.1$  to a maximum of  $x \approx 0.8$ . The structures of two members,  $LaSn_xSb_2$  ( $x = 0.61, 0.75$ ), were determined and feature nearly square sheets of Sb and disordered chains of Sn, in which the Sn atoms are distributed over three closely spaced sites. The nature of the Sn atoms was investigated by  $^{119}\text{Sn}$  Mössbauer spectroscopy, and the results of the study suggest that the chains consist of zero-valent Sn. Replacing tin with indium yielded the first series of rare-earth indium antimonides,  $REIn_{1-x}Sb_2$  ( $RE$  = La–Nd). The crystal structure of  $LaIn_{0.8}Sb_2$  was determined, and comprises alternating layers of nearly square Sb nets and edge-sharing  $InSb_4$  tetrahedra which are distorted to produce In–In zigzag chains, separated by the La atoms. Extended Hückel calculations predict that  $LaIn_{0.8}Sb_2$  should exhibit anisotropic metallic properties.





Two systems of ternary rare-earth transition metal antimonides,  $RE_3MSb_5$  ( $RE = \text{La-Nd, Sm}$ ;  $M = \text{Ti, Zr, Hf, Nb}$ ) and  $REMSb_3$  ( $RE = \text{La-Nd, Sm, Gd-Tb}$ ;  $M = \text{V, Cr}$ ), were studied. The series of compounds,  $La_3MSb_5$  ( $M = \text{Ti, Zr, Hf}$ ), were structurally characterized and possess strongly one-dimensional features, consisting of chains of face-sharing  $MSb_6$  octahedra and linear skewers of Sb atoms that are separated by the La atoms. All compounds in the  $RE_3TiSb_5$  series exhibit metallic behavior. Moreover,  $La_3TiSb_5$  undergoes two electronic transitions (at  $\sim 85$  K and 120 K) whose origins are currently unknown. The structure of  $LaCrSb_3$  was determined and is composed of nearly square sheets of Sb and buckled layers of face- and edge-sharing  $CrSb_6$  octahedra, which are separated by the La atoms. The series  $REMSb_3$  ( $M = \text{V, Cr}$ ), previously reported to exist for  $RE = \text{La-Nd, Sm}$ , has been extended to include  $RE = \text{Gd-Tb}$ . The electrical resistivity, magnetic, and neutron diffraction data indicate that  $LaCrSb_3$  undergoes an itinerant electron ferromagnetic transition at  $\sim 125$  K. The magnetic structure was also determined for  $NdCrSb_3$ , which at low temperatures exhibits ferromagnetic behavior with the Cr and Nd moments aligned.



## Acknowledgments

I wish to extend my gratitude to my supervisor, Dr. Arthur Mar, for his help and guidance throughout the course of my degree. Further, he was quick to send me to other institutions (UBC and Chalk River) when we were unable to perform particular experiments at the U of A, and encouraged me to attend several conferences and workshops. The people in the Mar group (Robert Lam, Allison Mills, Meitian Wang, and Laura Deakin) have not only been good coworkers but also good friends. I had the privilege of working with several excellent undergraduate students (Ryan Hushagen, Gwénaél Bolloré, Robert Ellenwood, Donna Chow, Josh Eulert, and Erica Anderson) during their summer work terms and fourth year honors projects.

There are several people who directly contributed to the work presented in this thesis that I need to thank. Much of the initial exploratory synthetic work that eventually became the ternary rare-earth antimonide project was performed by an outstanding student, Ryan Hushagen. Gwénaél Bolloré was involved in some of the synthetic work for the  $RE_3MSb_5$  project during the first summer of work. Robert Ellenwood performed some of the first experiments that led to the identification of the  $REIn_{0.8}Sb_2$  series of compounds. The neutron diffraction and magnetic experiments presented in Chapter 6 were the result of a collaborative effort with Professor John Greedan (McMaster University). I must thank Prof. Greedan for inviting me to travel to Chalk River to participate in the neutron diffraction experiments, even though they were pre-empted by a strike at the facility! Finally, Arthur worked in the lab for the first few years and was always willing to help us with all aspects of the research, including much of the writing that eventually became this thesis. Thank you Arthur.





I have met lots of good people during my stay here and made lots of good friends. There is no better way to kill a beautiful summer afternoon than to spend it golfing with Chris Daley, Steve Decker, Jason Cooke, Michael Finot, Brian Sterenberg, and more recently, Robert Lam and Chris Lee. Thanks guys. Thanks also to Steve Trepanier for organizing the softball team and always providing words of encouragement and keeping the team spirit high, even when we were not so good. And who can forget our favorite American post-doc, Greg Ferrence, who introduced us to the fine art of skeet shooting and other firearm-related activities. I have to thank Jason “Raging Bull” Wiles for being equally enthralled by the shooting sports. A big thanks goes out to Richard Schutte for instituting the daily morning coffee to help us (Jason W., Chris D., Chris L., Rob, myself, and now Bryan Rowsell) start our day. Thanks go to Dr. Robert McDonald (Structure Determination Laboratory) for collecting X-ray data for us, for teaching me small molecule crystallography, and for our interesting and enlightening conversations with Steve T. There are too many other people to list here, but I think they should know who they are. I will, however, single out Jackie Jorgensen for all of the little things that she does to make our days more cheerful and our lives easier. Thank you so much Jackie.

I would like to thank my family for their support and encouragement throughout the course of my degree. Finally, I thank Elizabeth for her unfaltering love and support and for always believing in me.





## Table of Contents

<b>Chapter 1: Introduction</b>	1
Synthetic Techniques in Solid-State Chemistry	2
Characterization Techniques	4
Physical Properties of Solids	7
Low-Dimensional Materials	15
Ternary Rare-Earth Antimonides	17
References	25
<b>Chapter 2: A New Family of Non-Stoichiometric Layered Rare-Earth Tin Antimonides, <math>RESn_xSb_2</math> (<math>RE = La, Ce, Pr, Nd, Sm</math>): Crystal Structure of <math>LaSn_{0.75}Sb_2</math></b>	30
Introduction	30
Experimental Section	32
Synthesis	32
Structure Determination	34
Electrical Resistivity	38
Results and Discussion	40
Description of the Structure	40
Non-stoichiometry of Sn	44
Structural Relationships and Bonding	51
Electrical Resistivity	58
Implications	60
References	63
<b>Chapter 3: Mössbauer Spectroscopy and Magnetic Properties of <math>RESn_xSb_2</math> (<math>RE = La, Ce, Pr, Nd, Sm</math>): Crystal Structure of <math>LaSn_{0.6}Sb_2</math></b>	66
Introduction	66



Experimental Section .....	67
Synthesis .....	67
Structure Determination .....	68
Mössbauer Spectroscopy .....	72
Magnetic Measurements .....	72
Results and Discussion .....	72
Description of the Structure .....	72
Mössbauer Spectroscopy .....	78
Magnetic Properties .....	82
References .....	92

**Chapter 4: A New Rare-Earth Indium Antimonide,  $REIn_{1-x}Sb_2$  ( $RE = La, Ce, Pr, Nd$ ), Featuring In Zigzag chains and Sb Square Nets .....**

Introduction .....	94
Experimental Section .....	95
Synthesis .....	95
Structure Determination .....	98
Band Structure .....	101
Results and Discussion .....	103
Description of the Structure .....	103
Structural Relationships .....	107
Bonding and Band Structure .....	110
References .....	122

**Chapter 5: New Ternary Rare-Earth Transition-Metal Antimonides  $RE_3MSb_5$  ( $RE = La, Ce, Pr, Nd, Sm$ ;  $M = Ti, Zr, Hf, Nb$ ): Crystal Structures of  $La_3TiSb_5$ ,  $La_3ZrSb_5$ , and  $La_3HfSb_5$  .....**

Introduction .....	126
--------------------	-----





Experimental Section .....	128
Synthesis .....	128
Structure Determination .....	131
Electrical Resistivity .....	138
Band Structure .....	138
Results and Discussion .....	138
Description of the Structure .....	138
Structural Relationships and Bonding .....	141
Electrical Resistivity .....	145
Band Structure .....	150
References .....	157

<b>Chapter 6: Magnetism and Neutron Diffraction Studies of New Itinerant Electron Ferromagnetic Materials <math>REMSb_3</math> (<math>RE = La, Ce, Pr, Nd, Sm,</math> <math>Gd, Tb, Dy</math>; <math>M = V, Cr</math>) .....</b>	<b>161</b>
Introduction .....	161
Experimental Section .....	162
Synthesis .....	162
Structure Determination .....	164
Electrical Resistivity .....	167
Magnetic Susceptibility .....	169
Neutron Diffraction .....	169
Band Structure .....	169
Results and Discussion .....	169
Description of the Structure .....	169
Electrical Resistivity .....	175



Magnetic Measurements .....	177
Neutron Diffraction .....	179
Band Structure .....	192
References .....	198
<b>Chapter 7: Structural Relationships in Ternary Rare-Earth Antimonides .....</b>	<b>200</b>
References .....	209
<b>Appendix .....</b>	<b>212</b>





## List of Tables

<b>Table 1-1.</b> Selected Examples of Low-Dimensional Materials and their Properties .....	16
<b>Table 1-2.</b> Properties of Selected Ternary Rare-Earth Antimonides .....	24
<b>Table 2-1.</b> Crystallographic Data for $\text{LaSn}_{0.75(3)}\text{Sb}_2$ .....	35
<b>Table 2-2.</b> Atomic Coordinates, Occupancies, and Equivalent Isotropic Displacement Parameters ( $\text{\AA}^2$ ) for $\text{LaSn}_{0.75(3)}\text{Sb}_2$ .....	39
<b>Table 2-3.</b> Selected Interatomic Distances ( $\text{\AA}$ ) and Angles ( $^\circ$ ) for $\text{LaSn}_{0.75(3)}\text{Sb}_2$ .....	42
<b>Table 2-4.</b> Cell Parameters for Ternary $\text{LaSn}_{0.75}\text{Sb}_2$ -type Compounds Obtained from the Reactions $\text{La} + x\text{Sn} + 2\text{Sb}$ .....	47
<b>Table 2-5.</b> X-ray Powder Diffraction Data for Starting Composition $\text{LaSn}_{0.75}\text{Sb}_2$ .....	49
<b>Table 2-6.</b> Cell Parameters for Ternary $\text{LaSn}_{0.75}\text{Sb}_2$ -type Compounds Obtained from the Reactions $RE + \text{Sn} + 2\text{Sb}$ .....	56
<b>Table 3-1.</b> Crystallographic Data for $\text{LaSn}_{0.61(1)}\text{Sb}_2$ .....	69
<b>Table 3-2.</b> Atomic Coordinates, Occupancies, and Equivalent Isotropic Displacement Parameters ( $\text{\AA}^2$ ) for $\text{LaSn}_{0.61(1)}\text{Sb}_2$ .....	73
<b>Table 3-3.</b> Selected Interatomic Distances ( $\text{\AA}$ ) and Angles ( $^\circ$ ) for $\text{LaSn}_{0.61(1)}\text{Sb}_2$ .....	75
<b>Table 3-4.</b> Mössbauer Data for $\text{LaSn}_x\text{Sb}_2$ ( $0.1 \leq x \leq 1.0$ ) .....	80
<b>Table 3-5.</b> Magnetic Data for $RE\text{SnSb}_2$ ( $RE = \text{Ce, Pr, Nd, Sm}; x = 0.3, 0.7$ ) .....	86
<b>Table 4-1.</b> Cell Parameters for Ternary $RE\text{In}_{0.8}\text{Sb}_2$ Compounds .....	97
<b>Table 4-2.</b> Crystallographic Data for $\text{LaIn}_{0.81(1)}\text{Sb}_2$ .....	99
<b>Table 4-3.</b> Atomic Coordinates, Occupancies, and Equivalent Isotropic Displacement Parameters ( $\text{\AA}^2$ ) for $\text{LaIn}_{0.81(1)}\text{Sb}_2$ .....	102
<b>Table 4-4.</b> Extended Hückel Parameters .....	102
<b>Table 4-5.</b> Selected Interatomic Distances ( $\text{\AA}$ ) and Angles ( $^\circ$ ) for $\text{LaIn}_{0.81(1)}\text{Sb}_2$ .....	105
<b>Table 5-1.</b> Cell Parameters for Compounds $RE_3MSb_5$ ( $RE = \text{La, Ce, Pr, Nd, Sm}; M = \text{Ti, Zr, Hf, Nb}$ ) with the $\text{La}_3\text{TiSb}_5$ Structure .....	130
<b>Table 5-2.</b> Crystallographic Data for $\text{La}_3\text{TiSb}_5$ , $\text{La}_3\text{ZrSb}_5$ , and $\text{La}_3\text{HfSb}_5$ .....	132



<b>Table 5-3.</b> Atomic Coordinates, and Equivalent Displacement Parameters ( $\text{\AA}^2$ ) for $\text{La}_3\text{TiSb}_5$ , $\text{La}_3\text{ZrSb}_5$ , and $\text{La}_3\text{HfSb}_5$ .....	135
<b>Table 5-4.</b> Cell Parameters for $\text{La}_3\text{TiSb}_5$ from Variable Temperature Study .....	137
<b>Table 5-5.</b> Extended Hückel Parameters .....	137
<b>Table 5-6.</b> Selected Interatomic Distances ( $\text{\AA}$ ) for $\text{La}_3\text{MSb}_5$ ( $M = \text{Ti, Zr, Hf}$ ) .....	140
<b>Table 6-1.</b> Lattice Parameters for Compounds with $\text{REMSb}_3$ Structure .....	163
<b>Table 6-2.</b> X-ray Crystallographic Data for $\text{LaCrSb}_3$ .....	165
<b>Table 6-3.</b> Atomic Coordinates, and Equivalent Displacement Parameters ( $\text{\AA}^2$ ) for $\text{LaCrSb}_3$ from the X-ray Structure Determination .....	168
<b>Table 6-4.</b> Extended Hückel Parameters .....	168
<b>Table 6-5.</b> Selected Interatomic Distances ( $\text{\AA}$ ) and Angles ( $^\circ$ ) for $\text{LaCrSb}_3$ .....	170
<b>Table 6-6.</b> Profile Refinement Results for $\text{LaCrSb}_3$ and $\text{NdCrSb}_3$ .....	184
<b>Table 6-7.</b> Atomic Coordinates and Occupancies for $\text{LaCrSb}_3$ from Profile Refinements .....	185
<b>Table 6-8.</b> Atomic Coordinates and Occupancies for $\text{NdCrSb}_3$ from Profile Refinements .....	189
<b>Table A-1.</b> Anisotropic Displacement Parameters ( $\text{\AA}^2$ ) for $\text{LaSn}_{0.75}\text{Sb}_2$ .....	212
<b>Table A-2.</b> Anisotropic Displacement Parameters ( $\text{\AA}^2$ ) for $\text{LaSn}_{0.61}\text{Sb}_2$ .....	212
<b>Table A-3.</b> Powder X-ray Diffraction Data for $\text{LaIn}_{0.8}\text{Sb}_2$ .....	213
<b>Table A-4.</b> Powder X-ray Diffraction Data for $\text{CeIn}_{0.8}\text{Sb}_2$ .....	215
<b>Table A-5.</b> Powder X-ray Diffraction Data for $\text{PrIn}_{0.8}\text{Sb}_2$ .....	216
<b>Table A-6.</b> Powder X-ray Diffraction Data for $\text{NdIn}_{0.8}\text{Sb}_2$ .....	217
<b>Table A-7.</b> Anisotropic Displacement Parameters ( $\text{\AA}^2$ ) for $\text{LaIn}_{0.8}\text{Sb}_2$ .....	218
<b>Table A-8.</b> Anisotropic Displacement Parameters ( $\text{\AA}^2$ ) for $\text{La}_3\text{TiSb}_5$ , $\text{La}_3\text{ZrSb}_5$ , and $\text{La}_3\text{HfSb}_5$ for Data Collections at $-60^\circ\text{C}$ .....	222
<b>Table A-9.</b> Crystallographic Data for $\text{La}_3\text{TiSb}_5$ for Data Collection at $-170^\circ\text{C}$ .....	223



<b>Table A-10.</b> Atomic Coordinates and Equivalent Displacement Parameters ( $\text{\AA}^2$ ) for $\text{La}_3\text{TiSb}_5$ for Data Collection at $-170^\circ\text{C}$ .....	225
<b>Table A-11.</b> Anisotropic Displacement Parameters ( $\text{\AA}^2$ ) for $\text{La}_3\text{TiSb}_5$ for Data Collection at $-170^\circ\text{C}$ .....	225
<b>Table A-12.</b> Anisotropic Displacement Parameters ( $\text{\AA}^2$ ) for $\text{LaCrSb}_3$ .....	226





## List of Figures

<b>Figure 1-1.</b> Ternary rare-earth antimonides $RE_xM_ySb_z$ ( $M$ = transition metal or main-group metal) known prior to 1995. ....	18
<b>Figure 1-2.</b> Examples of low-dimensional Sb networks. ....	21
<b>Figure 2-1.</b> (a) View down the $c$ axis of $LaSn_{0.75}Sb_2$ with the unit cell outlined. (b) View down the $a$ axis. ....	41
<b>Figure 2-2.</b> Coordination of the La atom in $LaSn_{0.75}Sb_2$ . ....	43
<b>Figure 2-3.</b> Coordination of the Sn atoms in $LaSn_{0.75}Sb_2$ : (a) Sn(1) site; (b) Sn(2) site; (c) Sn(3) site. ....	45
<b>Figure 2-4.</b> Plots of the cell parameters of the ternary $LaSn_{0.75}Sb_2$ -type compounds obtained as a function of amount of Sn used, $x$ , in the reaction $La + xSn + 2Sb$ . ....	48
<b>Figure 2-5.</b> Comparison of various rare-earth diantimonide $RESb_2$ structures and the $LaSn_{0.75}Sb_2$ structure. ....	52
<b>Figure 2-6.</b> Plot of the unit cell volumes of $LaSn_{0.75}Sb_2$ -type compounds obtained from reactions $RE + Sn + 2Sb$ for various rare-earths. ....	57
<b>Figure 2-7.</b> Plot of the electrical resistivity of $LaSn_{0.75}Sb_2$ measured along the needle axis $a$ . ....	59
<b>Figure 3-1.</b> (a) View down the $c$ axis of $LaSn_{0.61}Sb_2$ with the unit cell outlined. (b) View down the $a$ axis. ....	74
<b>Figure 3-2.</b> Two possible arrangements of the Sn atoms in $LaSn_{0.61}Sb_2$ , with 15% occupancy of the Sn sites. ....	77
<b>Figure 3-3.</b> The calculated Mössbauer parameters (a) isomer shift ( $\delta$ ) and (b) quadrupole splitting ( $\Delta$ ), and (c) the relative intensity of the high velocity line plotted as a function of $x$ in $LaSn_xSb_2$ . ....	81
<b>Figure 3-4.</b> Plot of the magnetic susceptibility as a function of temperature for $LaSn_{0.7}Sb_2$ . ....	83
<b>Figure 3-5.</b> Plots of the temperature dependence of $\chi_M^{-1}$ and $\chi T$ for (a) $CeSn_{0.3}Sb_2$ and (b) $CeSn_{0.7}Sb_2$ . Plot of the isothermal magnetization for $CeSn_{0.7}Sb_2$ . ....	85
<b>Figure 3-6.</b> Plots of the temperature dependence of $\chi_M^{-1}$ and $\chi T$ for (a) $PrSn_{0.3}Sb_2$ and (b) $PrSn_{0.7}Sb_2$ . Plot of the isothermal magnetization for $PrSn_{0.7}Sb_2$ . ....	87



<b>Figure 3-7.</b> Plots of the temperature dependence of $\chi_M^{-1}$ and $\chi T$ for (a) $\text{NdSn}_{0.3}\text{Sb}_2$ and (b) $\text{NdSn}_{0.7}\text{Sb}_2$ . Plot of the isothermal magnetization for $\text{NdSn}_{0.7}\text{Sb}_2$ . ....	88
<b>Figure 3-8.</b> Plots of the temperature dependence of $\chi_M$ for (a) $\text{SmSn}_{0.3}\text{Sb}_2$ and (b) $\text{SmSn}_{0.7}\text{Sb}_2$ . Plot of the isothermal magnetization for $\text{SmSn}_{0.7}\text{Sb}_2$ . ....	90
<b>Figure 4-1.</b> (a) View down the $b$ axis of $\text{LaIn}_{0.8}\text{Sb}_2$ with the unit cell outlined. (b) View of the structure down the $a$ axis. ....	104
<b>Figure 4-2.</b> Coordination of the (a) La atom and (b) In atom in $\text{LaIn}_{0.8}\text{Sb}_2$ . ....	106
<b>Figure 4-3.</b> Comparison of the layered $\text{RE}_x\text{M}_y\text{Sb}_2$ structures: (a) $\text{REMSb}_2$ , (b) $\text{REIn}_{0.8}\text{Sb}_2$ , (c) $\text{RESn}_{0.75}\text{Sb}_2$ . ....	108
<b>Figure 4-4.</b> Comparison of the ideal square $\text{MSb}$ layer in $\text{LaCd}_{0.7}\text{Sb}_2$ to the distorted layer in $\text{LaIn}_{0.8}\text{Sb}_2$ . ....	111
<b>Figure 4-5.</b> (a) Total density of states and (b) – (d) the individual atomic contributions (La, In, Sb) to the density of states for $\text{LaIn}_{0.8}\text{Sb}_2$ . ....	115
<b>Figure 4-6.</b> Band dispersion curves for $\text{LaIn}_{0.8}\text{Sb}_2$ along the special symmetry lines $\Gamma\text{X}$ , $\Gamma\text{Y}$ , and $\Gamma\text{Z}$ . ....	116
<b>Figure 4-7.</b> Crystal orbital overlap population curves for the In–In, In–Sb(1), and Sb(2)–Sb(2) interactions. ....	117
<b>Figure 4-8.</b> View of an ordered In chain with every fifth site vacant, as indicated by the dotted hollow circles. ....	119
<b>Figure 5-1.</b> View down the $c$ axis of $\text{La}_3\text{MSb}_5$ with the unit cell outlined. ....	139
<b>Figure 5-2.</b> View projected approximately (110) showing a column of face-sharing $\text{MSb}_6$ octahedra and a chain of Sb(2) atoms, both running along $c$ axis. ....	142
<b>Figure 5-3.</b> Coordination of the La atoms in $\text{La}_3\text{MSb}_5$ . ....	143
<b>Figure 5-4.</b> Plot of the unit cell volume for $\text{RE}_3\text{MSb}_5$ compounds. ....	146
<b>Figure 5-5.</b> Plot of the electrical resistivity measured along the needle $c$ axis for (a) $\text{La}_3\text{TiSb}_5$ , (b) $\text{Ce}_3\text{TiSb}_5$ , (c) $\text{Pr}_3\text{TiSb}_5$ , and (d) $\text{Nd}_3\text{TiSb}_5$ . ....	147
<b>Figure 5-6.</b> Plot showing the fit of the low-temperature resistivity data of $\text{Ce}_3\text{TiSb}_5$ to $\rho = \rho_0 + \alpha T^2$ . ....	149
<b>Figure 5-7.</b> (a) Total density of states and (b) – (d) the individual atomic contributions (La, Ti, Sb) to the density of states for $\text{La}_3\text{TiSb}_5$ . ....	151





<b>Figure 5-8.</b> (a) Band dispersion curves for $\text{La}_3\text{TiSb}_5$ along the special symmetry lines $\Gamma\text{K}$ , $\text{KM}$ , $\text{M}\Gamma$ , $\Gamma\text{A}$ , and $\text{AL}$ . (b) A representation of the hexagonal Brillouin zone with the irreducible wedge outlined. ....	153
<b>Figure 5-9.</b> Crystal orbital overlap population curves for the $\text{Ti-Sb}$ , $\text{Ti-Ti}$ , and $\text{Sb(2)-Sb(2)}$ interactions in $\text{La}_3\text{TiSb}_5$ . ....	155
<b>Figure 6-1.</b> View down the $c$ axis of $\text{LaCrSb}_3$ with the unit cell outlined. ....	171
<b>Figure 6-2.</b> Plot of the unit cell volume for $\text{REMSb}_3$ compounds. ....	174
<b>Figure 6-3.</b> (a) Plot of the electrical resistivity for $\text{LaCrSb}_3$ measured along the needle $c$ axis. The inset shows the temperature dependence of $d\rho/dT$ . (b) Fit of the low-temperature data to $\rho = \rho_0 + \alpha T^2$ . ....	176
<b>Figure 6-4.</b> (a) Plot of the magnetic susceptibility of $\text{LaCrSb}_3$ as a function of temperature. (b) Isothermal magnetization of $\text{LaCrSb}_3$ at 5 and 300 K. (c) Inverse susceptibility for $\text{LaCrSb}_3$ over the temperature range 25–700 K. ....	178
<b>Figure 6-5.</b> (a) Plot of the magnetic susceptibility of $\text{NdCrSb}_3$ as a function of temperature. (b) Isothermal magnetization of $\text{NdCrSb}_3$ at 4.8 K. ....	180
<b>Figure 6-6.</b> Plot of the neutron diffraction data for $\text{LaCrSb}_3$ near the 100 reflection at 25 and 150 K. ....	182
<b>Figure 6-7.</b> Rietveld refinement results for $\text{LaCrSb}_3$ at 5 K. ....	183
<b>Figure 6-8.</b> Plot showing the temperature dependence of the 100 reflection for $\text{LaCrSb}_3$ . ....	186
<b>Figure 6-9.</b> Plots showing the temperature dependence of the unit cell constants for $\text{LaCrSb}_3$ . ....	187
<b>Figure 6-10.</b> Plot showing the temperature dependence of the 111 and 100 reflections for $\text{NdCrSb}_3$ . ....	190
<b>Figure 6-11.</b> Rietveld refinement results for $\text{NdCrSb}_3$ at (a) 51 K and (b) 4 K. ....	191
<b>Figure 6-12.</b> (a) Total density of states and (b) – (d) the individual atomic contributions (La, Cr, Sb) to the density of states for $\text{LaCrSb}_3$ . ....	193
<b>Figure 6-13.</b> Band dispersion curves for $\text{LaCrSb}_3$ along the special symmetry lines $\Gamma\text{X}$ , $\Gamma\text{Y}$ , and $\Gamma\text{Z}$ . ....	194
<b>Figure 6-14.</b> Crystal orbital overlap population curves for the $\text{Cr-Cr}$ , $\text{Sb(1)-Sb(2)}$ and $\text{Sb(3)-Sb(3)}$ interactions in $\text{LaCrSb}_3$ . ....	197



<b>Figure 7-1.</b> Known ternary rare-earth antimonides $RE_xM_ySb_z$ ( $M$ = transition metal or main-group metal). .....	201
<b>Figure 7-2.</b> Coordination geometries of $RE$ atom in $RE_xM_ySb_z$ structures. ....	204
<b>Figure 7-3.</b> Comparison of various ternary rare-earth antimonides $RE_xM_ySb_z$ with low-dimensional structures. ....	206
<b>Figure A-1.</b> (a) Total density of states and (b) – (d) the individual atomic contributions (La, In, Sb) to the density of states for the ordered superstructure $LaIn_{0.75}Sb_2$ . ....	219
<b>Figure A-2.</b> Band dispersion curves for the ordered superstructure $LaIn_{0.75}Sb_2$ along the special symmetry lines $\Gamma X$ , $\Gamma Y$ , and $\Gamma Z$ . ....	220
<b>Figure A-3.</b> Crystal orbital overlap population curves for the In–In, In–Sb(1), and Sb(2)–Sb(2) interactions for the ordered superstructure $LaIn_{0.75}Sb_2$ . ....	221



## List of Abbreviations and Symbols

ac	alternating current	Hz	hertz
anal.	analysis	$k$	Boltzmann's constant
arb. units	arbitrary units	K	Kelvin
$\chi$	magnetic susceptibility	$\rho$	electrical resistivity
C	Celsius	$M$	magnetization
$C$	Curie constant	$\mu_B$	Bohr magneton
calcd	calculated	$\mu_{\text{eff}}$	effective magnetic moment
COOP	crystal orbital overlap population	$\mu_{\text{sat}}$	saturation magnetic moment
DOS	density of states	$N$	Avogadro's number
$\varepsilon_f$	Fermi level	$\theta$	Weiss temperature
EDX	energy dispersive X-ray	$T$	temperature
emu	electromagnetic unit	T	tesla
eV	electron volt	$\Omega$	ohm
f.u.	formula unit		
$H$	magnetic field strength		





## List of Crystallographic Abbreviations and Symbols

$a, b, c$	lengths of basis vectors, lengths of cell edges
$\alpha, \beta, \gamma$	interaxial (lattice) angles between $b$ and $c$ , $a$ and $c$ , and $a$ and $b$ axes, respectively
$\text{\AA}$	angström
$d$	interplanar distance, or spacing, of neighboring net planes ( $hkl$ )
$F_c$	calculated structure factor
$F_o$	observed structure factor
$hkl$	indices of the Bragg reflection (Laue indices) from the set of parallel equidistant net planes ( $hkl$ )
$(hkl)$	indices of a crystal face, or of a single net plane (Miller indices)
$[hkl]$	indices of a lattice direction
$\lambda$	wavelength
$\mu$	linear absorption coefficient
$P$	experimental instability factor in weighting scheme (used in the calculation of $\sigma(I)$ to downweight intense reflections)
$R$	residual index
$R_w$	weighted residual index
$R_{\text{int}}$	residual index for averaged symmetry equivalent reflections
$\rho$	density
$\sigma$	standard deviation
$U_{\text{eq}}$	equivalent isotropic atomic displacement parameter
$U_{ij}$	elements of anisotropic atomic displacement parameter tensor
$V$	cell volume of the direct lattice
$w$	weighting factor applied to structure factor
$Z$	number of formula units per unit cell



# Chapter 1

## Introduction

New materials drive the growth of civilization, a fact recognized by both anthropologists and archaeologists, who traditionally group together cultures based on the principal material used for their tools and ornaments.<sup>1</sup> During the Stone Age, flaked and polished stones were used and pottery was developed; copper was discovered next, and the realization that it could be shaped when heated ushered in the Bronze and Iron Ages, with the development of alloying and metallurgy.<sup>1</sup> We now find ourselves in the age of the semiconductors, which are found in everyday devices such as televisions, telephones, and computers, to name but a few. Curiosity and inquisitiveness of the surrounding world have always played a vital role in humankind's successes.

Materials research encompasses a wide range of disciplines, spanning metallurgical engineering, condensed matter physics, solid-state chemistry, and even molecular chemistry as it pertains to assemblies of molecules in the solid state. The traditional role of chemistry as the central science is vitally evident in the solid-state community, bridging together physicists, who seek an understanding of matter at its smallest level, and engineers, who try to develop new technology and applications. The solid-state chemist is responsible for synthesizing new materials, determining their structures, understanding their bonding, and measuring and explaining their physical properties. This certainly is not a small undertaking. The ultimate goal is to develop structure-property relationships – to understand why a particular compound exhibits a particular property, and to predict new materials with desirable characteristics.



The largest class of materials are undoubtedly the inorganic oxides and ceramics, owing to the natural tendency of the elements to react with ambient oxygen, and these have been extensively studied. At first glance, one might expect these materials to have rather uninteresting properties; when one thinks of ceramics, typically what comes to mind are materials that are both thermal and electronic insulators. However, many oxides exhibit interesting and unusual properties, including giant and colossal magnetoresistance in the lanthanum manganese perovskites ( $\text{LaMnO}_3$ ),<sup>2</sup> ferroelectricity in barium titanate ( $\text{BaTiO}_3$ ),<sup>3</sup> piezoelectricity in the lead zirconate titanate solid solution ( $\text{PbZrO}_3\text{--PbTiO}_3$ ),<sup>3</sup> and even superconductivity observed in the rare-earth cuprate systems.<sup>4</sup>

But why limit ourselves to compounds of oxygen? There are over 90 other elements and an infinite number of combinations and permutations to study. Intermetallic systems, too, have technologically important roles, exemplified by the superconducting compounds  $\text{Nb}_3\text{Sn}$  and  $\text{Nb}_3\text{Ge}$ .<sup>5</sup> Modern NMR spectroscopy, arguably the most powerful characterization technique for molecular chemists, would not be possible without the superconducting technology which relies on an intermetallic material that is the combination of two metals, with a deceptively simple structure, and when cooled generate huge, stable magnetic fields.<sup>5</sup>

### **Synthetic Techniques in Solid-State Chemistry<sup>3</sup>**

Before materials can be used in real-world applications, they first have to be created. The synthetic techniques employed in solid-state chemistry are unusual when compared to the traditional wet-chemistry methods. The method of choice is typically





the direct reaction of solid starting materials, either as powders of the elements or precursor compounds. However, there are huge barriers that need to be overcome to coerce solids to react together, which can usually be surmounted by simply heating the reaction mixture at high temperatures ( $>800\text{ }^{\circ}\text{C}$ ) for several days. Even though many of the reactions may be thermodynamically favored, they are kinetically extremely slow at normal temperatures, due in part to the very slow diffusion of atoms through solids. These problems are not unique to the synthesis of extended solids; the same difficulty would arise if one were to attempt the direct reaction of molecular solids. With judicious choice of solvent, however, the solid can be dissolved and the reactants brought into intimate contact. The solid-state approach is to grind the starting materials together into a very fine powder which greatly increases the surface area of the reactants, thereby allowing the solids to be in much closer contact and enhancing the rate of reaction. Consider a reaction occurring at the interface of two crystals – the product forms a layer between the crystals. If these crystals were ground to a powder, the number of interfaces at which the reaction occurs will increase dramatically. Furthermore, the kinetics are influenced by two factors: the rates of nucleation and diffusion. Nucleation of the product is primarily affected by the energetics of the structural reorganization of the reactants on their way to products. If the product is structurally very different from both of the reactants, many bonds will have to be broken before the product can form. As the initial product layer begins to grow, the reactants will have to diffuse through the layer to reach each other and continue the reactions. These difficulties can often be overcome by repeated grinding and heating cycles, which may also help form a homogeneous product.



The reaction timescale can be reduced by rapid melting of the starting materials in an arc-furnace, which uses an electric arc with temperatures  $>2000\text{ }^{\circ}\text{C}$  to quickly melt a pressed pellet of the reactants. Instead of taking days, the reactions take only seconds. This provides a quick method for exploring a new system, but it is not ideal for growing single crystals and frequently leads to products that are not single phase.

Although crystal growth is possible from direct reactions of powders, the typical products are themselves polycrystalline powders. Low-melting fluxes are often employed in the reactions, which yield single crystals suitable for X-ray diffraction and physical property measurements. A desirable flux should be non-reactive and easy to remove once the reaction is completed. In particular, Sn fluxes have been successfully used for growing large crystals of phosphides, and have been extended to systems of arsenides and antimonides.

## **Characterization Techniques<sup>6</sup>**

Extended solids present unique difficulties for their characterization that are not encountered in molecular or solution chemistry. Although routine techniques such as NMR and IR spectroscopy can be useful for elucidating the structures of insulating and nonmagnetic oxides, these techniques are generally not suitable for intermetallic compounds. Instead, the principal means of characterization is powder X-ray diffraction, supplemented by single crystal X-ray diffraction and elemental analysis from electron microscopy.



Powder X-ray diffraction is useful because it is a phase identification technique based on pattern-matching, but it is not a method for determining chemical identity. Every crystalline solid has its own unique powder pattern which serves as its fingerprint. Since the typical products from solid-state reactions are multiphase powders, the chemist can, in one step, identify all phases in the product by comparing the powder pattern against those for known compounds. As such, powder diffraction can be used to assess the relative purity of samples, with detection limits typically better than five percent. Moreover, the lattice constants determined from powder diffraction are significantly more accurate than those obtained from single crystal diffraction. Thus, the extent of solid solution formation can be investigated by the variation in the lattice constants with composition. Finally, structures can be refined using data from powder diffractometers, in principle, provided the structure is reasonably simple or if a good model for the structure is known *a priori*.

If crystals of the product are available, the structure is usually solved using single crystal X-ray diffraction. The crystals are screened using photographic methods which provide preliminary lattice constants and information about the crystal symmetry and space group. This information can be used in conjunction with a literature search for related structures, which can be extremely helpful when problems are encountered during structure solution. Ultimately, the structure is solved and refined using data from a diffractometer.

Although X-ray diffraction is the most commonly used technique, the wave properties of both electrons and neutrons can be exploited. While X-rays interact with





the electron clouds of the scattering atoms, whose scattering power follows a strict relation with atomic number, neutrons are scattered by the atomic nuclei, without any regular trend with atomic number. Neutrons therefore have the ability to distinguish between neighboring elements in the periodic table, such as Sn and Sb, while X-rays cannot. Furthermore, neutrons possess a magnetic moment and are scattered by magnetic ions; neutron diffraction can therefore be used to determine the magnetic structure of a compound.

Elemental compositions of crystals are typically found by analyses of the X-ray fluorescence spectra obtained from scanning electron microscopy. A high energy electron beam is directed at the sample, causing inner core electrons (for example, 1s) to be ejected from the atoms. Electrons from higher energy levels then fill the holes and release their excess energy as X-ray photons, with wavelengths characteristic of the particular atom. Thus, one can qualitatively determine the presence (or absence) of the elements, and therefore determine if the product contains all of the desired components. If suitable standards are available, quantitative analysis can also be performed and the results can be compared to that obtained from the crystal structure, for instance.

Several elements possess Mössbauer active nuclei, which undergo nuclear transitions with energies corresponding to the absorption of  $\gamma$ -rays. Mössbauer spectroscopy can give information about the electronic environment at the nuclei, providing a means to determine oxidation states. Furthermore, it is sensitive to the presence of electric field gradients and magnetic interactions at the nuclei, which can yield information about the coordination environment. The source of the  $\gamma$ -rays are



radioactive isotopes of the element of interest and the  $\gamma$ -rays emitted are essentially monochromatic. The energy of the emitted  $\gamma$ -rays must be tuned to the appropriate energy needed to excite the analyte, and is modulated by the Doppler effect. Mössbauer spectra yield two important parameters, the isomer shift ( $\delta$ ) and the quadrupole splitting ( $\Delta$ ). The isomer shift is the position of the absorption line relative to that of the source, and depends on the s-electron density at the nucleus (*i.e.* the oxidation state). For nuclei with a quadrupole moment ( $I > \frac{1}{2}$ ) in either the ground or excited state, the presence of an electric field gradient at the nucleus removes the degeneracy of that state, which separates into two (or more) energy levels. The absorption line is therefore split into a doublet (or higher multiplet), and the degree of separation is the quadrupole splitting. Since molecules with octahedral or tetrahedral symmetry do not have an electric field gradient, only molecules of lower symmetry will display quadrupole splitting.

### Physical Properties of Solids

Solids are interesting because of their physical properties, which can be broadly divided into two categories, mechanical and electronic. The obvious exploitation of the mechanical properties is as building materials, such as the concrete and steel used in high-rise buildings. For many applications, however, one needs to be concerned with both the strength and weight of a material. This is certainly the case for both the automotive and aerospace industries, where steel is being replaced by aluminum-lithium alloys, carbon-fiber composites, and plastics.<sup>7</sup>



However, of greater interest to the solid-state chemist are the physical properties that emerge as a result of the electronic structure of the material, which is intimately related to its crystal structure. These include electronic transport, dielectric, magnetic, and optical properties to name a few, and lead to technological applications such as lasers and superconducting magnets. Nevertheless, when choosing a material for a particular application, it is necessary to consider the physical robustness of the material too. To stay within the scope of the research presented in this thesis, only the electrical conductivity and magnetic behavior will be discussed.

*Conductivity.*<sup>8</sup> The ability of a solid to carry an electrical current is quantified by its conductivity,  $\sigma$ , or resistivity,  $\rho$ , given by

$$\sigma = \frac{1}{\rho} = ne\mu$$

where  $n$  and  $e$  are the number and charge of the carriers, and  $\mu$  is the mobility of the carriers. In most cases, the carriers are electrons and therefore  $e$  is constant and independent of temperature. There are three classifications for solids based on the magnitude and temperature dependence of their electrical conductivities: (1) metals, with typical values between  $10^1$  and  $10^5 \Omega^{-1} \text{ cm}^{-1}$ , (2) insulators, with values less than  $10^{-12} \Omega^{-1} \text{ cm}^{-1}$ , and (3) semiconductors, with values between  $10^{-5}$  and  $10^2 \Omega^{-1} \text{ cm}^{-1}$ .

The high conductivity (or conversely, low resistivity) observed for metals arises from partially filled, overlapping bands, through which the electrons are able to move and thus carry a current. For metals,  $n$  is essentially independent of temperature. The major factor affecting the conductivity is  $\mu$ , which increases as temperature decreases.





Electrons are scattered and their mobility can be impeded by imperfections or impurities in the crystal, which are essentially constant and independent of temperature, and by lattice vibrations, which decrease as temperature decreases. Since one normally measures the resistance of materials and not their conductance, the resistivity of metals can be expressed by

$$\rho = \rho_{\text{imp}} + \rho_{\text{vib}}$$

where  $\rho_{\text{imp}}$  is the resistivity due to impurities and  $\rho_{\text{vib}}$  is the resistivity due to the scattering of electrons by lattice vibrations. The resistivity decreases linearly with temperature and essentially reaches a plateau at low temperature with a value  $\sim \rho_{\text{imp}}$ .

Insulators and semiconductors have a completely filled valence band and an empty conduction band, separated by a band gap ( $E_g$ ); the division between insulators and semiconductors is based on the value of  $E_g$ , with a lower limit of  $\sim 3$  eV for insulators. For insulators, the band gap is large ( $E_g > 3$  eV) and at ambient conditions there is a negligible population of electrons in the conduction band. The number of carriers,  $n$ , is essentially zero, and therefore the conductivity is extremely low. For semiconductors, the band gap is much smaller, such that the conduction band is thermally accessible under ambient conditions. The exponential increase in the number of carriers in semiconductors with increasing temperature strongly outweighs the decrease in  $\mu$  due to phonon scattering. The net effect is that the conductivity increases with increasing temperature, or conversely, the resistivity increases with decreasing temperature.

These differences in electronic conductivity emerge from differences between the material's band structure. This is illustrated using the Group 4 elements, carbon, silicon,



and germanium, as the standard example. Carbon with the diamond structure is a transparent, colorless insulator with a band gap greater than 6 eV, whereas carbon with the graphite structure is a black conductor. Changing the crystal structure changes the electronic structure, which ultimately affects the behavior of the material. Both Si and Ge crystallize with the diamond structure, yet while diamond is an insulator, Si and Ge are semiconductors with band gaps of 1.1 and 0.7 eV respectively. Moreover, the nature of the charge carriers in semiconductors can be modified to be either negatively charged electrons (n-type semiconductors) or positively charged holes (p-type) by introducing impurities (doping). The properties at the junction of these two types of semiconductors when they are brought in contact serve as the foundation of the entire solid-state electronics industry, leading to devices such as diodes, LEDs, and transistors.

Electrons are not the only means for carrying a current in a solid. If the material contains a large number of mobile ions and an open framework structure, then ionic conduction may occur. Ideally, such a material should have a large number of vacant sites with similar potential energy, through which the mobile ions can easily move. The number of ions and their mobility are strongly temperature dependent, both increasing with temperature, thereby enhancing the conductivity. An important application for such compounds are Li ion batteries, which theoretically can have a very high charge density and thus efficiently store energy, suitable for batteries in electric cars.

*Magnetism.*<sup>9</sup> All substances can be classified as diamagnetic or paramagnetic depending on their behavior when they are placed in a magnetic field. If a material does not contain any unpaired electrons, it is weakly repelled by a magnetic field, and is called



diamagnetic. All atoms have an intrinsic or core diamagnetism, arising from the inner closed shells of electrons, and especially in the case of molecular compounds, the magnetic data need to be corrected for this. Compounds with unpaired electrons, however, are attracted into a magnetic field and are called paramagnetic. Interactions between these unpaired electrons can lead to several interesting possibilities: (1) parallel alignment of the spins of the electrons gives ferromagnetism, (2) antiparallel alignment of the spins gives antiferromagnetism, and (3) antiparallel alignment of unequal spins from different ions (for example  $\text{Fe}^{2+}/\text{Fe}^{3+}$ ) gives ferrimagnetism. These interactions result in different behavior for each class of magnetism, and therefore lead to different applications for each.

It is necessary to briefly consider some of the theoretical aspects of magnetism. When a sample is placed within a magnetic field,  $H$ , the magnetic induction,  $B$ , inside the sample is given by

$$B = H + 4\pi M$$

where  $M$  is the magnetic moment per unit volume of the sample. A useful quantity is the magnetic susceptibility, which is the response of a material to an applied magnetic field, and is given by

$$\chi = \frac{M}{H}.$$

Materials can be classified based on their value of  $\chi$  and its variation with temperature. Diamagnetic materials have a small, negative  $\chi$ , whose value is essentially independent of temperature. Paramagnetic, ferromagnetic, antiferromagnetic, and ferrimagnetic



materials have positive  $\chi$  values, but their relative values and temperature dependence differ dramatically.

The simplest case is paramagnetism, which involves non-interacting spins that are randomly oriented in the absence of a magnetic field ( $H$ ), but in the presence of an applied field align either parallel or antiparallel with  $H$ . The energy difference between the two configurations is small relative to the thermal energy,  $kT$ , at room temperature; both states are populated and the net susceptibility is small. As the temperature decreases, the lower energy state (parallel to  $H$ ) becomes more populated and the susceptibility increases. This temperature dependence is described by the Curie law

$$\chi = \frac{C}{T}$$

where  $C$  is the Curie constant

$$C = \frac{N\mu_B^2\mu_{\text{eff}}^2}{3k}$$

and  $N$  is Avogadro's number,  $\mu_B$  is the Bohr magneton,  $k$  is Boltzmann's constant and  $\mu_{\text{eff}}$  is the effective magnetic moment given by

$$\mu_{\text{eff}} = g\sqrt{J(J+1)}$$

where  $g$  is the Landé splitting factor

$$g = \frac{3J(J+1) + S(S+1) - L(L+1)}{2J(J+1)}$$

and  $J$ ,  $S$ , and  $L$  are the total angular, spin angular, and orbital angular momenta, respectively. The magnetic behavior of a material is simply related to the electron configuration of the magnetic ions within the material, and for the heavier elements





(especially the rare-earth metals), the value of  $\mu_{\text{eff}}$  calculated based on  $J$  agrees well with that obtained from experiment. In many other cases, particularly for the first-row transition metals, the orbital angular momentum is quenched ( $L = 0$ ) and the effective moment formula simplifies to the so-called spin-only formula

$$\mu_{\text{eff}} = 2\sqrt{S(S+1)} .$$

By measuring the susceptibility as a function of temperature, an experimentally determined moment can be extracted from the fit of the data to the Curie law. This value can be compared to the expected moment for a given electronic configuration, and thus information about the oxidation state of the magnetic ion(s) can be obtained.

A special type of paramagnetism called Pauli paramagnetism arises in metals due to the magnetic moment of the conduction electrons. Only those electrons with energies close to the Fermi energy are affected by a magnetic field, and the resulting magnetic susceptibility is small and essentially independent of temperature. In the presence of a magnetic field ( $H$ ), there is a slight displacement from the equilibrium population of electrons with spins aligned parallel with  $H$  versus those with spins aligned antiparallel with  $H$ , and this imbalance leads to a small magnetic susceptibility.

For ferromagnetic materials, the magnetic ions are coupled via an exchange interaction, resulting in parallel alignment of the moments. A critical temperature exists (Curie temperature,  $T_C$ ), above which the material is paramagnetic and the temperature dependence of the susceptibility can be described by the Curie-Weiss law

$$\chi = \frac{C}{T - \theta}$$



where  $\theta$  (the Weiss temperature) is positive and is an indication of the strength of interaction between the magnetic ions. Below  $T_C$ , the moments spontaneously align parallel with each other and  $\chi$  increases sharply, and the temperature dependence no longer follows the Curie-Weiss law. Eventually,  $\chi$  reaches a saturation value as all of the moments are aligned. The saturation moment,  $\mu_{\text{sat}}$ , differs from the effective moment, and is given by

$$\mu_{\text{sat}} = gJ.$$

Ferromagnetic materials are useful because once magnetized, they remain so until heated above their  $T_C$  or a sufficiently strong magnetic field (the coercive force) is applied in the opposite direction. This behavior can be studied through isothermal magnetization (hysteresis) curves, with magnetization plotted as a function of applied field.

Antiferromagnetic materials are similar to ferromagnetic materials in the sense that an exchange interaction is present which couples the magnetic ions. However, this exchange interaction causes the magnetic moments to align in an antiparallel fashion. Above the critical temperature (Néel temperature,  $T_N$ ), the material is paramagnetic and follows the Curie-Weiss law, although  $\theta$  is now negative. Below  $T_N$ , the magnetic moments interact, causing  $\chi$  to decrease and eventually approach zero.

Ferrimagnetism is a special case of antiferromagnetism, with two different magnetic sublattices aligned antiparallel to each other. Because the two sublattices are different and possess different magnetic moments, a net permanent magnetization results when the material is cooled below the critical temperature. For example, the spinel ferrite,  $\text{Fe}^{\text{II}}(\text{Fe}^{\text{III}})_2\text{O}_4$ , has one sublattice of  $\text{Fe}^{\text{II}}$  ions and a second of  $\text{Fe}^{\text{III}}$  ions. When



magnetized, these materials show similar behavior to ferromagnets, although the overall temperature dependence can be quite complex owing to different ordering temperatures for each sublattice.

## **Low-Dimensional Materials**

Low-dimensional materials are those which possess strongly one- or two-dimensional structural features, either as chains or layers, with covalent bonding within and van der Waals or ionic bonding between. Frequently, these materials exhibit phenomena such as anisotropic transport properties, complex magnetic ordering, and phase transitions associated with charge density wave formation.<sup>10-12</sup> Several examples of low-dimensional materials are listed in Table 1-1, along with their properties. One-dimensional materials are inherently prone to undergo Peierls (one-dimensional Jahn-Teller) distortions, leading to metal-to-insulator/semiconductor transitions.<sup>12</sup> Probably the most extensively investigated material is NbSe<sub>3</sub>, owing to two anomalies in the resistivity data that have been shown to arise from the formation of charge density waves.<sup>12</sup> The conduction in low-dimensional materials typically occurs through the chains or layers, while the resistivity between the chains or layers is orders of magnitude larger. This has been studied by the intercalation of organic molecules between the layers of Nb or Ta dichalcogenides, which leads to large interlayer separations.<sup>10</sup> The resistivity data indicate that while these compounds are metallic within the layers, they are semi-metallic to semiconducting between. Furthermore, some of these materials may even become two-dimensional superconductors at low temperatures.<sup>10</sup>





**Table 1-1.** Selected Examples of Low-Dimensional Materials and their Properties

Compound	Type	Properties
$MX_3$ ( $M = \text{Ti, Zr, Hf}; X = \text{S, Se}$ )	1-D	diamagnetic semiconductor; intercalation of alkali metals
$\text{NbSe}_3$	1-D	1-D metal; charge density waves; reversible intercalation of alkali metals
graphite	2-D	2-D semi-metal; intercalation of alkali metals
$\text{TiSe}_2$	2-D	charge density waves
$\text{NbSe}_2$	2-D	2-D superconductor
$\text{TaS}_2$	2-D	2-D metal; intercalation of alkali metals and organic molecules



## Ternary Rare-Earth Antimonides

The incorporation of rare-earth elements is a common strategy employed by solid state chemists wishing to design materials requiring subtle steric and electronic control to obtain desired structures and properties. One need only cite the torrent of activity associated with the high- $T_c$  rare-earth cuprate superconductors, for instance. From a structural standpoint, the rare-earth elements, serving as cations, are useful in stabilizing low-dimensional features, such as layers or chains, in the anionic component. They also provide a means of steric control, owing to the similar chemical reactivity of the entire series; the layers or chains can be extended or compressed by doping or substitution of one rare-earth for another, and may also influence the ionic interactions. Moreover, the  $f$ -electrons of the rare-earth metals are often responsible for the manifestation of unusual physical behavior, including heavy fermions, mixed valency, magnetic ordering, and the Kondo effect.<sup>13</sup> Interest in ternary rare-earth antimonides, which are not as well investigated as the corresponding phosphides or arsenides, stems from the desire to discover new low-dimensional compounds whose properties may be expected to be highly anisotropic and to lie in the metallic or semimetallic regime.

Figure 1-1 shows all the ternary rare-earth antimonides,  $RE_xM_ySb_z$  (where  $RE$  is a rare-earth metal and  $M$  is a transition metal or a main-group metal) that were reported prior to 1995.<sup>14-36</sup> Many of these compounds can be viewed as low-dimensional materials, composed of anionic chains or layers that are separated by the rare-earth cations. Furthermore, in some of these compounds, low-dimensional networks of antimony atoms can be identified, appearing as one-dimensional zigzag or linear chains



**Figure 1-1.** Ternary rare-earth antimonides  $RE_xM_ySb_z$  ( $M$  = transition metal or main-group metal) known prior to 1995. Two-dimensional structures ( $REMSb_2$ ,<sup>14-17</sup>  $REM_2Sb_2$ <sup>18-24</sup>) are adopted by compounds of the elements enclosed by a double-lined border, and three-dimensional structures ( $REM_4Sb_{12}$ ,<sup>25</sup>  $RE_3M_3Sb_4$ ,<sup>26-28</sup>  $REMSb$ <sup>29-35</sup>) in the shaded boxes. One-dimensional structures are not adopted by any of the compounds. By one- and two-dimensional are meant those structures in which chains and layers can be perceived as obvious building elements, respectively.  $RE_{14}MSb_{11}$  ( $RE = Eu$ ) is also known but consists of discrete molecular species.<sup>36</sup> No ternary rare-earth antimonides are known for elements in the empty boxes.



Ti	V	Cr	Mn <i>REMSb<sub>2</sub></i> <i>REM<sub>2</sub>Sb<sub>2</sub></i>	Fe <i>REMSb<sub>2</sub></i> <i>REM<sub>4</sub>Sb<sub>12</sub></i>	Co <i>REMSb<sub>2</sub></i>	Ni <i>REMSb<sub>2</sub></i> <i>REM<sub>2</sub>Sb<sub>2</sub></i> <i>REMSb</i>	Cu <i>REMSb<sub>2</sub></i> <i>REM<sub>2</sub>Sb<sub>2</sub></i> <i>RE<sub>3</sub>M<sub>3</sub>Sb<sub>4</sub></i> <i>REMSb</i>	Zn <i>REMSb<sub>2</sub></i> <i>REM<sub>2</sub>Sb<sub>2</sub></i>	Ga	Ge
Zr	Nb	Mo	Tc	Ru <i>REM<sub>4</sub>Sb<sub>12</sub></i>	Rh	Pd <i>REMSb<sub>2</sub></i> <i>REM<sub>2</sub>Sb<sub>2</sub></i> <i>REMSb</i>	Ag <i>REMSb<sub>2</sub></i> <i>REMSb</i>	Cd <i>REMSb<sub>2</sub></i>	In	Sn
Hf	Ta	W	Re	Os <i>REM<sub>4</sub>Sb<sub>12</sub></i>	Ir	Pt <i>RE<sub>3</sub>M<sub>3</sub>Sb<sub>4</sub></i> <i>REMSb</i>	Au <i>REMSb<sub>2</sub></i> <i>RE<sub>3</sub>M<sub>3</sub>Sb<sub>4</sub></i> <i>REMSb</i>	Hg	Tl	Pb

1 D	2 D	2 D 3 D	3 D
-----	-----	------------	-----





and two-dimensional square sheets. Several examples of such networks are shown in Figure 1-2.<sup>14-17,37-39</sup> For instance, two-dimensional square sheets are found in  $REMSb_2$  ( $M = Mn-Zn, Pd, Ag, Cd, Au$ ), with Sb–Sb distances of  $\sim 3.1$  Å, intermediate between the intralayer, full single bond distance of 2.908 Å and the interlayer, weakly bonding distance of 3.36 Å found in elemental antimony.<sup>39</sup> These intermediate distances have been successfully modeled as one-electron bonds.<sup>38,40,41</sup>

The Zintl concept is a useful electron counting scheme for describing the bonding in compounds of elements with different electronegativities, and has been quite successful for interpreting the bonding found in phosphides, arsenides, and antimonides.<sup>42-45</sup> It assumes full valence electron transfer from the electropositive component to the electronegative component, which uses the electrons to form bonds and complete its octet. For instance, isolated antimony anions are assigned as  $Sb^{3-}$ , while successive Sb–Sb bond formation occurs with oxidation of the Sb atoms. It follows that in isolated  $Sb_2$  dumbbells (*i.e.* one-bonded Sb atoms), each Sb atom is oxidized by one electron and formulated as  $Sb^{2-}$ , while two-bonded Sb atoms (as in zigzag chains) are  $Sb^{1-}$  and three bonded Sb atoms (as in elemental Sb) are  $Sb^0$ . One can therefore deduce if Sb–Sb bonding is present in a compound simply by examining its formula. For example, in  $CaSb_2$ , the Ca atoms donate their two valence electrons to the Sb atoms, yielding the formulation  $(Ca^{2+})(Sb^{1-})_2$ .<sup>46</sup> Since isolated anions of antimony are  $Sb^{3-}$ , we can conclude that Sb–Sb bonding must be important in  $CaSb_2$ , without any prior knowledge of the actual structure.



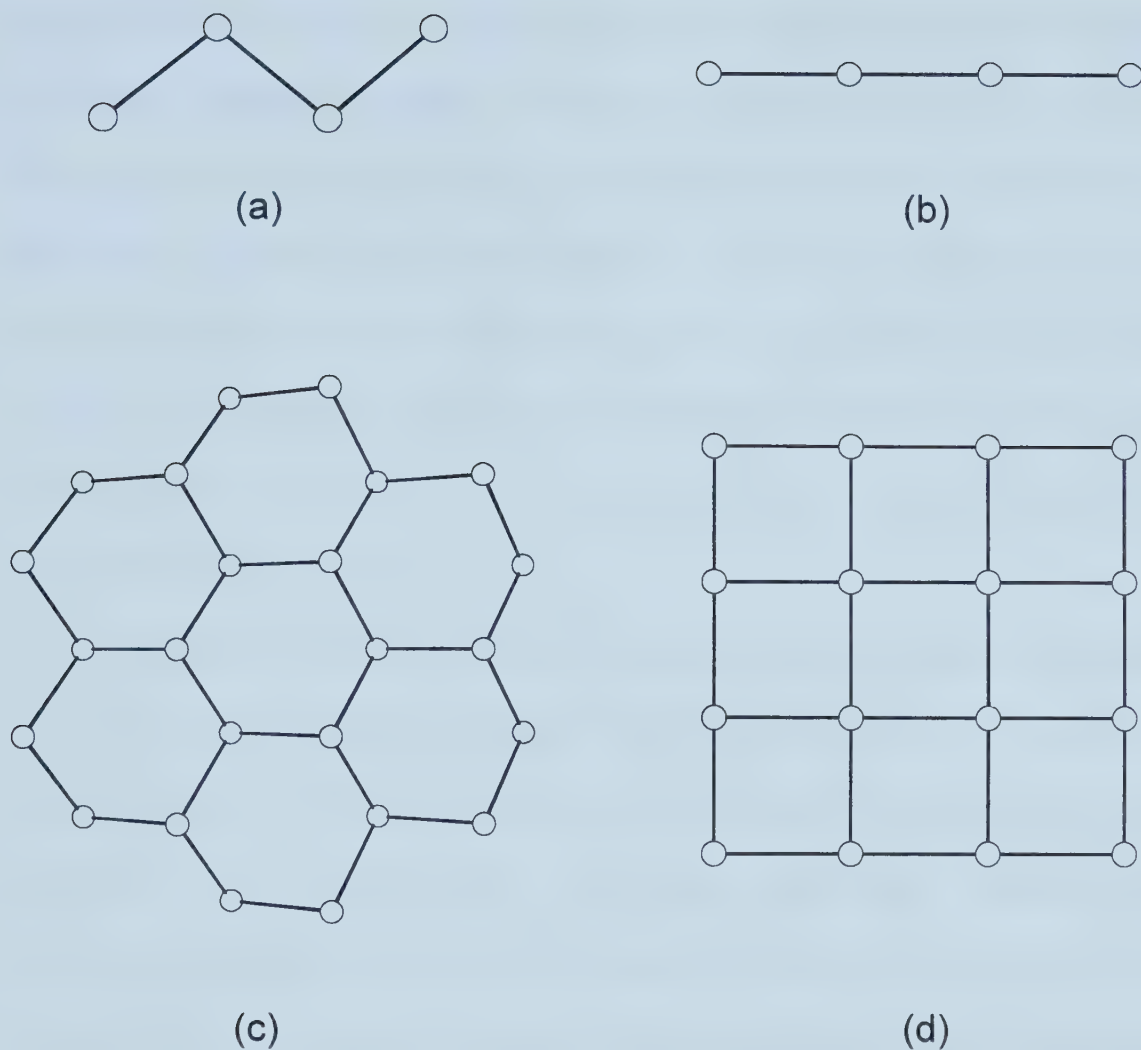


**Figure 1-2.** Examples of low-dimensional Sb networks: (a) 1-D zigzag chain in  $\text{YbSb}_2$ ;<sup>37</sup> (b) 1-D linear chain in  $\text{U}_3\text{MSb}_5$  ( $M = \text{Ti}, \text{V}, \text{Cr}, \text{Mn}$ );<sup>38</sup> (c) 2-D 3-connected puckered sheet in elemental Sb;<sup>39</sup> (d) 2-D 4-connected sheet in  $\text{REMSb}_2$  ( $M = \text{Mn-Zn}, \text{Pd}, \text{Au}$ ).<sup>14-17</sup>



If the artificial restriction to integral oxidation states is removed, the Zintl concept can be extended to explain the weaker Sb–Sb bonding that has been observed in some antimonides. Consider, for example, the two-dimensional square sheets of Sb (with Sb–Sb distances  $\sim 3.1$  Å) that are found in many rare-earth antimonides. Based strictly on bond length arguments, these Sb–Sb distances are considered one-electron bonds; each Sb atom makes four one-electron bonds to its neighbors, and to satisfy its octet, also has two lone pairs of electrons. The resulting formulation for the Sb atoms found in square nets is thus  $\text{Sb}^{1-}$ . By analogy, linear chains of Sb atoms (with Sb–Sb distances  $\sim 3.1$  Å) are formulated as  $\text{Sb}^{2-}$ .

Papouian and Hoffmann addressed the degree to which Sb–Sb bonding influences the geometry of the antimony networks.<sup>47</sup> They closely examined the bonding in a variety of binary and ternary antimonides, qualitatively with the Zintl concept, and then quantitatively with extended Hückel band structure calculations. Moreover, they proposed a classification scheme for the Sb networks based on whether they exhibited classical two-electron bonds (*i.e.* full single bonds), and therefore classical geometry such as zigzag chains, or the non-classical one-electron bonds and non-classical geometry such as linear chains and square sheets.<sup>47</sup> The electron counts of the linear chains and square sheets are such that they should be prone to undergo Peierls distortions, but because of reduced s-p mixing compared to P and As, Sb is more readily able to stabilize these unusual geometries.<sup>47</sup>

A major aim of the present thesis is to greatly expand the number of examples of antimonides with this type of weak Sb–Sb bonding to provide a means of structural systematization and to develop structure-property relationships. Given the multitude of





ternary rare-earth antimonides of the late transition metals that have been reported and the diversity of the structures adopted (see Figure 1-1), we believed that systems of the early transition metals or main-group metals should yield equally exciting results. Moreover, many of these compounds are now under extensive investigation because of their interesting physical properties, selected examples of which are listed in Table 1-2, including thermoelectricity in  $REM_4Sb_{12}$ <sup>52</sup> and  $RE_3M_3Sb_4$ <sup>53</sup> and colossal magnetoresistance in  $Eu_{14}MnSb_{11}$ .<sup>48</sup> The objectives of this research were to prepare new ternary rare-earth antimonides,  $RE_xM_ySb_z$ , where  $M$  is either an early transition metal or main-group metal, featuring low-dimensional structures with Sb–Sb bonding, to measure their physical properties (both electrical and magnetic), and finally, to interpret the bonding and properties observed via band structure calculations.



**Table 1-2.** Properties of Selected Ternary Rare-Earth Antimonides

Compound	Type	Properties
$\text{Eu}_{14}\text{MnSb}_{11}$	0-D	colossal magnetoresistance <sup>48</sup>
$\text{CeNiSb}_2$	2-D	heavy fermions <sup>49</sup>
$\text{CeCuSb}_2$	2-D	dense Kondo system <sup>49,50</sup>
$\text{CePdSb}$	3-D	ferromagnetic ordering <sup>51</sup>
$\text{REFe}_{4-x}\text{Co}_x\text{Sb}_{12}$ ( $\text{RE} = \text{La}, \text{Ce}$ )	3-D	thermoelectricity <sup>52</sup>
$\text{Nd}_x\text{Ce}_{3-x}\text{Pt}_3\text{Sb}_4$	3-D	thermoelectricity <sup>53</sup>



## REFERENCES

- (1) *An Encyclopedia of World History*; Langer, W. L., Ed.; Houghton Mifflin Company: Boston, 1968.
- (2) Jin, S.; Tiefel, T. H.; McCormack, M.; Fastnacht, A.; Ramesh, R.; Chen, L. H. *Science* **1994**, 264, 413.
- (3) West, A. R. *Solid State Chemistry and its Applications*; John Wiley & Sons, Inc.: New York, 1995.
- (4) For example: Cava, R. J.; Batlogg, B.; van Dover, R. B.; Murphy, D. W.; Sunshine, S.; Siegrist, T.; Remeika, J. P.; Rietman, E. A.; Zahurak, S.; Espinosa, G. P. *Phys. Rev. Lett.* **1987**, 58, 1676.
- (5) *Intermetallic Compounds: Principles and Practice*; Westbrook, J. H.; Fleischer, R. L., Eds.; Vol. 2 - Practice; John Wiley & Sons, Inc.: New York, 1995.
- (6) General references: (a) West, A. R. (Ref. 3 of this chapter). (b) Bacon, G. E. *Neutron Diffraction*, 3rd Ed.; Oxford University Press: London, U.K., 1975. (c) Greenwood, N. N.; Gibb, T. C. *Mössbauer Spectroscopy*; Chapman and Hall Ltd.: London, U.K., 1971.
- (7) Thrower, P. A. *Materials in Today's World*, 2nd Ed.; McGraw-Hill, Inc.: New York, 1996.
- (8) General references: (a) Meaden, G. T. *Electrical Resistance of Metals*; Plenum Press: New York, 1965. (b) Rosenberg, H. M. *The Solid State*, 3rd Ed.; Oxford University Press: Oxford, U.K., 1993. (c) West, A. R. (Ref. 3 of this chapter).
- (9) General references: (a) Rosenberg, H. M. *The Solid State*, 3rd Ed.; Oxford



University Press: Oxford, U.K., 1993. (b) Carlin, R. L. *Magnetochemistry*; Springer-Verlag: New York, 1986. (c) Zeiger, H. J.; Pratt, G. W. *Magnetic Interactions in Solids*; Oxford University Press: Oxford, U.K., 1973. (d) West, A. R. (Ref. 3 of this chapter).

- (10) *Optical and Electrical Properties*; Lee, P. A., Ed.; Physics and Chemistry of Materials with Layered Structures, Vol. 4; D. Reidel: Dordrecht, The Netherlands, 1976.
- (11) *Electronic Structure and Electronic Transitions in Layered Materials*; Grasso, V., Ed.; Physics and Chemistry of Materials with Low-Dimensional Structures, Series A; D. Reidel: Dordrecht, The Netherlands, 1986.
- (12) *Theoretical Aspects of Band Structures and Electronic Properties of Pseudo-One-Dimensional Solids*; Kamimura, H., Ed.; Physics and Chemistry of Materials with Low-Dimensional Structures, Series B; D. Reidel: Dordrecht, The Netherlands, 1986.
- (13) *Handbook of Crystal Structures and Magnetic Properties of Rare-Earth Intermetallics*; Szytula, A.; Leciejewicz, J., Eds.; CRC Press: Boca Raton, FL, 1994.
- (14) Sologub, O.; Hiebl, K.; Rogl, P.; Noël, H.; Bodak, O. *J. Alloys Compd.* **1994**, 210, 153.
- (15) Leithe-Jasper, A.; Rogl, P. *J. Alloys Compd.* **1994**, 203, 133.
- (16) Cordier, G.; Schäfer, H.; Woll, P. *Z. Naturforsch. B: Anorg. Chem., Org. Chem.* **1985**, 40, 1097.





- (17) Pankevich, Yu. V.; Pecharskii, V. K.; Bodak, O. I. *Izv. Akad. Nauk SSSR, Met.* **1983**, 227.
- (18) Mulder, F. M.; Thiel, R. C.; Buschow, K. H. J. *J. Alloys Compd.* **1994**, 210, 335.
- (19) Hofmann, W. K.; Jeitschko, W. *J. Less-Common Met.* **1988**, 138, 313.
- (20) Hofmann, W. K.; Jeitschko, W. *Monatsh. Chem.* **1985**, 116, 569.
- (21) Pecharskii, V. K.; Pankevich, Yu. V.; Bodak, O. I. *Dopov. Akad. Nauk Ukr. RSR. Ser. B: Geol., Khim. Biol. Nauki* **1982**, 44.
- (22) Zwiener, G.; Neumann, H.; Schuster, H.-U. *Z. Naturforsch. B: Anorg. Chem., Org. Chem.* **1981**, 36, 1195.
- (23) Rühl, R.; Jeitschko, W. *Mater. Res. Bull.* **1979**, 14, 513.
- (24) Marchand, R.; Jeitschko, W. *J. Solid State Chem.* **1978**, 24, 351.
- (25) Braun, D. J.; Jeitschko, W. *J. Less-Common Met.* **1980**, 72, 147.
- (26) Skolozdra, R. V.; Salamakha, P. S.; Ganzjuk, A. L.; Bodak, O. I. *Izv. Akad. Nauk SSSR, Neorg. Mater.* **1993**, 29, 25.
- (27) Kasaya, M.; Katoh, K.; Takegahara, K. *Solid State Commun.* **1991**, 78, 797.
- (28) Dwight, A. E. *Acta Crystallogr. Sect. B: Struct. Crystallogr. Cryst. Chem.* **1977**, 33, 1579.
- (29) Kasaya, M.; Suzuki, H.; Yamaguchi, T.; Katoh, K. *J. Phys. Soc. Jpn.* **1992**, 61, 4187.
- (30) Malik, S. K.; Adroja, D. T. *J. Magn. Magn. Mater.* **1991**, 102, 42.
- (31) Wenski, G.; Mewis, A. *Z. Anorg. Allg. Chem.* **1986**, 543, 49.
- (32) Pecharskii, V. K.; Pankevich, Yu. V.; Bodak, O. I. *Sov. Phys. Crystallogr. Engl.*



*Transl.* **1983**, 28, 97.

- (33) Rossi, D.; Marazza, R.; Mazzone, D.; Ferro, R. *J. Less-Common Met.* **1981**, 78, P1.
- (34) Tomuschat, C.; Schuster, H.-U. *Z. Naturforsch. B: Anorg. Chem., Org. Chem.* **1981**, 36, 1193.
- (35) Marazza, R.; Rossi, D.; Ferro, R. *J. Less-Common Met.* **1980**, 75, P25.
- (36) Rehr, A.; Kauzlarich, S. *J. Alloys Compd.* **1994**, 207/208, 424.
- (37) Wang, R.; Bodnar, R.; Steinfink, H. *Inorg. Chem.* **1966**, 5, 1468.
- (38) Brylak, M.; Jeitschko, W. *Z. Naturforsch. B: Chem. Sci.* **1994**, 49, 747.
- (39) Greenwood, N. N.; Earnshaw, A. *Chemistry of the Elements*; Pergamon Press: Oxford, U.K., 1994.
- (40) Brylak, M.; Jeitschko, W. *Z. Naturforsch. B: Chem. Sci.* **1995**, 50, 899.
- (41) Brylak, M.; Möller, M. H.; Jeitschko, W. *J. Solid State Chem.* **1995**, 115, 305.
- (42) *Chemistry, Structure, and Bonding of Zintl Phases and Ions*; Kauzlarich, S. M., Ed.; VCH Publishers: New York, 1996.
- (43) Schäfer, H. *Annu. Rev. Mater. Sci.* **1985**, 15, 1.
- (44) Corbett, J. D. *Chem. Rev.* **1985**, 85, 383.
- (45) von Schnering, H. G. *Angew. Chem. Int. Ed. Engl.* **1981**, 20, 33.
- (46) Deller, K.; Eisenmann, B. *Z. Anorg. Allg. Chem.* **1976**, 425, 104.
- (47) Papoian, G.; Hoffmann, R. Private communication.
- (48) Chan, J. Y.; Kauzlarich, S. M.; Klavins, P.; Shelton, R. N.; Webb, D. J. *Chem. Mater.* **1997**, 9, 3132.



- (49) Muro, Y.; Takeda, N.; Ishikawa, M. *J. Alloys Compd.* **1997**, 257, 23.
- (50) Houshiar, M.; Adroja, D. T.; Rainford, B. D. *J. Magn. Magn. Mater.* **1995**, 140-144, 1231.
- (51) Malik, S. K.; Adroja, D. T. *J. Magn. Magn. Mater.* **1991**, 102, 42.
- (52) Sales, B. C.; Mandrus, D.; Williams, R. K. *Science* **1996**, 272, 1325.
- (53) Jones, C. D. W.; Regan, K. A.; DiSalvo, F. J. *Phys. Rev. B: Condens. Matter* **1998**, 58, 16057.





## Chapter 2

### A New Family of Non-Stoichiometric Layered Rare-Earth Tin Antimonides, $RESn_xSb_2$ ( $RE = La, Ce, Pr, Nd, Sm$ ): Crystal Structure of $LaSn_{0.75}Sb_2$ <sup>†</sup>

#### Introduction

Low-dimensionality is an important prerequisite for the manifestation of unusual physical properties such as highly anisotropic electrical conductivity (perhaps even superconductivity), charge density waves, or magnetic ordering phenomena, and for an extensive intercalation chemistry.<sup>1-3</sup> In two-dimensional structures, for instance, the separation between layers may be characterized by weak van der Waals bonding, as in graphite or layered dichalcogenides, or by an alternation of ionic and covalent bonding, as in the cuprate superconductors. In an effort to steer away from the heavily traversed areas of oxides and chalcogenides, we have directed our search for such low-dimensional compounds among metal antimonides. In particular, we have been investigating ternary rare-earth antimonides  $RE/M/Sb$  in which the second component  $M$  is a main-group metal, in this case, Sn. Many binary as well as the few known ternary antimonides already adopt low-dimensional structures.<sup>4-7</sup> Moreover, we are propelled by the notion that if even simple binary stannides or antimonides are endowed with such useful physical properties, such as superconductivity in  $LaSn_3$  or  $La_4Sb_3$ ,<sup>8,9</sup> or have such technologically important applications such as GaSb or InSb in light-emitting diodes or

---

<sup>†</sup> Reproduced with permission from Ferguson, M. J.; Hushagen, R. W.; Mar, A. *Inorg. Chem.* **1996**, 35, 4505. Copyright 1996 American Chemical Society.



photoconductive IR detectors,<sup>10</sup> then ternary or higher multinary antimonides will provide us with an even greater opportunity for exerting fine steric and electronic control on structures and properties.

We report here our initial results from investigating the La/Sn/Sb system, and describe the structure of  $\text{LaSn}_{0.75}\text{Sb}_2$ , which forms a member of a new family of non-stoichiometric layered rare-earth tin antimonides. The ternary La/Sn/Sb system appears to have been studied earlier, but not at all comprehensively. Hulliger and Ott reported a ternary  $\text{La}_4\text{SnSb}_2$  compound in which Sn atoms substitute in a disordered fashion in the parent  $\text{La}_4\text{Sb}_3$  structure, an antitype of the *bcc*  $\text{Th}_3\text{P}_4$  structure.<sup>9</sup> Wang, Steinfink, and Raman studied the “ $\text{LaSn}_2$ ”– $\text{LaSb}_2$  sections and reported a ternary compound that they tentatively identified as “ $\text{LaSnSb}_2$ ”.<sup>11</sup> However, they did not pursue the crystal structure determination of this compound and made no further mention of it except to report its X-ray powder pattern and to suggest its probable similarity to the  $\text{NdTe}_3$  structure.<sup>12</sup> As we will show, the compound identified earlier as “ $\text{LaSnSb}_2$ ” is in fact a member of the non-stoichiometric  $\text{LaSn}_x\text{Sb}_2$  ( $x = \sim 0.1$  to  $\sim 0.8$ ) series that we fully characterize below. The structure of  $\text{LaSn}_{0.75}\text{Sb}_2$ , consisting of one-dimensional Sn chains and two-dimensional Sb sheets, is actually more complicated than being a mere variant of the  $\text{NdTe}_3$  structure, as was thought. Attempting to describe the nature of the Sn atoms in this structure poses challenging questions as to how bonding of metalloid elements should be viewed and tests the limits on how far the Zintl concept can be applied in systems containing elements of intermediate electronegativity.



## Experimental Section

**Synthesis.** The phase  $RESn_xSb_2$  was originally identified in our laboratory as a side product in tin flux reactions intended for the growth of single crystals of  $RE_3NbSb_5$ .<sup>5</sup> The persistent presence of this phase in yet other tin flux reactions led us to isolate the single crystals of  $LaSn_{0.75}Sb_2$  ultimately used in the structure determination. These crystals were obtained from a reaction of a 0.5 g mixture of the elements La, Si, and Sb in a 2:2:5 ratio to which a large excess of Sn was added (La, 74 mg, 0.53 mmol, 99.9%, Aesar; Si, 15 mg, 0.53 mmol, 99.96%, Cerac; Sb, 161 mg, 1.33 mmol, 99.999%, Cerac; Sn, 321 mg, 2.70 mmol, 99.8%, Cerac). The reactants were ground together and loaded into a fused-silica tube (8 cm length; 10 mm i.d.) that was then evacuated and sealed. The sample was heated at 570 °C for 1 day, 950 °C for 2 days, and then cooled to room temperature over 1 day. The excess Sn was dissolved with concentrated HCl and the product was found to contain silver flat needle-shaped crystals. EDX analysis (energy dispersive X-ray analysis) on these crystals with a JEOL JSM-6301FXV field-emission scanning electron microscope revealed the presence of the elements La, Sn, and Sb (but *no* Si) in the approximate ratio 1:<1:2, with a deficiency of Sn consistently observed. The Si apparently remained unreacted, as revealed from powder X-ray analysis of the product. The crystal structure determination (*vide infra*) ultimately established the stoichiometry, which was confirmed by quantitative EDX analyses with a JEOL 8900 microprobe. Anal. Calcd for  $LaSn_{0.75}Sb_2$ : La, 26.7%; Sn, 20.0%; Sb, 53.3%. Found (average of 10 analyses): La, 28.8(3)%; Sn, 18.9(5)%; Sb, 52.3(4)%.



Since the crystal structure suggested variable Sn occupancy, investigations were carried out to determine the extent to which Sn can be incorporated into the structure, as well as to confirm if rational syntheses of these compounds are possible. A series of 0.5 g samples was prepared from mixtures of the elements according to:  $\text{La} + x\text{Sn} + 2\text{Sb}$  (where  $x = 0, 0.10, 0.20, \dots, 1.00, 2.00$ ). Here, the Sn is now considered to serve as an actual reactant rather than merely as a nonreactive flux. The samples were loaded into fused-silica tubes as before, and heated using the same temperature profile as indicated above. These reactions resulted in the formation of the desired ternary phase (with the exception, of course, of the control sample with  $x = 0$ , which gave the expected  $\text{LaSb}_2$ ), as detected by powder X-ray diffraction patterns obtained on an Enraf-Nonius FR552 Guinier camera ( $\text{CuK}_{\alpha 1}$  radiation; Si standard). The cell parameters were refined by least-squares fits of typically 20 to 35 reflections in the powder patterns with the use of the program POLSQ.<sup>13</sup>

In a similar fashion, rare-earth substitutions were carried out by preparing 0.5-g samples containing mixtures of the elements *RE*, Sn, and Sb in the ratio 1:0.5:3 (where *RE* = La, Ce, Pr, Nd, Sm, and Gd), which were then heated as before. In all cases except for *RE* = Gd (which gave only known binary phases), needle-shaped crystals with metallic luster were obtained, which were verified by EDX analyses to be the desired ternary compounds. These compounds are stable indefinitely in air. Subsequently, reactions with starting composition  $\text{RESnSb}_2$  (*RE* = La, Ce, Pr, Nd, Sm) were carried out, which we assume yield the ternary phase with the maximum Sn content; these products were characterized by powder X-ray diffraction as well.







**Structure Determination.** Preliminary cell parameters were determined from Weissenberg photographs, which revealed Laue symmetry *mmm* and systematic extinctions (*hkl*:  $h + k = 2n + 1$ ; *h0l*:  $l = 2n + 1$ ) consistent with the orthorhombic space groups  $D_{2h}^{17} - Cmc$ ,  $C_{2v}^{12} - Cmc2_1$ , and  $C_{2v}^{16} - C2cm$ . Final cell parameters were determined from a least-squares analysis of the setting angles of 34 reflections in the range  $22^\circ \leq 2\theta(\text{MoK}_\alpha) \leq 28^\circ$  centered on a Siemens P4RA diffractometer. Intensity data were collected at  $-60^\circ\text{C}$  with the  $\theta$ - $2\theta$  scan technique in the range  $2^\circ \leq 2\theta(\text{MoK}_\alpha) \leq 70^\circ$ . Three standard reflections monitored at intervals of every 100 reflections showed no significant change during the data collection. Crystal data are given in Table 2-1.

Calculations were carried out with the use of programs in the SHELXTL (Version 5.0) package.<sup>14,15</sup> Conventional atomic scattering factors and anomalous dispersion corrections were used.<sup>16</sup> Intensity data were reduced and averaged, and face-indexed Gaussian-type absorption corrections were applied with the use of the program XPREP. Intensity statistics and satisfactory averaging ( $R_{int} = 0.034$ ) favored the centrosymmetric space group *Cmcm*. Initial positions of the La and Sb atoms were found by direct methods with the program XS. The ensuing difference Fourier syntheses persistently revealed additional electron density located between the layers of composition “LaSb<sub>2</sub>”. Introduction of a site at 0, 0, 0 that was permitted to be partially occupied by Sn atoms could account for this electron density, but this model was deemed unsatisfactory because it resulted in a highly elongated thermal ellipsoid for this site that stretches along the *c* direction. Restriction of the displacement parameter of this site to a more reasonable,



**Table 2-1.** Crystallographic Data for  $\text{LaSn}_{0.75(3)}\text{Sb}_2$ 

Formula	$\text{LaSn}_{0.75(3)}\text{Sb}_2$
Formula mass (amu)	471.43
Space group	$D_{2h}^{17} - Cmc m$
$a$ (Å)	4.2435(5) <sup>a</sup>
$b$ (Å)	23.121(2) <sup>a</sup>
$c$ (Å)	4.5053(6) <sup>a</sup>
$V$ (Å <sup>3</sup> )	442.03(5)
$Z$	4
$T$ (°C)	−60
Diffractometer	Siemens P4RA
$\rho_{\text{calc}}$ (g cm <sup>−3</sup> )	7.084
Crystal dimensions	Silver needle, $0.375 \times 0.053 \times 0.017$ mm <sup>3</sup>
Radiation	Graphite monochromated $\text{MoK}_\alpha$ , $\lambda = 0.71073$ Å
$\mu$ (cm <sup>−1</sup> )	255.4
Transmission factors <sup>b</sup>	0.276 – 0.648
Scan-type	$\theta$ – $2\theta$
$2\theta$ limits	$2^\circ \leq 2\theta(\text{MoK}_\alpha) \leq 70^\circ$
Data collected	$-6 \leq h \leq 6, -12 \leq k \leq 36, -7 \leq l \leq 7$
No. of data collected	1978
No. of unique data, including $F_o^2 < 0$	592 ( $R_{\text{int}} = 0.034$ )
No. of unique data, with $F_o^2 > 2\sigma(F_o^2)$	571
No. of variables	23



**Table 2-1.** Crystallographic Data for  $\text{LaSn}_{0.75(3)}\text{Sb}_2$  (cont'd)

Extinction coefficient <sup>c</sup>	0.0123(6)
$R(F)$ for $F_o^2 > 2\sigma(F_o^2)$ <sup>d</sup>	0.028
$R_w(F_o^2)$ <sup>e</sup>	0.067
Goodness of fit <sup>f</sup>	1.20

<sup>a</sup> Obtained from a refinement constrained so that  $\alpha = \beta = \gamma = 90^\circ$ .

<sup>b</sup> A Gaussian face-indexed absorption correction was applied with the use of the programs in the SHELXTL package (Sheldrick, G. M. *SHELXTL* Version 5.0; Siemens Analytical X-ray Instruments, Inc.: Madison, WI, 1994).

<sup>c</sup> An extinction parameter  $x$  was refined, where  $F_c$  is multiplied by:  $k[1 + 0.001 * x * F_c^2 * \lambda^3 / \sin(2\theta)]^{-1/4}$ .

$$^d R(F) = \sum \|F_o\| - \|F_c\| / \sum \|F_o\|.$$

$$^e R_w(F_o^2) = [\sum [w(F_o^2 - F_c^2)^2] / \sum wF_o^4]^{1/2}; w^{-1} = [\sigma^2(F_o^2) + (0.026P)^2 + 8.62P] \text{ where } P = [\max(F_o^2, 0) + 2F_c^2] / 3.$$

$$^f GooF = S = [\sum [w(F_o^2 - F_c^2)^2] / (n - p)]^{1/2} \text{ where } n \text{ is the number of reflections and } p \text{ is the total number of parameters refined.}$$



isotropic value allowed two additional sites, at  $0, y, \frac{1}{4}$  and  $0, y, z$ , to be resolved in the difference Fourier map. Together, these three closely-split sites were allowed to be partially occupied by Sn atoms but their thermal motion was constrained to be isotropic. There is no justification for introducing anisotropy for the Sn atoms given that values of the site occupation factors and displacement parameters are expected to be highly correlated in the least-squares refinements.

To minimize artifacts that may be associated with such correlations, refinements at this stage were performed very gradually and not indiscriminately. The displacement and then the site occupation factor of one Sn site was allowed to refine while all parameters associated with the other two Sn sites were fixed. This procedure was repeated in turn for all the Sn sites. In the final stage, the site occupation and displacement parameters of *all* three Sn sites were left unconstrained and allowed to refine freely. These converged in a well-behaved manner to reasonable values notwithstanding the relatively unencumbered stage of this refinement. We interpret this result as strong evidence for the existence of three distinct, partially occupied interlayer sites, as opposed to an ill-defined smearing of electron density. We attempted to formulate models in which these Sn atoms fully occupied sites in an ordered fashion in the lower symmetry space group  $Cmc2_1$ , but found no evidence to support these.

The possibility of disorder between Sn and Sb atoms was considered. Given the similar scattering powers of Sn and Sb, however, it is not surprising that they cannot be distinguished with the available X-ray data. Later, we will present chemical arguments *against* a disordered Sn/Sb model. A refinement in which the occupancies of *all* atoms





were unconstrained resulted in values of 100(3)% for La, 100(3)% for Sb(1), 99(3)% for Sb(2), 18.6(7)% for Sn(1), 18.1(8)% for Sn(2), and 19.7(9)% for Sn(3). This results in the formula  $\text{La}_{1.00(3)}\text{Sn}_{0.75(3)}\text{Sb}_{1.99(3)}$  (the multiplicity of the Sn(1) site is twice that of the Sn(2) or Sn(3) sites). We thus accept the formulation  $\text{LaSn}_{0.75}\text{Sb}_2$ , which agrees well with the chemical analysis obtained independently (*vide supra*).

The final cycle of least-squares refinement on  $F_o^2$  of 23 variables (including anisotropic displacement parameters for the La and Sb atoms, site occupation factors for the Sn atoms, and an isotropic extinction parameter) and 592 averaged reflections (including those having  $F_o^2 < 0$ ) converged to residuals of  $R_w(F_o^2)$  of 0.067 and  $R(F)$  (for  $F_o^2 > 2\sigma(F_o^2)$ ) of 0.028. The final difference electron density map is featureless ( $\Delta\rho_{\text{max}} = 1.8$ ;  $\Delta\rho_{\text{min}} = -3.6 \text{ e } \text{\AA}^3$ ). The maximum peak value ( $\Delta\rho_{\text{max}}$ ) is small relative to the atomic peaks observed and can be attributed to noise. The atomic positions were standardized with the program STRUCTURE TIDY.<sup>17</sup> Final values of the positional and displacement parameters are given in Table 2-2 and the anisotropic displacement parameters are given in Table A-1.

**Electrical Resistivity.** Single crystals of  $\text{LaSn}_{0.75}\text{Sb}_2$  (from the same batch used in the structure determination) ranging in length from 0.8 to 1.4 mm were mounted with Ag paint on Au wires with graphite extensions. Four-probe ac electrical resistivity measurements (15.9 Hz) were made down to 20 K, along the needle axis  $a$  of these crystals. The small cross-sectional dimensions of these crystals preclude measurements along the other directions.



**Table 2-2.** Atomic Coordinates, Occupancies, and Equivalent Isotropic Displacement Parameters ( $\text{\AA}^2$ ) for  $\text{LaSn}_{0.75(3)}\text{Sb}_2$

atom	Wyckoff position, site symmetry		$x$	$y$	$z$	occupancy	$U_{\text{eq}}^a$
La	4c	$m2m$	0	0.86085(2)	$\frac{1}{4}$	1	0.0062(1)
Sb(1)	4c	$m2m$	0	0.24860(2)	$\frac{1}{4}$	1	0.0071(2)
Sb(2)	4c	$m2m$	0	0.59076(2)	$\frac{1}{4}$	1	0.0081(2)
Sn(1)	8f	$m \dots$	0	0.0065(1)	0.1238(6)	0.186(4)	0.0114(8) <sup>b</sup>
Sn(2)	4c	$m2m$	0	0.0089(1)	$\frac{1}{4}$	0.181(6)	0.010(1) <sup>b</sup>
Sn(3)	4a	$2/m \dots$	0	0	0	0.197(6)	0.013(1) <sup>b</sup>

<sup>a</sup>  $U_{\text{eq}}$  is defined as one-third of the trace of the orthogonalized  $U_{ij}$  tensor.

<sup>b</sup> The Sn atoms were refined isotropically.



## Results and Discussion

**Description of the Structure.** A view of the structure of  $\text{LaSn}_{0.75}\text{Sb}_2$  down the  $c$  axis is given in Figure 2-1(a), which also shows the labeling scheme. Selected interatomic distances and angles are given in Table 2-3. The compound  $\text{LaSn}_{0.75}\text{Sb}_2$  adopts a novel layered structure type that comprises layers of composition  ${}^2_{\infty}[\text{LaSb}_2]$  lying parallel to the (010) plane. These layers are separated by an unusual arrangement of Sn atoms partially occupying sites aligned along the  $c$  axis (Figure 2-1(b)). The La atoms are coordinated by eight Sb atoms in a square-antiprismatic fashion, as shown in Figure 2-2. Four Sb(1) atoms at distances of 3.3523(6) (2 $\times$ ) and 3.3879(5) Å (2 $\times$ ) define one square of Sb atoms. Four Sb(2) atoms at distances of 3.2905(4) Å (4 $\times$ ) define a larger square twisted 45° relative to the first square. The Sb(1) atoms are surrounded by four other symmetry-equivalent Sb(1) atoms forming a nearly flat square sheet  ${}^2_{\infty}[\text{Sb}]$ , with Sb(1)–Sb(1)–Sb(1) angles of 177.60(4)°, 86.55(1)°, and 93.40(1)°, and Sb(1)–Sb(1) distances of 3.0952(3) Å (4 $\times$ ). The La square antiprisms are then positioned above and below this infinite Sb(1) square sheet in a checkerboard pattern to form the  ${}^2_{\infty}[\text{LaSb}_2]$  layers.

A view of the structure down the  $a$  axis, perpendicular to the previous view, shows the wavelike pattern of the Sn sites (Figure 2-1(b)). It must be strongly emphasized that these sites are only *partially* occupied (each at ~20%), as adjacent sites are obviously too close (<0.6 Å) for them to be fully occupied simultaneously. As shown in Figure 2-2, there are three distinct sites with Sn(1) in a position of twice the



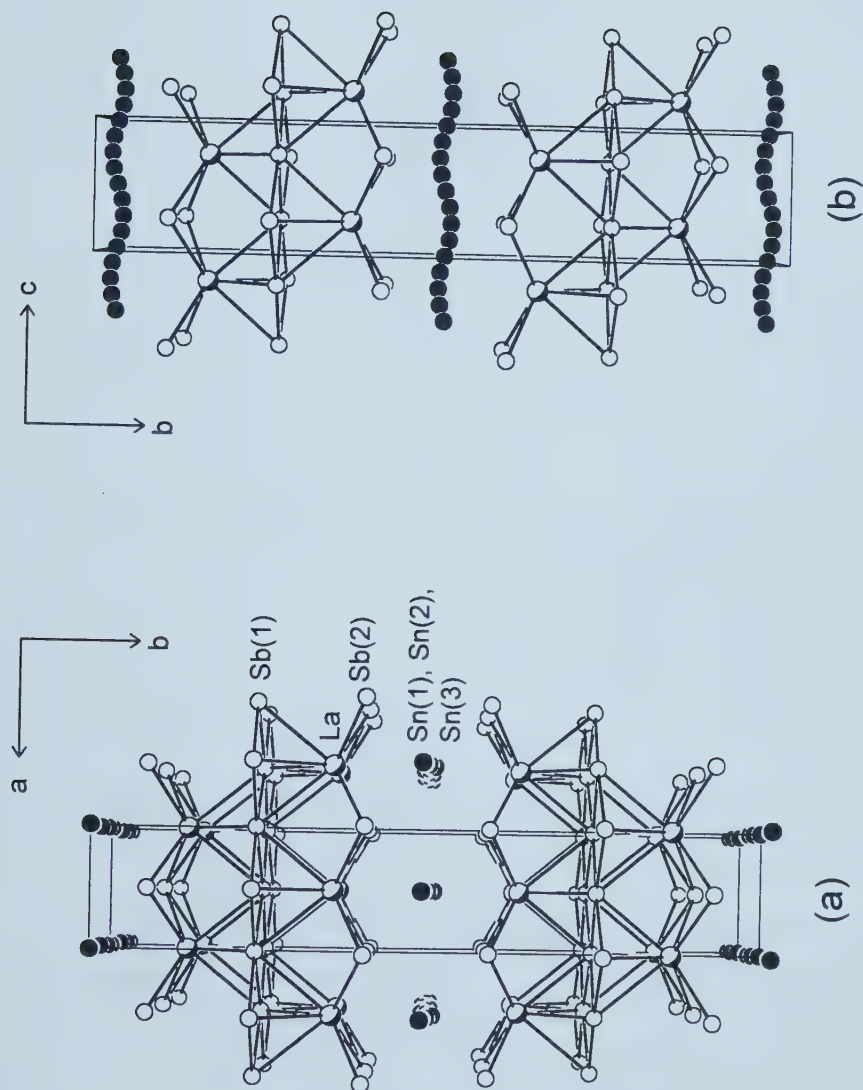


**Figure 2-1.** (a) View down the  $c$  axis of  $\text{LaSn}_{0.75}\text{Sb}_2$  with the unit cell outlined. The partly shaded circles are La atoms, the open circles are Sb atoms, and the shaded circles represent *sites* for the Sn atoms and do not imply the actual presence of the atoms themselves. (b) View down the  $a$  axis, showing the wavelike arrangement parallel to the  $c$  direction of the three Sn sites positioned between the layers of composition  $\text{LaSb}_2$ . These sites are only *partially* occupied, each at about 20%.





**Table 2-3.** Selected Interatomic Distances (Å) and Angles (°) for  $\text{LaSn}_{0.75(3)}\text{Sb}_2$ 

La–Sb(2)	3.2905(4) (4×)	Sb(1)–Sb(1)	3.0952(3) (4×)
La–Sb(1)	3.3523(6) (2×)	Sn(1)–Sb(2)	2.936(2) (2×)
La–Sb(1)	3.3879(5) (2×)	Sn(1)–Sb(2)	3.521(2) (2×)
La–Sn(3)	3.4087(5) (2×)	Sn(1)–Sn(3)	2.814(3)
La–Sn(1)	3.415(2) (2×)	Sn(1)–Sn(2)	2.844(3)
La–Sn(2)	3.423(3)	Sn(2)–Sb(2)	2.843(2) (2×)
La–Sn(1)	3.499(2) (2×)	Sn(2)–Sb(2)	3.858(2) (4×)
La–Sn(2)	3.761(3) (3×)	Sn(3)–Sb(2)	3.1897(4) (4×)
Sb(2)–La–Sb(2)	140.25(2)	La–Sb(2)–La	80.3(1)
Sb(2)–La–Sb(2)	80.30(1)	La–Sb(2)–La	140.2(2)
Sb(2)–La–Sb(2)	86.41(1)	La–Sb(2)–La	86.4(1)
Sb(2)–La–Sb(1)	132.17(1)	Sb(2)–Sn(1)–Sb(2)	92.54(7)
Sb(2)–La–Sb(1)	81.67(1)	Sb(2)–Sn(1)–Sn(2)	83.74(8)
Sb(2)–La–Sb(1)	135.16(1)	Sb(2)–Sn(1)–Sn(3)	103.22(7)
Sb(2)–La–Sb(1)	78.39(1)	Sn(2)–Sn(1)–Sn(3)	169.8(1)
Sb(1)–La–Sb(1)	78.53(2)	Sb(2)–Sn(2)–Sb(2)	96.5(1)
Sb(1)–La–Sb(1)	54.67(1)	Sb(2)–Sn(2)–Sn(1)	94.78(5)
Sb(1)–La–Sb(1)	83.35(2)	Sn(1)–Sn(2)–Sn(1)	165.6(1)
Sb(1)–Sb(1)–Sb(1)	177.60(4)	Sb(2)–Sn(3)–Sb(2)	83.4(1)
Sb(1)–Sb(1)–Sb(1)	86.55(1)	Sb(2)–Sn(3)–Sb(2)	96.6(1)
Sb(1)–Sb(1)–Sb(1)	93.40(1)	Sb(2)–Sn(3)–Sb(2)	180
La–Sb(1)–La	78.53(2)	Sn(1)–Sn(3)–Sn(1)	180
La–Sb(1)–La	125.33(1)		
La–Sb(1)–La	83.35(2)		



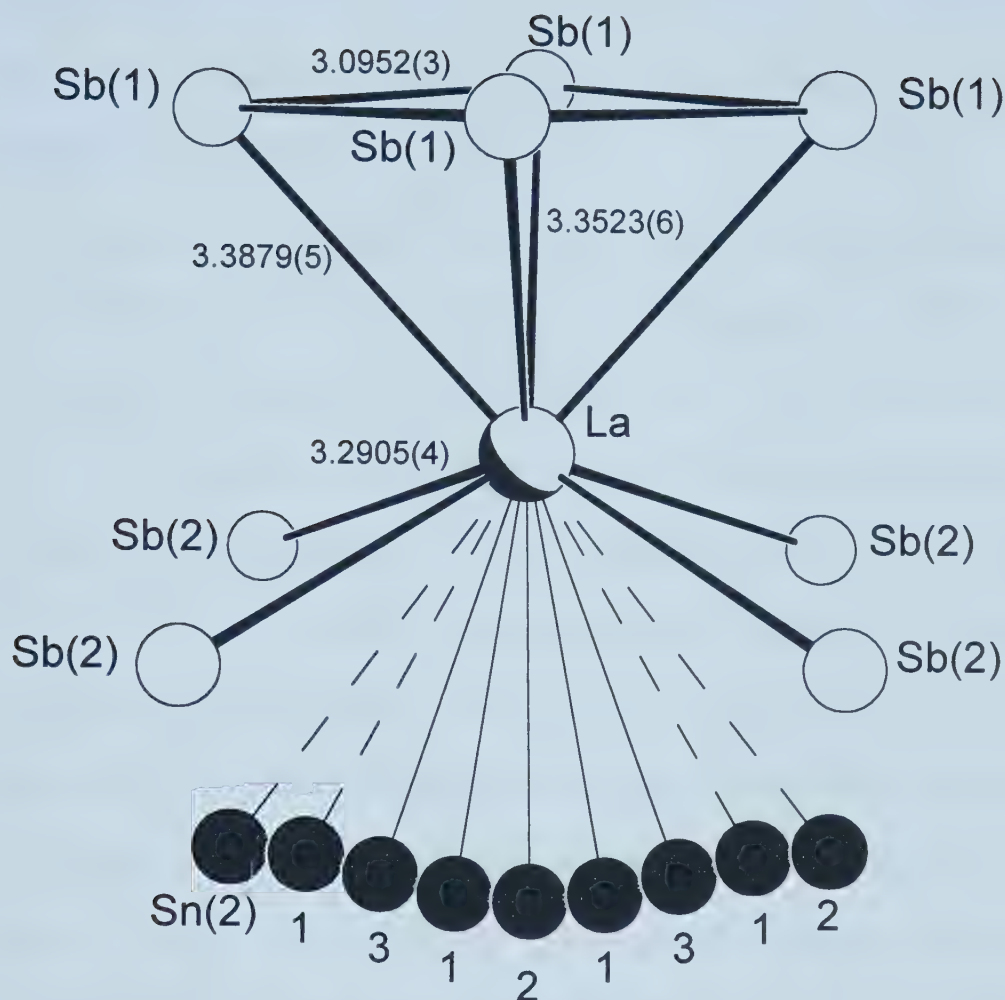


**Figure 2-2.** Coordination of the La atom in  $\text{LaSn}_{0.75}\text{Sb}_2$ , with the square-antiprismatic geometry of the Sb atoms shown and the La-Sb and Sb-Sb bond lengths indicated. The capping Sn sites beneath the La atom are labelled. In order from left to center, the La-Sn distances are  $3.761(3) \text{ \AA}$  to Sn(2),  $3.499(2) \text{ \AA}$  to Sn(1),  $3.4087(5) \text{ \AA}$  to Sn(3),  $3.415(2) \text{ \AA}$  to Sn(1), and  $3.423(3) \text{ \AA}$  to Sn(2).



multiplicity as that of Sn(2) or Sn(3), giving rise to an ordering of ...Sn(2)–Sn(1)–Sn(3)–Sn(1)... for the arrangement of these sites. The distances from these Sn sites to the La atom range from 3.4087(5) to 3.761(3) Å.

Located in the interlayer regions, the Sn atoms must be coordinated by the surrounding Sb(2) atoms. The Sn(1) site has two Sb(2) atoms at 2.936(2) Å on one side of it, subtending an angle of 92.54(7)° (Figure 2-3(a)). On the other side are two more Sb(2) atoms considerably further away, at 3.521(2) Å. Similarly, the Sn(2) site has two Sb(2) atoms at a short distance, 2.843(2) Å, subtending an angle of 96.5(1)° (Figure 2-3(b)). The four next nearest Sb(2) atoms are far away at 3.858(2) Å. Finally, the Sn(3) site is surrounded by four Sb(2) atoms at 3.1897(4) Å in a nearly square planar fashion (Figure 2-3(c)). With the Sn sites spaced at increments of ~0.5–0.6 Å from each other, all the generated Sn–Sn distances are unreasonable for bonding except for those in the vicinity of ~2.8 Å. In other words, one possible model that can be invoked to interpret the ~20% occupancy of *each* site is to suggest that every *fifth* site (or further) is fully occupied on a local level. Figures 2-3(a)-(c) show the nearly linear coordination of the Sn atoms by other Sn atoms within this reasonable bonding range (2.814(3) to 2.844(3) Å); the subtended angles range from 165.6(1)° to 180°.

**Non-stoichiometry of Sn.** Since the original synthesis producing the crystals for the structure determination involved a large excess of Sn, the amount of Sn actually incorporated into the compound  $\text{LaSn}_{0.75}\text{Sb}_2$  must represent a maximum limiting value. Is the Sn content variable? To determine the degree of non-stoichiometry in this phase, a series of reactions,  $\text{La} + x\text{Sn} + 2\text{Sb}$  ( $x = 0$  to 2.0), was prepared. Not surprisingly, the



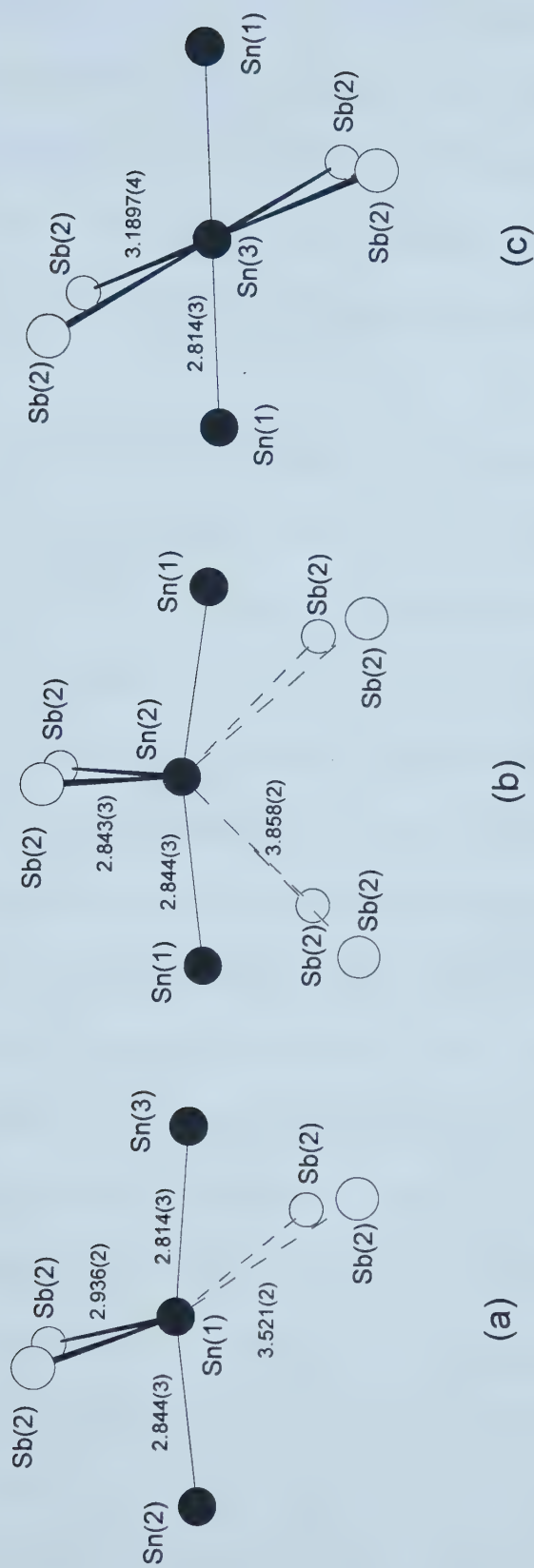


**Figure 2-3.** Coordination of the Sn atoms in  $\text{LaSn}_{0.75}\text{Sb}_2$ : (a) Sn(1) site; (b) Sn(2) site; (c) Sn(3) site. The Sn atoms at an appropriate distance for possible bonding interactions ( $\sim 2.8$  Å) are also shown. See text for interpretation.





control experiment,  $\text{La} + 0\text{Sn} + 2\text{Sb}$ , resulted in phase-pure  $\text{LaSb}_2$ .<sup>18</sup> More remarkably, however, the ternary phase could be formed as essentially the pure product (>95%) in all the other preparations, as observed in the powder X-ray diffraction patterns, even down to as low as  $x = 0.1$ . With  $x \geq 0.8$ , excess Sn and other unidentified phases can begin to be detected as minor impurities. The cell parameters refined from the powder data are listed in Table 2-4.

The variation in the cell parameters as a function of  $x$  is small, but is readily discernible in the case of the  $a$  and  $c$  parameters, as shown in Figure 2-4. The  $b$  parameter and the unit cell volume, however, do not exhibit as much variation. A number of important conclusions can be drawn from these data. Most significantly, the  $a$  parameter decreases while the  $c$  parameter increases steadily with increasing  $x$ , eventually reaching a plateau at approximately  $x = 0.7$  or  $0.8$ . With greater quantities of Sn loaded in the preparation, the cell parameters no longer change. This implies that  $x = 0.7$  or  $0.8$  also corresponds to the maximum Sn content. Note that this value agrees precisely with the formula obtained independently from the crystal structure,  $\text{LaSn}_{0.75(3)}\text{Sb}_2$ . The cell parameters refined from the single crystal data (Table 2-1) also agree reasonably well with those from the powder data for  $\text{LaSn}_{0.7}\text{Sb}_2$  or  $\text{LaSn}_{0.8}\text{Sb}_2$  (Table 2-4). During the structure refinement, we pointed out the difficulty in distinguishing between the Sn and Sb atoms. The observation of limiting values for the cell parameters at a stoichiometry consistent with the single-crystal formula argues strongly for an ordered model. The powder X-ray diffraction pattern for the preparation  $\text{LaSn}_{0.7}\text{Sb}_2$  matches well with the predicted pattern calculated from the structure determined from the single-crystal data



**Table 2-4.** Cell Parameters for Ternary  $\text{LaSn}_{0.75}\text{Sb}_2$ -type Compounds Obtained from the Reactions  $\text{La} + x\text{Sn} + 2\text{Sb}$ 

Loading Composition	$a$ (Å)	$b$ (Å)	$c$ (Å)	$V$ (Å <sup>3</sup> )
$\text{LaSn}_{0.10}\text{Sb}_2$	4.276(1)	23.090(4)	4.459(1)	440.2(1)
$\text{LaSn}_{0.20}\text{Sb}_2$	4.271(2)	23.100(9)	4.460(2)	440.1(2)
$\text{LaSn}_{0.30}\text{Sb}_2$	4.265(1)	23.128(5)	4.474(1)	441.4(1)
$\text{LaSn}_{0.40}\text{Sb}_2$	4.260(1)	23.119(6)	4.477(1)	440.9(1)
$\text{LaSn}_{0.50}\text{Sb}_2$	4.259(1)	23.139(5)	4.485(1)	442.0(1)
$\text{LaSn}_{0.60}\text{Sb}_2$	4.256(1)	23.120(5)	4.492(1)	442.0(1)
$\text{LaSn}_{0.70}\text{Sb}_2$	4.253(1)	23.140(3)	4.498(1)	442.7(1)
$\text{LaSn}_{0.80}\text{Sb}_2$	4.248(1)	23.128(6)	4.499(1)	442.1(1)
$\text{LaSn}_{0.90}\text{Sb}_2$	4.249(1)	23.130(4)	4.505(1)	442.7(1)
$\text{LaSn}_{1.00}\text{Sb}_2$	4.247(1)	23.139(6)	4.504(1)	442.6(1)
$\text{LaSn}_{2.00}\text{Sb}_2$	4.248(1)	23.135(5)	4.505(1)	442.7(1)



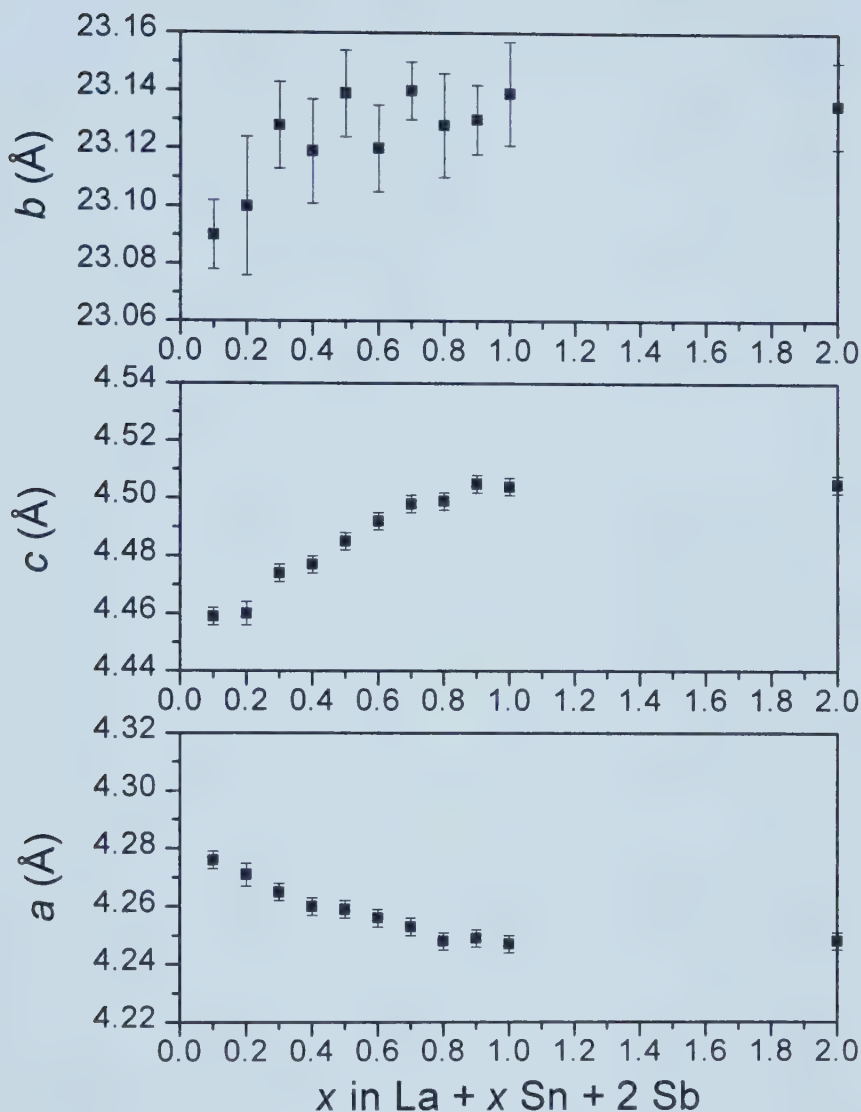


**Figure 2-4.** Plots of the cell parameters of the ternary  $\text{LaSn}_{0.75}\text{Sb}_2$ -type compounds obtained as a function of amount of Sn used,  $x$ , in the reaction  $\text{La} + x\text{Sn} + 2\text{Sb}$ . Note the attainment of a plateau at  $x = 0.7$  or  $0.8$ , most readily seen for the  $c$  or  $a$  parameters, corresponding to the maximum Sn content.



**Table 2-5.** X-ray Powder Diffraction Data for Starting Composition  $\text{LaSn}_{0.7}\text{Sb}_2$ 

$hkl$	$d_{obs}$ (Å)	$d_{calc}$ (Å)	$I/I_o^a$	$hkl$	$d_{obs}$ (Å)	$d_{calc}$ (Å)	$I/I_o^a$
1 1 0	4.180	4.183	8	1 5 2	} 1.825	1.827	2
0 6 0	3.856	3.857	4	2 4 1		1.824	7
0 4 1	3.549	3.551	20	0 8 2	} 1.774	1.775	6
1 5 0	3.130	3.132	19	0 12 1		1.772	6
1 1 1	3.064	3.063	2	2 6 1	1.720	1.721	3
0 6 1	2.927	2.928	6	2 8 0	1.714	1.713	11
0 8 0	2.892	2.893	24	1 7 2	1.704	1.704	10
1 3 1	2.868	2.869	100	2 8 1	1.602	1.601	9
1 7 0	2.609	2.610	36	0 14 1	1.552	1.551	5
1 5 1	2.569	2.570	41	2 0 2	} 1.545	1.545	14
0 8 1	2.433	2.433	14	1 13 1		1.542	5
0 0 2	2.250	2.249	20	1 11 2	1.445	1.445	13
0 2 2	2.208	2.208	3	2 6 2	1.435	1.434	5
2 0 0	2.126	2.127	27	2 12 0	1.428	1.429	5
0 4 2	2.095	2.096	2	1 3 3	1.391	1.391	15
0 10 1	2.058	2.058	3	1 15 1	1.380	1.380	10
1 9 1	1.977	1.977	6	2 8 2	} 1.363	1.363	6
0 6 2	1.943	1.943	6	2 12 1		1.362	6
0 12 0	1.927	1.928	5	1 5 3	—	1.352	7
1 11 0	1.886	1.886	6	3 3 1	1.332	1.332	13

<sup>a</sup> The intensities were calculated from the crystal structure of  $\text{LaSn}_{0.75}\text{Sb}_2$  with the use of the program LAZY-PULVERIX (Yvon, K.; Jeitschko, W.; Parthé, E. *J. Appl. Crystallogr.* **1977**, *10*, 73-74.)





(Table 2-5). Other related reactions that we have carried out in this laboratory support this model. For instance, using now an excess of *antimony* instead of tin, the reaction  $\text{La} + 0.5\text{Sn} + 3\text{Sb}$  led to the formation of crystals that were shown by quantitative microprobe analysis to contain the correct proportion of Sn. Anal. Calcd for  $\text{LaSn}_{0.5}\text{Sb}_2$ : La, 28.6%; Sn, 14.3%; Sb, 57.1%. Found (average of 10 analyses): La, 26.9(5)%; Sn, 13.3(1)%; Sb, 59.8(5)%.

Steric considerations would generally lead to the assumption that an increase in the Sn content should be accompanied by an increase in unit cell volume, but this is not the case here. The  $b$  parameter exhibits little variation, and this may be rationalized by inspecting Figure 2-1. When even a small amount of Sn is placed between the layers, it already fixes the interlayer spacing by virtue of a “pillaring” action. Apparently it is sufficient for a few initially placed Sn atoms to be located strategically in such a way as to buttress the layers apart at a fixed spacing; further addition of Sn atoms then has little effect on the  $b$  parameter. The increase of the  $c$  parameter with increasing Sn content can be explained by arguing that electrostatic repulsions are enhanced within the chains aligned along the  $c$  direction (Figure 2-1(b)). In contrast, the  $a$  parameter *decreases* with increasing Sn content, a rather surprising result. This can be explained on steric grounds if we postulate that the Sn atoms enter the structure with an initial preference for specific sites that bind the surrounding Sb(2) atoms at a further distance than in the final arrangement of  $\text{LaSn}_{0.75}\text{Sb}_2$ . Alternatively, there are likely to be more subtle electronic reasons that are not obvious from a simple analysis. In any case, given that both the contraction in  $a$  (−0.7%) and the expansion in  $c$  (+0.9%) are small on going from



$\text{LaSn}_{0.1}\text{Sb}_2$  to  $\text{LaSn}_{0.8}\text{Sb}_2$ , these explanations should be accepted guardedly pending further experiments.

**Structural Relationships and Bonding.** The compound  $\text{LaSn}_{0.75}\text{Sb}_2$  bears important structural relationships with the family of known rare-earth diantimonides,  $\text{RESb}_2$  (Figure 2-5). All of these structures contain rare-earth atoms in square antiprismatic coordination. These square antiprisms are condensed to form infinite layers consisting of rare-earth atoms above and below a nearly square net of Sb atoms. These layers are then stitched together through the formation of interlayer Sb–Sb bonds to form the three-dimensional frameworks of  $\text{RESb}_2$ . Formally, the structure of  $\text{LaSn}_{0.75}\text{Sb}_2$  is derived from those of the binary  $\text{RESb}_2$  compounds by: (1) excision of these interlayer Sb–Sb bonds, and (2) intercalation of Sn atoms between the separated layers.

It is instructive to review some of these structural features in more detail, as they will help provide useful starting notions of the bonding picture in  $\text{LaSn}_{0.75}\text{Sb}_2$ . The  $\text{LaSb}_2$ -type structure is adopted by the early rare-earth diantimonides  $\text{RESb}_2$  ( $\text{RE} = \text{La}, \text{Ce}, \text{Pr}, \text{Nd}, \text{Sm}$ ) (Figure 2-5(a)).<sup>18,19</sup> Even though the actual structure was determined for  $\text{SmSb}_2$ ,<sup>18</sup> we shall accept the designation “ $\text{LaSb}_2$ -type” because it is now firmly entrenched in the literature. The layers in  $\text{SmSb}_2$  are joined by short Sb–Sb *pairs* (2.79(2) Å), corresponding to strong two-electron single bonds in which an oxidation state of  $\text{Sb}^{2-}$  is attained. The Sb–Sb distances in the nearly square net range from 3.03(2) to 3.09(2) Å.<sup>20</sup> Such distances have been postulated to correspond to one-electron bonds, of one-half bond order, leading to an assignment of  $\text{Sb}^{1-}$  for these atoms.<sup>21,22</sup> The formulation  $\text{RE}^{3+}\text{Sb}^{1-}\text{Sb}^{2-}$  for the  $\text{LaSb}_2$ -type structure is thus consistent with the usual



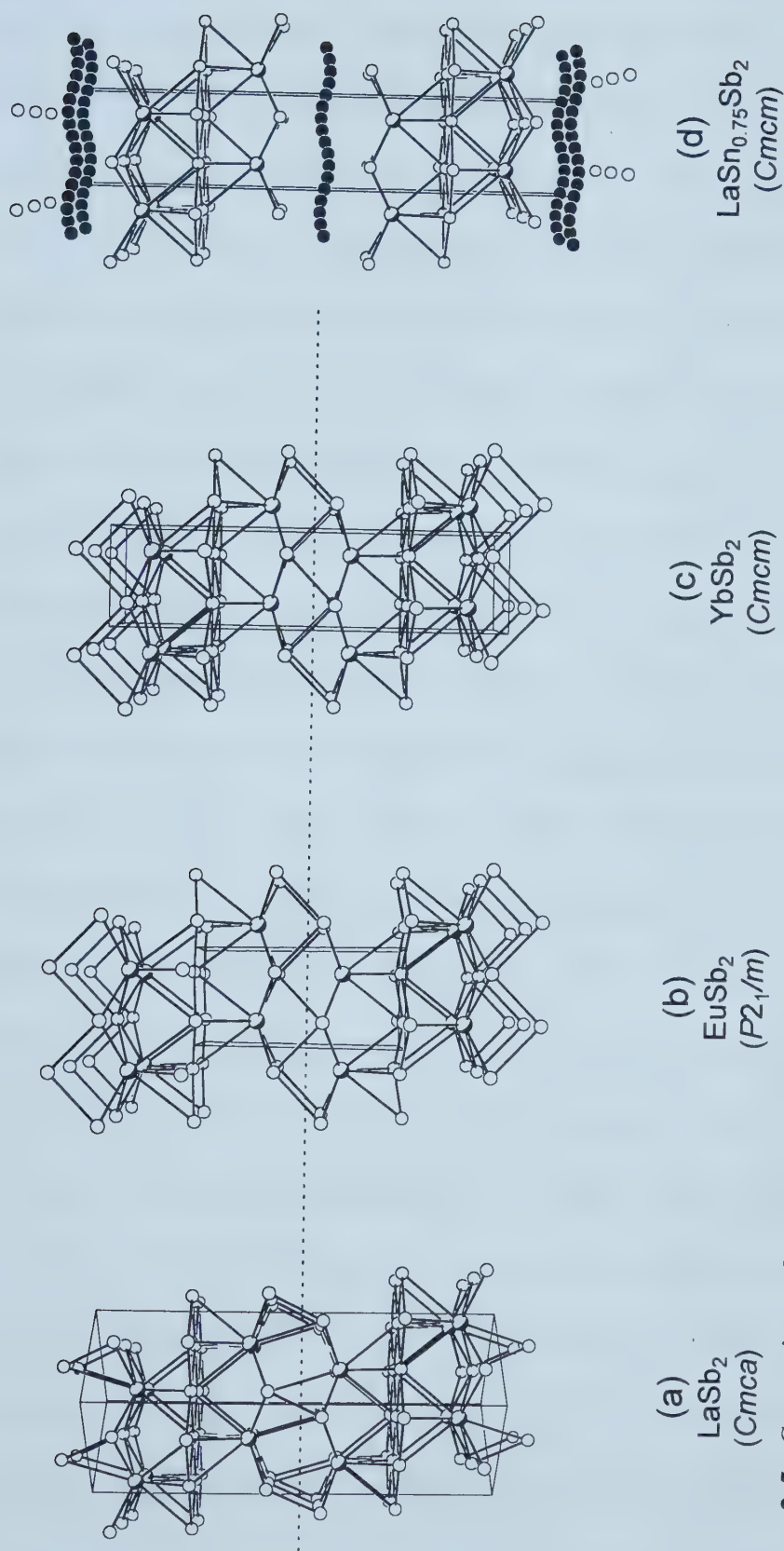


**Figure 2-5.** Comparison of various rare-earth diantimonide  $RESb_2$  structures and the  $\text{LaSn}_{0.75}\text{Sb}_2$  structure. The partly shaded circles are  $RE$  atoms, the open circles are  $Sb$  atoms, and, in the case of  $\text{LaSn}_{0.75}\text{Sb}_2$ , the solid circles are  $Sn$  atoms. Note the progressive breaking of interlayer bonds (horizontal dotted line) in the  $RESb_2$  structures followed by the insertion of  $Sn$  atoms to form the  $\text{LaSn}_{0.75}\text{Sb}_2$  structure.





Zintl concepts. A capping Sb atom 3.48(2) Å away in the adjacent layer completes the ninefold monocapped square antiprismatic coordination of the Sm atoms, which are condensed together between layers. The structures of  $\text{EuSb}_2$  and  $\text{YbSb}_2$  represent alternative ways of bond formation in response to the replacement of the trivalent rare-earth atom in the  $\text{LaSb}_2$ -type structure by a divalent one. In  $\text{EuSb}_2$ , the rare-earth layers slide relative to each other so as to form infinite zigzag Sb–Sb chains instead of pairs to hold the layers together; the Sb–Sb distance increases to 2.931(3) Å (Figure 2-5(b)).<sup>23</sup> Moreover, the square Sb net now becomes puckered and skewed so as to form parallel zigzag Sb–Sb chains: each two-connected Sb atom forms Sb–Sb bonds of 2.924(3) Å. If all the Sb–Sb bonds in  $\text{EuSb}_2$  are considered to be full two-electron single bonds, the resulting assignment is  $\text{Eu}^{2+}\text{Sb}^{1-}\text{Sb}^{1-}$ . In  $\text{YbSb}_2$ , which adopts the  $\text{ZrSi}_2$ -type structure, the same type of zigzag Sb–Sb chains holds the rare-earth layers together, with Sb–Sb distances of 2.97(1) Å (Figure 2-5(c)).<sup>24</sup> But the square Sb net contains four equally weak one-electron Sb–Sb half bonds, each of a distance of 3.12(1) Å. Here, too, the assignment is  $\text{Yb}^{2+}\text{Sb}^{1-}\text{Sb}^{1-}$ . At the extreme of this progression,  $\text{LaSn}_{0.75}\text{Sb}_2$  adopts a structure that is most directly related to that of  $\text{YbSb}_2$ : the bonds in the Sb–Sb zigzag chains are broken and the Sn atoms are put in their place (Figure 2-5(d)). The stacking axis  $b$  has been considerably expanded, from 16.63(1) Å in  $\text{YbSb}_2$  to 23.121(2) Å in  $\text{LaSn}_{0.75}\text{Sb}_2$ . The Sb–Sb distances in the square net, 3.095(1) Å, in  $\text{LaSn}_{0.75}\text{Sb}_2$  are close to those in  $\text{YbSb}_2$ , 3.12(1) Å. Accepting the validity of a half-bond approximation, we assign the Sb(1) atoms in the square net to be  $\text{Sb}^{1-}$ . Breaking the bonds in the Sb–Sb zigzag chain holding the layers together in  $\text{YbSb}_2$  causes the Sb(2) atoms to revert back





to  $\text{Sb}^{3-}$  in  $\text{LaSn}_{0.75}\text{Sb}_2$ . We are then left with a puzzling predicament: What is the oxidation state of Sn if we accept the formulation  $(\text{La}^{3+})(\text{Sn}^?)_{0.75}(\text{Sb}(1)^{1-})(\text{Sb}(2)^{3-})$ ? Is  $\text{Sn}^{1.5+}$  plausible? The apparent breakdown of the Zintl concept here arises from our insistence on assigning only integral oxidation states to the Sb atoms,<sup>25</sup> which we believe are prone to participate in intermediate Sb–Sb interactions. Moreover, the nature of the Sn atoms in  $\text{LaSn}_{0.75}\text{Sb}_2$  is not well-understood at this time. The distances from the Sn atoms to the Sb atoms that sandwich them above and below (2.936(2) to 3.190(1) Å) (Figure 2-3) are similar to, if somewhat longer than, the Sn–Sb distances found in  $\text{Na}_8\text{SnSb}_4$  (2.843(1) Å),<sup>26</sup>  $\text{Na}_5\text{SnSb}_3$  (2.805(1) to 2.945(1) Å),<sup>27</sup>  $\text{K}_8\text{SnSb}_4$  (2.898(1) Å),<sup>27</sup> and  $\text{KSnSb}$  (2.883(2) Å)<sup>28</sup> (*cf.*  $\sim 2.8$  Å for the sum of the covalent radii of Sn and Sb atoms<sup>29</sup>). Although we describe the Sn atoms to be occupying, on average, about 20% of all the available sites, we noted earlier that a local interpretation is possible in which Sn atoms occupying every fifth site are at a reasonable distance to participate in Sn–Sn bonding (2.814(3) to 2.844(3) Å); these distances are intermediate between those found in gray tin (2.80 Å) and white tin (3.02 to 3.18 Å).<sup>30</sup> An alternative explanation is to accept  $\text{Sn}^{2+}$  as the most reasonable oxidation state for tin, and postulate that the oxidation states of the Sb atoms are adjusted accordingly in response. This model would then predict that the Sb–Sb bond lengths are sensitive to the Sn content in  $\text{LaSn}_x\text{Sb}_2$ . This is reflected in the variation of the cell parameters (Table 2-4), but steric considerations are of course intimately involved as well. Mössbauer or EXAFS data would greatly aid in unraveling the nature of the Sn and Sb atoms.



Another structural consequence induced by the presence of the Sn atoms is that the La atoms are now coordinated by a ninth atom, forming a monocapped square antiprismatic geometry. Depending on the occupation of the Sn sites, the capping Sn atom may be directly beneath the La atom, at 3.423(3) Å, or it may be tilted progressively to one side, at distances of 3.415(2) Å or 3.4087(5) Å (Figure 2-2). The tilting of capping Sb atoms is seen in the LaSb<sub>2</sub>-type structure as well (Figure 2-5(a)).<sup>18</sup> The Sn atoms at 3.499(2) and 3.761(3) Å in LaSn<sub>0.75</sub>Sb<sub>2</sub> are probably too long and too tilted for there to be any bonding interactions. The shorter La–Sn distances of ~3.4 Å described above are comparable to that found in LaSn<sub>3</sub> (3.372 Å).<sup>31</sup> Moreover, the LaSn<sub>0.75</sub>Sb<sub>2</sub> structure is reminiscent of that of the mercury intercalation compound Hg<sub>1.24</sub>TiS<sub>2</sub>,<sup>32</sup> which also contains chains of Hg atoms that are best described to be nearly neutral rather than cationic. The oxidation state assignment formulated above, which assumes cationic Sn, may thus have to be modified although we are unsure precisely how.

For the moment, we have attempted some simple chemical substitutions to determine whether the LaSn<sub>0.75</sub>Sb<sub>2</sub> phase can be stabilized in other systems. Preparation of several rare-earth analogues has been successful for *RE* = La, Ce, Pr, Nd, and Sm. All of these analogues can support non-stoichiometry of the Sn atoms. Table 2-6 lists the cell parameters of the compounds prepared from the nominal stoichiometry *RE* + Sn + 2Sb, and should thus correspond to the maximum Sn content in these phases. Figure 2-6 plots the unit cell volume as a function of the rare-earth. The monotonic decrease of the cell volume is consistent with the expected lanthanide contraction, and the lack of deviation for any of these points implies that the oxidation state of the rare earth is *RE*<sup>3+</sup> in all



**Table 2-6.** Cell Parameters for Ternary  $\text{LaSn}_{0.75}\text{Sb}_2$ -type Compounds Obtained from the Reactions  $RE + \text{Sn} + 2\text{Sb}$ 

Loading Composition	$a$ (Å)	$b$ (Å)	$c$ (Å)	$V$ (Å <sup>3</sup> )
$\text{LaSnSb}_2$	4.246(1)	23.132(6)	4.507(1)	442.6(1)
$\text{CeSnSb}_2$	4.228(1)	22.868(4)	4.478(1)	433.0(1)
$\text{PrSnSb}_2$	4.204(1)	22.700(7)	4.469(2)	426.5(2)
$\text{NdSnSb}_2$	4.195(1)	22.606(5)	4.449(1)	422.0(1)
$\text{SmSnSb}_2$	4.174(1)	22.384(5)	4.416(1)	412.6(1)



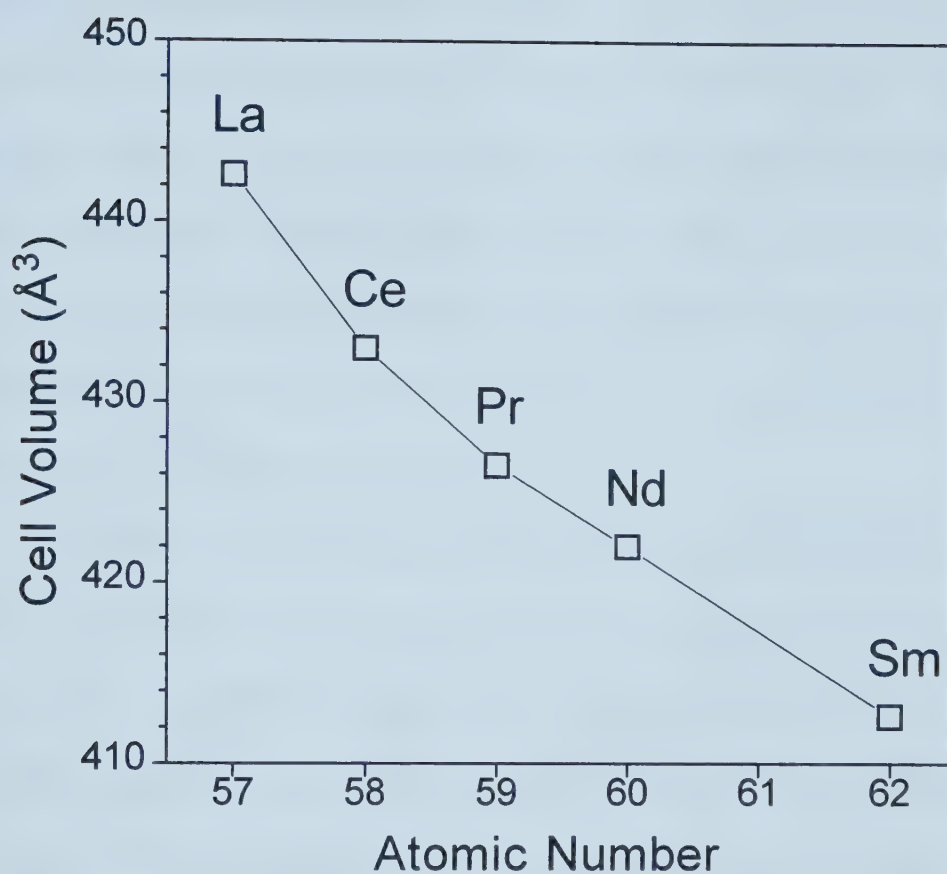


**Figure 2-6.** Plot of the unit cell volumes of  $\text{LaSn}_{0.75}\text{Sb}_2$ -type compounds obtained from reactions  $RE + \text{Sn} + 2\text{Sb}$  for various rare-earths.





cases. The  $\text{LaSn}_{0.75}\text{Sb}_2$  phase does not form with  $RE = \text{Gd}$ , suggesting that there may be a link between this result and the curious absence of an ambient pressure  $RE\text{Sb}_2$  phase with the late trivalent rare-earths  $RE = \text{Gd-Tm}$ .<sup>18,19</sup> The  $\text{LaSb}_2$ -type phase does form with Gd and Tb, but only at high pressures.<sup>19</sup> It may be worthwhile, therefore, to attempt to prepare the  $\text{LaSn}_{0.75}\text{Sb}_2$  phase with the late rare-earths by applying high pressure, as this may be sufficient to overcome unfavorable electrostatic repulsive forces that are enhanced as the structure is contracted by replacement with a smaller rare-earth atom. Substitution with a divalent rare-earth such as Eu or Yb, if it succeeds, should result in a distorted variant of the  $\text{LaSn}_{0.75}\text{Sb}_2$  structure.

Proceeding to the substitution of the second component, Sn, by its congener Ge, we have discovered a new ternary La/Ge/Sb compound that is *different* from  $\text{LaSn}_{0.75}\text{Sb}_2$ .<sup>33</sup> In contrast, preliminary experiments in doping In for Sn have resulted in quaternary compounds  $\text{La}(\text{In}_x\text{Sn}_y)\text{Sb}_2$  that appear to possess the *same* structure as that of  $\text{LaSn}_{0.75}\text{Sb}_2$ .<sup>34</sup> This has significant implications for exerting precise electronic control on the structure and properties of this system. Finally, substitution of Sb with As has resulted in a ternary La/Sn/As compound which we have yet to characterize.

**Electrical Resistivity.** The compound  $\text{LaSn}_{0.75}\text{Sb}_2$  is poorly metallic or semimetallic with a room-temperature resistivity, measured along the needle axis  $a$ , of  $\rho_{293} \approx 1 \times 10^{-3} \Omega \text{ cm}$ . Figure 2-7 shows a representative plot of the electrical resistivity as a function of temperature. Although the absolute values of the resistivity are imprecise owing to the difficulty in measuring the cross-sectional area of these crystals, the temperature dependence of the relative resistivity, expressed using the room-temperature



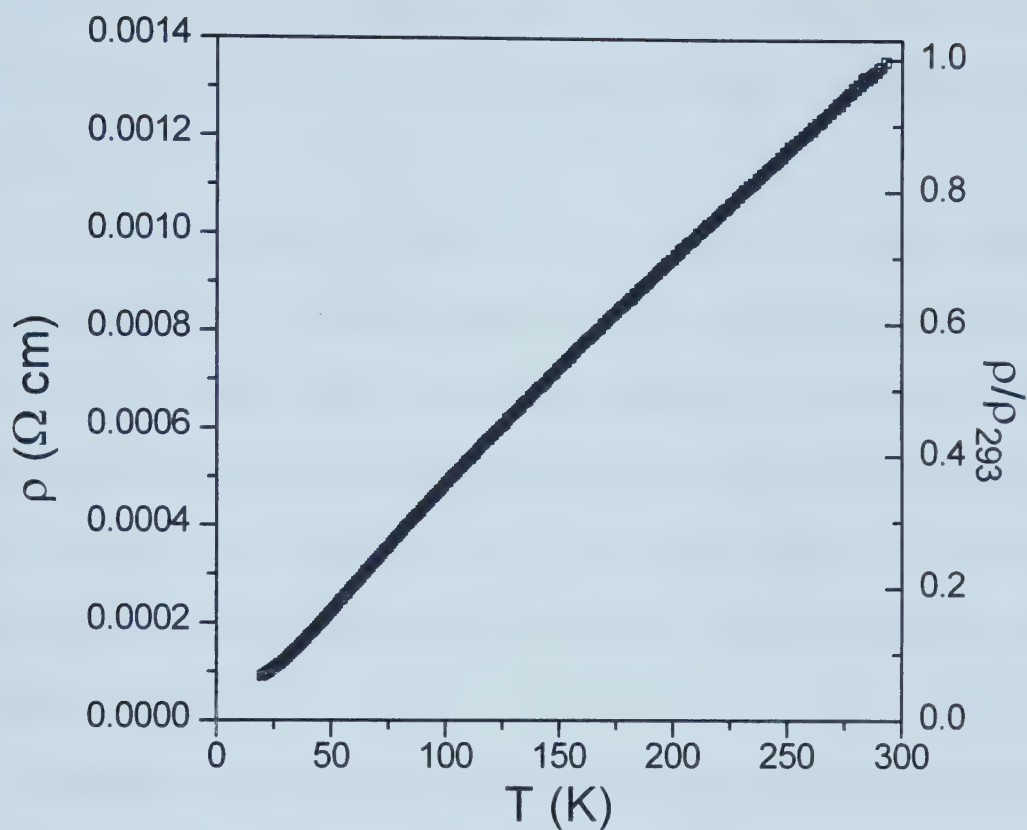


**Figure 2-7.** Plot of the electrical resistivity of  $\text{LaSn}_{0.75}\text{Sb}_2$  measured along the needle axis  $a$ . The left scale refers to the absolute resistivity and the right scale refers to the resistivity relative to the room-temperature value.



value as the reference, is highly reproducible among different specimens of  $\text{LaSn}_{0.75}\text{Sb}_2$ . The temperature coefficient for the linear portion extending through most of the curve is  $\sim 4 \times 10^{-6} \Omega \text{ cm K}^{-1}$ . At low temperatures,  $\rho_{20} \approx 1 \times 10^{-4} \Omega \text{ cm}$ , which may be taken to approach the residual resistivity arising from impurity scattering.<sup>35</sup> The resistivity ratio is thus  $\rho_{293}/\rho_{20} \approx 10$ .

It would be informative to determine the conductivity along the chains of Sn atoms, aligned along the  $c$  axis; unfortunately, these needle-shaped crystals tend to grow along the  $a$  axis instead, so the measurements made here correspond to conduction *perpendicular* to these Sn chains but parallel to the square net of Sb(1) atoms. The layered character of the crystal structure portends high electrical anisotropy, and conductivity parallel to the stacking axis  $b$  is expected to be much weaker than in the other two directions.

**Implications.** The  $\text{LaSn}_{0.75}\text{Sb}_2$  structure is a highly versatile structure type that can accommodate variable amounts of Sn in the interlayer sites. Clearly it is tempting to classify  $\text{LaSn}_{0.75}\text{Sb}_2$  as an intercalation compound, although formally the host structure  $\text{LaSb}_2$  itself does not exist with accessible van der Waals gaps, as in the layered dichalcogenides. In fact, the structure of  $\text{LaSb}_2$  is strongly bonded in the stacking direction, with the layers held together by Sb–Sb bonds.<sup>18</sup> Perhaps an alternative term that better describes the  $\text{LaSn}_{0.75}\text{Sb}_2$  structure is that of a symbiotic guest-host relationship between a  $\text{LaSb}_2$  substructure and the Sn guest atoms. A simple experiment to try is to see if the reaction  $\text{LaSb}_2 + \text{Sn}$  also results in the ternary phase, for this would



show if the formation of  $\text{LaSn}_{0.75}\text{Sb}_2$  is as literal as implied by Figure 2-6, with initial breaking of Sb–Sb bonds followed by insertion of the Sn atoms.

Given the common usage of Sn as a high-temperature flux to promote crystal growth of solid-state compounds, particularly pnictides,<sup>36</sup> it is surprising that this ternary compound has never been properly characterized before. The compound identified by Wang *et al.* as “ $\text{LaSnSb}_2$ ” was suggested,<sup>11</sup> correctly, to have a structure similar to  $\text{NdTe}_3$ ,<sup>12</sup> which also possesses layers of square antiprismatic rare-earth atoms and square Te sheets. However, the elongated 26 Å axis of  $\text{NdTe}_3$  arises from the insertion of an additional Te sheet, whereas the elongated 23 Å axis of  $\text{LaSn}_{0.75}\text{Sb}_2$  arises from the insertion of the Sn chains. We have thus shown that the structure of this phase is much more interesting than was originally postulated.

The unusual feature of the Sn chains should be investigated further. The Sn sites probably represent discrete local energy minima, and the potential energy barriers for a Sn atom to jump from one site to another ought to be low. The structure thus appears to satisfy the criteria for high mobility of the Sn atoms through open channels. Since the Sn content can be varied over a wide range, we would like to find out if Sn atoms can be reversibly inserted or removed.

In summary, the  $\text{RESn}_x\text{Sb}_2$  system provides a rare opportunity to exert formidable electronic and steric control on an unusual low-dimensional structure. Not only does it support a wide range of non-stoichiometry of the Sn atoms, it is also amenable to a variety of chemical substitutions. With rare-earth atoms that have partially-filled *f* subshells, low-dimensional magnetic ordering phenomena are expected. Doping





experiments in which some of the rare-earth atoms are substituted by alkaline earth atoms are under way. Further experiments to characterize the Sn atoms and to measure electrical properties as a function of Sn content are also in progress. It would be particularly interesting to calculate the electronic band structure of these compounds to elucidate the driving forces for the filling of the Sn sites, and we are currently planning to do this.



## REFERENCES

- (1) *Electronic Structure and Electronic Transitions in Layered Materials*; Grasso, V., Ed.; Physics and Chemistry of Materials with Low-Dimensional Structures, Series A; D. Reidel: Dordrecht, 1986.
- (2) *Crystal Chemistry and Properties of Materials with Quasi-One-Dimensional Structures*; Rouxel, J., Ed.; Physics and Chemistry of Materials with Low-Dimensional Structures, Series B; D. Reidel: Dordrecht, 1986.
- (3) *Intercalation Chemistry*; Whittingham, M. S.; Jacobson, A. J., Eds.; Academic Press: New York, 1982.
- (4) Brylak, M.; Jeitschko, W. *Z. Naturforsch. B* **1995**, *50*, 899.
- (5) Bolloré, G. ; Ferguson, M. J.; Hushagen, R. W.; Mar, A. *Chem. Mater.* **1995**, *7*, 2229.
- (6) Sologub, O.; Noël, H.; Leithe-Jasper, A.; Rogl, P.; Bodak, O. I. *J. Solid State Chem.* **1995**, *115*, 441.
- (7) Brylak, M.; Möller, M. H.; Jeitschko, W. *J. Solid State Chem.* **1995**, *115*, 305.
- (8) Havinga, E. E.; Damsma, H.; van Maaren, M. H. *J. Phys. Chem. Solids* **1970**, *31*, 2653.
- (9) Hulliger, F.; Ott, H. R. *J. Less-Common Met.* **1977**, *55*, 103.
- (10) *Concise Encyclopedia of Semiconducting Materials and Related Technologies*; Mahajan, S.; Kimerling, L. C., Eds.; Pergamon Press: Oxford, 1992.
- (11) Wang, R.; Steinfink, H.; Raman, A. *Inorg. Chem.* **1967**, *6*, 1298.
- (12) Norling, B. K.; Steinfink, H. *Inorg. Chem.* **1966**, *5*, 1488.



- (13) POLSQ: Program for least-squares unit cell refinement. Modified by D. Cahen and D. Keszler, Northwestern University, 1983.
- (14) Sheldrick, G. M. *SHELXTL* Version 5.0, Siemens Analytical X-ray Instruments, Inc., Madison, WI, 1994.
- (15) Sheldrick, G. M. *J. Appl. Crystallogr.*, in press.
- (16) *International Tables for X-ray Crystallography*; Wilson, A. J. C., Ed.; Kluwer: Dordrecht, 1992; Vol. C.
- (17) Gelato, L. M.; Parthé, E. *J. Appl. Crystallogr.* **1987**, *20*, 139.
- (18) Wang, R.; Steinfink, H. *Inorg. Chem.* **1967**, *6*, 1685.
- (19) Eatough, N. L.; Hall, H. T. *Inorg. Chem.* **1969**, *8*, 1439.
- (20) Some of the bond lengths reported by Wang and Steinfink are incorrect.<sup>18</sup> The atomic positions, however, are correct.<sup>19</sup>
- (21) Brylak, M.; Jeitschko, W. *Z. Naturforsch. B* **1994**, *49*, 747.
- (22) Garcia, E.; Corbett, J. D. *J. Solid State Chem.* **1988**, *73*, 452.
- (23) Hulliger, F.; Schmelczner, R. *J. Solid State Chem.* **1978**, *26*, 389.
- (24) Wang, R.; Bodnar, R.; Steinfink, H. *Inorg. Chem.* **1966**, *5*, 1468.
- (25) Alemany, P.; Alvarez, S.; Hoffmann, R. *Inorg. Chem.* **1990**, *29*, 3070.
- (26) Eisenmann, B.; Klein, J. *Z. Naturforsch. B* **1988**, *43*, 69.
- (27) Eisenmann, B.; Klein, J. *Z. Naturforsch. B* **1988**, *43*, 1156.
- (28) Eisenmann, B.; Klein, J. *Z. anorg. allg. Chem.* **1991**, *598/599*, 93.
- (29) O'Keeffe, M.; Brese, N. *Acta Crystallogr. Sect. B* **1992**, *48*, 152.



- (30) Wells, A. F. *Structural Inorganic Chemistry*, 5th ed.; Clarendon Press: Oxford, 1984.
- (31) Borzone, G.; Borsese, A.; Ferro, R. *Z. Anorg. Allg. Chem.* **1983**, 501, 199.
- (32) Ganal, P.; Moreau, P.; Ouvrard, G.; Sidorov, M.; McKelvy, M.; Glaunsinger, W. *Chem. Mater.* **1995**, 7, 1132.
- (33) Unpublished results. Lam, R.; Mar, A.
- (34) Unpublished results. Ellenwood, R. E.; Eulert, J. A.; Mar, A.
- (35) Ashcroft, N. W.; Mermin, N. D. *Solid State Physics*; Saunders: Philadelphia, 1976.
- (36) von Schnering, H.-G.; Hönlé, W. *Chem. Rev.* **1988**, 88, 243.





## Chapter 3

### Mössbauer Spectroscopy and Magnetic Properties of $RESn_xSb_2$ ( $RE = La, Ce, Pr, Nd, Sm$ ): Crystal Structure of $LaSn_{0.6}Sb_2$

#### Introduction

Compounds that exhibit nonstoichiometry provide an easy route for fine-tuning physical properties. For instance, the high  $T_c$  copper oxide superconductors, of which  $YBa_2Cu_3O_7$  is the parent compound, are only superconducting when slightly oxygen deficient.<sup>1</sup> With the additional flexibility imparted from partial substitution or doping of one or more of the components, the solid-state chemist is able to fully exploit the range of stability for a particular structure-type.

Recently, we reported the synthesis of a new family of nonstoichiometric rare-earth tin antimonides  $RESn_xSb_2$  and determined the structure of the prototypical member  $LaSn_{0.75}Sb_2$ , which features an unusual arrangement of Sn atoms in linear chains.<sup>2</sup> We demonstrated that the structure is able to incorporate a wide range of Sn content, from as low as  $x \approx 0.1$  to a maximum of  $x = 0.75$  for the La series.<sup>2</sup> However, we were still left with several questions, such as whether the Sn atoms adopt a different arrangement at lower  $x$ , and what exactly is the nature of the Sn atoms. The compound  $LaSn_{0.6}Sb_2$ , which possesses less than the maximum Sn content, was structurally characterized and found to crystallize with the same structure as  $LaSn_{0.75}Sb_2$ . <sup>119</sup>Sn Mössbauer spectroscopy was performed to probe the electronic environment of the Sn atoms, and



some magnetic properties of several members of the family were measured as a function of Sn content.

## Experimental Section

**Synthesis.** Bulk phase samples of  $RESn_xSb_2$  ( $RE = La, Ce, Pr, Nd, Sm$ ;  $x = 0.1 - 1.0$ ) for magnetic measurements and Mössbauer spectroscopy were prepared from reactions of powders of the elements (La, Ce, Pr, Nd, 99.9%, Alfa Aesar; Sm, 99.9%, Aldrich; Sn, 99.8%, Cerac; Sb, 99.995%, Aldrich). The elements in the appropriate ratios were loaded into fused-silica tubes (5 cm length, 10 mm i.d.), which were then evacuated, sealed, and heated in a furnace. The  $LaSn_xSb_2$  samples were heated at 570 °C for 1 day, 950 °C for 2 days, cooled to 500 °C over 1 day, and then cooled to room temperature over 5 hours. The sample of  $PrSn_{0.7}Sb_2$  was heated at 700 °C for 4 days and then cooled to room temperature over 3 days. The sample of  $SmSn_{0.3}Sb_2$  was heated at 630 °C for 1 day, 950 °C for 4 days, and cooled to room temperature over 1 day. The remaining samples were heated at 900 °C for 4 days and then cooled to room temperature over 9 hours. The samples were analyzed by their powder X-ray diffraction patterns collected on an Enraf-Nonius FR552 Guinier camera (Si standard). For all reactions with  $x < 0.8$ , the ternary compounds were the only identifiable products (to the detection limits of the Guinier camera). With  $x \geq 0.8$ , excess Sn and other unidentifiable phases were detected as minor impurities.

The single crystal used for the structure determination was obtained from a reaction with loaded composition of  $LaSn_{0.5}Sb_2$ . The product consisted of a dull gray



powder and small rectangular plate crystals. Five crystals were selected and mounted for EDX (energy dispersive X-ray) analysis on a Hitachi F2700 scanning electron microscope to determine their elemental compositions. Anal. Calcd for  $\text{LaSn}_{0.5}\text{Sb}_2$ : La, 31.4%; Sn, 13.4%; Sb, 55.1%. Found (average of five analyses): La, 31.8(5)%; Sn 13.1(5)%; Sb 55.0(6)%.

**Structure Determination.** Preliminary Weissenberg photographs were similar to those for the parent compound  $\text{LaSn}_{0.75}\text{Sb}_2$ , although the relative diffracted intensities differed. X-ray diffraction data were collected on an Enraf-Nonius CAD4 diffractometer at room temperature with the  $\theta$ - $2\theta$  scan technique. Final cell constants were determined from a least-squares analysis of the setting angles of 24 reflections in the range  $21^\circ \leq 2\theta$  ( $\text{MoK}_\alpha$ )  $\leq 39^\circ$ . Crystal data and further details of the data collection are given in Table 3-1.

All calculations were carried out using the SHELXTL (Version 5.1) software package.<sup>3,4</sup> Conventional atomic scattering factors and anomalous dispersion corrections were used.<sup>5</sup> Intensity data were processed and Gaussian face-indexed absorption corrections were applied with the program XPREP. The space group *Cmcm* was selected based on the systematic absence exceptions, satisfactory averaging ( $R_{\text{int}} = 0.098$ ), and successful structure solution. The initial positions of the La and Sb atoms were found by direct methods. Least-squares refinement revealed a peak in the difference Fourier map at (0, 0, 0) which was partially accounted for by placing a Sn atom at this site. The atomic displacement parameter for this Sn site was quite large suggesting partial occupancy, and the site occupation factor was allowed to refine. There was still a peak in



**Table 3-1.** Crystallographic Data for  $\text{LaSn}_{0.61(1)}\text{Sb}_2$ 

Formula	$\text{LaSn}_{0.61(1)}\text{Sb}_2$
Formula mass (amu)	453.62
Space group	$D_{2h}^{17} - Cmc m$
$a$ (Å)	4.2590(4) <sup>a</sup>
$b$ (Å)	23.1334(19) <sup>a</sup>
$c$ (Å)	4.4872(4) <sup>a</sup>
$V$ (Å <sup>3</sup> )	442.10(7)
$Z$	4
$T$ (°C)	20
Diffractometer	Enraf-Nonius CAD4
$\rho_{\text{calc}}$ (g cm <sup>-3</sup> )	6.815
Crystal dimensions	Silver plate, $0.150 \times 0.049 \times 0.009$ mm <sup>3</sup>
Radiation	Graphite monochromated $\text{MoK}_\alpha$ , $\lambda = 0.71073$ Å
$\mu$ (cm <sup>-1</sup> )	247.1
Transmission factors <sup>b</sup>	0.329 – 0.806
Scan type	$\theta$ – $2\theta$
$2\theta$ limits	$4^\circ \leq 2\theta(\text{MoK}_\alpha) \leq 70^\circ$
Data collected	$-6 \leq h \leq 6, -36 \leq k \leq 36, -7 \leq l \leq 7$
No. of data collected	3824
No. of unique data, including $F_o^2 < 0$	590 ( $R_{\text{int}} = 0.098$ )
No. of unique data, with $F_o^2 > 2\sigma(F_o^2)$	520
No. of variables	21





**Table 3-1.** Crystallographic Data for  $\text{LaSn}_{0.61(1)}\text{Sb}_2$  (cont'd)

Extinction coefficient <sup>c</sup>	0.0082(10)
$R(F)$ for $F_o^2 > 2\sigma(F_o^2)$ <sup>d</sup>	0.045
$R_w(F_o^2)$ <sup>e</sup>	0.112
Goodness of fit <sup>f</sup>	1.210
Restrained goodness of fit <sup>f</sup>	1.398

<sup>a</sup> Obtained from refinement constrained so that  $\alpha = \beta = \gamma = 90^\circ$ .

<sup>b</sup> A Gaussian face-indexed absorption correction was applied with the use of the programs in the SHELXTL package (Sheldrick, G. M. *SHELXTL* Version 5.1; Bruker Analytical X-ray Instruments, Inc.: Madison, WI, 1997).

<sup>c</sup> An extinction parameter  $x$  was refined, where  $F_c$  is multiplied by:  $k[1 + 0.001 * x * F_c^2 * \lambda^3 / \sin(2\theta)]^{-1/4}$ .

$$^d R(F) = \sum \|F_o\| - |F_c| / \sum |F_o|.$$

$$^e R_w(F_o^2) = [\sum [w(F_o^2 - F_c^2)^2] / \sum wF_o^4]^{1/2}; w^{-1} = [\sigma^2(F_o^2) + (0.0403P)^2 + 26.64P],$$

where  $P = [\max(F_o^2, 0) + 2F_c^2] / 3$ .

$$^f GooF = S = [\sum [w(F_o^2 - F_c^2)^2] / (n - p)]^{1/2} \text{ where } n \text{ is the number of reflections and } p \text{ is the total number of parameters refined.}$$



the difference Fourier map, this time at (0,  $\sim 0.008$ ,  $\sim 0.315$ ), which was also allowed to be partially occupied by Sn. The La and Sb atoms were refined anisotropically and were well behaved. However, the refined formula indicated that while the La and Sb sites are fully occupied, the refined Sn content was significantly higher than had been determined from the elemental analyses. A restraint was applied to the sum of the Sn occupancies, with a target value of 0.5 consistent with both the EDX analyses and the loaded stoichiometry. Moreover, given that the lattice constants determined from single crystal X-ray diffraction agree well with those obtained from powder X-ray diffraction on a reaction with loaded stoichiometry  $\text{LaSn}_{0.5}\text{Sb}_2$ , we feel this restraint is justified. The subsequent refinement and difference Fourier map yielded the third Sn site at (0,  $\sim 0.010$ ,  $\frac{1}{4}$ ) and was modeled as a partially occupied site. The displacement parameter for this new site was too low and therefore all the Sn displacement parameters were constrained to be equal. Given that occupancy factors and displacement parameters are highly correlated and dependent upon the accuracy of the absorption correction performed, one needs to carefully consider all of the available data before accepting refined occupancies. We feel that this model best incorporates all of the experimental data, and the model was refined until convergence was achieved. The atomic positions were standardized with the use of the program STRUCTURE TIDY.<sup>6</sup> The final cycle of least-squares refinement on  $F_o^2$  of 21 variables and 590 averaged reflections (including those having  $F_o^2 < 0$ ) converged to values of  $R_w(F_o^2)$  of 0.112 and  $R(F)$  (for  $F_o^2 > 2\sigma(F_o^2)$ ) of 0.045. The final electron density map is featureless ( $\Delta\rho_{\text{max}} = 6.26$ ,  $\Delta\rho_{\text{min}} = -5.14 \text{ e } \text{\AA}^{-3}$ ). The  $\Delta\rho_{\text{max}}$  value is small relative to the atomic peaks observed and can be attributed to noise. Final values



of the positional and equivalent isotropic displacement parameters are given in Table 3-2 and anisotropic displacement parameters are given in the Appendix (Table A-2).

**Mössbauer Spectroscopy.**  $^{119}\text{Sn}$  Mössbauer spectra were obtained for the series of compounds  $\text{LaSn}_x\text{Sb}_2$  ( $0.1 \leq x \leq 1.0$ ) at Simon Fraser University by Professor C. D. W. Jones and Dr. R. D. Sharma.

**Magnetic Measurements.** The magnetic data were collected on a Quantum Design SQUID magnetometer at the University of British Columbia. Approximately 50 mg of powdered sample was placed in a gelatin capsule and mounted inside a hollow quartz tube, which was then attached to the magnetometer sample rod. The samples were centered at 5 K and zero field cooled data were collected between 5 and 300 K with an applied magnetic field of 2 Tesla for  $RE = \text{La}$  and 0.1 Tesla for  $RE = \text{Ce, Pr, Nd, Sm}$ . Saturation moments were determined from the magnetization versus field curves at 5 K with applied fields from 0 to 5.5 Tesla.

## Results and Discussion

**Description of the Structure.**  $\text{LaSn}_{0.61}\text{Sb}_2$  is isostructural to  $\text{LaSn}_{0.75}\text{Sb}_2$ , which consists of layers of composition  ${}^2_\infty[\text{LaSb}_2]$  stacked along [010], separated by linear chains of Sn atoms.<sup>2</sup> Two views of the structure are shown in Figure 3-1, which also shows the labeling scheme. Selected interatomic distances and angles are listed in Table 3-3. A detailed description of the structure has already been given in Chapter 2.

The cell parameters for the single crystal data follow the same trend observed for the powder diffraction data; the  $a$  axis increases from 4.2435(5) to 4.2590(4) Å and the  $c$



**Table 3-2.** Atomic Coordinates, Occupancies, and Equivalent Isotropic Displacement Parameters ( $\text{\AA}^2$ ) for  $\text{LaSn}_{0.61(1)}\text{Sb}_2$

atom	Wyckoff position, site symmetry	<i>x</i>	<i>y</i>	<i>z</i>	occupancy	$U_{\text{eq}}^a$
La	4 <i>c</i> <i>m2m</i>	0	0.86090(4)	1/4	1	0.0088(3)
Sb(1)	4 <i>c</i> <i>m2m</i>	0	0.24875(5)	1/4	1	0.0100(3)
Sb(2)	4 <i>c</i> <i>m2m</i>	0	0.59028(5)	1/4	1	0.0112(3)
Sn(1)	8 <i>f</i> <i>m . .</i>	0	0.0064(2)	0.1221(12)	0.154(3) <sup><i>b</i></sup>	0.0093(8) <sup><i>c</i></sup>
Sn(2)	4 <i>c</i> <i>m2m</i>	0	0.0083(3)	1/4	0.147(4) <sup><i>b</i></sup>	0.0093(8) <sup><i>c</i></sup>
Sn(3)	4 <i>a</i> <i>2/m . .</i>	0	0	0	0.157(4) <sup><i>b</i></sup>	0.0093(8) <sup><i>c</i></sup>

<sup>*a*</sup>  $U_{\text{eq}}$  is defined as one-third of the trace of the orthogonalized  $U_{ij}$  tensor.

<sup>*b*</sup> The sum of the occupancies of the Sn atoms was restrained during refinement to be equal to 0.5, with a maximum deviation per least-squares cycle of 0.008.

<sup>*c*</sup> The Sn atoms were refined isotropically and constrained to have the same displacement parameter.





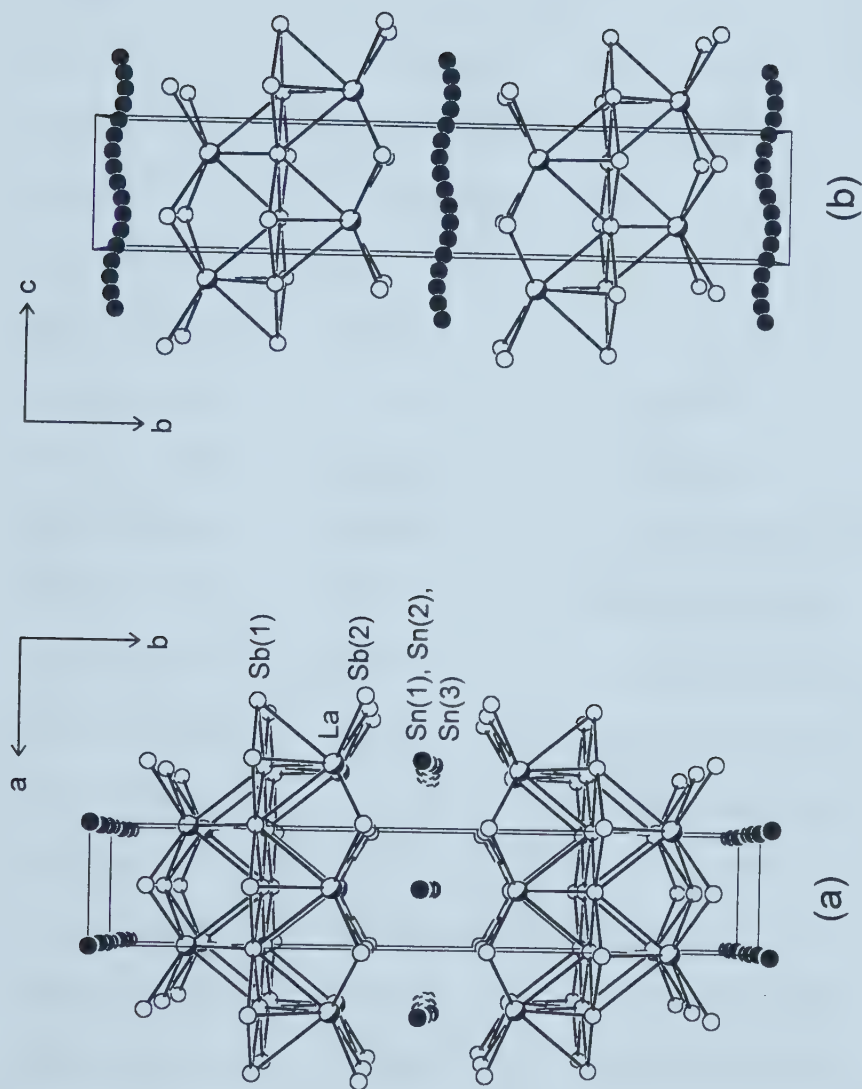


**Figure 3-1.** (a) View down the  $c$  axis of  $\text{LaSn}_{0.61}\text{Sb}_2$  with the unit cell outlined. The partly shaded circles are La atoms, the open circles are Sb atoms, and the shaded circles represent *sites* for the Sn atoms and do not imply the actual presence of the atoms themselves. (b) View down the  $a$  axis, showing the wavelike arrangement parallel to the  $c$  direction of the three Sn sites positioned between the layers of composition  $\text{LaSb}_2$ . These sites are only *partially* occupied, each at about 15%.



**Table 3-3.** Selected Interatomic Distances (Å) and Angles (°) for  $\text{LaSn}_{0.61(1)}\text{Sb}_2$ 

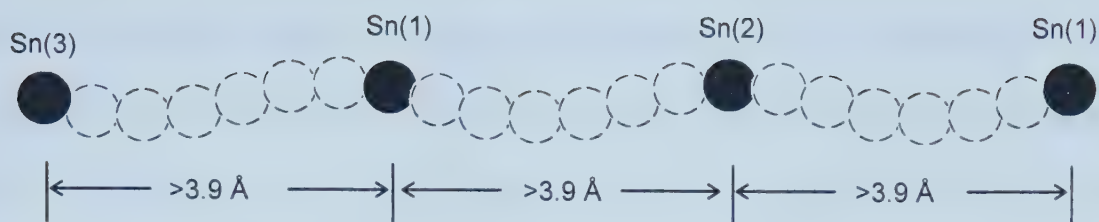
La–Sb(2)	3.2930(6) (4×)	Sb(1)–Sb(1)	3.0938(2) (4×)
La–Sb(1)	3.3565(12) (2×)	Sn(1)–Sb(2)	2.937(4) (2×)
La–Sb(1)	3.3866(11) (2×)	Sn(1)–Sb(2)	3.511(4) (2×)
La–Sn(3)	3.4077(9) (2×)	Sn(1)–Sn(3)	2.795(6)
La–Sn(2)	3.410(8)	Sn(1)–Sn(2)	2.838(6)
La–Sn(1)	3.416(5) (2×)	Sn(2)–Sb(2)	2.852(5) (2×)
La–Sn(1)	3.493(5) (2×)	Sn(2)–Sb(2)	3.843(5) (4×)
La–Sn(2)	3.767(8) (3×)	Sn(3)–Sb(2)	3.1868(8) (4×)
Sb(2)–La–Sb(2)	139.89(5)	La–Sb(2)–La	80.6(2)
Sb(2)–La–Sb(2)	80.58(2)	La–Sb(2)–La	139.85(5)
Sb(2)–La–Sb(2)	85.90(2)	La–Sb(2)–La	85.9(2)
Sb(2)–La–Sb(1)	132.48(2)	Sb(2)–Sn(1)–Sb(2)	92.95(15)
Sb(2)–La–Sb(1)	81.65(2)	Sb(2)–Sn(1)–Sn(2)	83.41(17)
Sb(2)–La–Sb(1)	135.09(2)	Sb(2)–Sn(1)–Sn(3)	103.32(14)
Sb(2)–La–Sb(1)	78.78(2)	Sn(2)–Sn(1)–Sn(3)	170.0(2)
Sb(1)–La–Sb(1)	78.76(3)	Sb(2)–Sn(2)–Sb(2)	96.6(2)
Sb(1)–La–Sb(1)	54.62(1)	Sb(2)–Sn(2)–Sn(1)	94.58(11)
Sb(1)–La–Sb(1)	82.98(3)	Sn(1)–Sn(2)–Sn(1)	166.2(1)
Sb(1)–Sb(1)–Sb(1)	177.86(8)	Sb(2)–Sn(3)–Sb(2)	83.9(2)
Sb(1)–Sb(1)–Sb(1)	86.99(1)	Sb(2)–Sn(3)–Sb(2)	96.1(2)
Sb(1)–Sb(1)–Sb(1)	92.97(1)	Sb(2)–Sn(3)–Sb(2)	180
La–Sb(1)–La	78.76(3)	Sn(1)–Sn(3)–Sn(1)	180
La–Sb(1)–La	125.38(1)		
La–Sb(1)–La	82.98(3)		



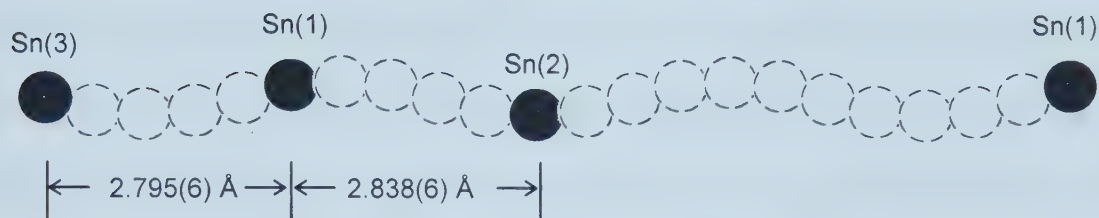
axis decreases from 4.5053(6) to 4.4872(4) Å with decreasing Sn content from  $\text{LaSn}_{0.75}\text{Sb}_2$  to  $\text{LaSn}_{0.61}\text{Sb}_2$ .<sup>2</sup> The contraction along the *c* axis was rationalized based on a steric argument – fewer Sn atoms in the chains will diminish the spatial requirements, thus shortening the *c* axis.<sup>2</sup> The formula  $\text{LaSn}_{0.75}\text{Sb}_2$  yields ~20% occupancy of each Sn site (or one in *five* sites, on a local level, is occupied by Sn), which corresponds to distances that are reasonable for Sn–Sn bonding. The formula  $\text{LaSn}_{0.61}\text{Sb}_2$  yields ~15% occupancy of each Sn site, and leads to two possibilities: (1) that one in *seven* sites are occupied, with Sn–Sn distances of ~3.9 Å that are probably too long for bonding, and (2) on a local level, one in five sites are occupied, but the chains are randomly segmented by vacancies such that on average only one in seven sites are occupied. This is illustrated in Figure 3-2, which shows a schematic representation of both situations. The Sn–Sn interatomic distances are only marginally smaller in  $\text{LaSn}_{0.61}\text{Sb}_2$  than in  $\text{LaSn}_{0.75}\text{Sb}_2$  (Sn(1)–Sn(3) distance 2.795(6) vs. 2.814(3) Å, Sn(1)–Sn(2) distance 2.838(6) vs. 2.844(3) Å),<sup>2</sup> suggesting that locally the Sn chains in both compounds are very similar. We favor the second interpretation as being more realistic, owing to the retention of the strong Sn–Sn bonds, which we believe are an integral part of the structure. The Sn–Sb bond distances and angles remain approximately unchanged; the origin of the increase of the *a* axis may simply arise from the slight compression of the structure along the *c* axis. Moreover, the introduction of new Sn vacancies results in fewer Sn–Sb bonds available to hold the structure together along *a*.

The square sheets of Sb(1) atoms show only a very slight decrease in the Sb–Sb bond distances (3.0952(3) vs. 3.0938(2) Å) and may reflect a small increase in the Sb–Sb bond strength as the Sn content is lowered.<sup>2</sup> The coordination around La does not appear





(a)



(b)

**Figure 3-2.** Two possible arrangements of the Sn atoms in  $\text{LaSn}_{0.61}\text{Sb}_2$ , with 15% occupancy of the Sn sites. (a) One in *seven* Sn sites occupied, with Sn–Sn distances greater than  $3.9 \text{ \AA}$  and outside the realm of bonding. (b) One in *five* sites occupied on a local level, with reasonable Sn–Sn bonding distances. The effect of reducing the Sn content from its maximum of  $x = 0.75$  is the creation of vacancies and the segmentation of the infinite Sn chains into finite units.





to show a significant change with decreasing Sn content, and this is reflected by relatively constant La–Sb and La–Sn bond distances and angles. Overall, reduction of the amount of Sn incorporated in the structure ultimately serves only to segment the Sn chains into finite units.

**Mössbauer Spectroscopy.** An oxidation state formulation for  $\text{LaSn}_{0.75}\text{Sb}_2$  was postulated based on the Zintl concept.<sup>2,7-10</sup> Within the concept, the electropositive La atoms serve only to donate their three valence electrons to the Sn and Sb atoms, which use them to form bonds and complete their octets. The initial partitioning of the valence electrons results in  $(\text{La}^{3+})[\text{Sn}_{0.75}\text{Sb}_2]^{3-}$ . The Sb(1)–Sb(1) distances (3.0938(2) Å) in the Sb square sheet are intermediate between the full single intralayer Sb–Sb bond and the interlayer distance found in elemental Sb (2.908 vs.  $\sim 3.36$  Å)<sup>11</sup> and are consistent with one-electron bonds.<sup>12,13</sup> The Sb(1) atoms are thus assigned an oxidation state of  $-1$ .<sup>12,13</sup> Since the Sb(2) atoms are not involved in homoatomic bonding (the nearest Sb(2)–Sb(2) interatomic distance is  $> 4.2$  Å, approximately equal to the sum of the van der Waals radius),<sup>14</sup> they are considered as isolated  $\text{Sb(2)}^{3-}$  anions. By charge balance, the Sn atoms must therefore have an average charge of  $+1.33$ , and an overall formulation of  $(\text{La}^{3+})(\text{Sn}^{1.33+})_{0.75}(\text{Sb(1)}^{1-})(\text{Sb(2)}^{3-})$  is attained. As the Sn content varies, either the average charge on Sn must change to accommodate the different electron counts, or the Sb squares net may serve as electron sources or sinks, absorbing or releasing electrons as needed, as has been previously postulated.<sup>15</sup> However, given that the electronegativities of Sn and Sb are quite similar (1.96 vs. 2.05 for Sn and Sb, respectively),<sup>16</sup> the Sn–Sb(2)



bonds will be strongly covalent and the above model based on oxidation states gives a poor approximation to the true charges.

$^{119}\text{Sn}$  Mössbauer spectroscopy was performed on the series  $\text{LaSn}_x\text{Sb}_2$  ( $0.1 \leq x \leq 1.0$ ) to probe the electronic environment of the Sn atoms as a function of Sn content. For all compounds, the spectra show two peaks centered at  $\sim 2.6 \text{ mm s}^{-1}$ , and were fit with two overlapping Lorentzian functions constrained to have equal linewidths. The linewidths are reasonably narrow and characteristic of those observed for elemental  $\beta\text{-Sn}$ .<sup>17</sup> Since there was no appreciable line broadening observed (which would give evidence for a set of overlapping unresolved doublets), it can be concluded that all three Sn atoms have very similar Mössbauer parameters and the spectra can be interpreted as a quadrupole split doublet. The results are collected in Table 3-4, which lists the line positions, line widths, relative intensities, calculated isomer shifts ( $\delta$ ), and quadrupole splittings ( $\Delta$ ). Plotted in Figure 3-3 are the isomer shift, quadrupole splitting, and relative intensity of the high velocity line as a function of Sn content. Both  $\delta$  and  $\Delta$  increase slightly with decreasing Sn content and the two lines become nearly equal in intensity. Interestingly, the observed isomer shifts for all of the compounds are very similar to that for  $\beta\text{-Sn}$  metal ( $2.54$  to  $2.81 \text{ mm s}^{-1}$  vs.  $2.52 \text{ mm s}^{-1}$ ),<sup>17</sup> suggesting that the Sn chains in  $\text{LaSn}_x\text{Sb}_2$  are composed of zero valent Sn. The slight increase in  $\delta$  with decreasing  $x$  is indicative of partial oxidation of the Sn atoms, and reflects the subtle changes that occur to accommodate the varying electron count with changing stoichiometry.

The similarity of the Mössbauer parameters for  $\text{LaSn}_x\text{Sb}_2$  to Sn metal is not entirely surprising given that the Sn–Sb bonds are strongly covalent, which the simple



**Table 3-4.** Mössbauer Data for  $\text{LaSn}_x\text{Sb}_2$  ( $0.1 \leq x \leq 1.0$ )

Compound	Line Positions ( $\text{mm s}^{-1}$ ) <sup>a</sup>	Line Width ( $\text{mm s}^{-1}$ )	Intensities (%) ( $\pm 1$ %)	$\delta$ ( $\text{mm s}^{-1}$ ) <sup>a</sup> ( $\pm 0.05$ )	$\Delta$ ( $\text{mm s}^{-1}$ ) ( $\pm 0.05$ )
Sn metal	2.52	1.10	100		
$\text{LaSn}_{0.1}\text{Sb}_2$	3.24	1.01	52.7	2.71	1.06
	2.18		47.3		
$\text{LaSn}_{0.2}\text{Sb}_2$	3.38	1.11	53.7	2.81	1.14
	2.24		46.3		
$\text{LaSn}_{0.3}\text{Sb}_2$	3.23	1.07	53.0	2.68	1.10
	2.13		47.0		
$\text{LaSn}_{0.4}\text{Sb}_2$	3.20	1.19	52.6	2.68	1.10
	2.11		47.4		
$\text{LaSn}_{0.5}\text{Sb}_2$	3.16	1.18	53.7	2.64	1.01
	2.12		46.3		
$\text{LaSn}_{0.6}\text{Sb}_2$	3.14	1.11	54.7	2.63	1.03
	2.11		45.3		
$\text{LaSn}_{0.7}\text{Sb}_2$	3.06	1.10	55.3	2.58	0.97
	2.09		44.7		
$\text{LaSn}_{0.8}\text{Sb}_2$	3.07	1.27	55.5	2.54	0.86
	2.11		44.5		
$\text{LaSn}_{0.9}\text{Sb}_2$	3.01	1.31	55.5	2.57	0.88
	2.13		44.5		
$\text{LaSn}_{1.0}\text{Sb}_2$	2.96	1.21	57.2	2.57	0.78
	2.18		42.8		

<sup>a</sup> Relative to  $\text{SnO}_2$ .



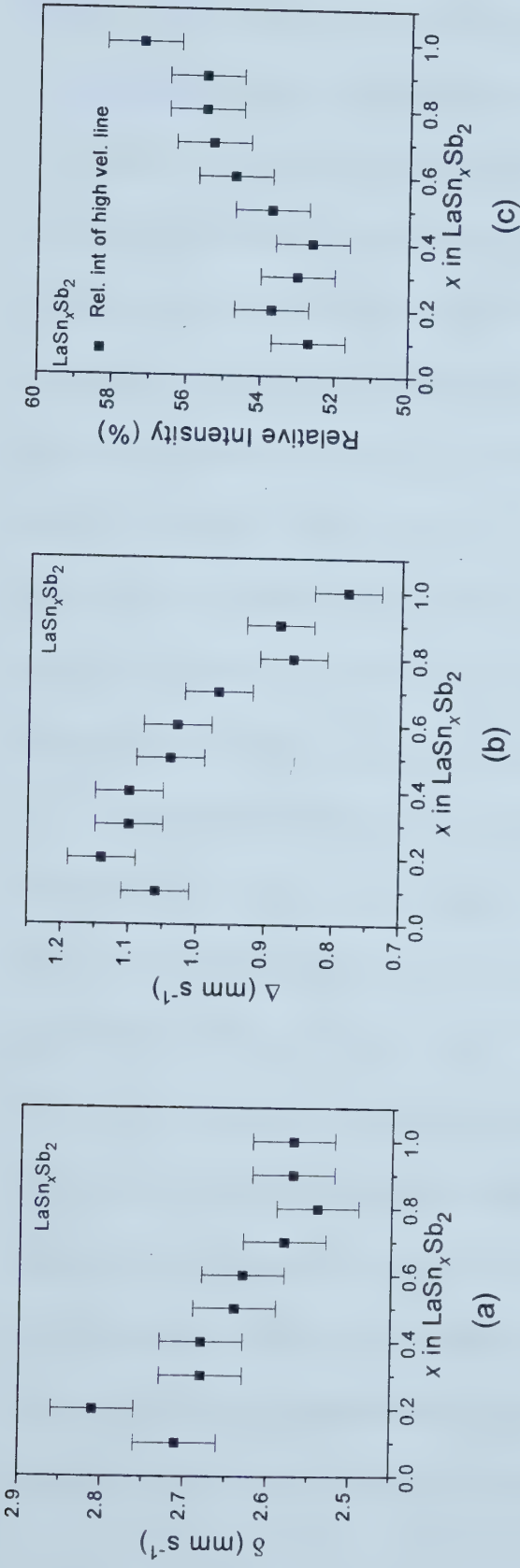


**Figure 3-3.** The calculated Mössbauer parameters (a) isomer shift ( $\delta$ ) and (b) quadrupole splitting ( $\Delta$ ), and (c) the relative intensity of the high velocity line plotted as a function of  $x$  in  $\text{LaSn}_x\text{Sb}_2$ . Note that as  $x$  decreases both  $\delta$  and  $\Delta$  increase and the intensities become more nearly equal.





model based on oxidation states fails to reflect (since it assumes full electron transfer from Sn to Sb). A more accurate model (developed based on formal charges) would have to recognize that since both the Sn(1) and Sn(2) atoms are each bonded to two other Sn atoms and two Sb(2) atoms, they should be considered as  $\text{Sn}^0$  (or at best slightly positive because of the slightly greater electronegativity of Sb). The Sn(3) atoms are also bonded to two other Sn atoms, but have four Sb(2) neighbors at distances (3.1868(8) Å) much larger than a typical Sn–Sb single bond and can be considered one-electron bonds. Thus, Sn(3) is also assigned as  $\text{Sn}^0$ . We now obtain the formulation  $(\text{La}^{\text{III}})(\text{Sn}^0)_{0.75}(\text{Sb(1)}^{-1})(\text{Sb(2)}^{-1})$ . However, lowering the Sn content not only introduces vacancies along the Sn chains (and thus eliminating Sn–Sn bonds) but also eliminates some of the Sn–Sb(2) bonds. This necessitates further modification, the easiest of which is to suggest that the electron count fluctuations are accommodated by the Sb(1) square nets.

**Magnetic Properties.**  $\text{LaSn}_{0.7}\text{Sb}_2$ : The magnetic susceptibility data as a function of temperature for  $\text{LaSn}_{0.7}\text{Sb}_2$  are plotted in Figure 3-4. The data were corrected for core diamagnetism using values for  $\text{La}^{3+}$  ( $-20 \times 10^{-6} \text{ emu mol}^{-1}$ ),  $\text{Sn}^{2+}$  ( $-20 \times 10^{-6} \text{ emu mol}^{-1}$ ), and Sb(III) ( $-74 \times 10^{-6} \text{ emu mol}^{-1}$ ).<sup>18</sup> Unfortunately, appropriate values for the diamagnetic contributions for Sn metal and  $\text{Sb}^{3-}$  are unavailable in the literature, but the above values are reasonable approximations.  $\text{LaSn}_{0.7}\text{Sb}_2$  displays essentially temperature independent paramagnetism ( $\chi_{\text{TIP}} = 1.1(1) \times 10^{-4} \text{ emu K mol}^{-1}$ ) with a weak Curie tail at low temperatures, which may be attributed to a minor paramagnetic impurity.<sup>19</sup> Because of the extremely weak magnetism exhibit by  $\text{LaSn}_{0.7}\text{Sb}_2$ , it was very difficult to obtain a good signal in the magnetometer and therefore the data may not be reliable. However,



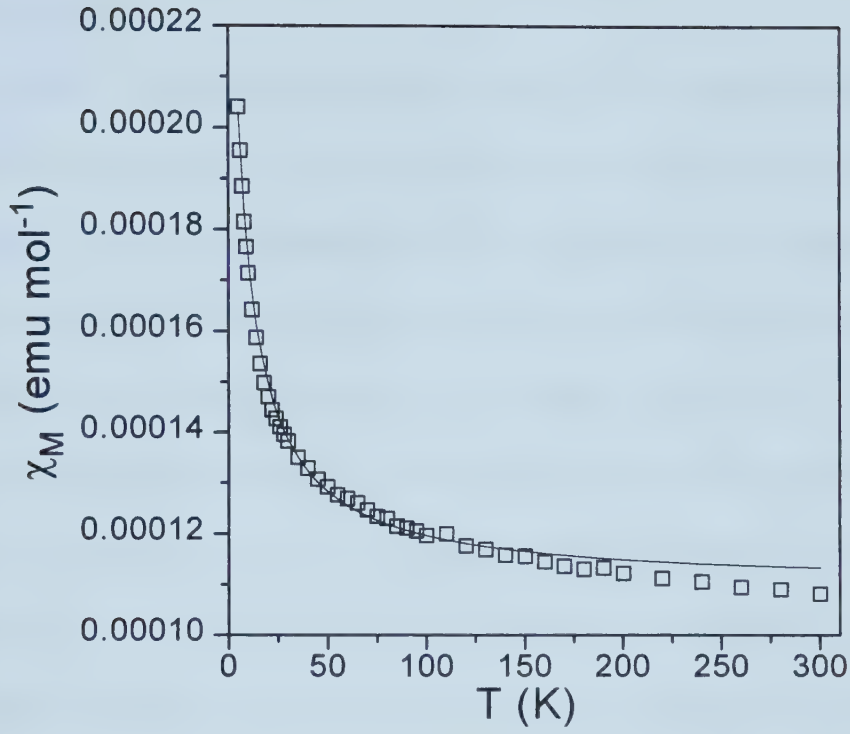


**Figure 3-4.** Plot of the magnetic susceptibility as a function of temperature for  $\text{LaSn}_{0.7}\text{Sb}_2$ . The solid line is the fit to  $\chi = \chi_{\text{TIP}} + C/(T - \theta)$ , where  $\chi_{\text{TIP}} = 1.1(1) \times 10^{-4} \text{ emu mol}^{-1}$ ,  $C = 0.00103(4) \text{ emu K mol}^{-1}$ , and  $\theta = -6.1(5) \text{ K}$ .



the temperature independent magnetism exhibited is consistent with the metallic behavior previously reported.<sup>2</sup>

*CeSn<sub>x</sub>Sb<sub>2</sub>*: The reciprocal susceptibility ( $\chi^{-1}$ ) and  $\chi T$  data for CeSn<sub>0.3</sub>Sb<sub>2</sub> and CeSn<sub>0.7</sub>Sb<sub>2</sub> are plotted as a function of temperature in Figure 3-5(a) and (b). The isothermal ( $T = 5$  K) magnetization data for CeSn<sub>0.7</sub>Sb<sub>2</sub> are plotted in Figure 3-5(c). The  $\chi^{-1}$  data were fit to the Curie-Weiss law and the values for the paramagnetic ordering temperature ( $\theta$ ) and Curie constant ( $C$ ) are collected in Table 3-5.<sup>19</sup> The effective magnetic moment ( $\mu_{\text{eff}}$ ) for the Ce ions extracted from the Curie constant yield 2.48 and 2.50  $\mu_B$  for CeSn<sub>0.3</sub>Sb<sub>2</sub> and CeSn<sub>0.7</sub>Sb<sub>2</sub> respectively, consistent with the theoretical moment for Ce<sup>3+</sup> (2.54  $\mu_B$ ).<sup>20</sup> The positive values of  $\theta$  are indicative of a predominantly ferromagnetic interaction between the Ce<sup>3+</sup> moments, which also is reflected in the  $\chi T$  plot by the strong upturn at low temperatures. A ferromagnetic ordering temperature ( $T_C$ ) can be obtained from the function  $-d(\chi T)/dT$ , which is plotted in the inset of Figures 3-5(a) and (b), and yields  $T_C \approx 9$  for both compounds. The isothermal magnetization data for CeSn<sub>0.7</sub>Sb<sub>2</sub> (Figure 3-5(c)) indicate that the Ce<sup>3+</sup> moments have reached only 65% of their expected saturation values at 5.5 T (experimental:  $\sim 1.4 \mu_B$ ; theoretical:  $2.14 \mu_B$ ).<sup>20</sup>

*PrSn<sub>x</sub>Sb<sub>2</sub> and NdSn<sub>x</sub>Sb<sub>2</sub>*: The magnetic data for Pr and Nd compounds are plotted in Figures 3-6 and 3-7, respectively. The  $\chi^{-1}$  data were fit to the Curie-Weiss law and the values are collected in Table 3-5.<sup>19</sup> The negative values for  $\theta$  are indicative of an antiferromagnetic interaction of the *RE* moments, although there was no indication of the onset of magnetic ordering down to 5 K. The  $\chi T$  plots for all four compounds show a marked decrease at low temperatures, typical for materials which exhibit



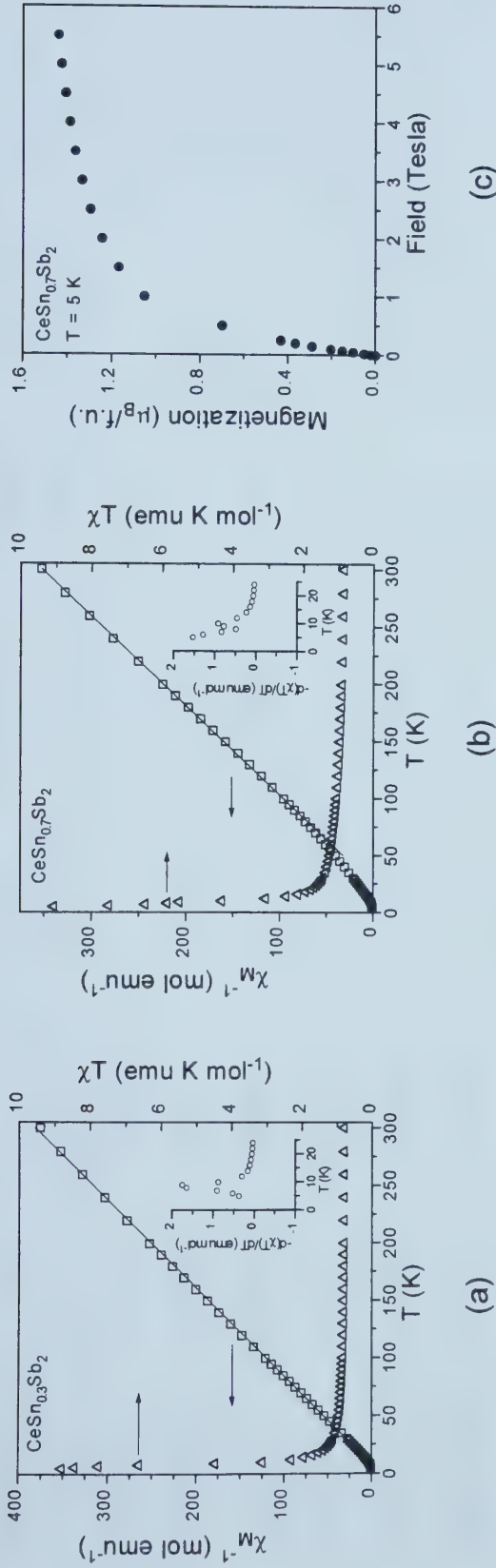


**Figure 3-5.** Plotted is the temperature dependence of  $\chi_M^{-1}$  (left axis) and  $\chi T$  (right axis) for (a)  $\text{CeSn}_{0.3}\text{Sb}_2$  and (b)  $\text{CeSn}_{0.7}\text{Sb}_2$ . The  $\chi_M^{-1}$  data were fit to the Curie-Weiss law (solid line). The inset shows the function  $d(\chi T)/dT$ . (c) Plot of the isothermal magnetization ( $T = 5$  K) for  $\text{CeSn}_{0.7}\text{Sb}_2$ , showing an approach to saturation with a moment of  $\sim 1.4 \mu_B$ .





**Table 3-5.** Magnetic Data for  $RESn_xSb_2$  ( $RE = Ce, Pr, Nd, Sm; x = 0.3, 0.7$ )

Compound	$\theta$ (K)	C (emu K mol <sup>-1</sup> )	$\chi_{TIP}$ (emu mol <sup>-1</sup> )	$\mu_{eff}$ (exp.) ( $\mu_B$ )	$\mu_{eff}$ (theory) ( $\mu_B$ )	$\mu_{sat}$ (exp.) ( $\mu_B$ )	$\mu_{sat}$ (theory) ( $\mu_B$ )	$T_c$ (K)
CeSn <sub>0.3</sub> Sb <sub>2</sub>	7.8(3)	0.765(2)		2.48	2.54			9
CeSn <sub>0.7</sub> Sb <sub>2</sub>	24.8(6)	0.780(3)		2.50	2.54	1.45	2.14	10
PrSn <sub>0.3</sub> Sb <sub>2</sub>	-3.5(2)	1.600(3)		3.58	3.58			
PrSn <sub>0.7</sub> Sb <sub>2</sub>	-6(2)	1.83(1)		3.83	3.58			
NdSn <sub>0.3</sub> Sb <sub>2</sub>	-16.2(2)	1.680(3)		3.67	3.62			
NdSn <sub>0.7</sub> Sb <sub>2</sub>	-11.0(2)	1.620(3)		3.60	3.62			
SmSn <sub>0.3</sub> Sb <sub>2</sub>	-20(1)	0.047(2)	8.7(1)×10 <sup>-4</sup>	0.61	0.85			
SmSn <sub>0.7</sub> Sb <sub>2</sub>	-20(1)	0.043(2)	8.7(2)×10 <sup>-4</sup>	0.59	0.85			



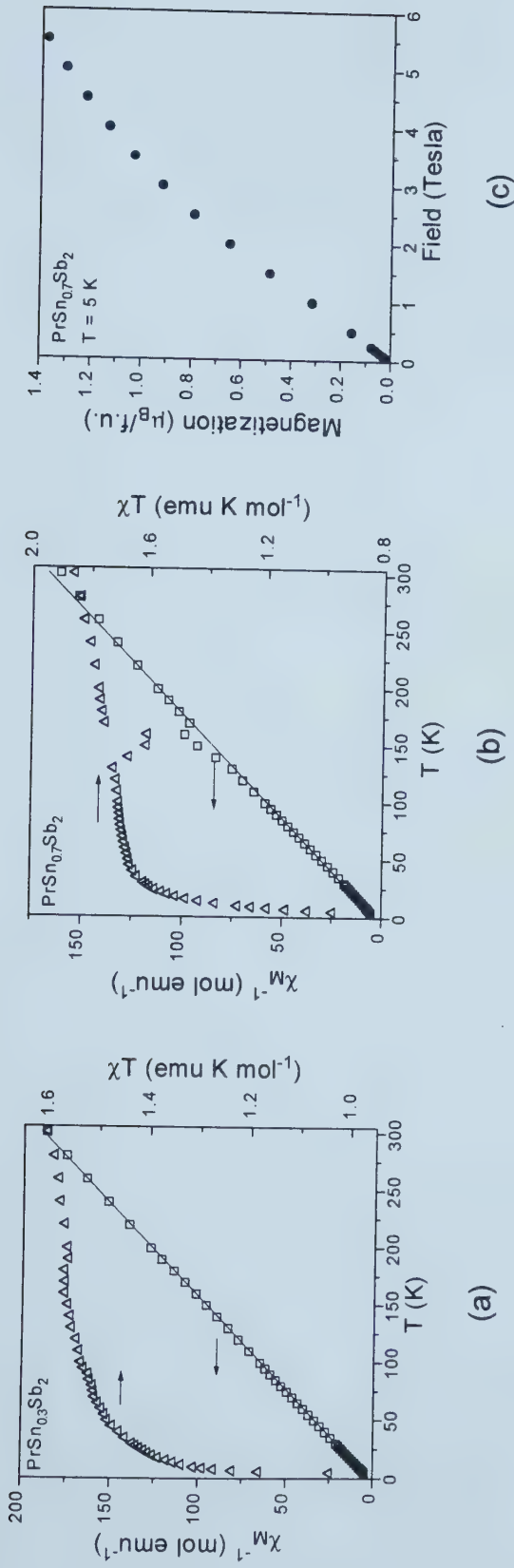


**Figure 3-6.** Plotted is the temperature dependence of  $\chi_M^{-1}$  (left axis) and  $\chi T$  (right axis) for (a)  $\text{PrSn}_{0.3}\text{Sb}_2$  and (b)  $\text{PrSn}_{0.7}\text{Sb}_2$ . The  $\chi_M^{-1}$  data were fit to the Curie-Weiss law (solid line). (c) Plot of the isothermal magnetization ( $T = 5 \text{ K}$ ) for  $\text{PrSn}_{0.7}\text{Sb}_2$ .



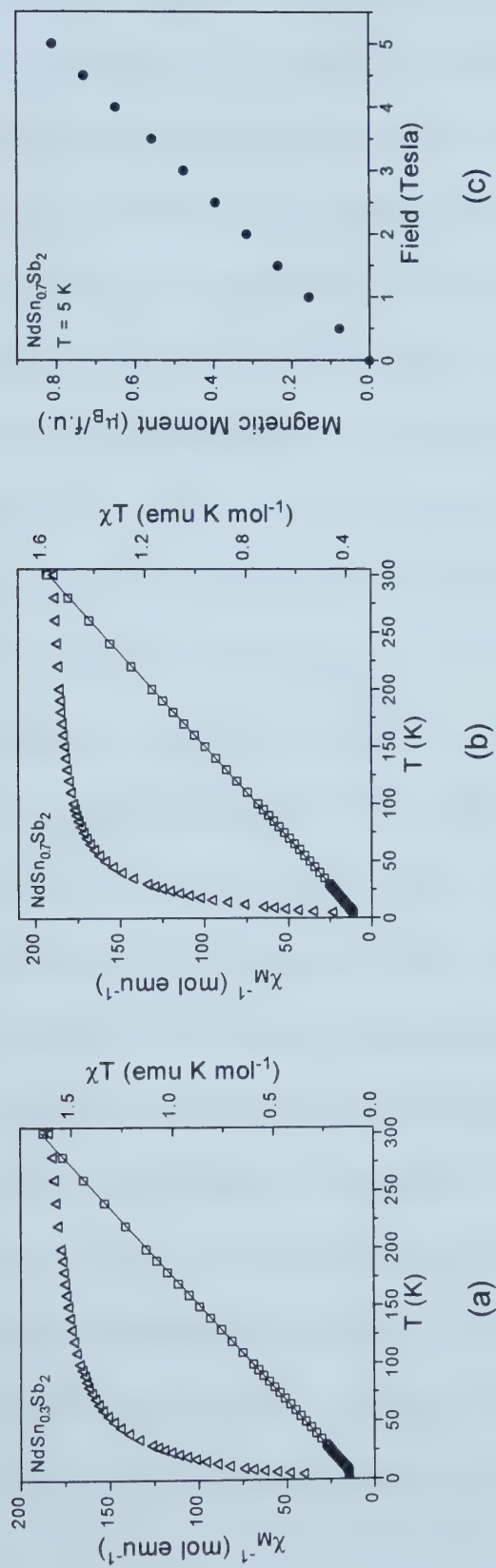


**Figure 3-7.** Plotted is the temperature dependence of  $\chi_M^{-1}$  (left axis) and  $\chi T$  (right axis) for (a)  $\text{NdSn}_{0.3}\text{Sb}_2$  and (b)  $\text{NdSn}_{0.7}\text{Sb}_2$ . The  $\chi_M^{-1}$  data were fit to the Curie-Weiss law (solid line). (c) Plot of the isothermal magnetization ( $T = 5$  K) for  $\text{NdSn}_{0.7}\text{Sb}_2$ .



antiferromagnetism. The  $\mu_{\text{eff}}$  values for  $\text{PrSn}_{0.3}\text{Sb}_2$  ( $3.58 \mu_{\text{B}}$ ),  $\text{NdSn}_{0.3}\text{Sb}_2$  ( $3.67 \mu_{\text{B}}$ ), and  $\text{NdSn}_{0.7}\text{Sb}_2$  ( $3.60 \mu_{\text{B}}$ ) show excellent agreement with the theoretical values for the  $RE^{3+}$  cations ( $3.58$  and  $3.62 \mu_{\text{B}}$  for Pr and Nd respectively), while for  $\text{PrSn}_{0.7}\text{Sb}_2$  the experimental moment is slightly larger than expected ( $3.83 \mu_{\text{B}}$ ).<sup>20</sup> The origin of the dip in the  $\chi T$  plot for  $\text{PrSn}_{0.7}\text{Sb}_2$  at  $\sim 150$  K is unexplained and further measurements are required to rule out the possibility of an instrumental error. Because the isothermal magnetization curves (Figures 3-6(c) and 3-7(c)) were collected at 5 K (above any potential ordering temperature), the conclusions derived from the data may not be exact. However, close examination of the curves for both the Pr and Nd compounds clearly reveals that neither display magnetization with a strictly linear field dependence, which would be typical of paramagnetism. The data may indicate the presence of metamagnetism or spin flop transitions – at a sufficiently high field the  $RE^{3+}$  moments which are antiferromagnetically coupled flop perpendicular to the magnetic field, and with increasing field begin to align parallel with the field.<sup>19</sup> Certainly, more data need to be collected before these conclusions can be completely accepted.

*SmSn<sub>x</sub>Sb<sub>2</sub>*: The magnetic susceptibility and isothermal magnetization ( $T = 5$  K) for  $\text{SmSn}_{0.3}\text{Sb}_2$  and  $\text{SmSn}_{0.7}\text{Sb}_2$  are plotted in Figure 3-8. The susceptibility data were fit to a modified Curie-Weiss type law with the inclusion of a temperature independent term ( $\chi = \chi_{\text{TIP}} + C/(T - \theta)$ ), and the results are collected in Table 3-5.<sup>19</sup> Values of the temperature independent susceptibility for both Sm compounds are within an order of magnitude of that observed for  $\text{LaSn}_{0.7}\text{Sb}_2$ . The large negative  $\theta$  values are consistent with antiferromagnetic coupling of the Sm moments, although there was no evidence of





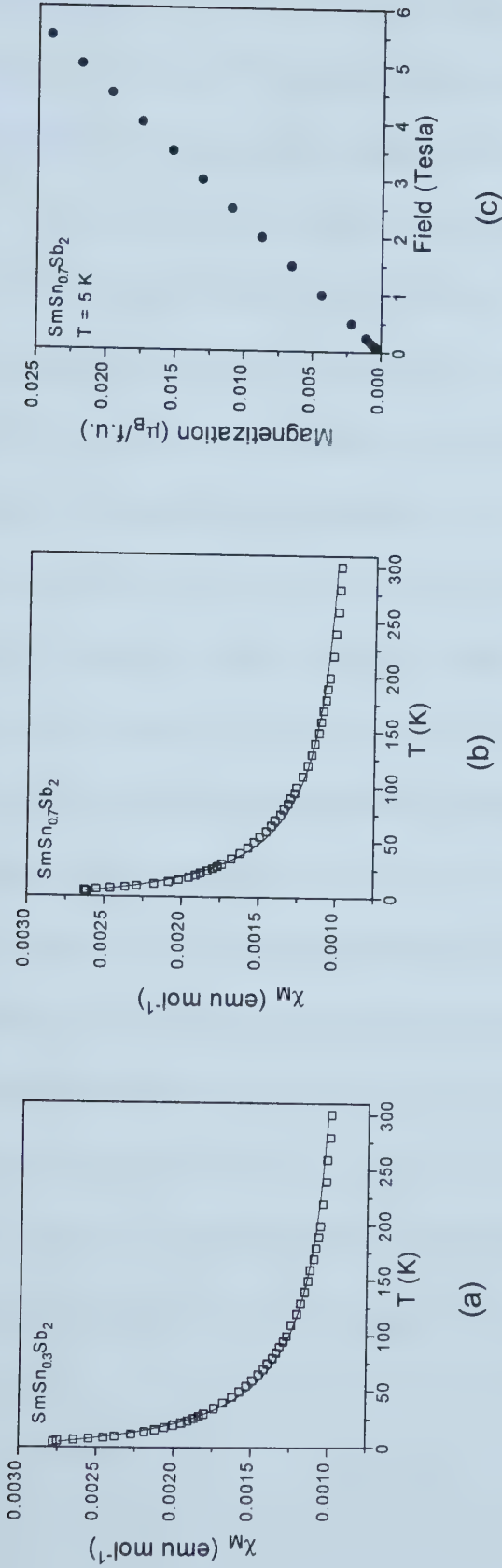


**Figure 3-8.** Plot of  $\chi_M$  as a function of temperature for (a)  $\text{SmSn}_{0.3}\text{Sb}_2$  and (b)  $\text{SmSn}_{0.7}\text{Sb}_2$ . The solid lines are the fit to  $\chi = \chi_{\text{TIP}} + C/(T - \theta)$ . (c) Plot of the isothermal magnetization ( $T = 5$  K) for  $\text{SmSn}_{0.7}\text{Sb}_2$ , showing the linear dependence on field typical for paramagnetic compounds.



magnetic ordering observed down to 5 K. The  $\mu_{\text{eff}}$  values extracted from the Curie constant of 0.61 and 0.59  $\mu_B$  for  $x = 0.3$  and 0.7 respectively, show reasonable agreement with theory (0.85  $\mu_B$ ).<sup>20</sup> The isothermal magnetization data for  $\text{SmSn}_{0.7}\text{Sb}_2$  show a linear dependence on the applied field, clearly indicating paramagnetic behavior at 5 K.

From these magnetic studies we can conclude that the rare earth ions are indeed in the +3 oxidation state for all members. The weak temperature independent paramagnetism observed for  $\text{LaSn}_{0.7}\text{Sb}_2$  is unsurprising given the nonmagnetic nature of the three components, and is consistent with the weakly metallic behavior previously reported. It appears that the magnitude of  $\theta$  is roughly correlated with the size of the rare earth ion, increasing with the decreasing radii from Pr to Nd to Sm, suggesting a stronger magnetic interaction in the smaller rare earths. Unfortunately, it is unclear whether any trends in the magnetic properties can be identified with changing Sn content because of the limited scope of the measurements performed. Further experiments are required, including magnetic susceptibility measured at lower fields and down to 2 K, which should help to extract magnetic ordering temperatures (if any) for Pr and Nd, and isothermal magnetization experiments collected at lower temperatures, which should help to elucidate the nature of the magnetic interactions. Additionally, if suitable crystals can be prepared, electrical resistivity as a function of both  $RE$  and  $x$  can be measured for the series  $RE\text{Sn}_x\text{Sb}_2$ . Finally, members with different Sn content should be synthesized to more closely explore the effect that nonstoichiometry has on the magnetic and electronic properties.



## REFERENCES

- (1) Cava, R. J.; Batlogg, B.; van Dover, R. B.; Murphy, D. W.; Sunshine, S.; Siegrist, T.; Remeika, J. P.; Rietman, E. A.; Zahurak, S.; Espinosa, G. P. *Phys. Rev. Lett.* **1987**, *58*, 1676.
- (2) Ferguson, M. J.; Hushagen, R. W.; Mar, A. *Inorg. Chem.* **1996**, *35*, 4505.
- (3) Sheldrick, G. M. *SHELXTL* Version 5.1; Bruker Analytical X-ray Systems, Inc.: Madison, WI, 1997.
- (4) Sheldrick, G. M. *J. Appl. Crystallogr.* in press.
- (5) *International Tables for X-ray Crystallography*; Wilson, A. J. C., Ed.; Kluwer: Dordrecht, The Netherlands, 1992, Vol. C.
- (6) Gelato, L. M.; Parthé, E. *J. Appl. Crystallogr.* **1987**, *20*, 139.
- (7) *Chemistry, Structure, and Bonding of Zintl Phases and Ions*; Kauzlarich, S. M., Ed.; VCH Publishers: New York, 1996.
- (8) Schäfer, H. *Annu. Rev. Mater. Sci.* **1985**, *15*, 1.
- (9) Corbett, J. D. *Chem. Rev.* **1985**, *85*, 383.
- (10) Von Schnering, H. G. *Angew. Chem. Int. Ed. Engl.* **1981**, *20*, 33.
- (11) Greenwood, N. N.; Earnshaw, A. *Chemistry of the Elements*; Pergamon Press: Oxford, U.K., 1994.
- (12) Brylak, M.; Jeitschko, W. *Z. Naturforsch. B: Chem. Sci.* **1995**, *50*, 899.
- (13) Brylak, M.; Jeitschko, W. *Z. Naturforsch. B: Chem. Sci.* **1994**, *49*, 747.
- (14) Pauling, L. *The Nature of the Chemical Bond*, 3rd Ed.; Cornell University Press: Ithaca, NY, 1960.



- (15) Ferguson, M. J.; Hushagen, R. W.; Mar, A. *J. Alloys Compd.* **1997**, 249, 191.
- (16) Cotton, F. A.; Wilkinson, G. *Advanced Inorganic Chemistry*, 3rd Ed.; John Wiley & Sons, Inc.: New York, 1972.
- (17) Greenwood, N. N.; Gibb, T. C. *Mössbauer Spectroscopy*; Chapman and Hall Ltd.: London, U.K., 1971.
- (18) Mulay, L. N.; Boudreaux, E. A. *Theory and Applications of Molecular Diamagnetism*; John Wiley & Sons: New York, 1976.
- (19) Carlin, R. L. *Magnetochemistry*; Springer-Verlag: New York, 1986.
- (20) Chikazumi, S.; Charap, S. H. *Physics of Magnetism*; John Wiley & Sons: New York, 1964.





## Chapter 4

### A New Rare-Earth Indium Antimonide, $REIn_{1-x}Sb_2$ ( $RE = La, Ce, Pr, Nd$ ), Featuring In Zigzag Chains and Sb Square Nets<sup>†</sup>

#### Introduction

The Zintl concept serves as a useful tool to interpret and understand the bonding in compounds of alkali or alkaline-earth metals and the elements of groups 13 – 16.<sup>1-4</sup> Within the concept, the electropositive elements serve to donate their valence electrons to the main-group elements, which use them to satisfy the octet rule, forming homoatomic bonds if necessary. This approximation can sometimes fail, particularly in cases where there are highly charged cations and small differences in electronegativities.

There exist a large number of ternary alkali- or alkaline-earth-metal main-group-element antimonides  $A_xM_ySb_z$  ( $M = Al, Ga, In, Si, Ge, Sn$ ), for which the Zintl concept works well in accounting for the structure of the anionic framework, which may contain both strong  $M-M$  and  $Sb-Sb$  bonds.<sup>5</sup> On the other hand, there are also many ternary rare-earth transition-metal antimonides  $RE_xM_ySb_z$  ( $M =$  transition metal) for which the Zintl concept has to be extended to account for weak  $Sb-Sb$  bonds which often form a characteristic feature of these structures.<sup>6</sup> The latter compounds display a wide variety of electrical and magnetic behavior,<sup>7-13</sup> the most well known being the promising thermoelectric properties of some filled skutterudites.<sup>14</sup>

---

<sup>†</sup> Reproduced with permission from Ferguson, M. J.; Ellenwood, R. E.; Mar, A. *Inorg. Chem.* **1999**, 38, 4503. Copyright 1999 American Chemical Society.



Curiously, the only example of a ternary rare-earth main-group-element antimonide in the systems  $RE_xM_ySb_z$  ( $M = \text{Al, Ga, In, Si, Ge, Sn}$ ) is  $\text{LaSn}_{0.75}\text{Sb}_2$ .<sup>15</sup> We report here the structure of  $\text{LaIn}_{0.8}\text{Sb}_2$ , which is the first example of a rare-earth indium antimonide. Although both  $\text{LaSn}_{0.75}\text{Sb}_2$  and  $\text{LaIn}_{0.8}\text{Sb}_2$  are nonstoichiometric compounds, a wide homogeneity range is possible in  $\text{LaSn}_x\text{Sb}_2$  ( $\sim 0.1 \leq x \leq \sim 0.8$ ) while  $\text{LaIn}_{0.8}\text{Sb}_2$  is a point phase. The structures of  $\text{LaSn}_{0.75}\text{Sb}_2$  and  $\text{LaIn}_{0.8}\text{Sb}_2$  share some common features, notably the presence of weak Sb–Sb bonds in square sheets and strong Sn–Sn or In–In bonds in chains. We examine the nature of this bonding through extended Hückel band structure calculations.

## Experimental Section

**Synthesis.** Starting materials were powders of the elements (La, Ce, Pr, Nd: 99.9%, Alfa-Aesar; In: 99.999%, Cerac; Sb: 99.995%, Aldrich). The elements were loaded into fused-silica tubes (5 cm long, 10 mm i.d.) in a 1:0.8:2 ratio (total weight: 250 mg). The tubes were then evacuated, sealed, and heated in a furnace at 570 °C for 1 day, 950 °C for 2 days, cooled to 500 °C over 1 day, and finally cooled to room temperature over 5 hours. The products were typically black powders interspersed with small plate-shaped crystals of the ternary compound. The crystal of  $\text{LaIn}_{0.8}\text{Sb}_2$  analyzed by X-ray diffraction was selected from a reaction with a loaded stoichiometry of 1:1:2. Elemental compositions were obtained by EDX (energy dispersive X-ray) analyses on a Hitachi F2700 scanning electron microscope, which indicated the presence of all three elements in a ratio consistent with the formula  $RE\text{In}_{0.8}\text{Sb}_2$ . Anal. Calcd for  $RE\text{In}_{0.8}\text{Sb}_2$ : RE 26%,



In 21%, Sb 53%. Found (average of three analyses each): La 26.8(4)%, In 22(3)%, Sb 52(3)%; Ce 27.0(3)%, In 21(2)%, Sb 53(2)%; Pr 28.3(8)%, In 20(2)%, Sb 51.7(7)%. Since only powder was obtained for  $RE = Nd$ , EDX analysis was not performed on this member. Powder X-ray diffraction patterns were collected on an Enraf-Nonius FR552 Guinier camera ( $CuK_{\alpha 1}$  radiation; Si standard). The cell parameters were refined by least-squares fits of 28 to 42 reflections in the powder patterns with the program POLSQ,<sup>16</sup> and are listed in Table 4-1. The observed powder X-ray diffraction patterns agree well with those calculated from the crystal structure of  $LaIn_{0.8}Sb_2$  by the program LAZY-PULVERIX<sup>17</sup> (Tables A-3 – A-6).

Since the related  $LaSn_xSb_2$  structure displays a wide homogeneity range ( $\sim 0.1 \leq x \leq \sim 0.8$ ),<sup>15</sup> the potential for nonstoichiometric behavior of  $LaIn_{0.8}Sb_2$  was investigated. Reactions performed as described above with loaded stoichiometry of  $LaIn_xSb_2$  ( $0.1 \leq x \leq 1.0$ ) were monitored by powder X-ray diffraction. The ternary phase could only be conclusively identified in reactions with  $x \geq 0.6$ , and from  $x = \sim 0.8$  and higher,  $InSb$  formed along with the ternary compound. The products of the reactions with  $x < 0.6$  could not be clearly identified, but possibly contained  $LaSb_2$  and other phases. In contrast to the nonstoichiometric behavior of  $LaSn_xSb_2$ , which was inferred by observing the shifting of the positions of reflections in the powder patterns,<sup>15</sup> the absence of such shifting for the  $LaIn_xSb_2$  reactions suggests that  $LaIn_{0.8}Sb_2$  either is a point phase or exists within a narrow range of composition. From the EDX analyses above, the other rare-earth members can be assumed to be substoichiometric in In as well. Redefining the



**Table 4-1.** Cell Parameters for Ternary  $REIn_{0.8}Sb_2$  Compounds

Compound	$a$ (Å)	$b$ (Å)	$c$ (Å)	$\beta$ (°)	$V$ (Å <sup>3</sup> )
$LaIn_{0.8}Sb_2$	4.508(1)	4.350(1)	11.914(3)	99.41(1)	230.29(8)
$CeIn_{0.8}Sb_2$	4.478(2)	4.323(2)	11.796(5)	99.36(2)	225.2(1)
$PrIn_{0.8}Sb_2$	4.465(2)	4.303(2)	11.733(5)	99.45(2)	222.2(1)
$NdIn_{0.8}Sb_2$	4.445(4)	4.297(4)	11.677(9)	99.22(5)	220.1(2)





subscript  $x$  to mean the deviation from full In occupancy, we refer to these compounds as “ $REIn_{1-x}Sb_2$ ,” where  $x$  is fixed at  $\sim 0.2$ .

**Structure Determination.** The thin plate-shaped crystals of  $LaIn_{0.8}Sb_2$  are soft and highly prone to being bent, rendering them unsuitable for diffraction studies. After numerous crystals were screened for singularity by Weissenberg photography, a rather small ( $0.100 \times 0.075 \times 0.005$  mm) crystal was finally selected. X-ray diffraction data were collected on two diffractometers, a Bruker P4/SMART CCD system and a Nonius Kappa CCD system. Both data sets led to the same structure solution and similar residuals in the final refinements, but as the Nonius data gave slightly better agreement with the EDX results and slightly better displacement parameters, these are the results reported. The data were collected at 20 °C using a combination of  $\phi$  rotations and  $\omega$  scans. The frames were integrated using the Nonius maXus program, giving 2887 reflections, of which 563 were unique ( $R_{int} = 0.045$ ). Final cell constants were determined using the HKL Scalepack program. Crystal data and further details of the data collection are given in Table 4-2.

All calculations were carried out using the SHELXTL (Version 5.1) software package.<sup>18,19</sup> Conventional atomic scattering factors and anomalous dispersion corrections were used.<sup>20</sup> Intensity data were processed and Gaussian face-indexed absorption corrections were applied with the program XPREP. The monoclinic space group  $P2_1/m$  was selected on the basis of the intensity statistics, satisfactory averaging, and the successful structure solution. Although the monoclinic structure of  $LaIn_{0.8}Sb_2$  is closely related to the orthorhombic structure of  $LaSn_{0.75}Sb_2$ , inspection of the reciprocal



**Table 4-2.** Crystallographic Data for  $\text{LaIn}_{0.81(1)}\text{Sb}_2$ 

Formula	$\text{LaIn}_{0.81(1)}\text{Sb}_2$
Formula mass (amu)	474.27
Space group	$C_{2h}^2-P2_1/m$
$a$ (Å)	4.521(3) <sup>a</sup>
$b$ (Å)	4.331(3) <sup>a</sup>
$c$ (Å)	11.913(7) <sup>a</sup>
$\beta$ (°)	99.6680(11)
$V$ (Å <sup>3</sup> )	229.9(2)
$Z$	2
$T$ (°C)	20
Diffractometer	Nonius KappaCCD
$\rho_{\text{calc}}$ (g cm <sup>-3</sup> )	6.850
Crystal dimensions	Silver plate, $0.100 \times 0.075 \times 0.005$ mm <sup>3</sup>
Radiation	Graphite monochromated $\text{MoK}_\alpha$ , $\lambda = 0.71073$ Å
$\mu$ (cm <sup>-1</sup> )	244.8
Transmission factors <sup>b</sup>	0.213 – 0.881
Scan-type	mixture of $\phi$ rotations and $\omega$ scans
$2\theta$ limits	$3^\circ \leq 2\theta(\text{MoK}_\alpha) \leq 61^\circ$
Data collected	$-5 \leq h \leq 4, -6 \leq k \leq 4, -15 \leq l \leq 12$
No. of data collected	2887
No. of unique data, including $F_o^2 < 0$	563 ( $R_{\text{int}} = 0.0452$ )
No. of unique data, with $F_o^2 > 2\sigma(F_o^2)$	515



**Table 4-2.** Crystallographic Data for  $\text{LaIn}_{0.81(1)}\text{Sb}_2$  (cont'd)

No. of variables	27
Extinction coefficient <sup>c</sup>	0.0029(10)
$R(F)$ for $F_o^2 > 2\sigma(F_o^2)$ <sup>d</sup>	0.0491
$R_w(F_o^2)$ <sup>e</sup>	0.1308
Goodness of fit <sup>f</sup>	1.177

<sup>a</sup> Obtained from a refinement constrained so that  $\alpha = \gamma = 90^\circ$ .

<sup>b</sup> A Gaussian face-indexed absorption correction was applied with the use of the programs in the SHELXTL package (Sheldrick, G. M. *SHELXTL* Version 5.1; Bruker Analytical X-ray Instruments, Inc.: Madison, WI, 1997).

<sup>c</sup> An extinction parameter  $x$  was refined, where  $F_c$  is multiplied by:  $k[1 + 0.001 * x * F_c^2 * \lambda^3 / \sin(2\theta)]^{-1/4}$ .

$$^d R(F) = \sum \|F_o\| - \|F_c\| / \sum \|F_o\|.$$

$$^e R_w(F_o^2) = [\sum [w(F_o^2 - F_c^2)^2] / \sum wF_o^4]^{1/2}; w^{-1} = [\sigma^2(F_o^2) + (0.0344P)^2 + 32.59P]$$

where  $P = [\max(F_o^2, 0) + 2F_c^2] / 3$ .

$$^f GooF = S = [\sum [w(F_o^2 - F_c^2)^2] / (n - p)]^{1/2} \text{ where } n \text{ is the number of reflections and } p \text{ is the total number of parameters refined.}$$



space plots shows the inequivalence of  $hkl$  and  $\bar{h}kl$  reflections, and analysis of the final structure reveals no higher symmetry elements. The positions of all atoms were found by direct methods, and the structure was refined by least-squares methods. At this stage, an anomalously large displacement parameter for the In site suggested partial occupancy. Refinement of the occupancies of all atoms confirmed that the compound is substoichiometric only in In. The displacement parameters for all atoms were refined anisotropically. Although  $U_{eq}$  for In is larger than normal, we have confidence in the results because the resulting formula,  $\text{LaIn}_{0.81(1)}\text{Sb}_2$ , is consistent with that obtained from EDX analyses (*vide supra*). The large  $U_{eq}$  for In may be an artifact of the absorption correction, but given that the displacement parameters for the other atoms are well behaved, it is more likely that this is a real effect representing the tendency of the atoms “inserted” between the  $\text{LaSb}_2$  layers to disorder over several sites, as has been observed in  $\text{LaSn}_{0.75}\text{Sb}_2$ .<sup>15</sup> The atomic positions were standardized with the use of the program STRUCTURE TIDY.<sup>21</sup> The final cycle of least-squares refinement on  $F_o^2$  of 27 variables and 563 averaged reflections (including those having  $F_o^2 < 0$ ) converged to values of  $R_w(F_o^2)$  of 0.1308 and  $R(F)$  (for  $F_o^2 > 2\sigma(F_o^2)$ ) of 0.0491. The final difference electron density map is featureless ( $\Delta\rho_{\max} = 4.15$ ,  $\Delta\rho_{\min} = -2.92 \text{ e } \text{\AA}^{-3}$ ). The  $\Delta\rho_{\max}$  value is small relative to the atomic peaks observed and can be attributed to noise. Final values of the positional and equivalent isotropic displacement parameters are given in Table 4-3 and the anisotropic displacement parameters are given in Table A-7.

**Band Structure.** One-electron band structure calculations on the hypothetical fully occupied  $\text{LaInSb}_2$  structure as well as a  $1 \times 2 \times 1$  superstructure model were





**Table 4-3.** Atomic Coordinates, Occupancies, and Equivalent Isotropic Displacement Parameters ( $\text{\AA}^2$ ) for  $\text{LaIn}_{0.81(1)}\text{Sb}_2$

atom	Wyckoff position, site symmetry		<i>x</i>	<i>y</i>	<i>z</i>	occupancy	$U_{\text{eq}}^a$
La	2 <i>e</i>	<i>m</i>	0.8440(4)	¼	0.2160(1)	1	0.0097(5)
In	2 <i>e</i>	<i>m</i>	0.2139(8)	¼	0.4846(2)	0.81(1)	0.0341(12)
Sb(1)	2 <i>e</i>	<i>m</i>	0.6158(4)	¼	0.6951(2)	1	0.0107(5)
Sb(2)	2 <i>e</i>	<i>m</i>	0.2489(4)	¼	0.0016(2)	1	0.0101(5)

<sup>a</sup>  $U_{\text{eq}}$  is defined as one-third of the trace of the orthogonalized  $U_{ij}$  tensor.

**Table 4-4.** Extended Hückel Parameters

atom	orbital	$H_{ii}$ (eV)	$\zeta_{i1}$	$c_1$	$\zeta_{i2}$	$c_2$
La	6s	−6.5613	2.14			
	6p	−4.3769	2.08			
	5d	−7.5155	3.78	0.77651	1.381	0.45861
In	5s	−12.60	1.903			
	5p	−6.19	1.677			
Sb	5s	−18.8	2.323			
	5p	−11.7	1.999			



performed by the tight-binding method with an extended Hückel-type Hamiltonian using the EHMACC suite of programs.<sup>22,23</sup> The atomic parameters used are listed in Table 4-4.<sup>24-26</sup> Properties were extracted from the band structure using 192  $k$  points in the irreducible portion of the Brillouin zone.

## Results and Discussion

**Description of the Structure.** A view of the structure down the  $b$  axis is shown in Figure 4-1(a), which also shows the labeling scheme. Selected interatomic distances and angles are given in Table 4-5. The structure consists of layers of compositions  ${}^2_{\infty}[\text{Sb}]$  and  ${}^2_{\infty}[\text{In}_{0.8}\text{Sb}]$  stacked parallel to the (001) plane, separated by La atoms. A perpendicular view of the structure down the  $a$  axis is shown in Figure 4-1(b). The La atoms are coordinated by eight Sb atoms in a square-antiprismatic fashion, as shown in Figure 4-2(a). Four Sb(1) atoms define one square of Sb atoms, and four Sb(2) atoms define the second square, which is twisted  $45^\circ$  relative to the first. A ninth capping atom of In is situated above the larger square of Sb(1) atoms and is tilted to one side. The Sb(2) atoms are surrounded by four other symmetry equivalent Sb(2) atoms, forming a nearly flat square sheet,  ${}^2_{\infty}[\text{Sb}]$ . The La atoms are positioned above and below this sheet in an alternating “checkerboard” fashion. The In atoms are coordinated by three Sb(1) atoms and two In atoms in a distorted square pyramidal fashion, as shown in Figure 4-2(b). The base of the pyramid is defined by two Sb(1) atoms and two In atoms while the apical site is the third Sb(1) atom. These square pyramidal units are condensed via



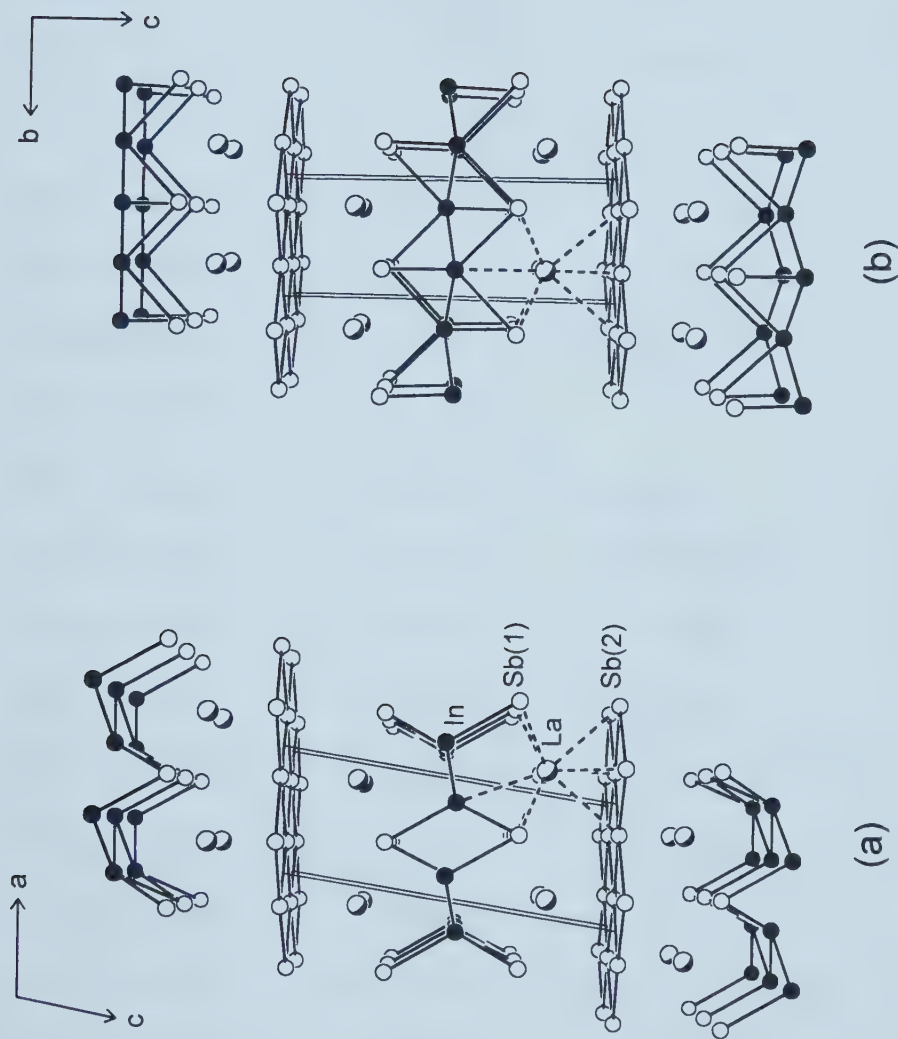


**Figure 4-1.** (a) View down the  $b$  axis of  $\text{LaIn}_{0.8}\text{Sb}_2$  with the unit cell outlined, showing the zigzag In chains and square nets of Sb. The partly shaded circles are La atoms, the solid circles are In atoms, and the open circles are Sb atoms. (b) View of the structure down the  $a$  axis.



**Table 4-5.** Selected Interatomic Distances (Å) and Angles (°) for  $\text{LaIn}_{0.81(1)}\text{Sb}_2$ 

La–Sb(1)	3.297(2) (2×)	In–Sb(1)	2.839(3)
La–Sb(1)	3.303(2) (2×)	In–Sb(1)	3.228(3) (2×)
La–Sb(2)	3.349(2) (2×)	In–In	2.967(5) (2×)
La–Sb(2)	3.384(3)	In–In	3.346(6) (2×)
La–Sb(2)	3.385(3)	Sb(2)–Sb(2)	3.119(3) (2×)
La–In	3.352(4)	Sb(2)–Sb(2)	3.142(3) (2×)
Sb(1)–La–Sb(1)	82.11(7)	Sb(1)–La–In	86.21(7)
Sb(1)–La–Sb(1)	143.11(8)	Sb(1)–La–In	58.02(6)
Sb(1)–La–Sb(1)	86.48(5)	Sb(2)–La–In	135.75(5)
Sb(1)–La–Sb(1)	81.94(7)		
Sb(1)–La–Sb(2)	79.63(5)	In–In–In	93.7(2)
Sb(1)–La–Sb(2)	132.01(7)	Sb(1)–In–Sb(1)	84.27(10)
Sb(1)–La–Sb(2)	131.45(6)	In–In–Sb(1)	79.95(8)
Sb(1)–La–Sb(2)	79.29(5)	In–In–Sb(1)	143.59(16)
Sb(1)–La–Sb(2)	133.85(4)	Sb(1)–In–Sb(1)	113.41(10)
Sb(1)–La–Sb(2)	77.13(6)	Sb(1)–In–In	103.93(16)
Sb(1)–La–Sb(2)	77.20(6)		
Sb(1)–La–Sb(2)	133.89(4)	Sb(2)–Sb(2)–Sb(2)	87.93(10)
Sb(2)–La–Sb(2)	80.56(7)	Sb(2)–Sb(2)–Sb(2)	178.61(12)
Sb(2)–La–Sb(2)	55.19(5)	Sb(2)–Sb(2)–Sb(2)	92.45(5)
Sb(2)–La–Sb(2)	55.62(5)	Sb(2)–Sb(2)–Sb(2)	87.13(10)
Sb(2)–La–Sb(2)	83.82(7)		





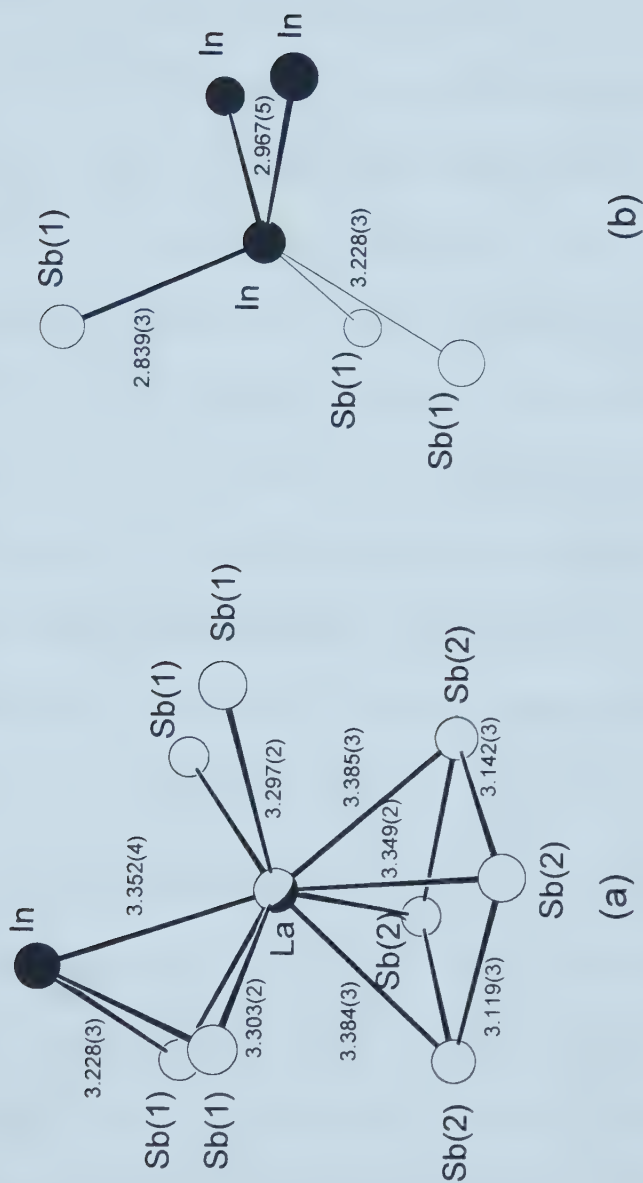


**Figure 4-2.** (a) Coordination of the La atom by eight Sb atoms in a square-antiprismatic fashion, capped by an In atom, with the La-Sb, La-In, and Sb(2)-Sb(2) bond lengths indicated. (b) Distorted square pyramidal coordination around the In atom, with the In-In and In-Sb(1) bond lengths shown.



corner-sharing of the basal atoms along [010] to form zigzag In chains (Figure 4-1) and coupled in a head-to-tail fashion along [100] to form the infinite sheet  $\left[ \text{In}_{0.8}\text{Sb} \right]_2$ .

**Structural Relationships.** The coordination environment around rare-earth metal atoms in solid-state compounds is flexible (typically CN 8 or 9), and is strongly influenced by the bonding requirements of the more electronegative components. The *RE* atoms are commonly found with square antiprismatic coordination by Sb in structures that feature Sb square nets, as observed in  $REM_x\text{Sb}_2$  ( $M = \text{Mn} - \text{Zn}, \text{Pd}, \text{Ag}, \text{Cd}, \text{Au}$ ),<sup>6b</sup> and sometimes have a ninth capping Sb atom, as observed in  $RE\text{Sb}_2$ <sup>27,28</sup> and  $REMSb_3$  ( $M = \text{V}, \text{Cr}$ ).<sup>6a,29</sup> The La–Sb bond lengths in  $\text{LaIn}_{0.8}\text{Sb}_2$  that define the square antiprism are within the range of interatomic distances found in these compounds (3.29 – 3.39 Å).<sup>6a,6b,15</sup> The ninth capping atom is In instead of Sb, at a distance of 3.352(4) Å, within the range found in binary lanthanum indides (3.168 – 3.721 Å).<sup>30</sup>

A natural choice of structures in which to examine relationships is the series  $\text{La}M_{1-x}\text{Sb}_2$ , where  $M = \text{Cd}, \text{In}, \text{and Sn}$ . All contain layers of  $\left[ \text{LaSb}_2 \right]_2$  composed of Sb square sheets and square antiprismatic coordination of La, separated by layers of the *M* atoms, as shown in Figure 4-3. The three closely related structures differ in the nature of these *M* layers. In the structure of  $\text{LaCd}_{0.7}\text{Sb}_2$  (HfCuSi<sub>2</sub>-type), the Cd atoms form a perfectly square sheet with Cd–Cd distances of 3.111(2) Å.<sup>6b</sup> When this is compared to the 3.02 Å distance found in elemental Cd,<sup>31</sup> it is tempting to suggest a weak d<sup>10</sup>–d<sup>10</sup> bonding interaction in  $\text{LaCd}_{0.7}\text{Sb}_2$ . The In layer in  $\text{LaIn}_{0.8}\text{Sb}_2$  can be viewed as a distortion of a square net to form parallel zigzag chains, with intra- and interchain In–In



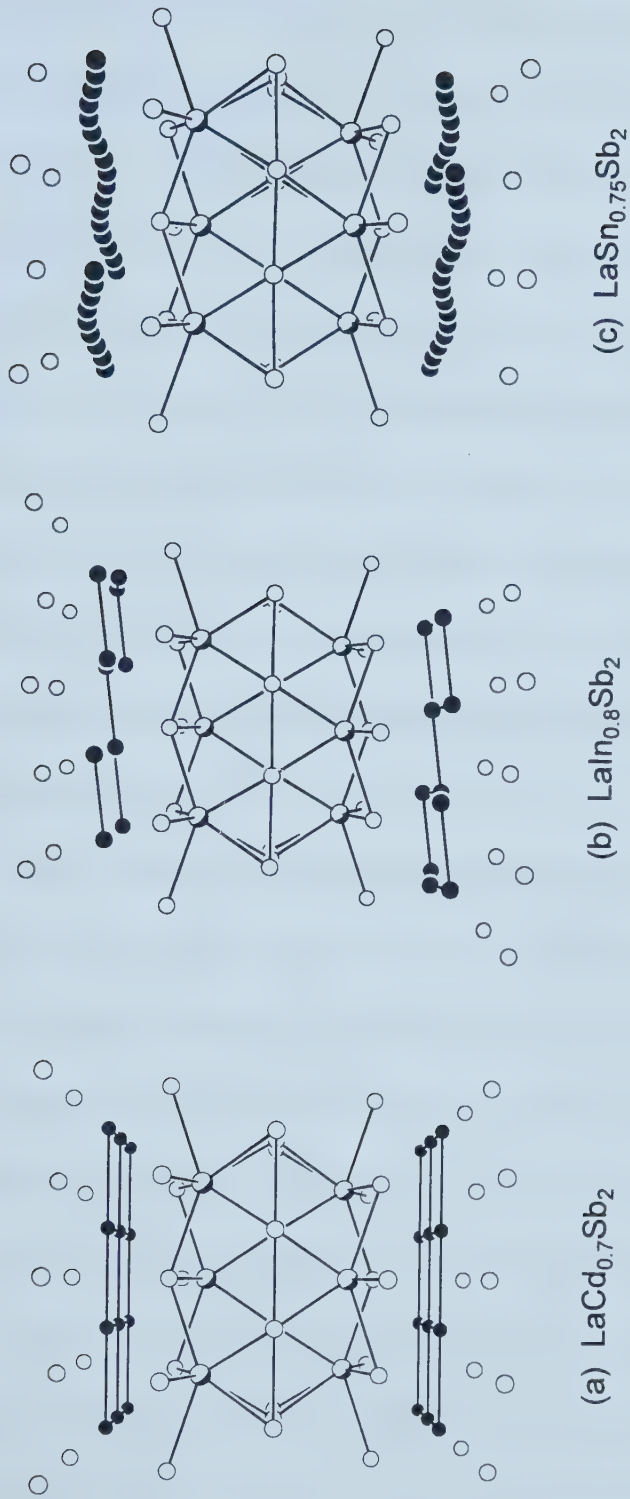


**Figure 4-3.** Comparison of the layered  $RE_xM_y\text{Sb}_2$  structures: (a)  $\text{LaCd}_{0.7}\text{Sb}_2$ , a member of the  $REMSb_2$  ( $M = \text{Mn} - \text{Zn}, \text{Pd}, \text{Ag}, \text{Cd}, \text{Au}$ ) series; (b)  $\text{LaIn}_{0.8}\text{Sb}_2$ ; (c)  $\text{LaSn}_{0.75}\text{Sb}_2$ . The partly shaded circles are the La atoms, the solid circles are the  $M$  atoms (Cd, In, or Sn), and the open circles are the Sb atoms. The perfectly square  $M$  layer in  $\text{LaCd}_{0.7}\text{Sb}_2$  distorts into zigzag chains in  $\text{LaIn}_{0.8}\text{Sb}_2$ , and finally to disordered linear chains in  $\text{LaSn}_{0.75}\text{Sb}_2$ .



distances of 2.967(5) and 3.346(6) Å, respectively. Zigzag chains with similar In–In intrachain distances are observed in the binary compound  $\text{Li}_2\text{In}$  (In–In distance 2.926 Å)<sup>32</sup> and significantly longer distances are observed in the ternary compounds  $\text{AE}_4\text{In}_2\text{N}$  (In–In distance: 3.162 Å when  $\text{AE} = \text{Ca}$ ; 3.320 Å when  $\text{AE} = \text{Sr}$ ).<sup>33</sup> Since even longer distances of 3.24 and 3.36 Å are found in the structure of elemental In,<sup>31</sup> it will be important to quantify the degree of In–In bonding in  $\text{LaIn}_{0.8}\text{Sb}_2$  to decide if the description of In zigzag chains or a distorted square net is more appropriate. As we demonstrate later from the results of the band structure calculations, the zigzag chains are an integral part of this structure. Finally, the structure of  $\text{LaSn}_{0.75}\text{Sb}_2$  represents an extreme in this distortion process, resulting in a Sn layer that consists of linear chains partially occupied in a disordered fashion, corresponding to every fifth site filled and Sn–Sn distances of 2.814 – 2.844 Å on a local level.<sup>15</sup>

The Sb square nets also undergo slight distortions from the perfectly square net found in  $\text{LaCd}_{0.7}\text{Sb}_2$  (Sb–Sb distance 3.111 Å; angles 90, 180°)<sup>6b</sup> to the nets observed in  $\text{LaIn}_{0.8}\text{Sb}_2$  (Sb–Sb distances 3.119 (2×), 3.142 Å (2×); angles 87.13, 87.93, 92.45, 178.61°) and  $\text{LaSn}_{0.75}\text{Sb}_2$  (Sb–Sb distance 3.0952 Å; angles 86.55, 93.40, 177.60°).<sup>15</sup> Since these bond lengths are similar, it is reasonable to assume that the Sb–Sb bond strength in each net is comparable. The distortion from a perfect square Sb net is driven by the nature of the bonding in the *M* layer and is reflected in the changing of the symmetry from tetragonal to monoclinic to orthorhombic; the geometry of the Sb net must change as well.





It is important to note that in Figure 4-3, the *M* layers were drawn without any *M*–Sb bonds shown to allow for easier comparison, but obviously they cannot be neglected. Several alkali and alkaline-earth metal indium antimonides are known with structures that are based on different connectivities of  $\text{InSb}_4$  tetrahedral units, although none display In–In bonding.<sup>5b,34</sup> It is more instructive to view the  $\text{In}_{0.8}\text{Sb}$  layer in  $\text{LaIn}_{0.8}\text{Sb}_2$  as a distortion of the  $\text{Cd}_{0.7}\text{Sb}$  layer in  $\text{LaCd}_{0.7}\text{Sb}_2$  (Figure 4-4). Antimony atoms reside above and below the centers of the Cd squares in an alternating “checkerboard” pattern. Each Cd is tetrahedrally coordinated by 4 Sb atoms, with bond lengths of 2.898 Å.<sup>6b</sup> The distortion of the In layer to zigzag chains is accompanied by a slight canting of the chains, such that they are no longer coplanar (Figure 4-1). The position of the Sb atom is shifted off-center and bonds to three In atoms inequivalently (In–Sb distances 2.839 Å and 3.228 Å (2×)). The shorter distance is typical of the In–Sb single bonds observed in  $\text{InSb}_4$  tetrahedra (2.804 – 3.100 Å)<sup>35</sup> found in ternary alkali and alkaline-earth metal indium antimonides and corresponds to the sum of the covalent radii (In, 1.44 Å; Sb, 1.36 Å).<sup>36</sup>

**Bonding and Band Structure.** As a first approximation, oxidation states can be assigned based on the Zintl concept. By considering the electronegativities of the three elements (Pauling: La, 1.10; In, 1.78; Sb, 2.05),<sup>37</sup> we can assume that the La atoms transfer their electrons to the In and Sb atoms, which use them to form bonds and complete their octets. We first consider the hypothetical, fully occupied structure,  $\text{LaInSb}_2$ , and then examine the effect of In substoichiometry. The structure naturally partitions into two anionic layers of  $\text{Sb}(2)$  and  $\text{InSb}(1)$  separated by La cations as



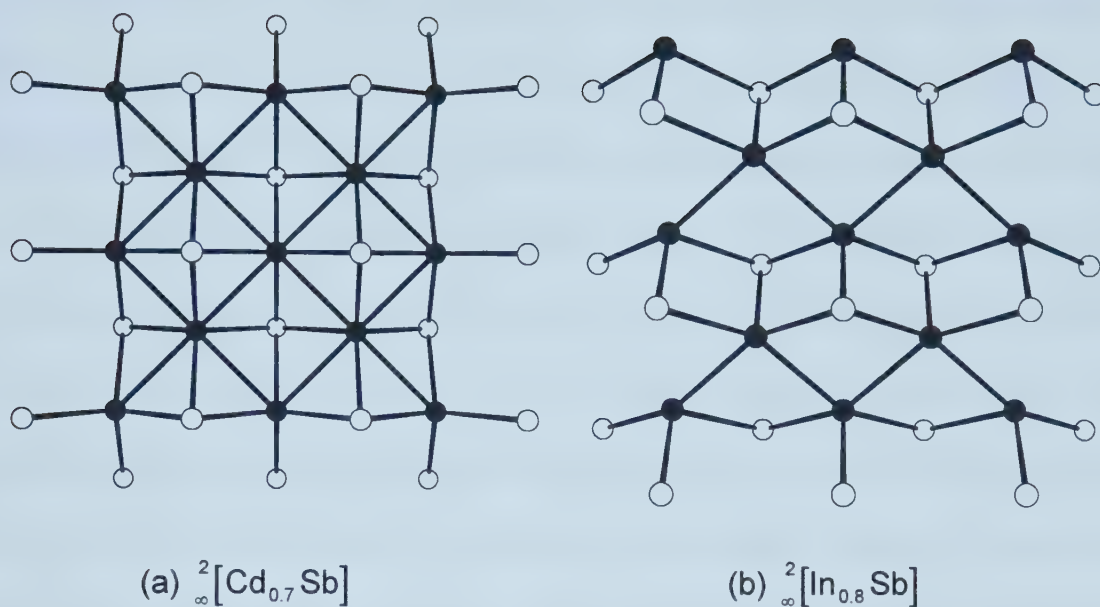


**Figure 4-4.** Comparison of the ideal square  $MSb$  layer in  $\text{LaCd}_{0.7}\text{Sb}_2$  to the distorted layer in  $\text{LaIn}_{0.8}\text{Sb}_2$ . Note that the  $\text{Sb}$  atoms no longer reside in the center of  $M$  squares in  $\text{LaIn}_{0.8}\text{Sb}_2$ .



represented by  $(\text{La}^{3+})[(\text{InSb}(1))(\text{Sb}(2))]^{3-}$ . The Sb(2)–Sb(2) bond lengths ( $\sim 3.1$  Å) are intermediate between the intralayer, single-bond length and the weakly bonding interlayer distance observed in elemental Sb (2.908 and 3.36 Å, respectively).<sup>31</sup> These  $\sim 3.1$  Å interactions have been successfully modeled as half-bonds (or one-electron bonds), and the Sb atoms have been assigned an oxidation state of  $-1$ .<sup>29,38</sup> Each Sb(2) atom has two lone pairs of electrons in the 5s and 5p<sub>z</sub> orbitals or some hybridized equivalent and bonds through the 5p<sub>x</sub> and 5p<sub>y</sub> orbitals to form the square net. The nearest Sb(1)–Sb(1) interactions are greater than 4.3 Å, approximately equal to the sum of the van der Waals radii ( $\sim 2.2$  Å),<sup>36</sup> and are therefore considered as isolated Sb(1)<sup>3-</sup> anions. Charge balance requires that the In atoms have an oxidation state of  $+1$ , resulting in an overall formulation of  $[(\text{La}^{3+})(\text{In}^{1+})(\text{Sb}(1)^{3-})(\text{Sb}(2)^{1-})]$ . Although this seems to imply the presence of a lone pair of electrons on In, these electrons are used to form the In–In zigzag chains. Using three sp<sup>3</sup> hybrid orbitals, each In makes two single bonds to neighboring In atoms (2.967 Å) and one single bond to an Sb(1) atom (2.839 Å). The fourth sp<sup>3</sup> hybrid orbital is involved in forming two longer In–Sb bonds (3.228 Å), which can be viewed together as a 3-center-2-electron bond (*i.e.*, each is a one-electron bond) consistent with the weaker and longer interaction.

But the actual formula is substoichiometric in In content, which reduces the valence electron count (*vec*) from 16 to 15.4 per formula unit and necessitates a modification of the oxidation state assignments. The easiest solution is to assign a fractional oxidation state to In to yield  $[(\text{La}^{3+})(\text{In}^{1.25+})_{0.8}(\text{Sb}(1)^{3-})(\text{Sb}(2)^{1-})]$  and assume that the rest of the atoms are unchanged. This would correspond to a weakening of the



bonding in the zigzag chains, while not altering the Sb bonding in the square net. A second possibility could be the oxidation of the Sb(2) square net, since such nets have been previously postulated to serve as electron “sources” or “sinks.”<sup>6a</sup> A combination of both oxidation processes could occur, of course. The question that arises is thus whether there is some underlying electronic reason that requires the In content to be substoichiometric. To attempt to answer this, and to test the validity of the bonding model proposed above, extended Hückel band structure calculations were performed.

Partial occupancy can be problematic to handle in the extended Hückel method. To address this, two models were considered: (1) a stoichiometric  $\text{LaInSb}_2$ , with the In deficiencies in  $\text{LaIn}_{0.81(1)}\text{Sb}_2$  modeled by lowering the *vec* from 16 to 15.4, and (2) a  $1 \times 2 \times 1$  superstructure (*i.e.*, the unit cell doubled along *b*) with every fourth In atom removed along the zigzag chain, corresponding to the formula  $\text{LaIn}_{0.75}\text{Sb}_2$ , which approximates the real formula of  $\text{LaIn}_{0.81(1)}\text{Sb}_2$ . The results obtained from calculations on these two models are similar, and while we discuss both, we only show plots for the first model.

Starting with the first model of a substoichiometric  $\text{LaIn}_{0.8}\text{Sb}_2$  produced by lowering the *vec* and following a “retrotheoretical analysis”<sup>39</sup> (whereby the complete structure is dissected into more manageable subunits to aid in interpretation, and then reassembled for the complete picture), we arrive at the same partitioning described earlier. Removal of the La cations leaves anionic layers of  $\text{Sb}^{1-}$  and  $\text{In}_{0.8}\text{Sb}^{2-}$ , which are sufficiently well separated and non-interacting, and the band structure of the anionic framework  $[\text{In}_{0.8}\text{Sb}_2]^{3-}$  is simply a superposition of the band structures of each layer. Incorporation of the La cations does not drastically alter the overall nature of the band





structure. Shown in Figures 4-5(a) is the density of states (DOS) curve for  $\text{LaIn}_{0.8}\text{Sb}_2$ , with the Fermi level ( $\epsilon_f = -8.65$  eV) corresponding to the substoichiometric formula indicated. The individual atomic contributions to the DOS are plotted in Figures 4-5(b)-(d). Although most of the La states are located above  $-7$  eV, they make a significant contribution below  $\epsilon_f$ , implying there is some degree of covalent character in the La-Sb and La-In bonds. The Fermi level crosses a small peak in the DOS and metallic behavior is expected.

The band dispersion plots along the special symmetry lines  $\Gamma\text{X}$ ,  $\Gamma\text{Y}$  (coplanar with the In chains), and  $\Gamma\text{Z}$  (parallel to the stacking axis) are shown in Figure 4-6. The Fermi level crosses two bands along  $\Gamma\text{X}$ , with orbital contributions from both the  $\text{In}_{0.8}\text{Sb}$  layer and the Sb net, as well as some contribution from La states. Along  $\Gamma\text{Y}$ , the Fermi level crosses only one band composed of Sb and La states. Although the In zigzag chains are randomly segmented by the vacancies, these segments are still crosslinked together by Sb(1) atoms, providing a pathway through which conduction can occur. Bands originating from the Sb(2) net are also crossed by the Fermi level and provide an additional pathway for conduction. Since there are no bands crossed along  $\Gamma\text{Z}$ ,  $\text{LaIn}_{0.8}\text{Sb}_2$  is predicted to be an anisotropic metal: conducting within the layers and insulating between. (The small dimensions of  $\text{LaIn}_{0.8}\text{Sb}_2$  crystals have thus far precluded us from carrying out resistivity measurements.)

The nature of the bonding is best examined through the crystal orbital overlap population (COOP) curves, plotted in Figure 4-7, for the In-In, In-Sb, and Sb-Sb contacts. Clearly, the representation of In zigzag chains (instead of a distorted square net



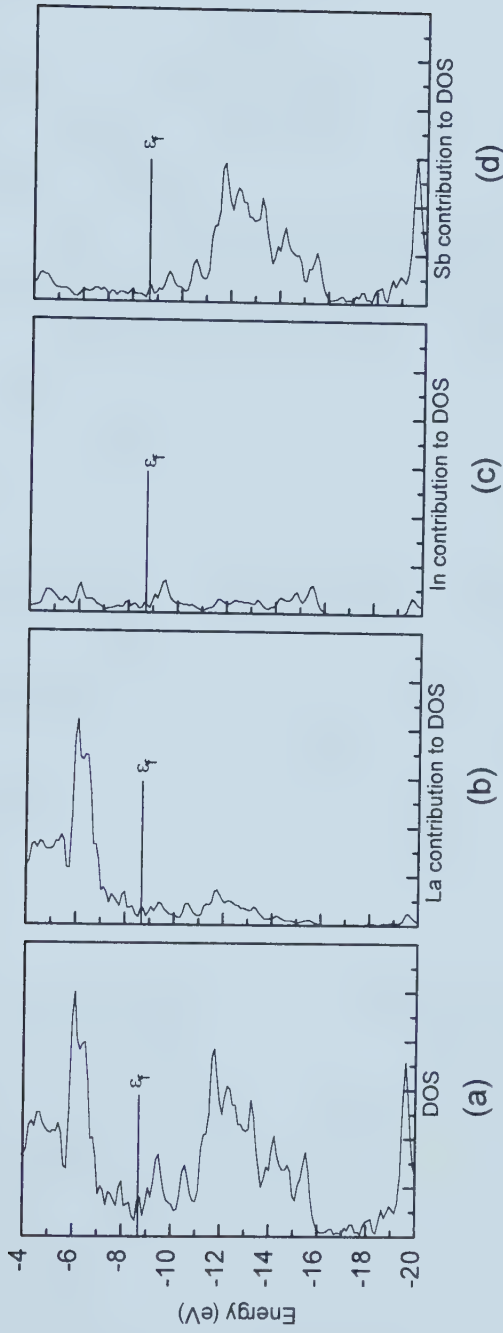


**Figure 4-5.** (a) Total density of states for  $\text{LaIn}_{0.8}\text{Sb}_2$ . The individual atomic contributions (La, In, and Sb) to the density of states are shown in (b) – (d). The Fermi level corresponding to the substoichiometric  $\text{LaIn}_{0.8}\text{Sb}_2$  is shown.



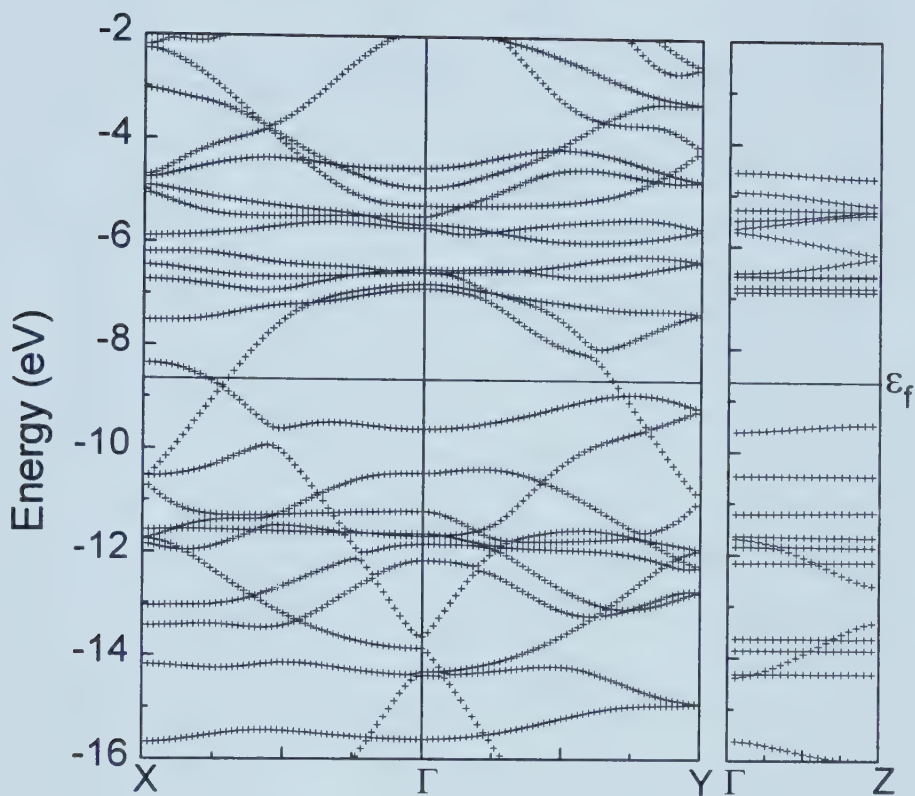


**Figure 4-6.** Band dispersion curves for  $\text{LaIn}_{0.8}\text{Sb}_2$  along the special symmetry lines  $\Gamma$ X,  $\Gamma$ Y, and  $\Gamma$ Z. The Fermi level corresponding to the substoichiometric  $\text{LaIn}_{0.8}\text{Sb}_2$  is shown.



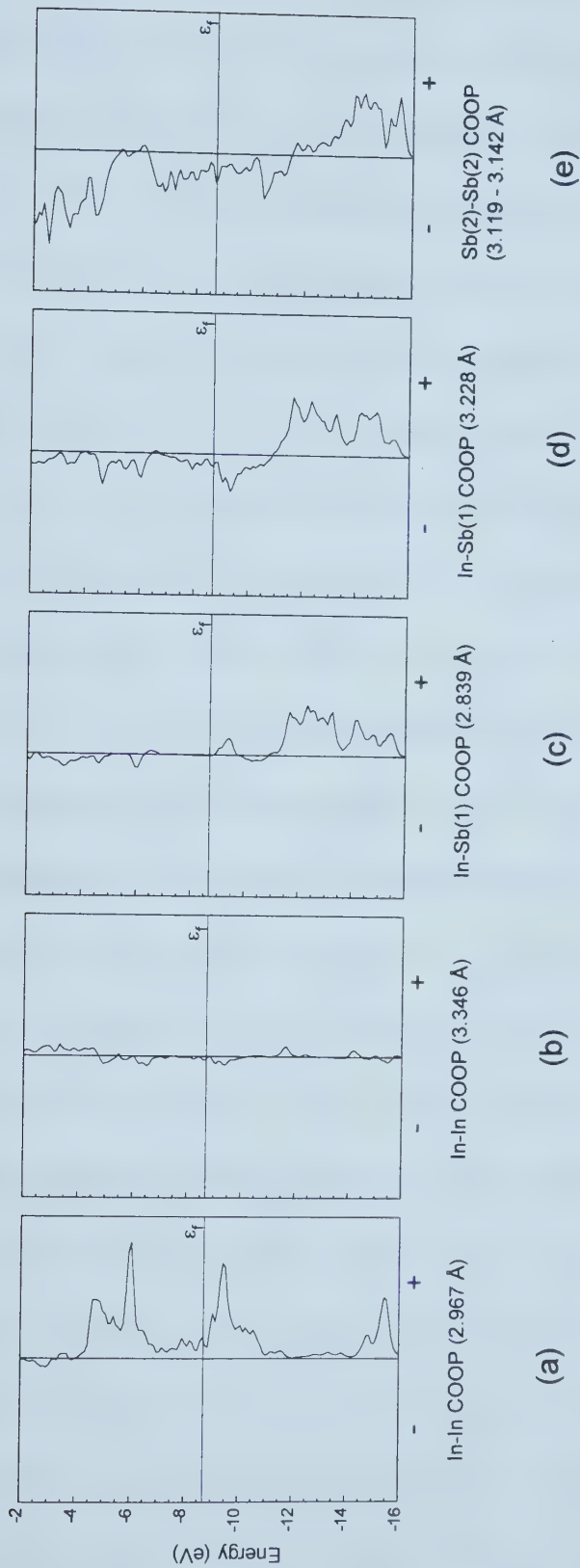


**Figure 4-7.** Crystal orbital overlap population curves for the In-In ((a) 2.967 and (b) 3.346 Å), In-Sb(1) ((c) 2.839 and (d) 3.228 Å), and (e) Sb(2)-Sb(2) interactions. The Fermi level corresponding to the substoichiometric  $\text{LaIn}_{0.8}\text{Sb}_2$  is shown.





with each In atom forming four homoatomic bonds) is correct since only the shorter intrachain distance of 2.967 Å has significant bonding character (considerable filling of bonding states), while at the longer interchain 3.346 Å distance, there are negligible interactions. On a local level, the 80% occupancy of In sites can be modeled as an infinite chain with every fifth site vacant, as shown in Figure 4-8. (This is one possibility of an ordered superstructure; in the actual structure, we assume that the chain is segmented randomly.) In a five-membered segment, the effect of one vacancy is to eliminate two of the five possible bonds, and therefore each In atom on average has only 60% of the maximum of two bonds (*i.e.*, 1.2 bonds each). This gives an overlap population per bond of 0.65, which is comparable to that calculated for In–In single bonds in BaIn<sub>2</sub> (distance 3.03 Å, overlap population  $\sim 0.64 - 0.76$ )<sup>40</sup> and for the 1-D linear In<sup>+</sup> chains (distance 2.90, overlap population 0.69)<sup>41</sup> found in InMo<sub>4</sub>O<sub>6</sub>.<sup>42</sup> In contrast, the overlap population for the longer In–In interchain distance (3.346 Å) is only  $\sim 0.05$ , confirming the zigzag chain representation. The short In–Sb contact maximizes its bonding at the Fermi level, with an overlap population of 0.69 corresponding to a full single bond, while the longer In–Sb contact corresponds to a significant amount of antibonding states being filled (overlap population 0.28), roughly corresponding to a half bond. Finally, the Sb–Sb bonding in the square net is exactly as expected, with some antibonding states filled and an overlap population (0.27) consistent with half bonds. The La–Sb and La–In bonds have overlap populations consistent with some degree of covalency (0.24 and 0.16, respectively), which is not unexpected as a fully charged La<sup>3+</sup> would strongly polarize the electron clouds of both the In and Sb atoms. The calculated



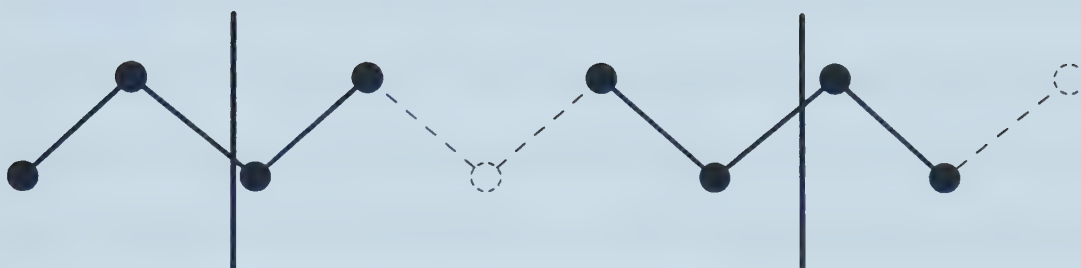


**Figure 4-8.** View of an ordered In chain with every fifth site vacant, as indicated by the dotted hollow circles. Removal of *one* In atom per five-membered segment removes *two* of the five possible In–In bonds.



atomic charges result in a formulation of  $(\text{La}^{0.85+})(\text{In}^{0.45+})_{0.8}(\text{Sb}(1)^{1-})(\text{Sb}(2)^{0.2-})$ . Considering that covalency will reduce extreme charges as required by the electroneutrality principle, these charges are in good agreement with the relative charges predicted by the Zintl concept.

The second model (an ordered  $1 \times 2 \times 1$  superstructure with unit cell contents “ $\text{La}_4\text{In}_3\text{Sb}_8$ ” or a formula  $\text{LaIn}_{0.75}\text{Sb}_2$  with  $Z = 4$ ) gave results that are generally consistent with those of the first model. In this case, every fourth In atom was removed in an ordered fashion along  $b$ , segmenting the infinite zigzag chains into finite three-membered units. The DOS curve and their individual atomic contributions, band dispersion, and COOP curves are given in the Appendix (Figures A-1 – A-3). As before, the Fermi level ( $\epsilon_f = -8.06$  eV) crosses a small peak in the DOS, with two bands being crossed along  $\Gamma\text{X}$ , one band along  $\Gamma\text{Y}$ , and none along  $\Gamma\text{Z}$ ; the picture of an anisotropic metal is still valid. There are slight differences in the values of the overlap population per bond, with the largest effect noted for the In–In intrachain (2.967 Å) interaction which decreases from 0.65 (model 1) to 0.48 (model 2). This remains a strongly bonding interaction, especially when compared to the negligible interchain overlap population of 0.03 (model 2). Finally, the calculated atomic charges from the second model give the formulation  $(\text{La}^{0.75+})(\text{In}^{0.88+})_{0.75}(\text{Sb}(1)^{1.16-})(\text{Sb}(2)^{0.25-})$ . The greater positive charge on In versus La can be explained by noting that the orbital energy for the La 5d states are lower than that of the In 5p states (Table 4-4) and that the 5d states are therefore likely to be more highly populated.



In conclusion, we have shown that  $\text{LaIn}_{0.8}\text{Sb}_2$  provides an interesting example of how strong bonding between the heavier main-group elements (In–In) can coexist with weaker bonding (Sb–Sb). In particular, substoichiometry of the In sites seems to be necessary to provide a balance between the locally maximize In–In bonding within the zigzag chains and the weak Sb–Sb bonding within the square net. Although the immediate effect of increasing the number of electrons would be to slightly increase the strength of the In–In bonding, this would be strongly offset by the dramatic weakening of the Sb–Sb bonding, so the Sb square net remains intact in the real structure. This provides a clue to the origins of the substantial range of homogeneity observed for the corresponding  $\text{LaSn}_x\text{Sb}_2$  ( $0.1 < x < 0.8$ ) system on one hand and the point phase nature of  $\text{LaIn}_{0.8}\text{Sb}_2$  on the other. Replacing In with Sn puts more electrons into the system, which can be absorbed by the Sb square net to only a certain degree before other bonds (the Sn–Sn bonds in the  ${}^2_\infty[\text{Sn}_x\text{Sb}]$  layer) must break. This occurs, not by substantial lengthening of Sn–Sn bonds, but rather by creation of vacancies to retain strong Sn–Sn bonds on a local level. It would be interesting, then, to explore the quaternary  $\text{LaIn}_x\text{Sn}_y\text{Sb}_2$  system and preliminary results suggest that such phases can be prepared.<sup>43</sup>





## REFERENCES

- (1) *Chemistry, Structure, and Bonding of Zintl Phases and Ions*; Kauzlarich, S. M., Ed.; VCH Publishers: New York, 1996.
- (2) Schäfer, H. *Annu. Rev. Mater. Sci.* **1985**, *15*, 1.
- (3) Corbett, J. D. *Chem. Rev.* **1985**, *85*, 383.
- (4) von Schnering, H. G. *Angew. Chem. Int. Ed. Engl.* **1981**, *20*, 33.
- (5) For example, see the following. (a)  $\text{Na}_7\text{Al}_2\text{Sb}_5$ : Cordier, G.; Ochmann, H.; Schäfer, H.; Stelter, M. *Z. Anorg. Allg. Chem.* **1984**, *517*, 118. (b)  $\text{Ca}_5\text{Ga}_2\text{Sb}_6$ ,  $\text{Ca}_5\text{In}_2\text{Sb}_6$ ,  $\text{Sr}_5\text{In}_2\text{Sb}_6$ : Cordier, G.; Schäfer, H.; Stelter, M.; *Z. Naturforsch. B: Anorg. Chem., Org. Chem.* **1985**, *40*, 5. (c)  $\text{Na}_2\text{Ga}_3\text{Sb}_3$ : Cordier, G.; Ochmann, H.; Schäfer, H. *Mater. Res. Bull.* **1986**, *21*, 331. (d)  $\text{Ba}_2\text{Sn}_3\text{Sb}_6$ : Lam, R.; Mar, A. *Inorg. Chem.* **1996**, *21*, 6959. (e)  $\text{Na}_5\text{SnSb}_3$ ,  $\text{K}_8\text{SnSb}_4$ : Eisenmann, B.; Klein, J. *Z. Naturforsch. B: Chem. Sci.* **1988**, *43*, 1156.
- (6) For example, see the following. (a)  $\text{La}_3\text{ZrSb}_5$ ,  $\text{La}_3\text{HfSb}_5$ ,  $\text{RECrSb}_3$  ( $\text{RE} = \text{La-Nd}$ ,  $\text{Sm}$ ,  $\text{Gd-Dy}$ ): Ferguson, M. J.; Hushagen, R. W.; Mar, A. *J. Alloys Compd.* **1997**, *249*, 191 and references therein. (b)  $\text{REM}_{1-x}\text{Sb}_2$  ( $\text{RE} = \text{La-Nd}$ ,  $\text{Sm}$ ,  $\text{Gd}$ ,  $\text{Tb}$ ;  $M = \text{Mn}$ ,  $\text{Co}$ ,  $\text{Au}$ ,  $\text{Zn}$ ,  $\text{Cd}$ ): Wollesen, P.; Jeitschko, W.; Brylak, M.; Dietrich, L. *J. Alloys Compd.* **1996**, *245*, L5. (c)  $\text{REM}_4\text{Sb}_{12}$  ( $\text{RE} = \text{La-Nd}$ ,  $\text{Sm}$ ,  $\text{Eu}$ ;  $M = \text{Fe}$ ,  $\text{Ru}$ ,  $\text{Os}$ ): Braun, D. J.; Jeitschko, W. *J. Less-Common Met.* **1980**, *72*, 147.
- (7) Raju, N. P.; Greedan, J. E.; Ferguson, M. J.; Mar, A. *Chem. Mater.* **1998**, *10*, 3630.
- (8) Hartjes, K.; Jeitschko, W.; Brylak, M. *J. Magn. Magn. Mat.* **1997**, *137*, 109.



- (9) Muro, Y.; Takeda, N.; Ishikawa, M. *J. Alloys Compd.* **1997**, 257, 23.
- (10) André, G.; Bourée, F.; Oles, A.; Penc, B.; Sikora, W.; Szytula, A.; Zygmunt, A. *J. Alloys Compd.* **1997**, 255, 31.
- (11) Sologub, O.; Hiebl, K.; Rogl, P.; Bodak, O. *J. Alloys Compd.* **1995**, 227, 40.
- (12) Sologub, O.; Noël, H.; Leithe-Jasper, A.; Rogl, P.; Bodak, O. I. *J. Solid State Chem.* **1995**, 115, 441.
- (13) Sologub, O.; Hiebl, K.; Rogl, P.; Noël, H.; Bodak, O. *J. Alloys Compd.* **1994**, 210, 153.
- (14) Sales, B. C.; Mandrus, D.; Williams, P. K. *Science* **1996**, 272, 1325.
- (15) Ferguson, M. J.; Hushagen, R. W.; Mar, A. *Inorg. Chem.* **1996**, 35, 4505.
- (16) POLSQ: Program for least-squares unit cell refinement. Modified by D. Cahen and D. Keszler, Northwestern University, 1983.
- (17) Yvon, K.; Jeitschko, W.; Parthé, E. *J. Appl. Crystallogr.* **1977**, 10, 73.
- (18) Sheldrick, G. M. *SHELXTL* Version 5.1; Bruker Analytical X-ray Systems, Inc.: Madison, WI, 1997.
- (19) Sheldrick, G. M. *J. Appl. Crystallogr.* in press.
- (20) *International Tables for X-ray Crystallography*; Wilson, A. J. C., Ed.; Kluwer: Dordrecht, The Netherlands, 1992, Vol. C.
- (21) Gelato, L. M.; Parthé, E. *J. Appl. Crystallogr.* **1987**, 20, 139.
- (22) Whangbo, M.-H.; Hoffmann, R. *J. Am. Chem. Soc.* **1978**, 100, 6093.
- (23) Hoffmann, R. *Solids and Surfaces: A Chemist's View of Bonding in Extended Structures*; VCH Publishers: New York, 1988.



- (24) Lulei, M.; Martin, J. D.; Hoistad, L. M.; Corbett, J. D. *J. Am. Chem. Soc.* **1997**, *119*, 513.
- (25) Canadell, E.; Eisenstein, O.; Rubio, J. *Organometallics* **1984**, *3*, 759.
- (26) Hughbanks, T.; Hoffmann, R.; Whangbo, M.-H.; Stewart, K. R.; Eisenstein, O.; Canadell, E. *J. Am. Chem. Soc.* **1982**, *104*, 3876.
- (27) Wang, R.; Steinfink, H. *Inorg. Chem.* **1967**, *6*, 1685.
- (28) Eatough, N. L.; Hall, H. T. *Inorg. Chem.* **1969**, *8*, 1439.
- (29) Brylak, M.; Jeitschko, W. *Z. Naturforsch. B: Chem. Sci.* **1995**, *50*, 899.
- (30)  $\text{La}_3\text{In}$ : 3.596 Å;  $\text{La}_2\text{In}$ : 3.251 – 3.704 Å;  $\text{La}_3\text{In}_5$ : 3.168 – 3.639 Å;  $\text{LaIn}_2$ : 3.378 – 3.721 Å;  $\text{LaIn}_3$ : 3.348 Å. McMasters, O. D.; Gschneidner, Jr., K. A. *J. Less-Common Met.* **1974**, *38*, 137 and references therein.
- (31) Greenwood, N. N.; Earnshaw, A. *Chemistry of the Elements*; Pergamon Press: Oxford, U.K., 1994.
- (32) Stöhr, J.; Müller, W.; Schäfer, H. *Z. Naturforsch. B: Anorg. Chem., Org. Chem.* **1978**, *33*, 1434.
- (33) Cordier, G.; Rönninger, S. *Z. Naturforsch. B: Chem. Sci.* **1987**, *42*, 825.
- (34) (a)  $\text{Na}_2\text{In}_2\text{Sb}_3$ : Cordier, G.; Ochmann, H. *Z. Kristallogr.* **1991**, *197*, 281. (b)  $\text{K}_2\text{In}_2\text{Sb}_3$ : Cordier, G.; Ochmann, H. *Z. Kristallogr.* **1991**, *197*, 291. (c)  $\text{Rb}_2\text{In}_2\text{Sb}_3$ : Gourdon, O.; Boucher, F.; Gareh, J.; Evain, M.; O'Connor, C. J.; Jin-Seung, J. *Acta Crystallogr., Sect C: Cryst. Struct. Commun.* **1996**, *52*, 2963. (d)  $\text{Cs}_2\text{In}_2\text{Sb}_3$ : Blase, W.; Cordier, G.; Poth, L.; Weil, K. G. *Z. Kristallogr.* **1995**, *210*, 60. (e)  $\text{Ba}_5\text{In}_2\text{Sb}_6$ : Cordier, G.; Stelter, M. *Z. Naturforsch. B: Chem. Sci.*



- 1988**, 43, 463. (f)  $\text{Na}_3\text{InSb}_2$ : Cordier, G.; Ochmann, H. *Z. Kristallogr.* **1991**, 195, 107. (g)  $\text{Ca}_{11}\text{InSb}_9$ : Cordier, G.; Schäfer, H.; Stelter, M. *Z. Naturforsch. B: Anorg. Chem., Org. Chem.* **1985**, 40, 868.
- (35) In–Sb distances:  $\text{Cs}_2\text{In}_2\text{Sb}_3$ : 2.804 – 2.962 Å;<sup>34d</sup>  $\text{Ba}_5\text{In}_2\text{Sb}_6$ : 2.853 – 3.100 Å;<sup>34e</sup>  $\text{Na}_3\text{InSb}_2$ : 2.846 – 2.962 Å;<sup>34f</sup>  $\text{Ca}_{11}\text{InSb}_9$ : 2.881 – 2.886 Å.<sup>34g</sup>
- (36) Pauling, L. *The Nature of the Chemical Bond*, 3rd Ed.; Cornell University Press: Ithaca, NY, 1960.
- (37) Cotton, F. A.; Wilkinson, G. *Advanced Inorganic Chemistry*, 3rd Ed.; John Wiley & Sons, Inc.: New York, 1972.
- (38) Brylak, M.; Jeitschko, W. *Z. Naturforsch. B: Chem. Sci.* **1994**, 49, 747.
- (39) Papoian, G.; Hoffmann, R. *J. Solid State Chem.* **1998**, 139, 8.
- (40) Nuspl, G.; Polborn, K.; Evers, J.; Landrum, G. A.; Hoffmann, R. *Inorg. Chem.* **1996**, 35, 6922.
- (41) Janiak, C.; Hoffmann, R. *J. Am. Chem. Soc.* **1990**, 112, 5924.
- (42) McCarley, R. E.; Lii, K.-H.; Edwards, P. A.; Brough, L. F. *J. Solid State Chem.* **1985**, 57, 17.
- (43) Ellenwood, R. E.; Eulert, J. A.; Mar, A. Unpublished results.





## Chapter 5

### New Ternary Rare-Earth Transition-Metal Antimonides $RE_3MSb_5$ ( $RE = La, Ce, Pr, Nd, Sm$ ; $M = Ti, Zr, Hf, Nb$ ): Crystal Structures of $La_3TiSb_5$ , $La_3ZrSb_5$ , and $La_3HfSb_5$ <sup>†</sup>

#### Introduction

Materials possessing one-dimensional structures are of great interest because they are prone to a variety of phase transitions, including Peierls (1-D Jahn-Teller) distortions, charge density waves (CDWs), spin density waves (SDWs), and even superconductivity.<sup>1,2</sup> These transitions originate from changes in the electronic structures of the compounds near the Fermi level, often resulting in metal-to-insulator/semiconductor transitions. The best examples of such materials are the halides and chalcogenides of the early transition-metals, which often adopt one-dimensional structures consisting of metal-centered octahedra or trigonal prisms condensed via edge- or face-sharing to form linear columns.<sup>1</sup> These compounds frequently undergo Peierls distortions accompanied by the formation of CDWs. Depending on the electron count, the transition metals are able to use the “extra” electrons (the electrons not needed by the anions) to form  $M-M$  bonds, and the degree of the  $M-M$  interaction strongly influences the electronic properties. Because there are only a few examples of such one-dimensional

---

<sup>†</sup> Portions of this chapter have been published. Ferguson, M. J.; Hushagen, R. W.; Mar, A. *J. Alloys Compd.* **1997**, 249, 191. Reproduced in part with permission from Bolloré, G.; Ferguson, M. J.; Hushagen, R. W.; Mar, A. *Chem. Mater.* **1995**, 7, 2229. Copyright 1995 American Chemical Society.



materials, the discovery of new classes of compounds with low-dimensional structures is significant.

Investigations into ternary rare-earth transition-metal antimonide systems  $RE_xM_ySb_z$  have been going on for at least two decades. These studies have been carried out variously to search for new magnetic materials,<sup>3-5</sup> to test the validity of bonding models,<sup>6,7</sup> and perhaps most importantly, to systematize an interesting structural chemistry that is not as well understood as that of the corresponding phosphides or arsenides.<sup>3-18</sup> Some of these antimonides have counterparts in phosphides or arsenides, such as  $REMSb_2$  ( $M = \text{Mn-Zn, Pd, Ag, Au}$ )<sup>4-8</sup> with the  $\text{HfCuSi}_2$ -structure,  $REM_2Sb_2$  ( $M = \text{Mn, Ni, Pd}$ )<sup>3,9-12</sup> with the  $\text{CaBe}_2\text{Ge}_2$ - and  $\text{ThCr}_2\text{Si}_2$ -structures, and  $REM_4Sb_{12}$  ( $M = \text{Fe, Ru, Os}$ )<sup>13,14</sup> with the filled skutterudite  $\text{LaFe}_4\text{P}_{12}$ -structure. Others, such as  $RE_3M_3Sb_4$  ( $M = \text{Pt, Cu, Au}$ )<sup>15-17</sup> and  $REMSb_3$  ( $M = \text{V, Cr}$ ),<sup>18</sup> are unique to antimonides so far. Recently, some of these materials have been shown to display exotic behavior, such as heavy fermions, valence fluctuations, and the Kondo effect, which can typically be attributed to the localized  $f$ -electrons of the rare-earth metals.<sup>19-21</sup> Even more interesting are the filled skutterudites which are promising thermoelectric materials<sup>22</sup> and the compound  $\text{Eu}_{14}\text{MnSb}_{11}$  which exhibits colossal magnetoresistance.<sup>23</sup>

Although the ternary systems of the later transition-metals have been heavily studied, reports of new compounds with an early transition-metal have so far been few. A new series of ternary antimonides  $RE_3MSb_5$  containing an early transition metal ( $M = \text{Ti, Zr, Hf, Nb}$ ) has been synthesized and structurally characterized, and unlike the known  $RE_xM_ySb_z$  systems which possess two- or three-dimensional structures,  $RE_3MSb_5$  adopts a



strongly one-dimensional structure. The electrical resistivity of the  $RE_3TiSb_5$  members has been measured, and extended Hückel band structure calculations performed to explain the bonding.

## Experimental Section

**Synthesis.** The title compounds were prepared by reactions of powders of the rare-earth metals (La, Ce, Pr, Nd, Sm; 99.9%, Cerac or Alfa-Aesar), transition metals (Ti, 99.98%; Zr, 99.7%; Hf, 99.8%; Nb, 99.8%, Cerac), and antimony (99.999%, Cerac or Aldrich). Initial investigations were carried out in the La/Ti/Sb phase system by analyzing arc-melted samples with diverse starting compositions. In general, 0.25 g samples were prepared in an argon drybox in the form of pressed pellets, which were then melted in a Centorr 5TA tri-arc furnace under argon (gettered by melting a titanium pellet) at slightly greater than atmospheric pressure. The cooled buttons were flipped over and re-melted. Since some vaporization occurs during the arc-melting, the weight loss is assumed to be attributable entirely to Sb, and was compensated for by adding a 10% weight excess of Sb prior to melting. Aggregates of thin, shiny silver, needle-shaped crystals were first observed in the sample prepared from the ratio La:Ti:Sb = 2:3:6. EDX analysis (energy dispersive X-ray analysis) on these crystals with a JEOL JSM-6301FXV field-emission scanning electron microscope revealed the presence of the elements La, Ti, and Sb in the ratio 3:1:5. Subsequently, the isotypic compounds  $RE_3MSb_5$  with  $RE = La, Ce, Pr, Nd, Sm$  and  $M = Ti, Zr, Hf, Nb$  were prepared by arc-melting pellets containing the stoichiometric ratio of the elements. The phase  $Sm_3NbSb_5$





could not be prepared, and attempts at substituting  $M$  with V or Ta resulted in the known  $REVSb_3$  or the binary rare-earth and tantalum antimonides.

Although  $RE_3MSb_5$  is the major phase formed in these reactions, minor amounts of binary antimonides could not be completely eliminated. The compounds are slightly sensitive in air; they begin to degrade over one day and completely decompose within one week. Powder X-ray diffraction patterns were collected on an Enraf-Nonius FR552 Guinier camera ( $CuK_{\alpha 1}$  radiation; Si standard). The cell parameters were refined by least-squares fits of 20 to 30 reflections in the powder pattern with the program POLSQ,<sup>24</sup> and are listed in Table 5-1. The observed powder X-ray diffraction patterns agree well with those calculated from the crystal structure of  $La_3TiSb_5$  by the program LAZY-PULVERIX.<sup>25</sup> Small variations in the cell parameters are observed, depending on the initial pellet composition (e.g., “ $La_3TiSb_5$ ” led to  $a = 9.526(1)$ ,  $c = 6.278(2)$  Å,  $V = 493.3(2)$  Å<sup>3</sup>, while “ $La_2Ti_3Sb_6$ ” led to  $a = 9.520(3)$ ,  $c = 6.267(3)$  Å,  $V = 491.9(3)$  Å<sup>3</sup>); this may suggest the existence of a narrow homogeneity range.

Subsequently, single crystals for the structure determinations of  $La_3ZrSb_5$  and  $La_3HfSb_5$  were prepared by Sn flux reactions of the elements in a 3:1:5 ratio (total mass 0.25 g) with a 10-fold excess amount of Sn. The elements were loaded into fused-silica tubes (5 cm long, 10 mm i.d.), which were then evacuated, sealed, and heated in a furnace at 600 °C for 1 day, 900 °C for 2 days, cooled to 600 °C over 1 day, and then cooled to room temperature over 10 hours. The Sn flux was dissolved with concentrated HCl and the product was washed with distilled water and ethanol. The hexagonal silver needle-shaped crystals obtained tarnish within minutes and decompose in a week upon





**Table 5-1.** Cell Parameters for Compounds  $RE_3MSb_5$  ( $RE = \text{La, Ce, Pr, Nd, Sm}$ ;  $M = \text{Ti, Zr, Hf, Nb}$ ) with the  $\text{La}_3\text{TiSb}_5$  Structure (Obtained from arc-melting reactions)

Compound	$a$ (Å)	$c$ (Å)	$c/a$	$V$ (Å <sup>3</sup> )
$\text{La}_3\text{TiSb}_5$	9.526(1)	6.278(2)	0.6590	493.3(2)
$\text{Ce}_3\text{TiSb}_5$	9.439(2)	6.235(2)	0.6606	481.1(2)
$\text{Pr}_3\text{TiSb}_5$	9.401(3)	6.224(2)	0.6621	476.4(3)
$\text{Nd}_3\text{TiSb}_5$	9.353(1)	6.196(1)	0.6625	469.4(1)
$\text{Sm}_3\text{TiSb}_5$	9.275(1)	6.162(1)	0.6643	459.1(2)
$\text{La}_3\text{ZrSb}_5$	9.587(1)	6.358(1)	0.6632	506.1(1)
$\text{Ce}_3\text{ZrSb}_5$	9.506(1)	6.318(2)	0.6646	494.4(1)
$\text{Pr}_3\text{ZrSb}_5$	9.450(1)	6.293(1)	0.6659	486.7(1)
$\text{Nd}_3\text{ZrSb}_5$	9.413(1)	6.275(1)	0.6666	481.6(2)
$\text{Sm}_3\text{ZrSb}_5$	9.344(1)	6.234(2)	0.6672	471.4(2)
$\text{La}_3\text{HfSb}_5$	9.582(1)	6.356(1)	0.6633	505.3(1)
$\text{Ce}_3\text{HfSb}_5$	9.483(2)	6.298(2)	0.6641	490.4(2)
$\text{Pr}_3\text{HfSb}_5$	9.419(2)	6.271(3)	0.6658	481.8(2)
$\text{Nd}_3\text{HfSb}_5$	9.390(2)	6.261(2)	0.6668	478.1(2)
$\text{Sm}_3\text{HfSb}_5$	9.340(2)	6.230(2)	0.6670	470.6(2)
$\text{La}_3\text{NbSb}_5$	9.534(2)	6.264(2)	0.6570	493.1(2)
$\text{Ce}_3\text{NbSb}_5$	9.438(2)	6.219(2)	0.6589	479.7(2)
$\text{Pr}_3\text{NbSb}_5$	9.396(1)	6.201(2)	0.6600	474.1(2)
$\text{Nd}_3\text{NbSb}_5$	9.360(2)	6.186(2)	0.6609	469.4(2)



exposure to air. EDX analyses on these ternary compounds revealed the presence of all three elements in ratios that are consistent with the formulas obtained from the structure determinations.

The single crystals of  $RE_3TiSb_5$  used for the resistivity measurements were prepared by Sn flux reactions, but with a slightly different temperature program (570 °C for 1 day, 950 °C for 2 days, cooled to 500 °C over 1 day, cooled to room temperature over 5 hours). EDX analyses were performed on these crystals on a Hitachi F2700 scanning electron microscope to confirm their identity. Anal. Calcd for  $RE_3TiSb_5$ :  $RE$  33.3%, Ti 11.1%, Sb 55.6%. Found (average of three to four analyses each): La 36.0(5)%, Ti 9.7(8)%, Sb 54(1)%; Ce 38.4(5)%, Ti 9.1(4)%, Sb 52.5(5)%; Pr 39.3(3)%, Ti 9.2(3)%, Sb 51.6(3)%; Nd 39.3(3)%, Ti 9.4(4)%, Sb 51.3(2)%.

**Structure Determination.**  $La_3TiSb_5$ : Initial cell parameters for  $La_3TiSb_5$  were determined from Weissenberg photographs which revealed Laue symmetry  $6/mmm$  and systematic absences consistent with the hexagonal space groups  $P6_3/mcm$ ,  $P6_3cm$ , and  $P\bar{6}c2$ . Final cell parameters were obtained from a least-squares analysis of the setting angles of 40 reflections in the range  $26^\circ \leq 2\theta(MoK_\alpha) \leq 29^\circ$  centered on a Siemens P4RA diffractometer. X-ray diffraction data were collected at  $-60^\circ C$  with the  $\omega$  scan technique in the range  $5^\circ \leq 2\theta(MoK_\alpha) \leq 60^\circ$ . Crystal data and further details of the data collection are given in Table 5-2.

All calculations were carried out using the SHELXTL (Version 5.0) software package.<sup>26,27</sup> Conventional atomic scattering factors and anomalous dispersion corrections were used.<sup>28</sup> Intensity data were processed and Gaussian face-indexed



**Table 5-2.** Crystallographic Data for La<sub>3</sub>TiSb<sub>5</sub>, La<sub>3</sub>ZrSb<sub>5</sub>, and La<sub>3</sub>HfSb<sub>5</sub>

Formula	La <sub>3</sub> TiSb <sub>5</sub>	La <sub>3</sub> ZrSb <sub>5</sub>	La <sub>3</sub> HfSb <sub>5</sub>
Formula mass (amu)	1073.38	1116.69	1203.97
Space group	$D_{6h}^3 - P6_3/mcm$	$D_{6h}^3 - P6_3/mcm$	$D_{6h}^3 - P6_3/mcm$
<i>a</i> (Å)	9.5294(8) <sup>a</sup>	9.5743(9) <sup>a</sup>	9.557(2) <sup>a</sup>
<i>c</i> (Å)	6.2801(11) <sup>a</sup>	6.3495(7) <sup>a</sup>	6.3388(6) <sup>a</sup>
<i>V</i> (Å <sup>3</sup> )	493.9(1)	504.1(1)	501.4(1)
<i>Z</i>	2	2	2
<i>T</i> (°C)	−60	−60	−60
Diffractometer	Siemens P4RA	Enraf-Nonius CAD4	Enraf-Nonius CAD4
ρ <sub>calc</sub> (g cm <sup>−3</sup> )	7.218	7.358	7.975
Crystal dimensions (mm)	Silver needle, 0.335 × 0.039 × 0.033	Silver needle, 0.308 × 0.088 × 0.087	Silver needle, 0.212 × 0.032 × 0.032
Radiation	Graphite-monochromated MoK <sub>α</sub> , λ = 0.71073 Å	Graphite-monochromated MoK <sub>α</sub> , λ = 0.71073 Å	Graphite-monochromated MoK <sub>α</sub> , λ = 0.71073 Å
μ (cm <sup>−1</sup> )	267.9	264.9	359.4
Transmission factors <sup>b</sup>	0.213–0.439	0.094–0.227	0.194–0.404
Scan-type	ω	θ–2θ	θ–2θ
2θ limits	5° ≤ 2θ(MoK <sub>α</sub> ) ≤ 60°	2° ≤ 2θ(MoK <sub>α</sub> ) ≤ 60°	2° ≤ 2θ(MoK <sub>α</sub> ) ≤ 60°
Data collected	−1 ≤ <i>h</i> ≤ 11, −13 ≤ <i>k</i> ≤ 12, −8 ≤ <i>l</i> ≤ 8	0 ≤ <i>h</i> ≤ 13, −13 ≤ <i>k</i> ≤ 11, −8 ≤ <i>l</i> ≤ 8	0 ≤ <i>h</i> ≤ 13, −13 ≤ <i>k</i> ≤ 11, −8 ≤ <i>l</i> ≤ 8



**Table 5-2.** Crystallographic Data for La<sub>3</sub>TiSb<sub>5</sub>, La<sub>3</sub>ZrSb<sub>5</sub>, and La<sub>3</sub>HfSb<sub>5</sub> (cont'd)

No. of data collected	3063	2788	2764
No. of unique data, including $F_o^2 < 0$	290 ( $R_{int} = 0.142$ )	296 ( $R_{int} = 0.238$ )	294 ( $R_{int} = 0.174$ )
No. of unique data, with $F_o^2 > 2\sigma(F_o^2)$	280	291	277
No. of variables	13	14	14
Extinction coefficient <sup>c</sup>	—	0.030(3)	0.0011(4)
$R(F)$ for $F_o^2 > 2\sigma(F_o^2)$ <sup>d</sup>	0.041	0.062	0.042
$R_w(F_o^2)$ <sup>e</sup>	0.102	0.115	0.098
Goodness of fit <sup>f</sup>	1.41	1.32	1.22
$\Delta\rho_{max}, \Delta\rho_{min}$ ( $e \text{ \AA}^{-3}$ )	1.35, -3.31	7.94, -3.45	6.81, -6.51

<sup>a</sup> Obtained from a refinement constrained so that  $\alpha = \beta = 90^\circ$  and  $\gamma = 120^\circ$ .

<sup>b</sup> Face-indexed absorption corrections were applied, with the use of the programs in the SHELXTL package (Sheldrick, G. M. SHELXTL Version 5.0, Siemens Analytical X-ray Instruments, Inc.: Madison, WI, 1994).

<sup>c</sup> An extinction parameter  $x$  was refined, where  $F_c$  is multiplied by:  $k[1 + 0.001 * x * F_c^2 * \lambda^3 / \sin(2\theta)]^{-1/4}$ .

<sup>d</sup>  $R(F) = \sum \|F_o| - |F_c\| / \sum |F_o|$ .

<sup>e</sup>  $R_w(F_o^2) = [\sum [w(F_o^2 - F_c^2)^2] / \sum wF_o^4]^{1/2}$ ;  $w^{-1} = [\sigma^2(F_o^2) + (aP)^2 + bP]$  where  $P = [\max(F_o^2, 0) + 2F_c^2] / 3$ . For La<sub>3</sub>TiSb<sub>5</sub>,  $a = 0.036$ ,  $b = 6.96$ ; for La<sub>3</sub>ZrSb<sub>5</sub>,  $a = 0$ ,  $b = 9.46$ ; for La<sub>3</sub>HfSb<sub>5</sub>,  $a = 0.044$ ,  $b = 1.52$ .

<sup>f</sup>  $GoodF = S = [\sum [w(F_o^2 - F_c^2)^2] / (n - p)]^{1/2}$  where  $n$  is the number of reflections and  $p$  is the total number of parameters refined.





absorption corrections were applied with the program XPREP. The centrosymmetric space group  $P6_3/mcm$  was chosen on the basis of the intensity statistics, satisfactory averaging, and the successful structure solution. The positions of all atoms were found by direct methods and the structure was refined by least-squares methods. Refinements in which the occupancies of successive atoms were allowed to vary (while the isotropic displacement parameters were fixed) resulted in values of 100(1)% for La, 96(3)% for Ti, 98(1)% for Sb(1), and 103(1)% for Sb(2) in  $\text{La}_3\text{TiSb}_5$ . Moreover, the displacement parameters are unexceptional and so the ideal stoichiometry may be assumed. The atomic positions were standardized with the program STRUCTURE TIDY.<sup>29</sup> The final cycle of least-squares refinements on  $F_o^2$  of 13 variables and 290 averaged reflections (including those having  $F_o^2 < 0$ ) converged to values of  $R_w(F_o^2)$  of 0.102 and  $R(F)$  of 0.041. The difference electron density map is featureless ( $\Delta\rho_{\text{max}} = 1.35$ ,  $\Delta\rho_{\text{min}} = -3.31$   $e \text{ \AA}^{-3}$ ). Final values of the positional and equivalent isotropic displacement parameters are given in Table 5-3 and the anisotropic displacement parameters are given in the Appendix (Table A-8).

*La<sub>3</sub>ZrSb<sub>5</sub> and La<sub>3</sub>HfSb<sub>5</sub>*: Crystals of  $\text{La}_3\text{ZrSb}_5$  and  $\text{La}_3\text{HfSb}_5$  were screened for singularity by Weissenberg photography, which revealed Laue symmetry  $6/mmm$  and the same systematic absences as  $\text{La}_3\text{TiSb}_5$ . Final cell parameters were obtained from least-squares analyses of the setting angles of 24 reflections in the range  $21^\circ \leq 2\theta(\text{MoK}_\alpha) \leq 34^\circ$  ( $\text{La}_3\text{ZrSb}_5$ ) and  $21^\circ \leq 2\theta(\text{MoK}_\alpha) \leq 30^\circ$  ( $\text{La}_3\text{HfSb}_5$ ), centered on an Enraf-Nonius CAD4 diffractometer. X-ray data were collected at  $-60^\circ\text{C}$  with the  $\theta$ - $2\theta$  scan technique in the range  $2^\circ \leq 2\theta(\text{MoK}_\alpha) \leq 60^\circ$ , and further details are collected in Table 5-2.



**Table 5-3.** Atomic Coordinates and Equivalent Displacement Parameters ( $\text{\AA}^2$ ) for  $\text{La}_3\text{TiSb}_5$ ,  $\text{La}_3\text{ZrSb}_5$ , and  $\text{La}_3\text{HfSb}_5$

atom	Wyckoff position, site symmetry		$x$	$y$	$z$	$U_{\text{eq}}^a$
La <sub>3</sub> TiSb <sub>5</sub>						
La	6g	$m2m$	0.6176(1)	0	$\frac{1}{4}$	0.0054(3)
Ti	2b	$\bar{3} . m$	0	0	0	0.0066(9)
Sb(1)	6g	$m2m$	0.2507(1)	0	$\frac{1}{4}$	0.0057(3)
Sb(2)	4d	$3 . 2$	$\frac{1}{3}$	$\frac{2}{3}$	0	0.0057(4)
La <sub>3</sub> ZrSb <sub>5</sub>						
La	6g	$m2m$	0.6173(1)	0	$\frac{1}{4}$	0.0078(5)
Zr	2b	$\bar{3} . m$	0	0	0	0.0062(7)
Sb(1)	6g	$m2m$	0.2600(1)	0	$\frac{1}{4}$	0.0072(5)
Sb(2)	4d	$3 . 2$	$\frac{1}{3}$	$\frac{2}{3}$	0	0.0088(5)
La <sub>3</sub> HfSb <sub>5</sub>						
La	6g	$m2m$	0.6175(1)	0	$\frac{1}{4}$	0.0059(3)
Hf	2b	$\bar{3} . m$	0	0	0	0.0060(4)
Sb(1)	6g	$m2m$	0.2580(1)	0	$\frac{1}{4}$	0.0054(3)
Sb(2)	4d	$3 . 2$	$\frac{1}{3}$	$\frac{2}{3}$	0	0.0073(4)

<sup>a</sup>  $U_{\text{eq}}$  is defined as one-third of the trace of the orthogonalized  $U_{ij}$  tensor.



Based on the similarity of the powder X-ray diffraction patterns and Weissenberg photographs with those of  $\text{La}_3\text{TiSb}_5$ , the space group  $P6_3/mcm$  was chosen, and examination of the initial atomic positions obtained by direct methods confirmed that these compounds are isostructural. Refinements in which the occupancies of successive atoms were allowed to vary (while the isotropic displacement parameters were fixed) resulted in values of 100(1)% for La, 104(2)% for Zr, 100(1)% for Sb(1), and 99(1)% for Sb(2) in  $\text{La}_3\text{ZrSb}_5$ , and 102(1)% for La, 97(1)% for Hf, 100(1)% for Sb(1), and 100(1)% for Sb(2) in  $\text{La}_3\text{HfSb}_5$ , and thus the ideal stoichiometry may also be assumed for these two compounds. The atomic positions were standardized, and details of the final cycle of refinement are listed in Table 5-2. Final values of the positional and equivalent isotropic displacement parameters are given in Table 5-3 and the anisotropic displacement parameters are in the Appendix (Table A-8).

*Variable Temperature Study of  $\text{La}_3\text{TiSb}_5$ :*  $\text{La}_3\text{TiSb}_5$  undergoes an electronic transition at  $-153\text{ }^\circ\text{C}$  (*vide infra*). To determine if this transition has structural origin, a variable temperature single crystal X-ray diffraction study was performed. The cell constants were determined as a function of temperature on a Siemens P4RA diffractometer equipped with a SMART 1000 CCD detector. Initial matrix data collections (four sets of 50 frames) at 20,  $-80$ , and  $-120\text{ }^\circ\text{C}$  were performed and the cell parameters refined by least-squares method with the program SMART; the cell parameters are listed in Table 5-4 and do not show any significant variations. A complete data collection was performed at  $-170\text{ }^\circ\text{C}$  and the structure solved and refined as described above. The structure is identical to that determined from the data collected at



**Table 5-4.** Cell Parameters for La<sub>3</sub>TiSb<sub>5</sub> from Variable Temperature Study

Temperature (°C)	<i>a</i> (Å)	<i>c</i> (Å)	<i>V</i> (Å <sup>3</sup> )
20	9.527(4)	6.273(3)	493.1(6)
−80	9.521(8)	9.268(5)	492(1)
−120	9.525(9)	6.271(7)	493(1)
−170	9.5198(13)	6.2693(8)	492.05(19)

**Table 5-5.** Extended Hückel Parameters

atom	orbital	<i>H<sub>ii</sub></i> (eV)	ζ <sub>1</sub>	<i>c</i> <sub>1</sub>	ζ <sub>2</sub>	<i>c</i> <sub>2</sub>
La	6s	−6.5613	2.14			
	6p	−4.3769	2.08			
	5d	−7.5155	3.78	0.77651	1.381	0.45861
Ti	4s	−8.90	1.30			
	4p	−5.40	1.30			
	3d	−11.20	4.55	0.4391	1.60	0.7397
Sb	5s	−18.8	2.323			
	5p	−11.7	1.999			





–60 °C, and details of the data collection and structure refinement are given in the Appendix (Tables A-9 – A-11).

**Electrical Resistivity.** Single crystals of  $RE_3TiSb_5$  ( $RE = La, Ce, Pr, Nd$ ) with lengths between 0.8 and 1.5 mm were available for resistivity measurements. Their elemental compositions were verified by EDX analyses (*vide supra*). The crystals were carefully removed from the sample holder and cleaned with ethanol. Four Au wires with graphite extensions were attached with Ag paint to the crystals for the four-probe ac resistivity technique at 15.9 Hz. Data were collected on cooling and warming between 25 and 290 K.

**Band Structure.** One-electron band structure calculations on  $La_3TiSb_5$  were performed by the tight-binding method with an extended Hückel-type Hamiltonian using the EHMACC suite of programs.<sup>30,31</sup> The atomic parameters used are listed in Table 5-5.<sup>32-34</sup> Properties were extracted from the band structure using 50  $k$  points in the irreducible portion of the Brillouin zone.

## Results and Discussion

**Description of the Structure.** A view of the structure of  $La_3MSb_5$  down the  $c$  axis is shown in Figure 5-1, which also shows the labeling scheme. Selected interatomic distances are given in Table 5-6. The structure possesses a strongly one-dimensional character, built up from chains of compositions  ${}_2^1[MSb_{6/2}]$  and  ${}_2^1[SbSb_{2/2}]$  aligned along the  $c$  axis that are separated by La atoms. The  $M$  atoms are coordinated by six Sb(1) atoms in an octahedral fashion, with bond distances comparable to those observed in



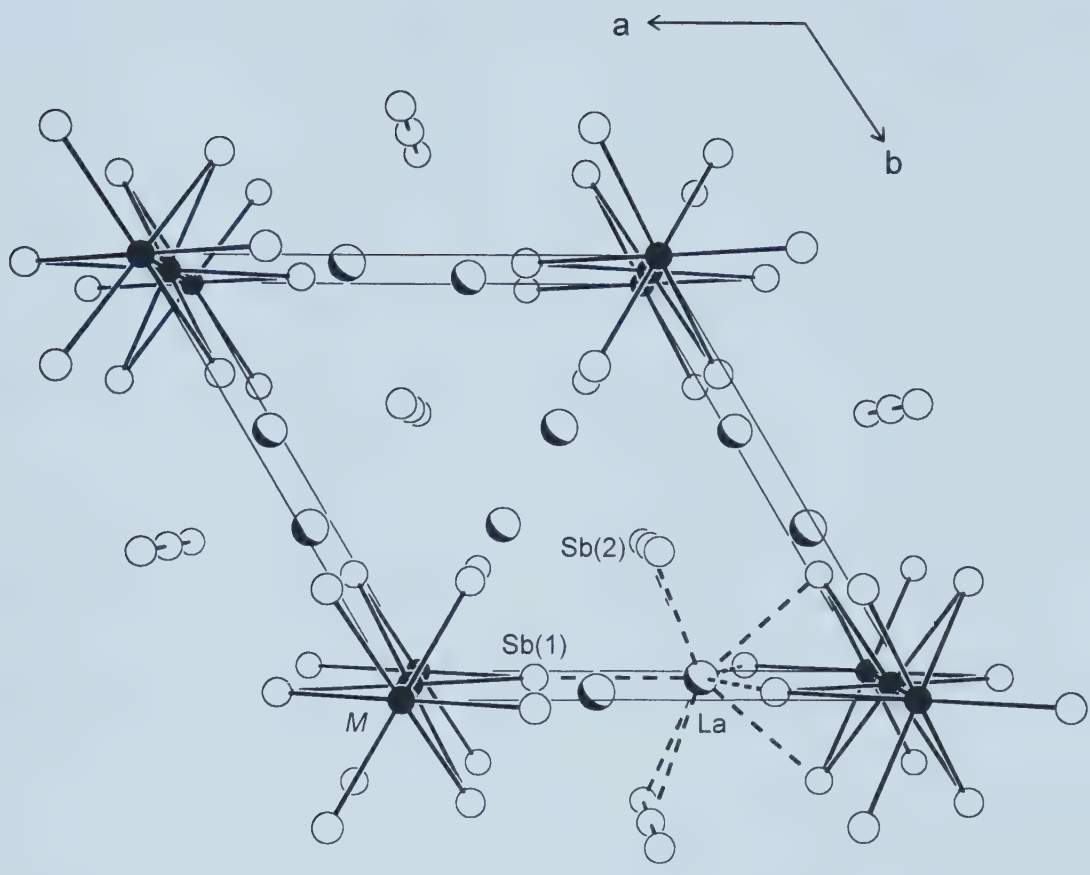


**Figure 5-1.** View down the  $c$  axis of  $\text{La}_3\text{MSb}_5$  with the unit cell outlined. The partly shaded circles are  $\text{La}$  atoms, the solid circles are  $M$  atoms (where  $M = \text{Ti}, \text{Zr},$  and  $\text{Hf}$ ), and the open circles are  $\text{Sb}$  atoms. The coordination around one  $\text{La}$  atom is depicted by dashed lines.



**Table 5-6.** Selected Interatomic Distances (Å) for  $\text{La}_3M\text{Sb}_5$  ( $M = \text{Ti, Zr, Hf}$ )

	$\text{La}_3\text{TiSb}_5$	$\text{La}_3\text{ZrSb}_5$	$\text{La}_3\text{HfSb}_5$
La–Sb(1)	3.2064(8) (2×)	3.2407(8) (2×)	3.2298(8) (2×)
La–Sb(2)	3.3598(4) (4×)	3.3792(4) (4×)	3.3738(5) (4×)
La–Sb(1)	3.3815(8) (2×)	3.3853(6) (2×)	3.3855(6) (2×)
La–Sb(1)	3.496(1)	3.421(1)	3.435(1)
La–La	3.858(1) (2×)	3.889(1) (2×)	3.884(1) (2×)
$M$ –Sb(1)	2.859(1) (6×)	2.952(1) (6×)	2.931(1) (6×)
$M$ – $M$	3.1400(5) (2×)	3.1748(4) (2×)	3.1694(3) (2×)
Sb(2)–Sb(2)	3.1400(5) (2×)	3.1748(4) (2×)	3.1694(3) (2×)
Sb(1)–Sb(1)	3.9456(8) (4×)	4.034(1) (4×)	4.016(1) (4×)
Sb(1)–Sb(1)	4.138(2) (2×)	4.311(2) (2×)	4.271(2) (2×)



TiSb<sub>2</sub>,  $\alpha$ -ZrSb<sub>2</sub>, or  $\alpha$ -HfSb<sub>2</sub>, in which the transition metal is in the +4 oxidation state.<sup>35-37</sup> These octahedra share their faces along the *c* axis to form infinite columns, as shown in Figure 5-2. The Sb(2) atoms are surrounded above and below by symmetry-equivalent Sb(2) atoms at 3.14 – 3.18 Å (exactly one-half the *c* parameter), forming an infinite skewer (Figure 5-2). The coordination of the La atoms by five Sb(1) and four Sb(2) atoms, at distances typical for La–Sb bonds, in a roughly tricapped trigonal prismatic geometry is shown in Figure 5-3. Two Sb(1) and four Sb(2) atoms define the trigonal prism while the remaining three Sb(1) atoms are located above each of the rectangular faces. Each La atom is ~3.9 Å from two other La atoms in a zigzag arrangement running parallel to [001] (Figure 5-1). Metrical details for La<sub>3</sub>ZrSb<sub>5</sub> and La<sub>3</sub>HfSb<sub>5</sub> are similar, which is expected considering the nearly identical radii of Zr<sup>4+</sup> and Hf<sup>4+</sup> (0.86 and 0.85 Å, respectively, for crystal radii with CN6).<sup>38</sup>

**Structural Relationships and Bonding.** The *RE*<sub>3</sub>*MSb*<sub>5</sub> family of compounds is isostructural to the recently discovered compounds U<sub>3</sub>*MSb*<sub>5</sub> (*M* = Ti, V, Cr, Mn).<sup>39</sup> However, the rare-earth analogues for *M* = V, Cr, and Mn do not form, but adopt different structures (*REMSb*<sub>3</sub>, *M* = V, Cr;<sup>18</sup> *REMn*<sub>1-*x*</sub>Sb<sub>2</sub>;<sup>6</sup> *RE*<sub>6</sub>MnSb<sub>15</sub><sup>40</sup>). As in U<sub>3</sub>*MSb*<sub>5</sub>, the *RE*<sub>3</sub>*MSb*<sub>5</sub> structure may be regarded as an antitype of the Hf<sub>5</sub>Sn<sub>3</sub>Cu structure<sup>41</sup> (an ordered variant of the Ti<sub>5</sub>Ga<sub>4</sub> structure<sup>42</sup>), which in turn is derived by filling the octahedral interstitial sites<sup>43</sup> of the prevalent Mn<sub>5</sub>Si<sub>3</sub> structure.<sup>44</sup> For those compounds in which all the atoms participate considerably in covalent bonding, this is a valid and useful way of building up the structure. But the rare-earth element La is significantly more electropositive than U (Pauling electronegativities 1.10 versus 1.38, respectively),<sup>45</sup> and if





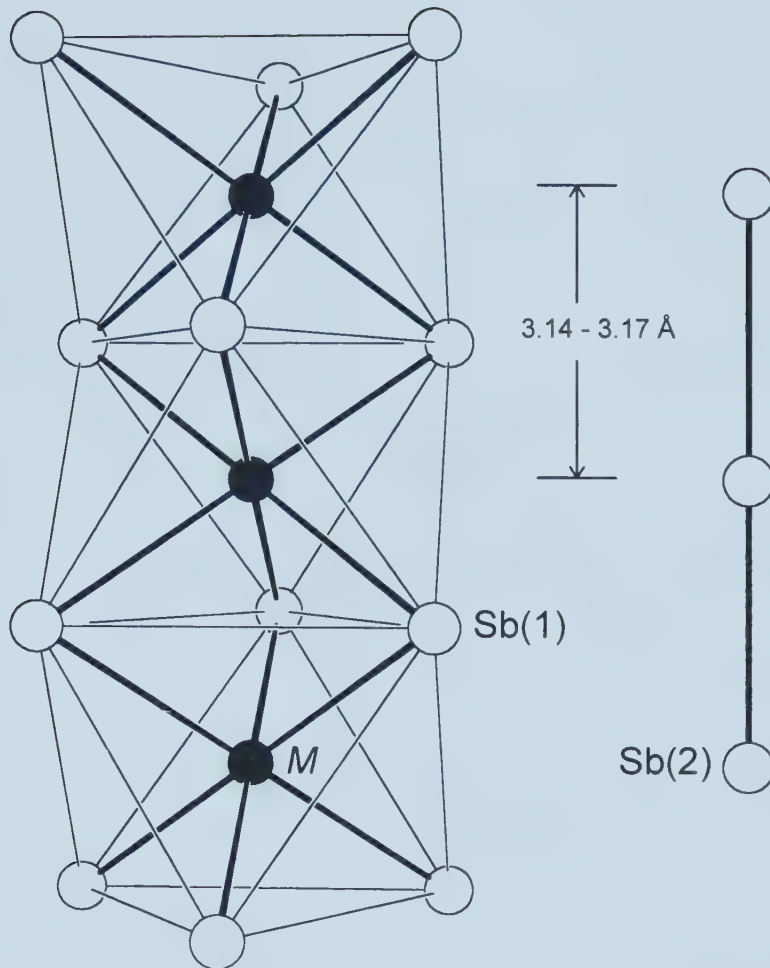


**Figure 5-2.** View projected approximately (110) showing a column of face-sharing  $MSb_6$  ( $M = \text{Ti, Zr, and Hf}$ ) octahedra (outlined by light lines) and a chain of Sb(2) atoms, both running along the  $c$  direction.



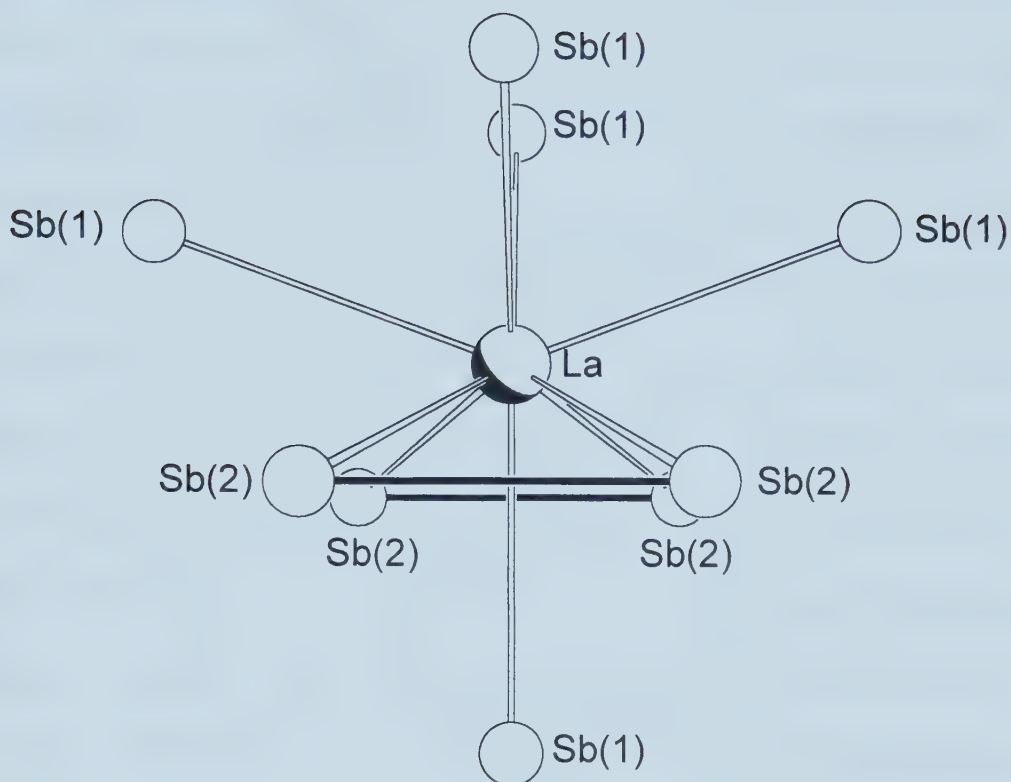


**Figure 5-3.** Coordination of the La atom by six Sb atoms in a trigonal prismatic fashion in  $\text{La}_3\text{MSb}_5$  ( $M = \text{Ti, Zr, Hf}$ ), with three Sb capping atoms located above each of the rectangular faces.



the bonding component from the La is regarded to be entirely ionic, the one-dimensional character of the structure can be emphasized by the crystal chemical formulation:<sup>46</sup>  $(\text{La}^{3+})_3 \frac{1}{\infty} [\text{MSb}_{6/2}]^{(9-x)-} \frac{1}{\infty} [\text{SbSb}_{2/2}]^{x-}$ . That is, the structure consists of anionic chains parallel to the  $c$  axis that are held together by intervening  $\text{La}^{3+}$  cations; the ionic and covalent components of the bonding can be separated in a Zintl-type approximation.<sup>47</sup>

In attempting to formulate a first approximation of an oxidation state assignment for  $\text{La}_3\text{TiSb}_5$ , it is reasonable to assume that the more electropositive components (La and Ti) transfer their valence electrons to the more electronegative Sb atoms. The Sb(1)–Sb(1) distances are approximately equal to the sum of the van der Waals radius of Sb ( $\sim 2.2$  Å)<sup>48</sup> and therefore the Sb(1) atoms can be considered as isolated  $\text{Sb}^{3-}$  anions. The Sb(2)–Sb(2) interactions of 3.14 Å fall in an intermediate regime between the intralayer full single bond distance and the weakly bonding interlayer distance observed in elemental Sb (2.908 versus 3.36 Å, respectively).<sup>49</sup> These Sb–Sb interactions are prevalent in many solid-state antimonides and can be manifested as chains in  $RE_3\text{MSb}_5$  or as sheets in  $RE\text{Sn}_{0.75}\text{Sb}_2$  and  $RE\text{In}_{0.8}\text{Sb}_2$ , for instance. A two-bonded antimony atom would normally be assigned  $\text{Sb}^{1-}$ , but the Sb(2)–Sb(2) distance is too long for a single bond and is considered a half bond (one-electron bond), resulting in the assignment  $\text{Sb}^{2-}$ . Thus, the tentative formulation  $(\text{La}^{3+})_3(\text{Ti}^{4+})(\text{Sb}(1)^{3-})_3(\text{Sb}(2)^{2-})_2$  is reached.

However, the situation may be different for the other transition-metal analogues. The  $\text{MSb}_{6/2}$  columns run parallel to the  $c$  direction, and the  $M$ – $M$  is equal to half the  $c$  parameter. Based strictly on bond length arguments, the Ti–Ti distance of 3.14 Å in  $\text{La}_3\text{TiSb}_5$  is likely too long to be bonding, but for  $\text{La}_3\text{ZrSb}_5$  and  $\text{La}_3\text{HfSb}_5$ , the  $M$ – $M$



distances of  $\sim 3.17$  Å cannot be dismissed as non-bonding, given that similar distances observed in other compounds, such as  $\text{ZrI}_3$  (which contains chains of Zr-centered face-sharing octahedra) and  $\text{Zr}_5\text{Sb}_3$ , are deemed to be significant.<sup>43,50</sup> Thus, the presence of  $M$ – $M$  interactions may necessitate a slight modification to the oxidation state formulation. As will be demonstrated later from the band structure calculations, even the somewhat long Ti–Ti interaction is found to be slightly bonding. Generalizing this scheme to the niobium analogue  $\text{La}_3\text{NbSb}_5$ , there would be isolated chains of  $\text{Nb}^{4+}$  ( $d^1$ ) atoms separated  $\sim 3.13$  Å from each other, which may be prone to undergo a one-dimensional pairing or Peierls distortion. However, there is currently no compelling evidence that suggests the presence of any superstructure. Finally, the isostructural analogues with  $RE = \text{Ce}, \text{Pr}, \text{Nd}$ , and  $\text{Sm}$  can be prepared, and plotted in Figure 5-4 is the unit cell volume as a function of rare-earth metal. The monotonic decrease in volume observed is expected based on the lanthanide contraction, and the absence of any deviation implies that the oxidation state of the rare-earth metal is +3 in all cases.

**Electrical Resistivity.** Resistivity measurements were performed on single crystals of  $RE_3\text{TiSb}_5$  (where  $RE = \text{La}, \text{Ce}, \text{Pr}, \text{Nd}$ ) along the needle  $c$  axis, and the data are plotted in Figure 5-5. All compounds are metallic, with room temperature resistivities ( $\rho_{290}$ ) between  $\sim 4 \times 10^{-5} - 1 \times 10^{-4}$  Ω cm. The measurements were reproducible with several samples and showed excellent agreement of both the general shape of the curves and the absolute values of the resistivity. The plots for  $\text{Pr}_3\text{TiSb}_5$  and  $\text{Nd}_3\text{TiSb}_5$  deviate only slightly from a linear dependence on temperature (Figure 5-5(c) and (d)), where the linear temperature coefficient is  $\sim 4 \times 10^{-7}$  and  $\sim 1 \times 10^{-7}$  Ω cm  $\text{K}^{-1}$  for the Pr and Nd





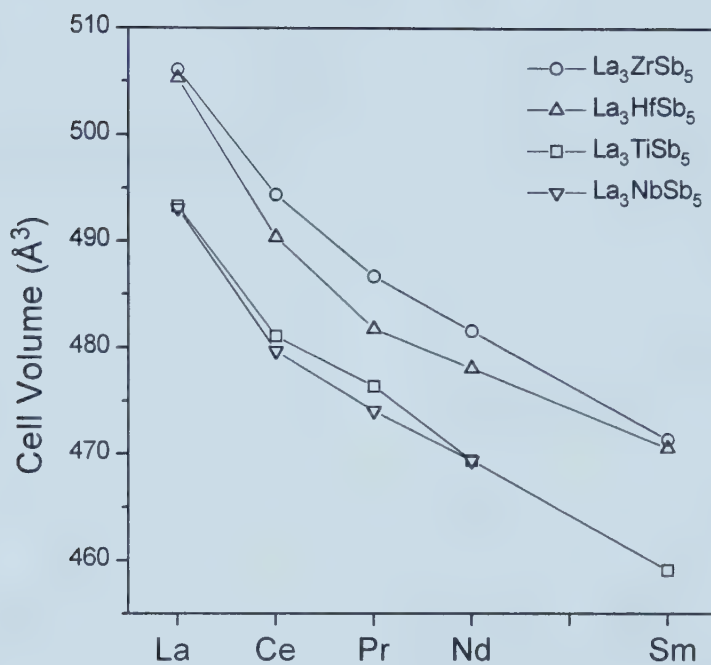


**Figure 5-4.** Plot of the unit cell volume for  $\text{RE}_3\text{MSb}_5$  compounds, with the legend indicated. The lines are drawn only to guide the eye.



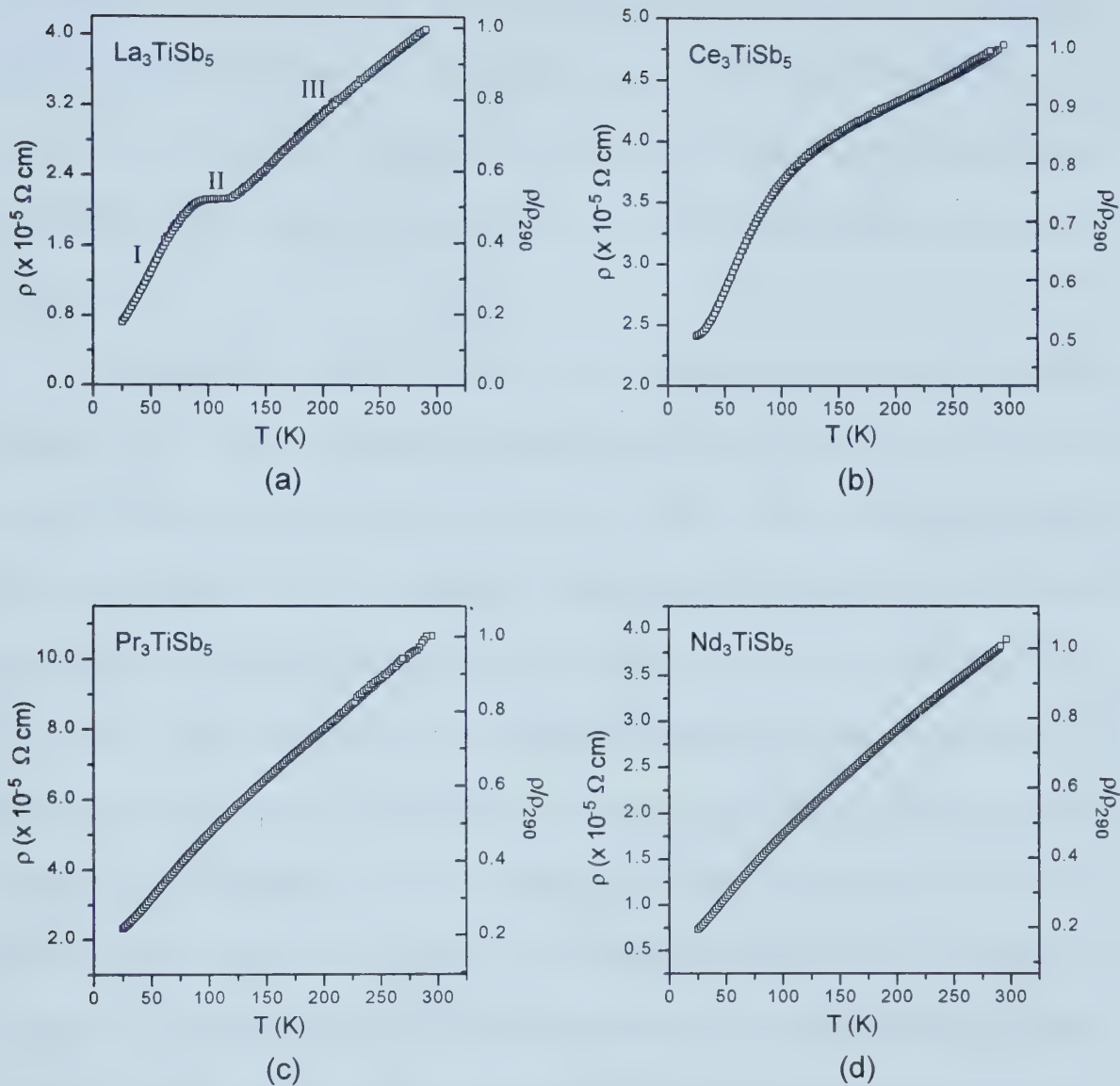


**Figure 5-5.** Plot of the electrical resistivity measured along the needle  $c$  axis for (a)  $\text{La}_3\text{TiSb}_5$ , (b)  $\text{Ce}_3\text{TiSb}_5$ , (c)  $\text{Pr}_3\text{TiSb}_5$ , and (d)  $\text{Nd}_3\text{TiSb}_5$ . The left scale refers to the absolute resistivity and the right scale refers to the resistivity relative to the value at 290 K.



compounds respectively. If the residual resistivity that arises from impurity scattering is approximated by the value at low temperature ( $\rho_{25} \approx 2.1 \times 10^{-5}$  and  $0.7 \times 10^{-7} \Omega \text{ cm}$ ), the resistivity ratios  $\rho_{290}/\rho_{25} \approx 5$  are obtained for both. However, the actual ratio may be significantly larger because the resistivity data at low temperature have not reached a plateau.

The resistivity data for  $\text{Ce}_3\text{TiSb}_5$  show a non-linear temperature dependence (Figure 5-5(b)). There are at least two thermal regimes, one between 25 and  $\sim 60$  K where the  $\rho$  vs.  $T$  curve is concave, and the second up to  $\sim 290$  K where the curve is convex and the increase in resistivity with temperature is more gradual. Shown in Figure 5-6 are the resistivity data below 60 K fit to a power law of the type  $\rho = \rho_0 + \alpha T^2$ , where  $\alpha = 2 \times 10^{-9} \Omega \text{ cm K}^{-2}$ , similar to that observed for itinerant electron ferromagnetic materials.<sup>51-53</sup> However, the origin of this  $T^2$  dependence of the resistivity data for  $\text{Ce}_3\text{TiSb}_5$  is currently unknown. More extensive physical property characterization needs to be performed, including both magnetic susceptibility and specific heat measurements, to determine the nature of the electronic transition. At low temperature ( $< 30$  K), the data begin to reach a plateau, indicating a residual resistivity value of  $\rho_{25} \approx 2.4 \times 10^{-5} \Omega \text{ cm}$ , and  $\rho_{290}/\rho_{25} \approx 2$ .

The data for  $\text{La}_3\text{TiSb}_5$  show the most interesting behavior, with two electronic phase transitions at  $\sim 85$  and  $120$  K from metallic (I) to poorly metallic (II) to metallic (III) states (Figure 5-5(a)). There is essentially a linear temperature dependence in both regions I and III, although the temperature coefficient for I ( $\sim 2 \times 10^{-7} \Omega \text{ cm K}^{-1}$ ) is larger than III ( $\sim 1 \times 10^{-7} \Omega \text{ cm K}^{-1}$ ). These transitions are reminiscent of the behavior observed for the niobium and tantalum trichalcogenides. The structures adopted by these



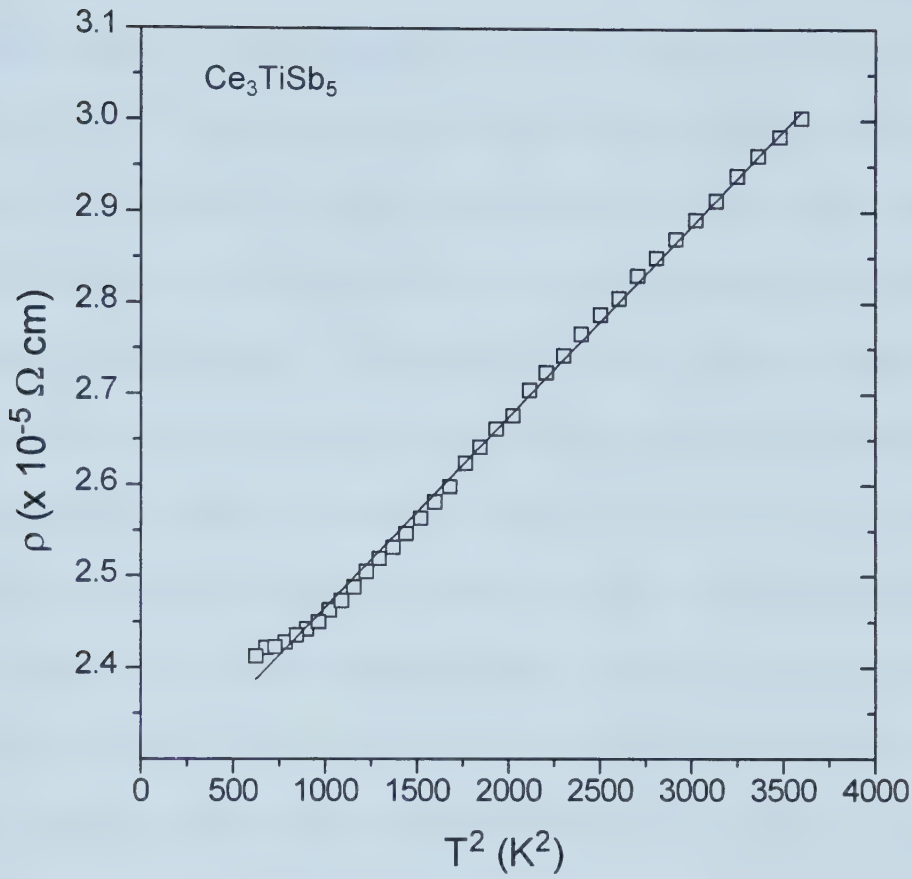


**Figure 5-6.** Plot showing the fit of the low-temperature ( $T < 60 \text{ K}$ ) resistivity data of  $\text{Ce}_3\text{TiSb}_5$  to  $\rho = \rho_0 + \alpha T^2$ , where  $\alpha = 2 \times 10^{-9} \Omega \text{ cm K}^{-2}$ .





compounds consist of one-dimensional columns of face-sharing *M*-centered trigonal prisms, which undergo distortions at low temperature.<sup>1</sup> In particular, NbSe<sub>3</sub> undergoes two metal-to-insulator-to-metal transitions that have been shown to originate from the formation of CDWs.<sup>1</sup> For NbSe<sub>3</sub>, nonohmic behavior was observed below the transition temperatures by performing the resistivity measurements at various applied currents, and evidence for superstructure formation at the transition temperatures was obtained by electron and X-ray diffraction.<sup>1</sup> For La<sub>3</sub>TiSb<sub>5</sub>, however, nonohmic behavior was not observed, suggesting that these transitions are not likely due to the formation of CDWs. The possibility of a structural transition occurring at 120 K was investigated through a variable temperature single crystal X-ray diffraction study. This study showed that there was no evidence of any structural change at 103 K. Moreover, the refined structure did not show any anomalies such as elongated anisotropic displacement parameters. Perhaps extensive magnetic and neutron diffraction studies could help elucidate the origin of these electronic phase transitions.

**Band Structure.** Extended Hückel band structure calculations on La<sub>3</sub>TiSb<sub>5</sub> were carried out to confirm the metallic conductivity and the extent of Ti–Ti and Sb–Sb bonding. Removal of the La cations leaves non-interacting anionic chains of composition [TiSb<sub>3</sub>]<sup>5–</sup> and [Sb<sub>2</sub>]<sup>4–</sup> and thus the total anionic framework can simply be considered as the superposition of the two independent chains. Analysis of the anionic substructure [TiSb<sub>5</sub>]<sup>9–</sup> yields results similar to the full structure including the La cations and the latter is reported for completeness. Shown in Figure 5-7 is the density of states (DOS) curve and the individual atomic contributions. The Fermi level ( $\epsilon_f = -10.4$  eV) crosses a large



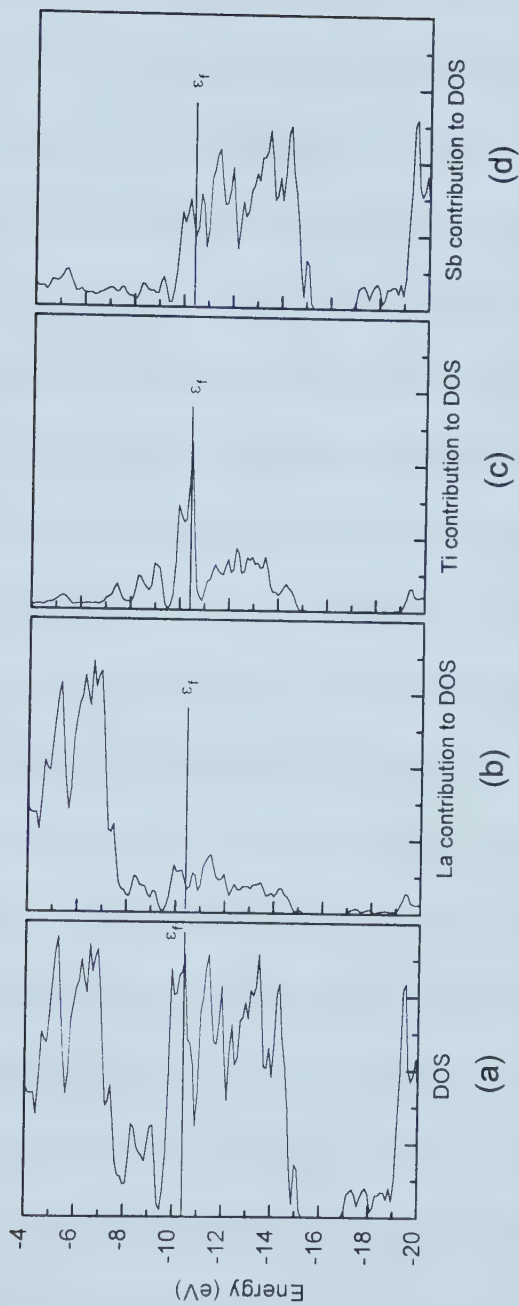


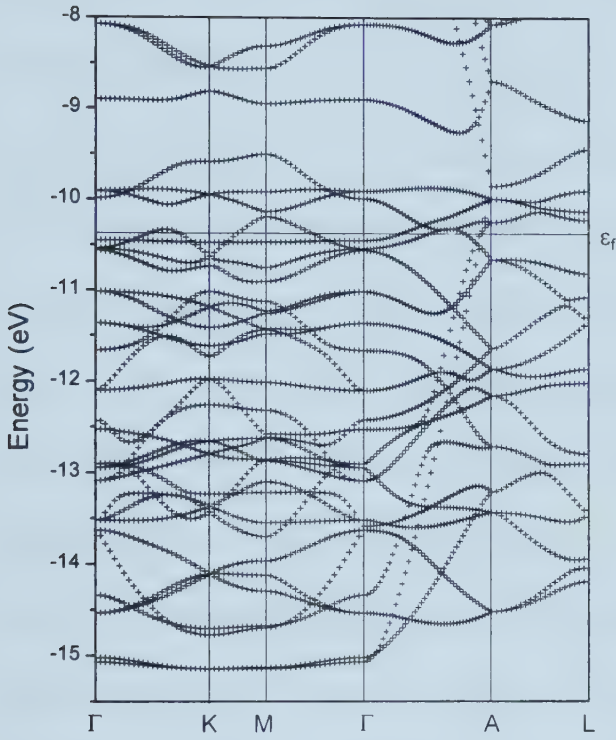
**Figure 5-7.** (a) Total density of states for  $\text{La}_3\text{TiSb}_5$ . The individual atomic contributions (La, Ti, and Sb) to the density of states are shown in (b) – (d). The Fermi level ( $\epsilon_f = -10.4$  eV) is shown.



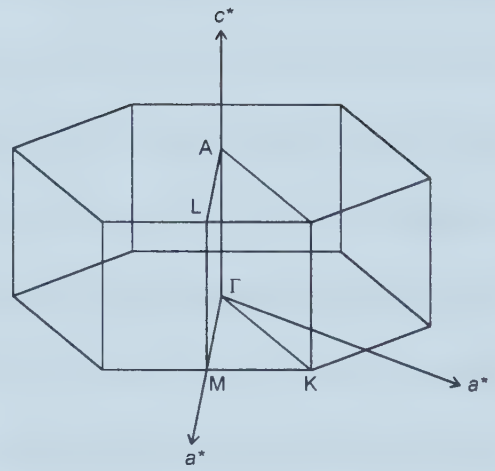
peak in the DOS curve, consistent with the metallic behavior observed. Even though most of the La states are located above  $-8$  eV, there are a considerable number filled below the Fermi level, suggesting some covalency in the La–Sb bonds. Most striking is that the Fermi level falls exactly at the maximum in the Ti contribution to the DOS, corresponding to a substantial filling of Ti d-states.

The band dispersion plot for  $\text{La}_3\text{TiSb}_5$  along the special symmetry lines  $\Gamma\text{K}$ ,  $\text{KM}$ ,  $\text{M}\Gamma$ ,  $\Gamma\text{A}$ , and  $\text{AL}$  is shown in Figure 5-8(a). Figure 5-8(b) shows the Brillouin zone for a hexagonal unit cell, with the special  $k$  points indicated. Six bands are crossed by the Fermi level along  $\Gamma\text{A}$ , which corresponds to the crystal  $c$  axis, while along  $\Gamma\text{K}$ ,  $\Gamma\text{M}$ , and  $\text{KM}$  (directions perpendicular to the  $c$  axis) there is only one band crossed for each. The most disperse band ranges from approximately  $-15$  to  $-10$  eV and is composed of  $\text{Sb}(2)$   $5p_z$  orbitals from the linear Sb chain. A second band ranging from  $-12.5$  to  $-10.5$  eV is composed of  $\text{Sb}(2)$   $5p_z$  orbitals and Ti  $4p_z$  and  $\text{Sb}(1)$   $5p_x$  and  $5p_y$  orbitals. There are also two bands consisting entirely of Ti 3d orbitals that are crossed along  $\Gamma\text{A}$  with a band width of  $\sim 0.5$  eV. These bands show no dispersion along any other direction which is expected since the nearest Ti–Ti interaction between the chains is  $>9$  Å. The last two bands that are crossed along  $\Gamma\text{A}$  are rather narrow and also cross along  $\Gamma\text{K}$ ,  $\Gamma\text{M}$ , and  $\text{KM}$ . These bands consist of orbital contributions from La,  $\text{Sb}(1)$ , and  $\text{Sb}(2)$  and is indicative of some degree of covalency in the La–Sb bonding, which is not surprising given that fully charged La cations would be highly polarizing. Thus,  $\text{La}_3\text{TiSb}_5$  can be viewed as an anisotropic metal with the conductivity along the needle  $c$  axis much greater than that





(a)



(b)

**Figure 5-8.** (a) Band dispersion curves for  $\text{La}_3\text{TiSb}_5$  along the special symmetry lines  $\Gamma\text{K}$ ,  $\text{KM}$ ,  $\text{M}\Gamma$ ,  $\Gamma\text{A}$ , and  $\text{AL}$ . The Fermi level ( $\epsilon_f = -10.4$  eV) is shown. (b) A representation of the hexagonal Brillouin zone with the irreducible wedge outlined.





perpendicular to it, and the bulk of the electrical conductivity is carried by the linear chains of Sb(2) atoms and the chains of face-sharing  $\text{TiSb}_6$  octahedra.

Plotted in Figure 5-9 are the crystal orbital overlap population (COOP) curves, which provide a qualitative analysis of the degree of bonding in  $\text{La}_3\text{TiSb}_5$ . The Fermi level falls at a position that maximizes the Ti-Sb bonding (Figure 5-9(a)), resulting in an overlap population of 0.50. Clearly, these are the primary covalent interactions that hold the structure together. However, there are weaker Ti-Ti and Sb-Sb bonding interactions that also play an important role. Shown in Figures 5-9(b) and (c) are the COOP curves for the 3.14 Å Ti-Ti and Sb-Sb interactions. The position of the Fermi level corresponds to a complete filling of the bonding states and a partial filling of the antibonding states for both interactions. The overlap population for the Sb-Sb bond (0.27) is roughly half of that expected for a full single bond ( $\sim 0.6$ ) and consistent with a half bond. Even for the long Ti-Ti interaction there is a small but positive overlap population (0.07), indicating that weak bonding is present. The La-Sb bonds have an average overlap population (0.19) consistent with some covalent character. The atomic charges calculated result in the overall oxidation state formulation of  $(\text{La}^{1.36+})_3(\text{Ti}^{2.59-})(\text{Sb}(1)^{0.28-})_3(\text{Sb}(2)^{0.32-})_2$ . The greatest discrepancy between the predicted charges from the Zintl concept and those calculated is for Ti (+4 versus  $-2.59$ ). This arises from the high degree of covalency in the Ti-Sb bonds, resulting in an increase in electron density on the Ti atoms and concurrent decrease in electron density of the Sb(1) atoms. In particular, the Ti *d*-bands are slightly more than half-filled ( $\sim 5.4 e$ ), and this may be one source of the electronic transitions observed in both  $\text{La}_3\text{TiSb}_5$  and  $\text{Ce}_3\text{TiSb}_5$ .



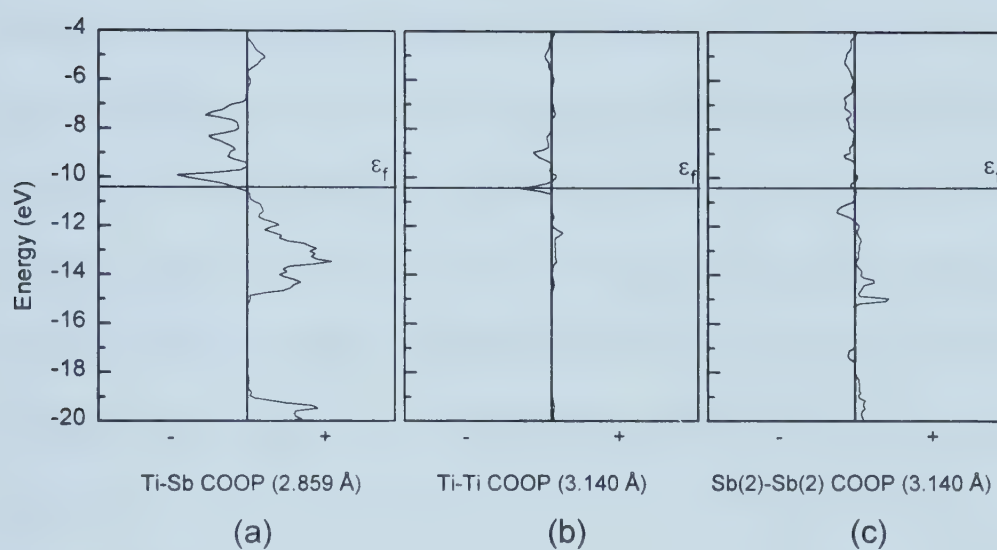


**Figure 5-9.** Crystal orbital overlap population curves for the (a) Ti–Sb, (b) Ti–Ti, and (c) Sb(2)–Sb(2) interactions in  $\text{La}_3\text{TiSb}_5$ . The Fermi level ( $\epsilon_f = -10.4$  eV) is shown.



In conclusion, the key feature in  $RE_3MSb_5$  is the flexibility that is conferred by introducing the electropositive rare-earth atoms, allowing the ionic and covalent components of the bonding to be clearly separated. The significance of the  $RE_3MSb_5$  series rests on its particular suitability as a model system for probing some important properties of low-dimensional systems, since the steric effects ( $RE$  substitution) can be separated from largely electronic effects ( $M$  substitution). These compounds likely exhibit interesting magnetic properties that reflect the low dimensional nature of the isolated  ${}^1_{\infty}[MSb_{6/2}]$  columns and the arrangement of  $RE$  atoms between them. It would be interesting to further pursue the physical property characterization of the complete  $RE_3MSb_5$  series to elucidate the origin of the electronic phase transitions observed in  $La_3TiSb_5$ , to study the degree of  $M-M$  interactions upon substitution of  $Ti$  with the 4d and 5d transition metals, and to determine the influence of the magnetic rare-earth ions on the properties.



## REFERENCES

- (1) *Theoretical Aspects of Band Structures and Electronic Properties of Pseudo-One-Dimensional Solids*; Kamimura, H., Ed.; Physics and Chemistry of Materials with Low-Dimensional Structures, Series B; D. Reidel: Dordrecht, The Netherlands, 1985.
- (2) Kagoshima, S., Nagasawa, H., Sambonji, T. *One-Dimensional Conductors*; Springer-Verlag: Berlin, Germany, 1988.
- (3) Mulder, F. M.; Thiel, R. C.; Buschow, K. H. J. *J. Alloys Compd.* **1994**, 210, 335.
- (4) Sologub, O.; Noël, H.; Leithe-Jasper, A.; Rogl, P.; Bodak, O. I. *J. Solid State Chem.* **1995**, 115, 441.
- (5) Sologub, O.; Hiebl, K.; Rogl, P.; Noël, H.; Bodak, O. *J. Alloys Compd.* **1994**, 210, 153.
- (6) Cordier, G.; Schäfer, H.; Woll, P. *Z. Naturforsch. B* **1985**, 40, 1097.
- (7) Brylak, M.; Möller, M. H.; Jeitschko, W. *J. Solid State Chem.* **1995**, 115, 305.
- (8) Leithe-Jasper, A.; Rogl, P. *J. Alloys Compd.* **1994**, 203, 133.
- (9) Hofmann, W. K.; Jeitschko, W. *J. Less-Common Met.* **1988**, 138, 313.
- (10) Hofmann, W. K.; Jeitschko, W. *Monatsh. Chem.* **1985**, 116, 569.
- (11) Rühl, R.; Jeitschko, W. *Mater. Res. Bull.* **1979**, 14, 513.
- (12) Pecharskii, V. K.; Pankevich, Yu. V.; Bodak, O. I. *Dopov. Akad. Nauk Ukr. RSR, Ser. B* **1982**, 44.
- (13) Braun, D. J.; Jeitschko, W. *J. Less-Common Met.* **1980**, 72, 147.





- (14) Evers, C. B. H.; Jeitschko, W.; Boonk, L.; Braun, D. J.; Ebel, T.; Scholz, U. D. *J. Alloys Compd.* **1995**, 224, 184.
- (15) Dwight, A. E. *Acta Crystallogr. B* **1968**, 24, 456.
- (16) Kasaya, M.; Katoh, K.; Takegahara, K. *Solid State Commun.* **1991**, 78, 797.
- (17) Skolozdra, R. V.; Salamakha, P. S.; Ganzyuk, A. L.; Bodak, O. I. *Neorg. Mater.* **1993**, 29, 25.
- (18) Brylak, M.; Jeitschko, W. *Z. Naturforsch. B* **1995**, 50, 899.
- (19) Malik, S. K.; Adroja, D. T. *J. Magn. Magn. Mater.* **1991**, 102, 42.
- (20) Houshair, M.; Adroja, D. T.; Rainford, B. D. *J. Magn. Magn. Mater.* **1995**, 140-144, 1231.
- (21) Muro, Y.; Takeda, N.; Ishikawa, M. *J. Alloys Compd.* **1997**, 257, 23.
- (22) Sales, B. C.; Mandrus, D.; Williams, R. K. *Science* **1996**, 272, 1325.
- (23) Chan, J. Y.; Kauzlarich, S. M.; Klavins, P.; Shelton, R. N.; Webb, D. J. *Chem. Mater.* **1997**, 9, 3132.
- (24) POLSQ: Program for least-squares unit cell refinement. Modified by D. Cahen and D. Keszler, Northwestern University, 1983.
- (25) Yvon, K.; Jeitschko, W.; Parthé, E. *J. Appl. Crystallogr.* **1977**, 10, 73.
- (26) Sheldrick, G. M. *SHELXTL* Version 5.0; Siemens Analytical X-ray Instruments, Inc.: Madison, WI, 1994.
- (27) Sheldrick, G. M. *J. Appl. Crystallogr.* in press.
- (28) *International Tables for X-ray Crystallography*; Wilson, A. J. C., Ed.; Kluwer: Dordrecht, The Netherlands, 1992, Vol. C.



- (29) Gelato, L. M.; Parthé, E. *J. Appl. Crystallogr.* **1987**, 20, 139.
- (30) Whangbo, M.-H.; Hoffmann, R. *J. Am. Chem. Soc.* **1978**, 100, 6093.
- (31) Hoffmann, R. *Solids and Surfaces: A Chemist's View of Bonding in Extended Structures*; VCH Publishers: New York, 1988.
- (32) Lulei, M.; Martin, J. D.; Hoistad, L. M.; Corbett, J. D. *J. Am. Chem. Soc.* **1997**, 119, 513.
- (33) Canadell, E.; Jobic, S.; Brec, R.; Rouxel, J. *J. Solid State Chem.* **1992**, 99, 189.
- (34) Hughbanks, T.; Hoffmann, R.; Whangbo, M.-H.; Stewart, K. R.; Eisenstein, O.; Canadell, E. *J. Am. Chem. Soc.* **1982**, 104, 3876.
- (35) Havinga, E. E.; Damsma, H.; Hokkeling, P. *J. Less-Common Met.* **1972**, 27, 169.
- (36) Kjekshus, A. *Acta Chem. Scand.* **1972**, 26, 1633.
- (37) Garcia, E.; Corbett, J. D. *J. Solid State Chem.* **1988**, 73, 452.
- (38) Shannon, R. D. *Acta Crystallogr. Sect. A: Cryst. Phys., Diff., Theor. Gen. Crystallogr.* **1976**, 32, 751.
- (39) Brylak, M.; Jeitschko, W. *Z. Naturforsch. B* **1994**, 49, 747.
- (40) Sologub, O.; Vybornov, M.; Rogl, P.; Hiebl, K.; Cordier, G.; Woll, P. *J. Solid State Chem.* **1996**, 122, 266.
- (41) Rieger, W.; Nowotny, H.; Benesovsky, F. *Monatsh. Chem.* **1965**, 96, 98.
- (42) Pötzschke, M.; Schubert, K. *Z. Metallkunde* **1962**, 53, 474.
- (43) Garcia, E.; Corbett, J. D. *Inorg. Chem.* **1988**, 27, 2353.
- (44) Aronsson, B. *Acta Chem. Scand.* **1960**, 14, 1414.
- (45) Emsley, J. *The Elements*; Clarendon Press: Oxford, 1989.



- (46) Parthé, E. *Elements of Inorganic Structural Chemistry*; K. Sutter Parthé: Petit-Lancy, Switzerland, 1990.
- (47) Nesper, R. *Angew. Chem., Int. Ed. Engl.* **1991**, 30, 789.
- (48) Pauling, L. *The Nature of the Chemical Bond*, 3rd Ed.; Cornell University Press: Ithaca, NY, 1960.
- (49) Greenwood, N. N.; Earnshaw, A. *Chemistry of the Elements*; Pergamon Press: Oxford, U.K., 1994.
- (50) Lachgar, A.; Dudis, D. S.; Corbett, J. D. *Inorg. Chem.* **1990**, 29, 2242.
- (51) Bouchard, R. J.; Gillson, J. L. *Mater. Res. Bull.* **1972**, 7, 873.
- (52) Allen, P.B.; Berger, H.; Chauvet, O.; Forro, L.; Jarlborg, T.; Junod, A.; Ravez, B.; Santi, G. *Phys. Rev. B: Condens. Matter* **1996**, 53, 4393 (and references therein).
- (53) Greedan, J. E.; Sato, M.; Ali, N.; Datars, W. R. *J. Solid State Chem.* **1987**, 68, 300.



## Chapter 6

### Magnetism and Neutron Diffraction Studies of New Itinerant Electron Ferromagnetic Materials $REMSb_3$ ( $RE = La, Ce, Pr, Nd, Sm, Gd, Tb, Dy$ ; $M = V, Cr$ )<sup>†</sup>

#### Introduction

Recently, Brylak and Jeitschko reported the preparation of a new series of rare-earth transition-metal antimonides  $REMSb_3$  ( $RE = La, Ce, Pr, Nd, Sm$ ;  $M = V, Cr$ ) and determined the crystal structures of  $CeVSb_3$  and  $CeCrSb_3$ .<sup>1</sup> We have determined the crystal structure of  $LaCrSb_3$  and further examined the extent of rare-earth substitution in both the  $REVSb_3$  and  $RECrSb_3$  series. Jeitschko and coworkers have also reported preliminary magnetism studies which indicated that while magnetic ordering of the rare-earth moments at low temperature occurs in  $REVSb_3$ , both the chromium and rare-earth moments order in  $RECrSb_3$ .<sup>2</sup> In particular, the  $RECrSb_3$  compounds for  $RE = Ce, Pr$ , and  $Nd$  exhibit both ferromagnetic ordering of the  $Cr$  moments and antiferromagnetic ordering of the rare-earth sublattice.<sup>2</sup> We have further investigated the electronic properties of  $LaCrSb_3$  and  $NdCrSb_3$ , and discovered they are far more interesting than originally thought.

---

<sup>†</sup> Portions of this chapter have been published. Ferguson, M. J.; Hushagen, R. W.; Mar, A. *J. Alloys Compd.* **1997**, *249*, 191. Reproduced in part with permission from Raju, N. P.; Greedan, J. E.; Ferguson, M. J.; Mar, A. *Chem. Mater.* **1998**, *10*, 3630. Copyright 1998 American Chemical Society.





## Experimental Section

**Synthesis.** Starting materials were powders of the rare-earth elements (99.9%, Alfa-Aesar or Cerac), vanadium (99.5%, Cerac), chromium (99.95%, Cerac), and antimony (99.995%, Aldrich or Cerac). Powder samples of the compounds  $RECrSb_3$  ( $RE = La, Ce, Pr, Nd, Sm, Gd, Tb, Dy$ ) and  $REVSb_3$  ( $RE = Gd, Tb, Dy$ ) could be successfully prepared by arc-melting stoichiometric mixtures of the elements in the form of pressed pellets (with a 10% weight excess of Sb added to compensate for partial loss through volatilization) in a Centorr 5TA tri-arc furnace under argon (gettered by melting a Ti pellet). The products were characterized by their powder X-ray diffraction patterns collected on an Enraf-Nonius FR552 Guinier camera ( $CuK_{\alpha 1}$  radiation, Si standard). The cell parameters were refined by least-squares fits with the program POLSQ,<sup>3</sup> and are listed in Table 6-1. The observed powder X-ray diffraction patterns agree well with those calculated based on the crystal structure of  $LaCrSb_3$  with the program LAZY-PULVERIX.<sup>4</sup>

Bulk phase samples of  $LaCrSb_3$  and  $NdCrSb_3$  were prepared by traditional high-temperature reactions for magnetic susceptibility measurements and neutron diffraction. The elements were loaded into fused-silica tubes (5 cm length, 10 mm i.d.) in a 1:1:3 ratio, which were then evacuated, sealed, and heated in a furnace. For  $LaCrSb_3$ , the tubes were heated at 570 °C for 1 day and 1000 °C for 3 days and then cooled to 20 °C over 2–4 days. For  $NdCrSb_3$ , the tubes were heated at 630 °C for 1 day and 900 °C for 4 days and then cooled to 20 °C over 1 day. The products were analyzed by their powder X-ray diffraction patterns, and the ternary compounds were identified as the major phase with



**Table 6-1.** Lattice Parameters for Compounds with  $REMSb_3$  Structure (obtained from arc-melting reactions)

Compound	$a$ (Å)	$b$ (Å)	$c$ (Å)	$V$ (Å <sup>3</sup> )
LaCrSb <sub>3</sub>	13.269(3)	6.202(2)	6.111(2)	502.9(2)
CeCrSb <sub>3</sub>	13.127(3)	6.199(1)	6.092(1)	495.7(2)
PrCrSb <sub>3</sub>	13.043(3)	6.183(1)	6.078(1)	490.2(1)
NdCrSb <sub>3</sub>	12.974(2)	6.175(1)	6.061(1)	485.6(1)
SmCrSb <sub>3</sub>	12.847(2)	6.164(1)	6.038(1)	478.1(1)
GdCrSb <sub>3</sub>	12.760(4)	6.153(2)	6.014(2)	472.2(2)
TbCrSb <sub>3</sub>	12.680(2)	6.143(1)	6.003(1)	467.6(1)
DyCrSb <sub>3</sub>	12.609(5)	6.135(2)	5.978(2)	462.4(2)
GdVSb <sub>3</sub>	12.794(3)	6.212(1)	5.959(1)	473.6(1)
TbVSb <sub>3</sub>	12.728(4)	6.213(2)	5.951(2)	470.6(2)
DyVSb <sub>3</sub>	12.690(3)	6.219(1)	5.946(1)	469.2(1)



only minor amounts (<10%) of Sb impurity in the La reactions and even lesser amounts (<5%) of NdSb<sub>2</sub> in the Nd reaction.

The single crystal of LaCrSb<sub>3</sub> used for the structure determination was obtained from a reaction of the elements in a 1:2:3 ratio, with a similar temperature program. The shiny flat needle-shaped crystals were easily extracted from the regulus. The single crystals used for the resistivity measurements were obtained from a stoichiometric reaction involving a slow cooling from 1000 °C to 20 °C over 8 days. Elemental compositions of selected crystals were verified by EDX (energy dispersive X-ray) analyses on either a JEOL JSM-6301FXV field emission or a Hitachi F2700 scanning electron microscope, which revealed the presence of all three elements in a ratio consistent with the formula.

**Structure Determination.** Initial cell parameters for LaCrSb<sub>3</sub> were determined from Weissenberg photographs which revealed Laue symmetry *mmm* and systematic absences consistent with the orthorhombic space groups *Pbcm* and *Pbc2<sub>1</sub>*. Final cell parameters were obtained from least-squares analysis of 34 centered reflections in the range  $30^\circ \leq 2\theta(\text{CuK}_\alpha) \leq 108^\circ$  on a Siemens P4RA diffractometer. X-ray diffraction data were collected at 22 °C with the  $\omega$  scan technique in the range  $6^\circ \leq 2\theta(\text{CuK}_\alpha) \leq 113^\circ$ . Crystal data and further details of the data collection are given in Table 6-2.

All calculations were carried out using the SHELXTL (Version 5.0) software package.<sup>5,6</sup> Conventional atomic scattering factors and anomalous dispersion corrections were used.<sup>7</sup> Intensity data were processed and Gaussian face-indexed absorption corrections were applied with the program XPREP. Based on satisfactory averaging and



**Table 6-2.** X-ray Crystallographic Data for LaCrSb<sub>3</sub>

Formula	LaCrSb <sub>3</sub>
Formula mass (amu)	556.16
Space group	$D_{2h}^{11} - Pbcm$
$a$ (Å)	13.2835(7) <sup>a</sup>
$b$ (Å)	6.2127(2) <sup>a</sup>
$c$ (Å)	6.116(1) <sup>a</sup>
$V$ (Å <sup>3</sup> )	504.8(1)
$Z$	4
$T$ (°C)	22
Diffractometer	Siemens P4RA
$\rho_{\text{calc}}$ (g cm <sup>-3</sup> )	7.319
Crystal dimensions	Black needle, $0.235 \times 0.040 \times 0.008$ mm <sup>3</sup>
Radiation	Graphite monochromated CuK <sub><math>\alpha</math></sub> , $\lambda = 1.54178$ Å
$\mu$ (cm <sup>-1</sup> )	2053
Transmission factors <sup>b</sup>	0.041 – 0.500
Scan-type	$\omega$
2 $\theta$ limits	$6^\circ \leq 2\theta(\text{CuK}_\alpha) \leq 113^\circ$
Data collected	$-14 \leq h \leq 14, -6 \leq k \leq 6, -6 \leq l \leq 6$
No. of data collected	2163
No. of unique data, including $F_o^2 < 0$	351 ( $R_{\text{int}} = 0.053$ )
No. of unique data, with $F_o^2 > 2\sigma(F_o^2)$	322
No. of variables	30





**Table 6-2.** X-ray Crystallographic Data for LaCrSb<sub>3</sub> (cont'd)

Extinction coefficient <sup>c</sup>	0.00049(10)
$R(F)$ for $F_o^2 > 2\sigma(F_o^2)$ <sup>d</sup>	0.047
$R_w(F_o^2)$ <sup>e</sup>	0.131
Goodness of fit <sup>f</sup>	1.12

<sup>a</sup> Obtained from a refinement constrained so that  $\alpha = \beta = \gamma = 90^\circ$ .

<sup>b</sup> A Gaussian face-indexed absorption correction was applied with the use of the programs in the SHELXTL package (Sheldrick, G. M. *SHELXTL* Version 5.0; Siemens Analytical X-ray Instruments, Inc.: Madison, WI, 1994).

<sup>c</sup> An extinction parameter  $x$  was refined, where  $F_c$  is multiplied by:  $k[1 + 0.001 * x * F_c^2 * \lambda^3 / \sin(2\theta)]^{-1/4}$ .

$$^d R(F) = \sum \|F_o\| - \|F_c\| / \sum \|F_o\|.$$

$$^e R_w(F_o^2) = [\sum [w(F_o^2 - F_c^2)^2] / \sum wF_o^4]^{1/2}; w^{-1} = [\sigma^2(F_o^2) + (0.0812P)^2 + 36.60P]$$

where  $P = [\max(F_o^2, 0) + 2F_c^2] / 3$ .

<sup>f</sup>  $GooF = S = [\sum [w(F_o^2 - F_c^2)^2] / (n - p)]^{1/2}$  where  $n$  is the number of reflections and  $p$  is the total number of parameters refined.



the successful structure solution, the centrosymmetric space group *Pbcm* was chosen. The positions of all atoms were found by direct methods and the structure was refined by least-squares methods. Refinements in which the occupancies of successive atoms were allowed to vary (while the isotropic displacement parameters were fixed) resulted in values of 100(1)% for La, 95(2)% for Cr, 100(1)% for Sb(1), 100(1)% for Sb(2), and 102(1)% for Sb(3). Although  $\text{CeCrSb}_3$  has been suggested to be slightly substoichiometric in Cr ( $\text{CeCr}_{0.901(9)}\text{Sb}_{2.909(4)}$ ),<sup>1</sup> we feel that this conclusion is tenuous at best, since refinements of occupancies are highly dependent on the reliability of the absorption corrections made. However, it is possible that as the rare-earth atom decreases in size, the Cr content also decreases. Given that the displacement parameters for  $\text{LaCrSb}_3$  are unexceptional we accept the ideal stoichiometry. The atomic positions were standardized with the program STRUCTURE TIDY.<sup>8</sup> The final cycle of least-squares refinements on  $F_o^2$  of 30 variables and 351 averaged reflections (including those having  $F_o^2 < 0$ ) converged to values of  $R_w(F_o^2)$  of 0.131 and  $R(F)$  of 0.047. The difference electron density map is featureless ( $\Delta\rho_{\text{max}} = 7.29$ ,  $\Delta\rho_{\text{min}} = -4.58 \text{ e } \text{\AA}^{-3}$ ). Final values of the positional and equivalent displacement parameters are given in Table 6-3 and the anisotropic displacement parameters are given in the Appendix (Table A-12).

**Electrical Resistivity.** The same crystals that were analyzed on the scanning electron microscope were used for the resistivity measurements. Four Au wires with graphite extensions were attached with Ag paint to crystals with lengths between 0.7 and 1.0 mm for the four-probe ac resistivity technique at 15.9 Hz. Data were collected on cooling and warming between 25 and 275 K.



**Table 6-3.** Atomic Coordinates and Equivalent Isotropic Displacement Parameters ( $\text{\AA}^2$ ) for  $\text{LaCrSb}_3$  from the X-ray Structure Determination

atom	Wyckoff position, site symmetry		$x$	$y$	$z$	$U_{\text{eq}}^a$
La	$4d$	$\dots m$	0.3084(1)	0.0024(2)	$\frac{1}{4}$	0.0039(7)
Cr	$4c$	$2\dots$	0.9095(4)	$\frac{1}{4}$	0	0.0104(12)
Sb(1)	$4d$	$\dots m$	0.0628(1)	0.1064(3)	$\frac{1}{4}$	0.0094(8)
Sb(2)	$4d$	$\dots m$	0.2159(2)	0.4989(2)	$\frac{1}{4}$	0.0063(7)
Sb(3)	$4c$	$2\dots$	0.5011(1)	$\frac{1}{4}$	0	0.0053(7)

<sup>a</sup>  $U_{\text{eq}}$  is defined as one-third of the trace of the orthogonalized  $U_{ij}$  tensor.

**Table 6-4.** Extended Hückel Parameters

atom	orbital	$H_{ii}$ (eV)	$\zeta_{i1}$	$c_1$	$\zeta_{i2}$	$c_2$
La	6s	-6.5613	2.14			
	6p	-4.3769	2.08			
	5d	-7.5155	3.78	0.77651	1.381	0.45861
Cr	4s	-8.66	1.7			
	4p	-5.24	1.7			
	3d	-11.22	4.95	0.5060	1.80	0.6750
Sb	5s	-18.8	2.323			
	5p	-11.7	1.999			



**Magnetic Susceptibility.** The magnetic data were collected on Quantum Design SQUID magnetometers at McMaster University and the University of British Columbia. Data were collected at various applied fields (0.01 – 5.5 T) and over the temperature range 2 – 700 K.

**Neutron Diffraction.** Neutron diffraction data were collected on the C2 instrument of the DUALSPEC installation at the Chalk River Nuclear Laboratories and the Neutron Program for Materials of the National Research Council of Canada. The neutron wavelength was 2.3692 and 2.3735 Å for the LaCrSb<sub>3</sub> and NdCrSb<sub>3</sub> data collections, respectively. The polycrystalline sample was contained in a vanadium can sealed under helium exchange gas with an indium gasket and attached to the cold stage of a liquid helium cryostat. Temperature control was to within  $\pm 0.1$  K. Analysis of the neutron diffraction data was carried out using either DBWS PC96005 or FULLPROF Version 3.5.<sup>9,10</sup>

**Band Structure.** One-electron band structure calculations on the room-temperature structure of LaCrSb<sub>3</sub> were performed by the tight-binding method with an extended Hückel-type Hamiltonian using the EHMACC suite of programs.<sup>11,12</sup> The atomic parameters used are listed in Table 6-4.<sup>13-15</sup> Properties were extracted from the band structure using 50 *k* points in the irreducible portion of the Brillouin zone.

## Results and Discussion

**Description of the Structure.** Selected interatomic distances are listed in Table 6-5. A view of the structure with its labeling scheme is given in Figure 6-1. LaCrSb<sub>3</sub> is





**Table 6-5.** Selected Interatomic Distances (Å) and Angles (°) for LaCrSb<sub>3</sub>

La–Sb(2)	3.296(1) (2×)	Cr–Sb(1)	2.698(4) (2×)
La–Sb(2)	3.321(2)	Cr–Sb(1)	2.716(1) (2×)
La–Sb(1)	3.325(3)	Cr–Sb(2)	2.747(3) (2×)
La–Sb(3)	3.347(2) (2×)	Cr–Cr	3.0581(5) (2×)
La–Sb(3)	3.355(2) (2×)	Sb(1)–Sb(2)	3.175(2)
La–Sb(2)	3.361(2)	Sb(3)–Sb(3)	3.0581(5) (2×)
La–Cr	3.630(4) (2×)	Sb(3)–Sb(3)	3.1065(1) (2×)
Sb(2)–La–Sb(2)	136.21(8)	Sb(3)–La–Sb(3)	81.15(4)
Sb(2)–La–Sb(2)	82.20(4)	Sb(3)–La–Sb(2)	80.82(4)
Sb(2)–La–Sb(1)	68.57(4)	Sb(3)–La–Sb(3)	54.23(3)
Sb(2)–La–Sb(3)	134.80(5)	Sb(3)–La–Sb(2)	134.89(4)
Sb(2)–La–Sb(3)	81.78(4)		
Sb(2)–La–Sb(3)	135.12(5)	Sb(1)–Cr–Sb(1)	82.0(1)
Sb(2)–La–Sb(3)	82.11(4)	Sb(1)–Cr–Sb(1)	81.28(9)
Sb(2)–La–Sb(2)	82.03(4)	Sb(1)–Cr–Sb(1)	86.98(9)
Sb(2)–La–Sb(1)	57.08(5)	Sb(1)–Cr–Sb(2)	163.9(1)
Sb(2)–La–Sb(3)	135.65(4)	Sb(1)–Cr–Sb(2)	87.38(5)
Sb(2)–La–Sb(3)	81.74(4)	Sb(1)–Cr–Sb(1)	164.4(2)
Sb(2)–La–Sb(2)	136.83(8)	Sb(1)–Cr–Sb(2)	86.13(6)
Sb(1)–La–Sb(3)	146.39(4)	Sb(1)–Cr–Sb(2)	103.39(7)
Sb(1)–La–Sb(3)	131.25(4)	Sb(2)–Cr–Sb(2)	105.4(2)
Sb(1)–La–Sb(2)	79.75(5)		
Sb(3)–La–Sb(3)	54.36(4)	Sb(3)–Sb(3)–Sb(3)	180.0(1)
Sb(3)–La–Sb(3)	55.23(3)	Sb(3)–Sb(3)–Sb(3)	90



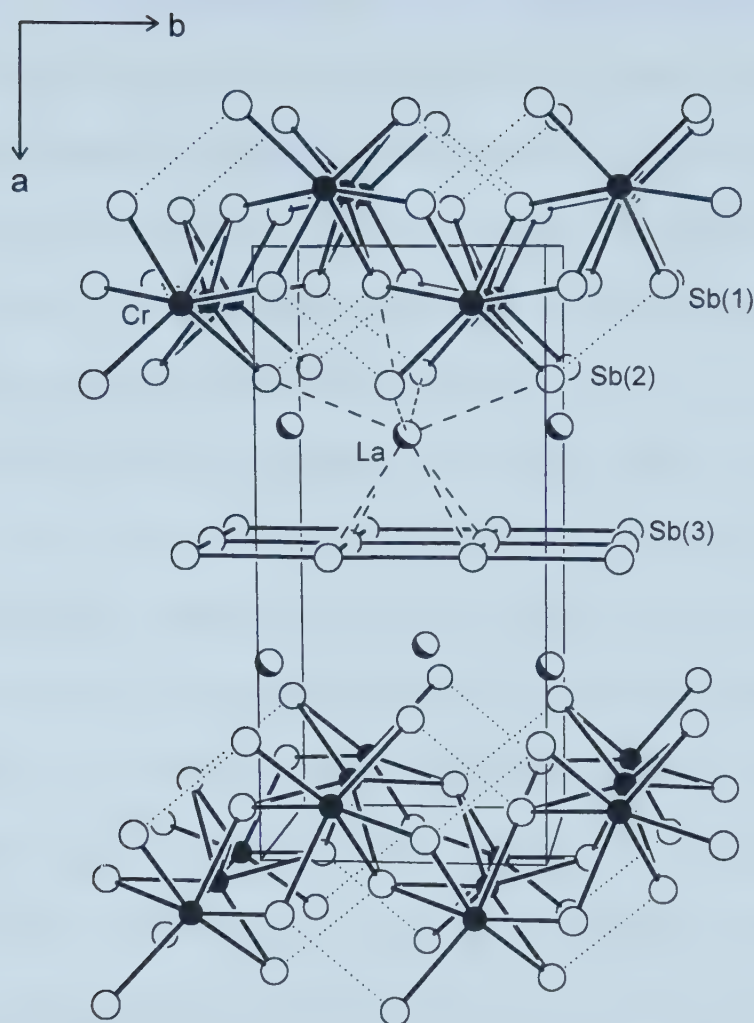


**Figure 6-1.** View down the  $c$  axis of  $\text{LaCrSb}_3$  with the unit cell outlined. The partly shaded circles are La atoms, the solid circles are Cr atoms, and the open circles are Sb atoms. The coordination around one La atoms is depicted by dashed lines. The dotted lines connecting Sb(1) and Sb(2) correspond to distances of 3.175 Å.



isostructural to the recently reported structures of  $\text{CeCrSb}_3$  and  $\text{CeVSb}_3$ .<sup>1</sup> It consists of anionic layers parallel to the (100) plane separated by  $\text{La}^{3+}$  cations. One layer contains octahedra (Cr coordinated by six Sb(1) and Sb(2) atoms) that are face-sharing along the  $c$  direction and edge-sharing along the  $b$  direction, while the other layer is a nearly square sheet of Sb(3) atoms. The La atoms are nine-coordinate, forming a monocapped square antiprism whose capping Sb(1) atom is tilted to one side.

Substitution of La for Ce in  $\text{RECrSb}_3$  results in little change in the Cr–Sb or Sb–Sb distances. The Cr–Sb distances in  $\text{LaCrSb}_3$  (2.698(4)–2.747(3) Å) and  $\text{CeCrSb}_3$  (2.696(1)–2.736(1) Å) are similar, as are the Sb(3)–Sb(3) distances in the square sheet of  $\text{LaCrSb}_3$  (3.0581(5) and 3.1065(1) Å) and  $\text{CeCrSb}_3$  (3.040(1) and 3.092(1) Å).<sup>1</sup> The Sb(1) atom of one Cr octahedron is bent towards the Sb(2) atom of a neighboring edge-sharing octahedron at a distance of 3.175(2) Å, as represented by the dotted lines in Figure 6-1. These Sb–Sb distances are considered to be weakly bonding. The Sb(3)–Sb(3) bond extending along the  $c$  direction is also necessarily identical to the Cr–Cr distance across a shared face of octahedra, 3.0581(5) Å, equal to half the  $c$  parameter. This Cr–Cr distance is somewhat longer than the 2.735 Å distance found in  $\text{CrSb}$ , where metal-metal bonding is thought to be important to stability of this structure.<sup>16</sup> As well, the average Cr–Sb distance in  $\text{LaCrSb}_3$  (2.720(3) Å) is slightly shorter than that in  $\text{CrSb}$  (2.745 Å), in which  $\text{Cr}^{3+}$  appears,<sup>16</sup> but slightly longer than that found in marcasite-type  $\text{CrSb}_2$  (2.708(1) Å), which  $\text{Cr}^{4+}$  appears.<sup>17</sup> An oxidation state formulation can be developed based on the Zintl concept.<sup>18</sup> The Sb(3)–Sb(3) distances are typical of one-electron or half-bond interactions and yield  $\text{Sb(3)}^{1-}$ .<sup>1,19,20</sup> The rather long Sb(1)–Sb(2)



interaction is also considered a one-electron bond, giving  $\text{Sb}(1)^{2.5-}$  and  $\text{Sb}(2)^{2.5-}$ . Thus, the overall formulation is  $(\text{La}^{3+})(\text{Cr}^{3+})(\text{Sb}(1)^{2.5-})(\text{Sb}(2)^{2.5-})(\text{Sb}(3)^{1-})$ .

A more significant difference between  $\text{LaCrSb}_3$  and  $\text{CeCrSb}_3$  lies in the  $RE$ –Sb distances, which decrease (as expected because of lanthanide contraction) from 3.296(1)–3.361(2) Å in  $\text{LaCrSb}_3$  to 3.259(1)–3.334(1) Å in  $\text{CeCrSb}_3$ .<sup>1</sup> The replacement of a smaller rare-earth atom, however, has little effect on the Sb(3)–Sb(3) distances, as mentioned above, and this is reflected in the small change in the  $b$  and  $c$  parameters. Rather, the sole effect of the rare-earth substitution is to contract the structure along  $a$ , bringing the layers closer together (Figure 6-1). This observation provides an explanation of why the  $RE\text{MSb}_3$  ( $M = \text{V}, \text{Cr}$ ) phase may be difficult to prepare for the late rare-earth elements. The  $RE\text{MSb}_3$  series was earlier reported to exist for  $RE = \text{La}, \text{Ce}, \text{Pr}, \text{Nd}, \text{Sm}$ , but has now been extended to include  $RE = \text{Gd}, \text{Tb}, \text{Dy}$ . A plot of the unit cell volume for these compounds is shown in Figure 6-2. The cell volumes from this work are slightly larger than those reported earlier,<sup>1</sup> but this may be due to the different preparative conditions used (arc-melted samples were analyzed in our work) and the possible existence of a narrow homogeneity range. The contraction of the  $RE\text{MSb}_3$  structure with substitution of a smaller  $RE$  is clearly seen in Table 6-1. The relative decrease in  $a$  (5%) is more pronounced than in  $b$  or  $c$  (1–2%) on going from  $\text{LaMSb}_3$  to  $\text{DyMSb}_3$ . In order to maintain the same Sb(3)–Sb(3) distances in the square sheet, a monocapped square antiprism centered by a smaller  $RE$  atom must become flatter along  $a$  (Sb(3)–La–Sb(3) angles must decrease). Since the  $RE$  atoms are also bonded to Sb(1) and Sb(2), this action necessitates a further buckling of the  $M$  octahedral layer, entailing severe bond





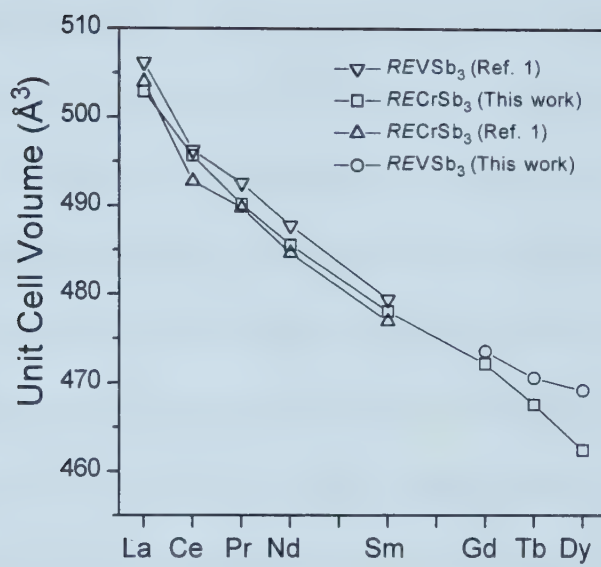


**Figure 6-2.** Plot of the unit cell volume for  $REMSb_3$  compounds, with the legend indicated. The lines are drawn only to guide the eye.



strain. Moreover, electrostatic repulsive forces should be enhanced as the anionic layers come closer together. Application of high pressures may be able to overcome these repulsions and force the  $REMSb_3$  structure to be adopted by  $RE$  atoms that are even smaller.

**Electrical Resistivity.** Single crystals of  $LaCrSb_3$  were available with the  $c$  axis corresponding to the long dimension. The four-probe method measurements thus give a component of the resistivity tensor normal to the stacking axis  $a$ . Results for one crystal with dimensions  $0.05 \times 0.05 \times 0.925$  mm are shown in Figure 6-3(a). Results for other crystals were in good agreement regarding the general shape of the  $\rho$  versus  $T$  curve and differed in magnitude by less than 20% for the same temperature throughout the measured range. The results clearly indicate metallic behavior. Furthermore, two distinct thermal regimes exist, one from about 20 K to 120–125 K in which the  $\rho$  vs.  $T$  curve is concave, and the second to 300 K in which the curvature changes to convex and the increase in  $\rho$  is more gradual, approaching perhaps, a linear temperature dependence. The observed shape is typical for itinerant electron ferromagnetic materials such as  $SrRuO_3$  and the pyrochlores  $RE_2Mo_2O_7$ ,  $RE = Nd, Sm, \text{ and } Gd$ .<sup>21-23</sup> The rapid decrease in the resistivity below the kink at 125 K is attributed to the loss of spin disorder scattering due to the onset of ferromagnetic spin order. The low temperature data were fit to a power law of the type  $\rho = \rho_0 + \alpha T^2$  (Figure 6-3(b)), as has been reported for  $SrRuO_3$  for example, although the exponent in the latter case was reported to be sample dependent. A plot of  $d\rho/dT$  versus  $T$  (Figure 6-3(a) (inset)) shows a maximum at 120–125 K, which strongly suggests an electronic phase transition that is probably magnetic in origin in



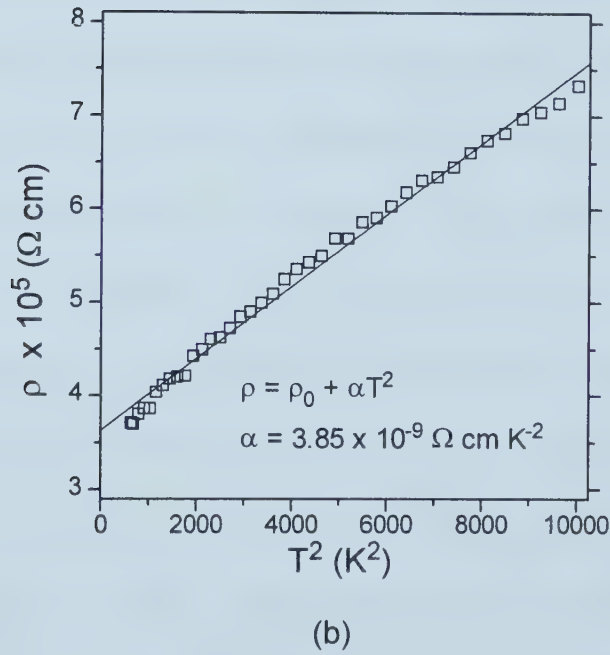
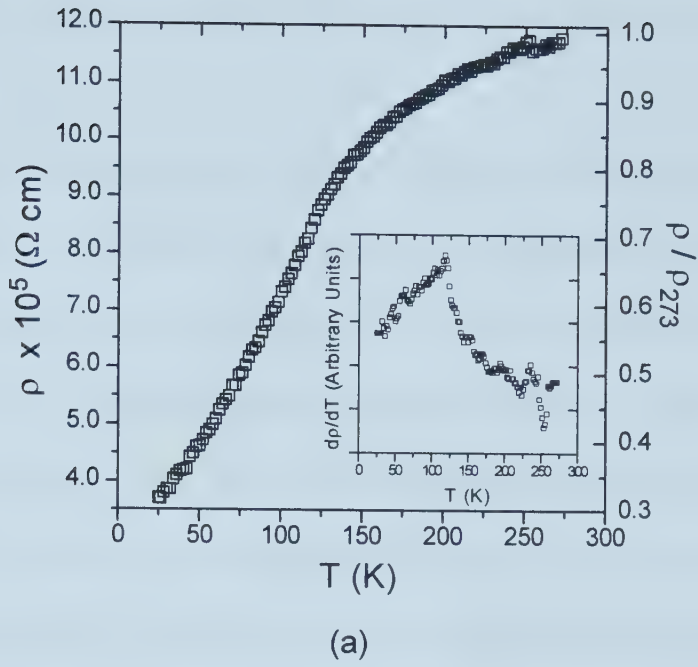


**Figure 6-3.** (a) Plot of the electrical resistivity for  $\text{LaCrSb}_3$  measured along the needle  $c$  axis. The inset shows the temperature dependence of  $dp/dT$ . (b) Fit of the low-temperature data to  $\rho = \rho_0 + \alpha T^2$ .



view of the evidence just presented. Unfortunately, the shape of the available crystals precludes measurements normal to the layers as a significant anisotropy might be expected.

**Magnetic Measurements.** *LaCrSb<sub>3</sub>*: The nature of the phase transition seen in the resistivity data is clarified in Figure 6-4(a) which shows the susceptibility of *LaCrSb<sub>3</sub>* and  $-d(\chi T)/dT$  as a function of temperature. A ferromagnetic-like ordering is indicated below a  $T_c$  of 125 K. Isothermal magnetization data, shown in Figure 6-4(b), disclose a linear field dependence at 300 K, consistent with paramagnetism, and an approach to saturation at 5 K, indicative of ferromagnetism. The apparent saturation moment is about  $0.8 \mu_B$  per Cr atom at 5 T but the weak linear dependence throughout the field regime examined makes this value somewhat uncertain. Above  $T_c$  the inverse susceptibility does not obey the Curie-Weiss law up to 700 K (Figure 6-4(c)). An attempt to fit the data in the region from 300 to 700 K to a modified Curie-Weiss law by inclusion of a temperature independent term,  $\chi = C/(T - \theta_C) + \chi_{TIP}$ , yields the parameters  $C = 0.53 \text{ emu K mol}^{-1}$ ,  $\theta_C = 195 \text{ K}$ , and  $\chi_{TIP} = 5.4 \times 10^{-4} \text{ emu mol}^{-1}$ . The large, positive  $\theta_C$  is consistent with ferromagnetic behavior and the fairly large TIP term with the metallic transport properties. Given the latter, it is unclear how to interpret the value of  $C$ . As mentioned earlier, Cr-Sb bond distance correlations place the Cr oxidation state intermediate between +3 and +4. The expected Curie constants for  $\text{Cr}^{3+} (3d^3)$  and  $\text{Cr}^{4+} (3d^2)$  are respectively, 1.87 and 1.00, and the saturation magnetic moments are 3.0 and  $2.0 \mu_B$ . It is clear that the observed Curie constant is not consistent with any straightforward assignment of a formal oxidation state for Cr in *LaCrSb<sub>3</sub>*. The only





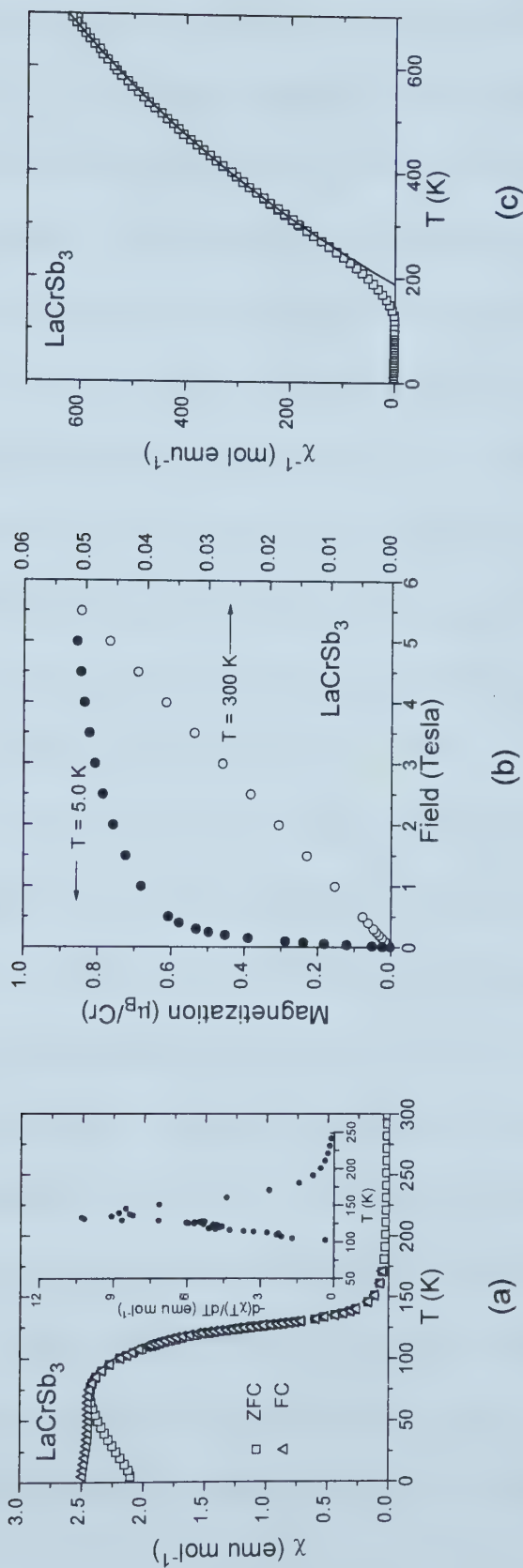


**Figure 6-4.** (a) Plot of the magnetic susceptibility of  $\text{LaCrSb}_3$  as a function of temperature at an applied field of 0.01 T. The inset shows the function  $-d(\chi T)/dT$  versus temperature. (b) Isothermal magnetization of  $\text{LaCrSb}_3$  at 5 and 300 K. (c) Inverse susceptibility for  $\text{LaCrSb}_3$  over the temperature range 25–700 K.



statement that can be made with certainty is that the non-Curie-Weiss susceptibility is consistent with an itinerant electron picture for the Cr *d*-electrons.

*NdCrSb<sub>3</sub>*: The magnetic susceptibility data for NdCrSb<sub>3</sub>, shown in Figure 6-5(a), indicate ferromagnetic ordering with a  $T_c \approx 110$  K, similar to the ordering temperature observed in LaCrSb<sub>3</sub>. A second transition is observed at low temperatures ( $\sim 9$  K), arising from magnetic ordering of the Nd moments. These transitions are more clearly observed in the plot of  $-d(\chi T)/dT$  versus temperature, shown in the inset of Figure 6-5(a). The isothermal magnetization data collected at 4.8 K, shown in Figure 6-5(b), indicate an approach to saturation with a moment of  $3.75 \mu_B$ /formula unit. If we assume that each Cr atom contributes  $0.8 \mu_B$ , the remaining  $2.95 \mu_B$  can be attributed to the Nd<sup>3+</sup> ions, showing reasonable agreement with theory ( $gJ = 3.27 \mu_B$ ).<sup>24</sup> The susceptibility data from 130–300 K were fit to the Curie-Weiss law  $\chi = C/(T - \theta_C)$  and yielded  $\theta_C = 119(1)$  K and  $C = 2.61(2) \text{ emu K mol}^{-1}$ , and the large, positive  $\theta_C$  is consistent with the observed ferromagnetism. However, these values may not be overly reliable given that they were extracted from data within a factor of 2 from the ordering temperature.

**Neutron Diffraction.** *LaCrSb<sub>3</sub>*: The bulk magnetic properties of LaCrSb<sub>3</sub> indicate ferromagnetism. Given the layered nature of the structure, it is not possible to rule out a situation in which, while the intraplanar exchange is strongly ferromagnetic, there exists a weak interplanar antiferromagnetic coupling such that a small applied field could induce a metamagnetic transition giving the appearance of bulk ferromagnetism. The true magnetic structure at zero applied field is best investigated by neutron diffraction. Data obtained at a relatively long wavelength,  $\lambda = 2.3692 \text{ \AA}$ , for temperatures



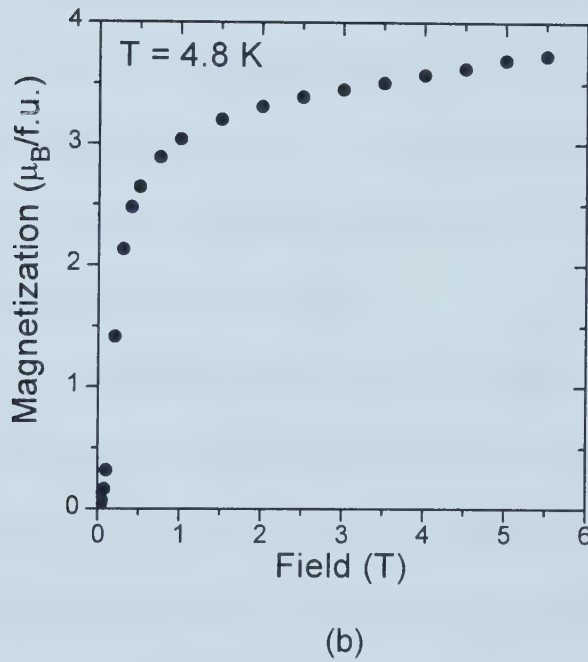
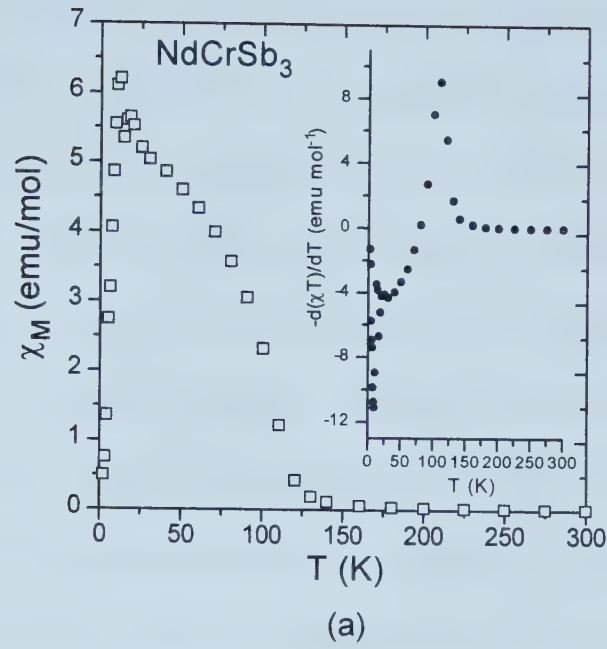


**Figure 6-5.** (a) Plot of the zero field cooled magnetic susceptibility of  $\text{NdCrSb}_3$  as a function of temperature at an applied field of 0.1 T. The inset shows the function  $-d(\chi T)/dT$  versus temperature. (b) Isothermal magnetization of  $\text{NdCrSb}_3$  at 4.8 K.



above and below the apparent  $T_c$  of 125 K were examined and the observation made that only the 100 reflection is enhanced at low temperatures (Figure 6-6). This is not consistent with a layered antiferromagnetic structure as reflections of the type  $(h/2 \ k \ l)$  would be expected. In fact, a simulation of a simple AF structure shows a relatively strong  $\frac{1}{2}00$  reflection. A fit to the diffraction profile at 5 K including the crystal structure and a ferromagnetic magnetic structure (Figure 6-7) demonstrates the essential correctness of this model. Refinement details for the 5 K and 150 K data are collected in Tables 6-6 and 6-7. The refined value for the Cr moment is  $0.79(3) \mu_B$  at 5 K with a moment direction of [010]. This is in good agreement with the saturation moment derived from the bulk polycrystalline data. The temperature dependence of the intensity of the 100 reflection (Figure 6-8) is consistent with a  $T_c$  of 125 K, in excellent agreement with the magnetization and resistivity data. The small residual intensity found above  $T_c$  results from the fact that 100 is an allowed reflection in  $Pbcm$ . These observations establish the ferromagnetic model, unequivocally.

Inspection of the refinement results shows a highly anisotropic temperature dependence of the cell constants (Figure 6-9). The  $a$  axis (stacking direction) length is temperature independent and the  $b$  axis is nearly so. However, the dependence of the  $c$  axis exhibits a change in slope at 125 K ( $T_c$ ), the temperature at which magnetic ordering also occurs; this implies a strong coupling between the magnetic  $d$ -electrons and the lattice phonons.

*NdCrSb<sub>3</sub>*: Although the magnetism studies suggest ferromagnetic ordering of both Nd and Cr moments in *NdCrSb<sub>3</sub>*, confirmation by neutron diffraction is required.





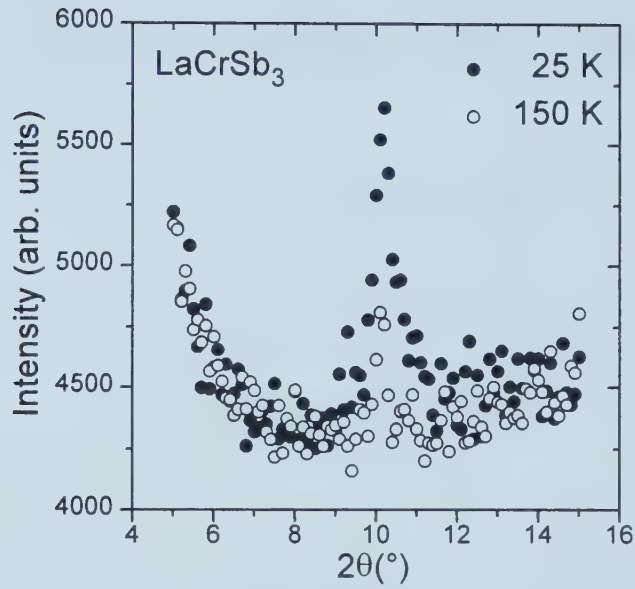


**Figure 6-6.** Plot of the neutron diffraction data for  $\text{LaCrSb}_3$  near the 100 reflection at 25 and 150 K, showing the increased intensity at low temperature.



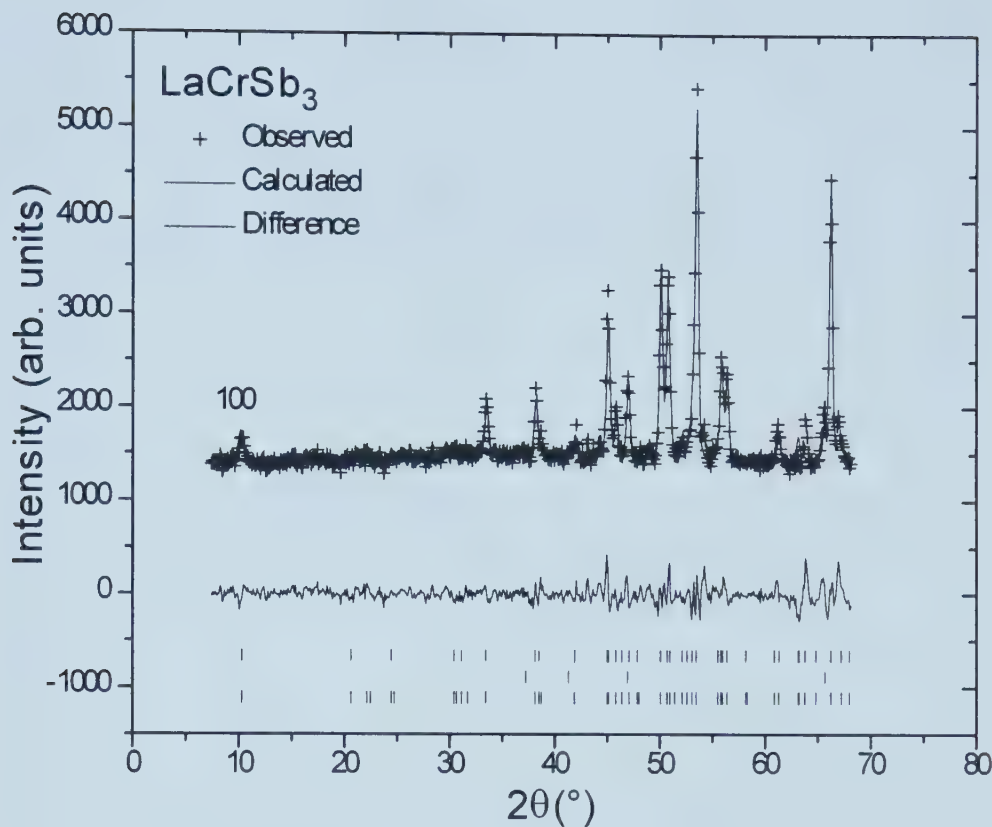


**Figure 6-7.** Rietveld refinement results for  $\text{LaCrSb}_3$  at 5 K. The crosses represent the observed profile, the solid line is the fitted profile, and the difference is shown below. The three sets of vertical tic marks represent the Bragg peak positions for the  $\text{LaCrSb}_3$  crystal structure (top), those for a Sb impurity phase (middle), and the magnetic peak positions (bottom). The 100 peak of largely magnetic origin is labeled.



Table 6-6. Profile Refinement Results for LaCrSb<sub>3</sub> and NdCrSb<sub>3</sub>

LaCrSb <sub>3</sub>			NdCrSb <sub>3</sub>		
Temperature (K)	5	150	4	51	130
Space Group	<i>Pbcm</i>	<i>Pbcm</i>	<i>Pbcm</i>	<i>Pbcm</i>	<i>Pbcm</i>
<i>a</i> (Å)	13.264(3)	13.264(3)	12.9708(2)	12.9701(3)	12.9764(2)
<i>b</i> (Å)	6.182(2)	6.186(1)	6.1699(1)	6.1676(1)	6.1707(1)
<i>c</i> (Å)	6.094(2)	6.099(1)	6.0669(1)	6.0651(1)	6.0686(1)
<i>R</i> <sub>wp</sub> (%)	4.94	4.58	6.81	6.72	5.67
<i>R</i> <sub>E</sub> (%)	2.50	1.36	3.70	3.83	3.65
Cr moment (μ <sub>B</sub> )	0.79(3)	—	1.1	1.1(1)	—
Cr moment direction	[010]	—	[100]	[010]	—
<i>RE</i> moment (μ <sub>B</sub> )	—	—	2.6(1)	—	—
<i>RE</i> moment direction	—	—	[100]	—	—
<i>R</i> <sub>mag</sub> (%)	14.3	—	8.70	30.9	—



**Table 6-7.** Atomic Coordinates and Occupancies for LaCrSb<sub>3</sub> from Profile Refinements

atom	x	y	z	occupancy
LaCrSb <sub>3</sub> , 5 K				
La	0.3229(10)	0.0130(42)	¼	1
Cr	0.9253(32)	¼	0	1
Sb(1)	0.0662(19)	0.0787(39)	¼	1
Sb(2)	0.2240(13)	0.5284(70)	¼	1
Sb(3)	0.4856(31)	¼	0	1
LaCrSb <sub>3</sub> , 150 K				
La	0.3213(9)	0.0149(37)	¼	1
Cr	0.9266(20)	¼	0	1
Sb(1)	0.0681(17)	0.0809(35)	¼	1
Sb(2)	0.2250(12)	0.5220(64)	¼	1
Sb(3)	0.4883(29)	¼	0	1





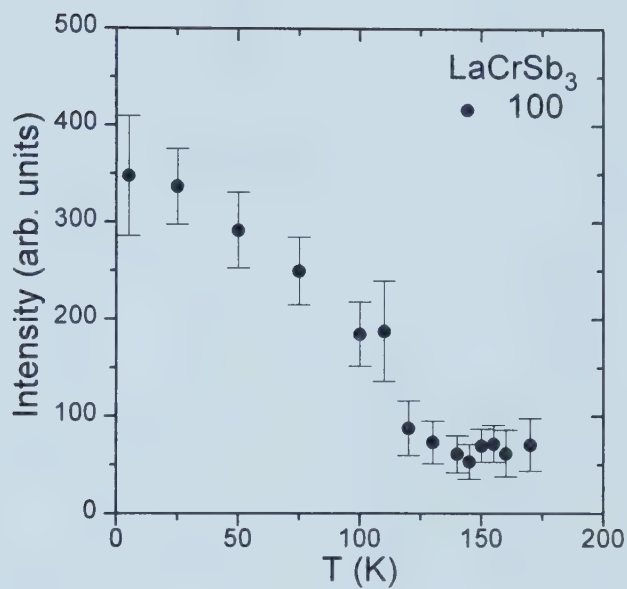


**Figure 6-8.** Plot showing the temperature dependence of the 100 reflection for  $\text{LaCrSb}_3$ .

Note that the  $T_c \approx 125$  K.



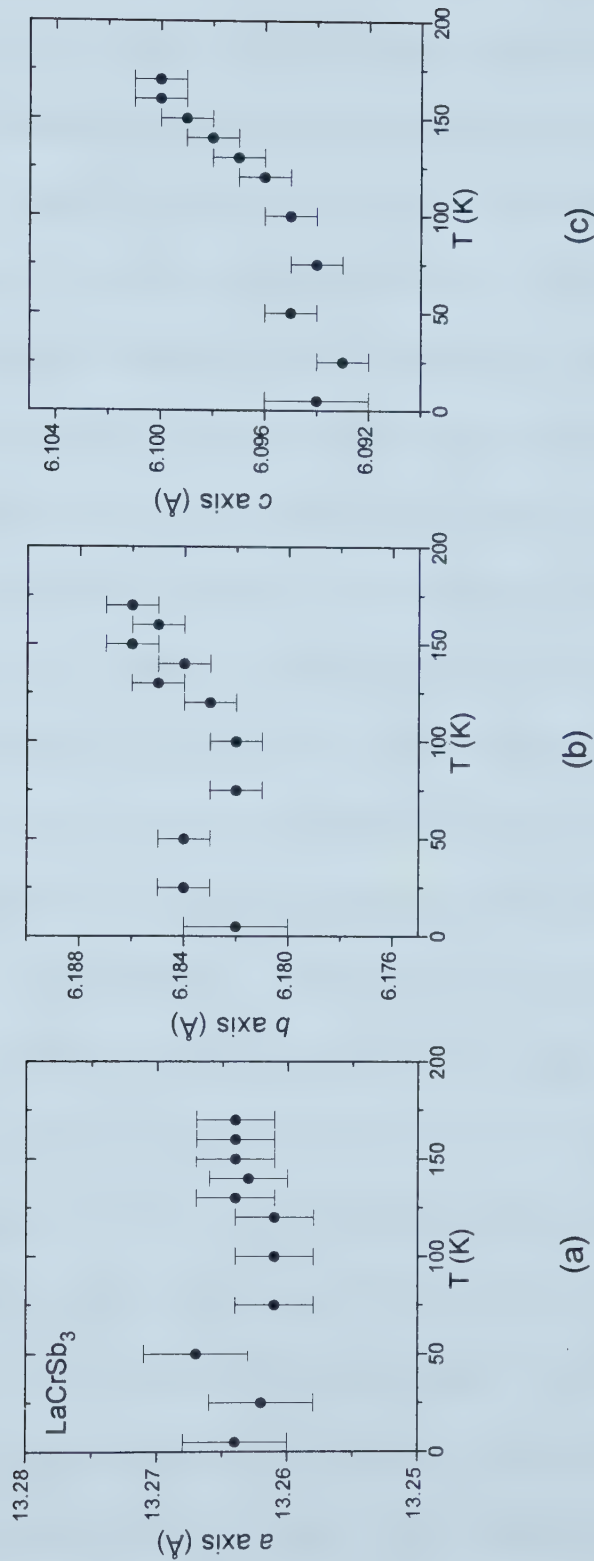


**Figure 6-9.** Plots showing the temperature dependence of the unit cell constants for  $\text{LaCrSb}_3$ , (a)  $a$  axis, (b)  $b$  axis, and (c)  $c$  axis.



Data were collected between 4 and 130 K, encompassing both transitions observed in the magnetic susceptibility curve. Refinement details for the 4, 51, and 130 K data are collected in Tables 6-6 and 6-8. The 130 K data refined well with the structural model, although the occupancy of the Cr site was found to be slightly substoichiometric, giving  $\text{NdCr}_{0.88(6)}\text{Sb}_3$ . Thus, it appears that the compounds of the smaller rare-earth metals have a slightly lower Cr content, as suggested earlier. Lowering the temperature initially results in an increase of intensity of the 100 reflection, reaching a maximum at  $\sim 50$  K, before losing all intensity at low temperatures and a concurrent strengthening of the 111 reflection, plotted in Figure 6-10. This behavior between 50 and 130 K is consistent with the magnetic structure of  $\text{LaCrSb}_3$ , with ferromagnetic ordering of the Cr moments directed along [010]. Refinement of the 51 K data with this model showed excellent agreement (see Figure 6-11(a)) and gave a refined Cr moment of  $1.1(1) \mu_B$ . (If the Cr site is assumed to be fully occupied as is the case for  $\text{LaCrSb}_3$ , the refined moment is  $0.9(1) \mu_B$ .) Decreasing the temperature more results in the 100 reflection disappearing and the 111 reflection gaining intensity. Clearly, the ferromagnetic model with the moment directed along [010] is no longer suitable. A new model, with both the Cr and Nd moments along [100], was selected and fits the data very well, as shown in Figure 6-11(b) for the 4 K data set. However, the reflection near  $42^\circ$  is significantly broader than the other reflections and leads to a peak in the difference plot (see Fig. 6-11(b)). It is unclear whether there is a shortcoming of the magnetic model for  $\text{NdCrSb}_3$  or if the peak can be attributed to an impurity phase. The Cr moment was constrained to  $1.1 \mu_B$  (as obtained from the 51 K data) during refinement, which yielded a Nd moment of  $2.6(1) \mu_B$ .



**Table 6-8.** Atomic Coordinates and Occupancies for NdCrSb<sub>3</sub> from Profile Refinements

atom	<i>x</i>	<i>y</i>	<i>z</i>	occupancy
NdCrSb <sub>3</sub> , 4 K				
Nd	0.3098(14)	0.0018(35)	¼	1
Cr	0.9077(35)	¼	0	0.88 <sup>a</sup>
Sb(1)	0.0646(23)	0.1046(37)	¼	1
Sb(2)	0.2209(19)	0.4931(47)	¼	1
Sb(3)	0.5028(21)	¼	0	1
NdCrSb <sub>3</sub> , 51 K				
Nd	0.3100(14)	0.0038(35)	¼	1
Cr	0.9036(37)	¼	0	0.88 <sup>a</sup>
Sb(1)	0.0658(21)	0.1055(37)	¼	1
Sb(2)	0.2209(19)	0.4960(50)	¼	1
Sb(3)	0.5039(21)	¼	0	1
NdCrSb <sub>3</sub> , 130 K				
Nd	0.3096(12)	0.0033(31)	¼	1
Cr	0.9059(31)	¼	0	0.88(6)
Sb(1)	0.0644(19)	0.1057(31)	¼	1
Sb(2)	0.2204(17)	0.4984(43)	¼	1
Sb(3)	0.5044(19)	¼	0	1

<sup>a</sup> The Cr occupancy was constrained to be equal to 0.88 for the 51 K and 4 K data refinements.





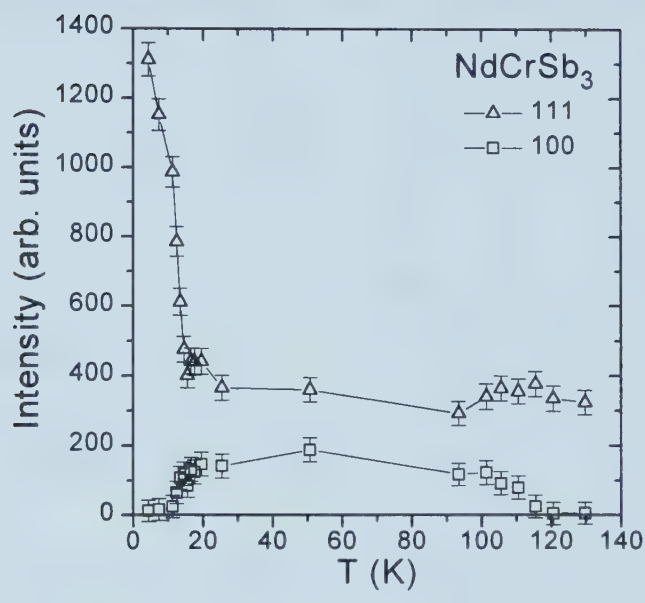
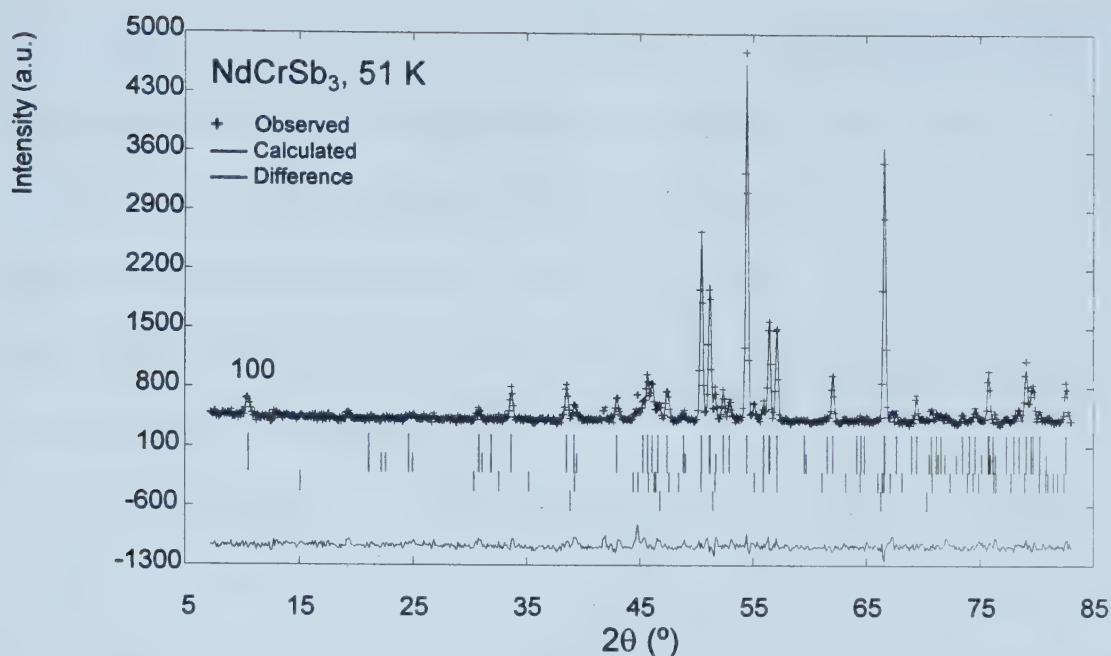
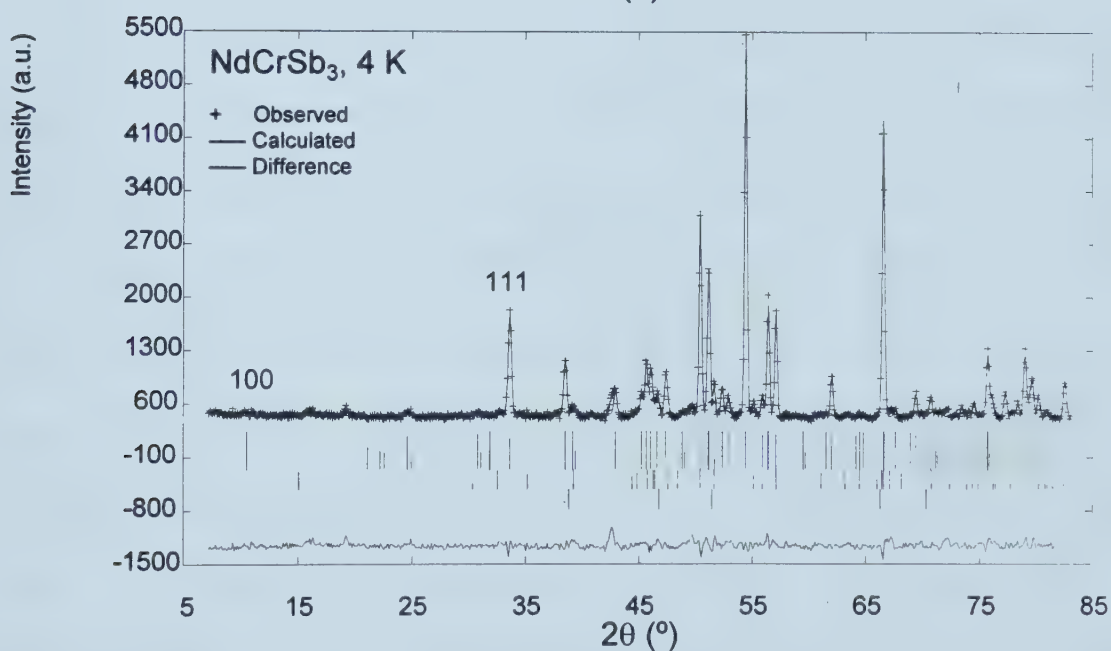


**Figure 6-10.** Plot showing the temperature dependence of the 111 and 100 reflections for NdCrSb<sub>3</sub>. The lines are drawn only to guide the eye.





(a)



(b)

**Figure 6-11.** Rietveld refinement results for NdCrSb<sub>3</sub> at (a) 51 K and (b) 4 K. The crosses represent the observed profile, the solid line is the fitted profile, and the difference is shown at the bottom. The four sets of vertical tick marks represent the Bragg peak positions for the NdCrSb<sub>3</sub> crystal structure (top), the magnetic peak positions (second from top), and those from NdSb<sub>2</sub> (second from bottom) and CrSb (bottom) impurities.



Overall, the magnetic moment of  $3.7(1) \mu_B$  obtained from neutron diffraction is in excellent agreement with that obtained from the magnetization study ( $3.75 \mu_B$ ). Initially,  $\text{NdCrSb}_3$  exhibits the same magnetic structure as  $\text{LaCrSb}_3$  – ferromagnetic ordering of the Cr moments directed along [010]. However, as the Nd moments begin to interact at lower temperatures, the Cr moments flip and order ferromagnetically with the Nd moments, directed along [100].

**Band Structure.** As a first approximation, extended Hückel calculations were carried out. Since this method is inherently based on a one-electron model, it is not intended to provide accurate results for magnetic compounds such as  $\text{LaCrSb}_3$ . Rather, confirmation is sought for its gross features, namely, the metallic conductivity, the band ferromagnetism, and the extent of Cr–Cr and Sb–Sb bonding. Assuming that full electron transfer takes place, the structure of  $\text{LaCrSb}_3$  partitions naturally into  $(\text{La}^{3+})[\text{CrSb}_3]^{3-}$ . Accordingly, a band structure calculation for only the anionic  $[\text{CrSb}_3]^{3-}$  substructure yields results that are similar to one including the La cations as well; we report the latter results for completeness. The density of states (DOS) curve for the full 3D structure of  $\text{LaCrSb}_3$  is shown in Figure 6-12, along with the atomic projections for each element. Figure 6-13 shows the band dispersion curves along the special symmetry lines  $\Gamma X$  (along the stacking axis of the  $\text{CrSb}_2$  and Sb layers),  $\Gamma Y$  (along the “zigzag” chains of edge-sharing  $\text{CrSb}_6$  octahedra), and  $\Gamma Z$  (along the chains of face-sharing  $\text{CrSb}_6$  octahedra).

The Fermi level ( $\epsilon_f = -10.5$  eV) crosses partially filled bands in the DOS curve, consistent with metallic behavior. The La states are located well above the Fermi level,



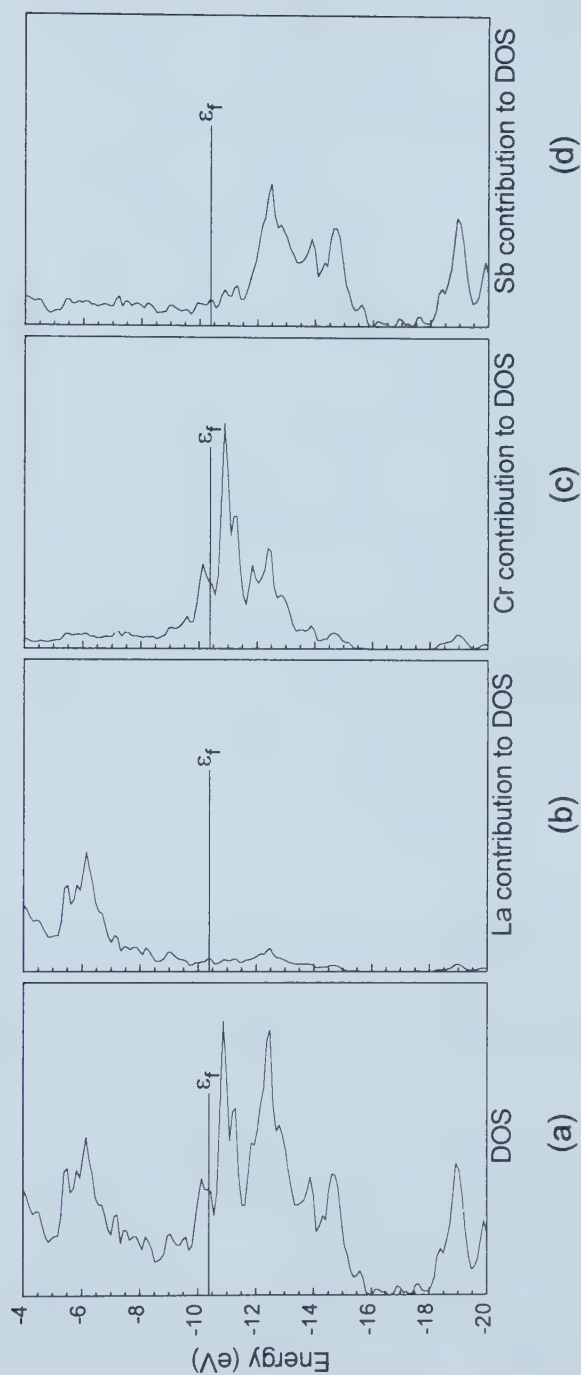


**Figure 6-12.** (a) Total density of states for  $\text{LaCrSb}_3$ . The individual atomic contributions (La, Cr, and Sb) to the density of states are shown in (b) – (d). The Fermi level ( $\epsilon_f = -10.5$  eV) is shown.





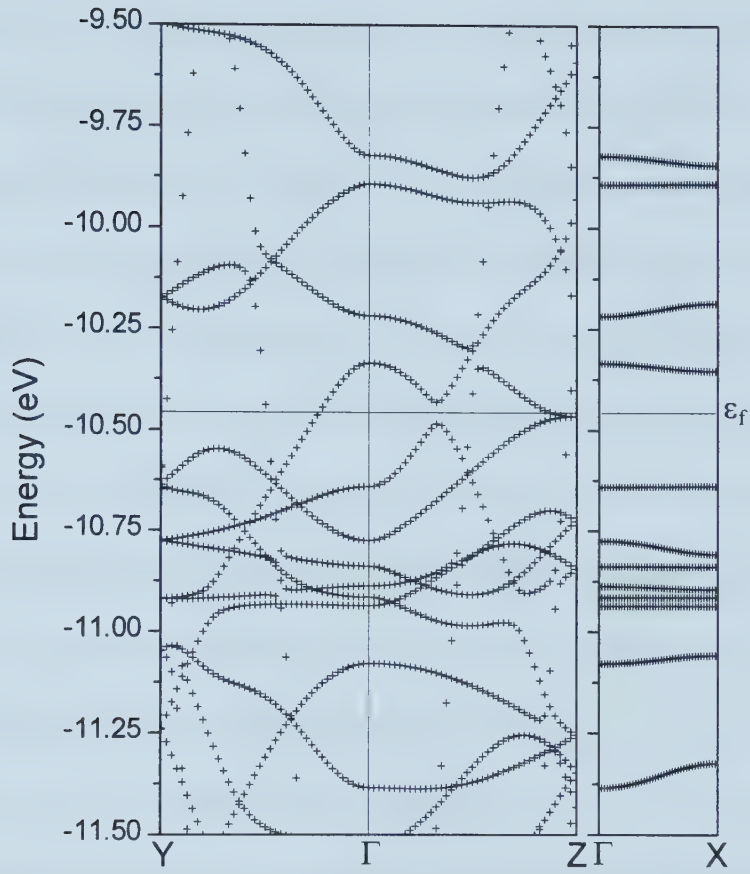


**Figure 6-13.** Band dispersion curves for LaCrSb<sub>3</sub> along the special symmetry lines  $\Gamma X$ ,  $\Gamma Y$ , and  $\Gamma Z$ . The Fermi level ( $\epsilon_f = -10.5$  eV) is shown.



as expected for such an electropositive element, but there are also small contributions at lower energies below. Some mixing of La and Sb states may introduce a small degree of covalent character in La–Sb bonding, which is not surprising as a fully-charged  $\text{La}^{3+}$  cation would be highly polarizing. Significant contributions of Cr d and Sb p states are clustered at and below the Fermi level, in the region from  $-9$  to  $-16$  eV. Along  $\Gamma\text{Y}$ , bands crossed by the Fermi level are wide and their orbital compositions are primarily those of the Sb(3) atoms of the square net. Along  $\Gamma\text{Z}$ , bands crossed by the Fermi level are composed of orbitals from either the  $\text{CrSb}_2$  layer or the Sb(3) square net. No bands are crossed, of course, along  $\Gamma\text{X}$ , because of the presence of the intervening layers of La cations. The interpretation is that  $\text{LaCrSb}_3$  is a highly anisotropic metal in which the Sb(3) square net permits conduction in two dimensions, while the  $\text{CrSb}_2$  layer conducts largely along the chains of face-sharing  $\text{CrSb}_6$  octahedra.

The position of the Fermi level corresponds to nearly filling narrow, Cr-based d bands, in a region where the DOS is relatively high. (Note also its proximity to a spike in the DOS at about  $-11.0$  eV.) These features satisfy the general requirements for band ferromagnetism to occur – there is then the possibility that a substantial concentration of conduction electrons can populate higher energy levels with parallel spins, such that the promotion energy is still small enough to be compensated by the decrease in electron-electron repulsion. With no interactions possible along the stacking direction  $\Gamma\text{X}$ , the picture that emerges is one in which there is only strong ferromagnetic exchange of conduction electrons within each  $\text{CrSb}_2$  layer, consistent with the neutron diffraction results.



The electronic structure is thus quite accurately described as a superposition of noninteracting  $\text{CrSb}_2$  and Sb layers. After the strong Cr–Sb bonds are accounted for, Cr–Cr and Sb–Sb bonding are important secondary covalent interactions, as suggested by the COOP (crystal orbital overlap population) curves shown in Figure 6-14. Up to the Fermi level, all of the bonding levels are filled, but some Cr–Cr and Sb(3)–Sb(3) antibonding levels also start to fill. The cumulated overlap populations are 0.376 for Sb(1)–Sb(2) (3.175(2) Å) and 0.339 for Sb(3)–Sb(3) (3.0581(5)–3.1065(1) Å), indicating that these are significant bonding interactions. Compared with a typical overlap population of  $\sim 0.6$  for a Sb–Sb single bond of  $\sim 2.8$  Å, our earlier approximation that the  $\sim 3.0$  Å Sb–Sb bonds are of one-half bond order is fairly accurate. The  $\sim 3.0$  Å Cr–Cr interaction shows a small but non-negligible, positive overlap population of 0.086, indicating that there is weak bonding even at this distance. The La–Sb interactions have an average overlap population of 0.190. The calculated atomic charges yield the overall formulation ( $\text{La}^{1.44+}$ ) ( $\text{Cr}^{1.97-}$ ) ( $\text{Sb}(1)^{0.50+}$ ) ( $\text{Sb}(2)^{0.19-}$ ) ( $\text{Sb}(3)^{0.22+}$ ). Given that the Cr–Sb bonds are highly covalent, the large discrepancy between the calculated Cr oxidation state and that predicted from the Zintl concept is not surprising.



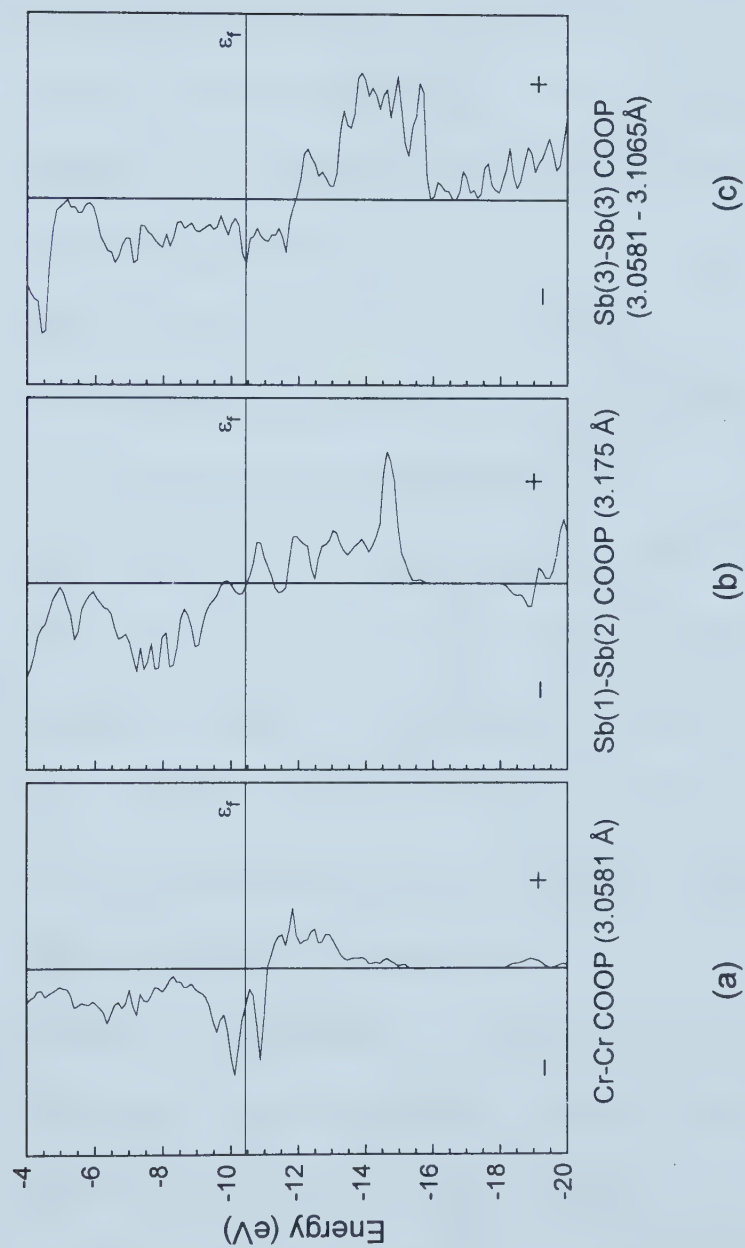


**Figure 6-14.** Crystal orbital overlap population curves for the (a) Cr-Cr, (b) Sb(1)-Sb(2), and (c) Sb(3)-Sb(3) interactions in  $\text{LaCrSb}_3$ . The Fermi level ( $\epsilon_f = -10.5$  eV) is shown.





## REFERENCES

- (1) Brylak, M.; Jeitschko, W. *Z. Naturforsch. B: Chem. Sci.* **1995**, *50*, 899.
- (2) Hartjes, K.; Jeitschko, W.; Brylak, M. *J. Magn. Magn. Mater.* **1997**, *173*, 109.
- (3) POLSQ: Program for least-squares unit cell refinement. Modified by D. Cahen and D. Keszler, Northwestern University, 1983.
- (4) Yvon, K.; Jeitschko, W.; Parthé, E. *J. Appl. Crystallogr.* **1977**, *10*, 73.
- (5) Sheldrick, G. M. *SHELXTL* Version 5.0; Siemens Analytical X-ray Instruments, Inc.: Madison, WI, 1994.
- (6) Sheldrick, G. M. *J. Appl. Crystallogr.* in press.
- (7) *International Tables for X-ray Crystallography*; Wilson, A. J. C., Ed.; Kluwer: Dordrecht, The Netherlands, 1992, Vol. C.
- (8) Gelato, L. M.; Parthé, E. *J. Appl. Crystallogr.* **1987**, *20*, 139.
- (9) Wiles, D. B.; Young, R. A. *J. Appl. Crystallogr.* **1981**, *14*, 149.
- (10) Rodriguez-Carvajal, J. *FULLPROF: A Program for Rietveld Refinement and Profile Matching Analysis*; Laboratoire Leon Brillouin (CEA-CNRS): Saclay, France. For information on version 3.5 contact J. Rodriguez-Carvajal: (fax (33) 1 6908 8261; email [juan@bali.saclay.fr](mailto:juan@bali.saclay.fr)).
- (11) Whangbo, M.-H.; Hoffmann, R. *J. Am. Chem. Soc.* **1978**, *100*, 6093.
- (12) Hoffmann, R. *Solids and Surfaces: A Chemist's View of Bonding in Extended Structures*; VCH Publishers: New York, 1988.
- (13) Lulei, M.; Martin, J. D.; Hoistad, L. M.; Corbett, J. D. *J. Am. Chem. Soc.* **1997**, *119*, 513



- (14) Summerville, R. H.; Hoffmann, R. *J. Am. Chem. Soc.* **1976**, *98*, 7240.
- (15) Hughbanks, T.; Hoffmann, R.; Whangbo, M.-H.; Stewart, K. R.; Eisenstein, O.; Canadell, E. *J. Am. Chem. Soc.* **1982**, *104*, 3876.
- (16) Kjekshus, A.; Walseth, K. P. *Acta Chem. Scand.* **1969**, *23*, 2621.
- (17) Holseth, H.; Kjekshus, A. *Acta Chem. Scand.* **1968**, *22*, 3284.
- (18) Nesper, R. *Angew. Chem., Int. Ed. Engl.* **1991**, *30*, 789.
- (19) Ferguson, M. J.; Ellenwood, R. E.; Mar, A. *Inorg. Chem.* accepted July 18, 1999.
- (20) Ferguson, M. J.; Hushagen, R. W.; Mar, A. *Inorg. Chem.* **1996**, *35*, 4505.
- (21) Bouchard, R. J.; Gillson, J. L. *Mater. Res. Bull.* **1972**, *7*, 873.
- (22) Allen, P.B.; Berger, H.; Chauvet, O.; Forro, L.; Jarlborg, T.; Junod, A.; Ravez, B.; Santi, G. *Phys. Rev. B: Condens. Matter* **1996**, *53*, 4393 (and references therein).
- (23) Greedan, J. E.; Sato, M.; Ali, N.; Datars, W. R. *J. Solid State Chem.* **1987**, *68*, 300.
- (24) Chikazumi, S. *Physics of Magnetism*; John Wiley & Sons: New York, 1964.



## Chapter 7

### Structural Relationships in Ternary Rare-Earth Antimonides

Several new ternary rare-earth antimonides  $RE_xM_ySb_z$  ( $M$  = transition metal or main-group metal) have been prepared and characterized since the research presented in this thesis was begun. Figure 7-1, which is an extension of Figure 1-1, shows all of the known  $RE_xM_ySb_z$  compounds prepared to date, including the four low-dimensional structures reported here.<sup>1-41</sup> The range of  $M$ -metals for which ternary compounds form has now been extended to include both the early-transition metals ( $M$  = Ti, Zr, Hf, V, Nb, Cr) and the main-group metals ( $M$  = Ga, Ge, In, Sn). Moreover, the number of structures adopted by  $RE_xM_ySb_z$  for a given  $M$ -metal has been increased, most notably for  $M$  = Pd, owing to the interesting properties exhibited by some of the members. This diversity of structures adopted by the ternary rare-earth antimonides provides great flexibility for designing new compounds; one can envision a palette of building blocks from which the chemist can choose to synthesize new compounds with desirable structural features, and therefore provide a route to rational materials design. Although preliminary physical properties have been measured for many of the compounds, a great deal of work still remains, especially when considering the ultimate goal of developing structure-property relationships.

A key feature of the ternary rare-earth antimonides presented in this thesis are the low-dimensional networks of antimony atoms. The weak Sb–Sb bonds must play an important role in stabilizing the low-dimensional structures, given the numerous



**Figure 7-1.** Known ternary rare-earth antimonides  $RE_xM_ySb_z$  ( $M$  = transition metal or main-group metal). One-dimensional structures ( $RE_3MSb_5^{1,2}$ ) are adopted by compounds of elements enclosed by a plain border, two-dimensional ( $REMSb_3^{2,3}$ ,  $REMSb_2^{4-13}$ ,  $REM_2Sb_2^{14-20}$ ,  $RE_3M_6Sb_5^{21}$ ) by a double-lined border, and three-dimensional structures ( $REM_4Sb_{12}^{22,23}$ ,  $RE_3M_3Sb_4^{24-27}$ ,  $REMSb^{28-35}$ ,  $RE_6MSb_{15}^{36}$ ,  $RE_8M_{24}Sb^{37}$ ,  $RE_2M_9Sb_3^{38}$ ,  $RE_{13}M_8Sb_{21}^{13}$ ,  $RE_{12}M_4Sb_{23}^{13}$  and  $RE_6M_5Sb_{11}^{39}$ ) in the shaded boxes. By one- and two-dimensional are meant those structures in which chains and layers can be perceived as obvious building elements, respectively.  $RE_{14}MSb_{11}$  ( $RE = Eu$ ) is also known but consists of discrete molecular species.<sup>40,41</sup> No ternary rare-earth antimonides are known to date for elements in empty boxes.





Ti <i>RE<sub>3</sub>MSb<sub>5</sub></i>	V <i>REMSb<sub>3</sub></i>	Cr <i>REMSb<sub>3</sub></i>	Mn <i>REMSb<sub>2</sub></i> <i>RE<sub>2</sub>Sb<sub>2</sub></i> <i>RE<sub>4</sub>MSb<sub>15</sub></i>	Fe <i>REMSb<sub>2</sub></i> <i>RE<sub>4</sub>Sb<sub>12</sub></i>	Co <i>REMSb<sub>2</sub></i>	Ni <i>REMSb<sub>2</sub></i> <i>RE<sub>2</sub>Sb<sub>2</sub></i> <i>REMSb</i> <i>RE<sub>4</sub>MSb<sub>15</sub></i>	Cu <i>REMSb<sub>2</sub></i> <i>RE<sub>2</sub>Sb<sub>2</sub></i> <i>RE<sub>3</sub>M<sub>3</sub>Sb<sub>4</sub></i> <i>REMSb</i> <i>RE<sub>4</sub>MSb<sub>15</sub></i>	Zn <i>REMSb<sub>2</sub></i> <i>RE<sub>2</sub>Sb<sub>2</sub></i> <i>RE<sub>6</sub>MSb<sub>14</sub></i>	Ga <i>REMSb<sub>2</sub></i> <i>RE<sub>13</sub>M<sub>8</sub>Sb<sub>31</sub></i> <i>RE<sub>12</sub>M<sub>4</sub>Sb<sub>23</sub></i>	Ge <i>RE<sub>6</sub>M<sub>4</sub>Sb<sub>11</sub></i>
Zr <i>RE<sub>3</sub>MSb<sub>5</sub></i>	Nb <i>RE<sub>3</sub>MSb<sub>5</sub></i>	Mo	Tc	Ru <i>RE<sub>4</sub>Sb<sub>12</sub></i>	Rh	Pd <i>REMSb<sub>2</sub></i> <i>RE<sub>2</sub>Sb<sub>2</sub></i> <i>RE<sub>3</sub>M<sub>6</sub>Sb<sub>5</sub></i> <i>REMSb</i> <i>RE<sub>2</sub>M<sub>9</sub>Sb<sub>3</sub></i> <i>RE<sub>8</sub>M<sub>34</sub>Sb</i>	Ag <i>REMSb<sub>2</sub></i> <i>REMSb</i>	Cd <i>REMSb<sub>2</sub></i>	In <i>REMSb<sub>2</sub></i>	Sn <i>REMSb<sub>2</sub></i>
Hf <i>RE<sub>3</sub>MSb<sub>5</sub></i>	Ta	W	Re	Os <i>RE<sub>4</sub>Sb<sub>12</sub></i>	Ir	Pt <i>RE<sub>3</sub>M<sub>3</sub>Sb<sub>4</sub></i> <i>REMSb</i>	Au <i>REMSb<sub>2</sub></i> <i>RE<sub>3</sub>M<sub>3</sub>Sb<sub>4</sub></i> <i>REMSb</i>	Hg	Tl	Pb

1 D	2 D	2 D 3 D	3 D
-----	-----	------------	-----



examples of chains and sheets with Sb–Sb distances on the order of 3.1 Å. These distances are intermediate between the full single intralayer bonds (2.908 Å) and the longer interlayer distances ( $\sim 3.36$  Å) observed in elemental Sb.<sup>42</sup> A model that has been used successfully is to consider Sb–Sb distances in this range as one-half bond order, or one-electron bonds, and results in the assignment of  $\text{Sb}^{2-}$  for chains of two-bonded Sb atoms and  $\text{Sb}^{1-}$  for sheets of four-bonded Sb atoms. These Sb–Sb interactions have been quantified by extended Hückel band structure calculations, which yield results consistent with one-electron bonds. The calculations predict that the networks should be metallic, and resistivity measurements on several compounds seem to provide confirmation. Moreover, these low-dimensional networks should give rise to a strong anisotropy – conducting electricity within the chains or sheets while the intervening *RE* cations serve to insulate between. Although the electron count of the networks suggests they should be prone to structural distortions and the formation of strong two-electron bonds (*i.e.* linear chains of  $\text{Sb}^{2-}$  atoms distorting to  $(\text{Sb}^{2-})_2$  dumbbells; square sheets of  $\text{Sb}^{1-}$  to zigzag chains of  $\text{Sb}^{1-}$ ), which would yield a metal-to-insulator transition, the stability of these networks seems to prevent such distortions from occurring.

Much of the structural diversity exhibited by these ternary rare-earth antimonides derives in part from the flexibility of coordination geometries that the *RE* atom can take on, as shown in Figure 7-2. At the same time, however, the presence of chains or square sheets of Sb atoms imposes certain restrictions on the *RE* coordination geometry. The common theme is the square antiprismatic geometry, consisting of a smaller square of Sb atoms (forming part of the infinite square Sb sheets) and a larger square twisted  $45^\circ$  with



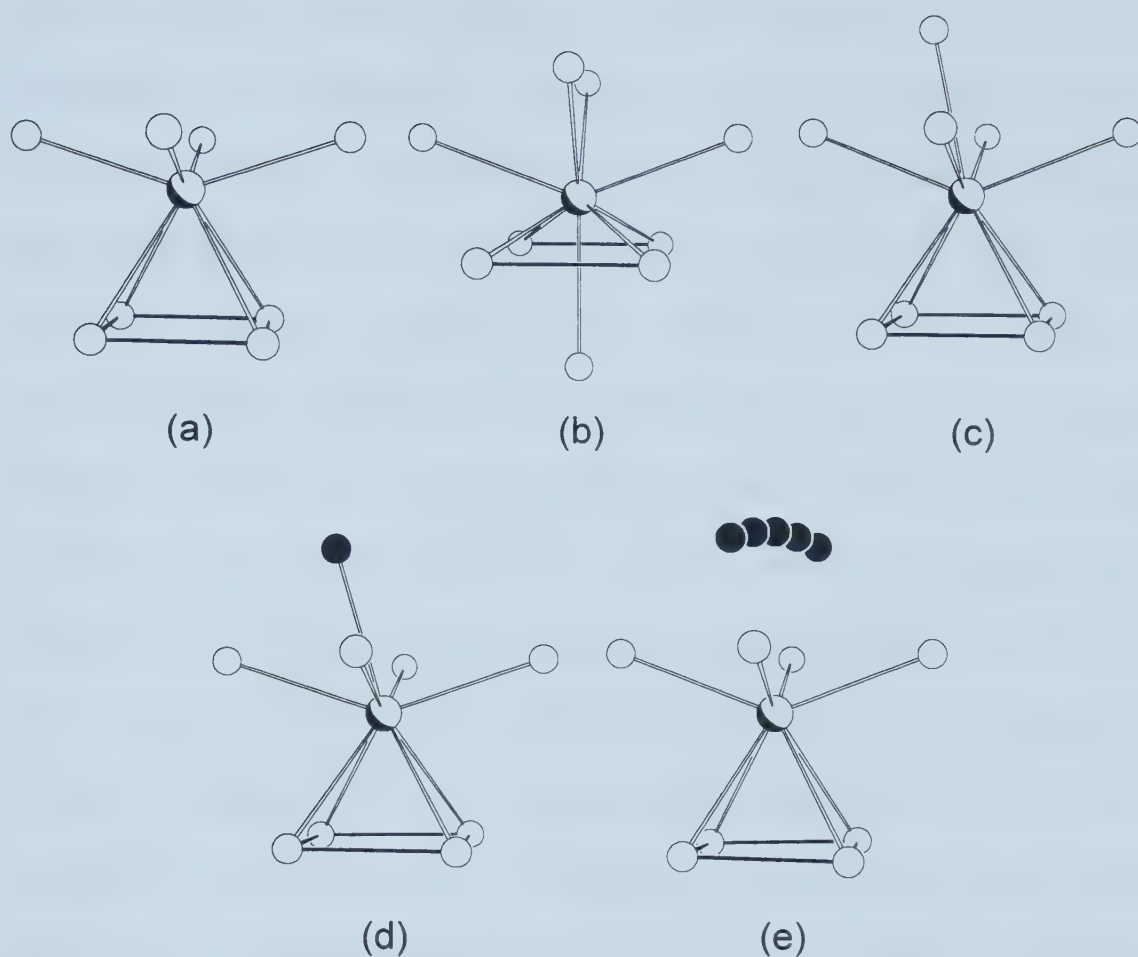


**Figure 7-2.** Coordination geometries of *RE* atom: (a) square antiprism in  $REMSb_2$  ( $M = \text{Mn-Zn, Pd, Ag, Cd, Au}$ ); (b) tricapped trigonal prism in  $RE_3MSb_5$  ( $M = \text{Ti, Zr, Hf, Nb}$ ); (c) monocapped square antiprism in  $REMSb_3$  ( $M = \text{V, Cr}$ ); (d) monocapped square antiprism in  $REIn_{1-x}Sb_2$ ; (e) monocapped square antiprism with a range of positions for the capping atom in  $RESn_{0.75}Sb_2$ .



respect to the first, as shown in Figure 7-2(a). This eight-coordination geometry is prevalent in  $REMSb_2$  ( $M = \text{Mn–Zn, Pd, Ag, Cd, Au}$ ).<sup>6–13</sup> Variations on this theme arise from attaching a ninth capping atom. The roughly tricapped trigonal prism in  $RE_3MSb_5$  ( $M = \text{Ti, Zr, Hf, Nb}$ )<sup>1,2</sup> is derived by distorting the larger Sb square, and placing the capping Sb atom below the smaller Sb square, shown in Figure 7-2(b). (Note that the smaller square is actually two parallel chains.) In  $REMSb_3$  ( $M = \text{V, Cr}$ ),<sup>2,3</sup> the capping Sb atom is positioned above the larger Sb square (Figure 7-2(c)) and is tilted off-center to accompany the formation of a weak Sb(1)–Sb(2) bond. But why should the capping atom be restricted to Sb? In  $REIn_{0.8}Sb_2$ ,<sup>4</sup> the coordination around  $RE$  is completed by a capping In atom, which is also positioned above the larger Sb square and tilted off-center to accompany the formation of two weak In–Sb bonds (Figure 7-2(d)). Moreover, the position of the capping atom can be rather flexible, and will readily adapt to other requirements of the crystal structure. For instance, in  $LaSn_{0.75}Sb_2$ , the cap is a Sn atom that occupies sites corresponding to a *range* of positions above the larger Sb square of the La square antiprism (Figure 7-2(e)).<sup>5</sup> The ultimate example of this flexibility is that of the 12-fold coordination in the skutterudite  $REM_4Sb_{12}$  ( $M = \text{Fe, Ru, Os}$ ),<sup>22,23</sup> in which the  $RE$  atom has been described to “rattle” around in its environment; the large displacement parameter for the  $RE$  is thought to be responsible for the low thermal conductivity and consequently the origin of the thermoelectric behavior of these compounds.<sup>43</sup>

Despite this diversity, there are some common threads, as shown in Figure 7-3. The structure of  $RE_3MSb_5$  ( $M = \text{Ti, Zr, Hf, Nb}$ )<sup>1,2</sup> is strongly one-dimensional, comprising Sb chains and face-sharing octahedral  $MSb_6$  chains (Figure 7-3(a)). These







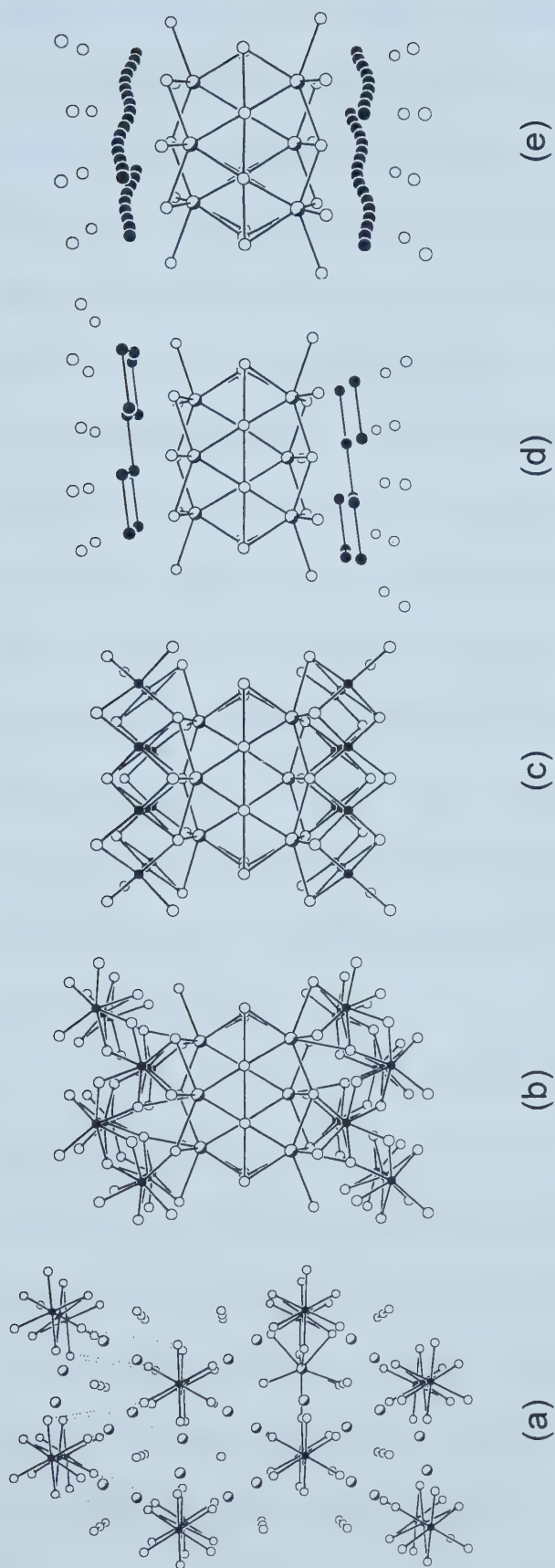


**Figure 7-3.** Comparison of various ternary rare-earth antimonides  $RE_xM_ySb_z$  with low-dimensional structures: (a)  $RE_3MSb_5$  ( $M = \text{Ti, Zr, Hf, Nb}$ ) with isolated chains of octahedra; (b)  $REMSb_3$  ( $M = \text{V, Cr}$ ) with layers of condensed chains of octahedra; (c)  $REMSb_2$  ( $M = \text{Mn-Zn, Pd, Ag, Cd, Au}$ ) with layers of condensed chains of tetrahedra; (d)  $REIn_{1-x}Sb_2$  with zigzag chains of In; (e)  $RESn_{0.75}Sb_2$  with disordered Sn sites and linear chains of Sn.



building blocks may be conceptually envisioned to be condensed together to form the structure of  $REMSb_3$  ( $M = V, Cr$ )<sup>2,3</sup> (Figure 7-3(b)). Several Sb chains aligned together in the same plane become a square Sb sheet, and face-sharing  $MSb_6$  octahedral chains share their edges to form the buckled layers of  $M$ -centered octahedra.  $RE$  atoms are then situated above and below the square Sb sheet in a “checkerboard” pattern. Proceeding further to the right of the periodic table, most of the structures adopted by ternary rare-earth antimonides of the *late* transition metals favor tetrahedral coordination of  $M$ . But the common tetragonal  $REMSb_2$  structure is derived by simply replacing the layers of metal-centered octahedra by ones of tetrahedra (Figure 7-3(c)).<sup>6-13</sup> Beyond the transition metals to the main-group metals, the structure adopted by  $LaIn_{0.8}Sb_2$  can be viewed as a modification of the  $MSb$  tetrahedra layer in  $REMSb_2$ , whereby the perfectly square arrangement of  $M$  atoms distorts to give zigzag In chains (Figure 7-3(d)).<sup>4</sup> Finally, the structure of  $LaSn_{0.75}Sb_2$  retains the same relative positions of the  $RE$  and Sb atoms, but the Sn atoms are now disordered in closely spaced sites (each ~20% occupied or less), as shown in Figure 7-3(e).<sup>5</sup>

*Future work.* The electrical resistivity data for the  $RE_3TiSb_5$  compounds show interesting behavior, in particular, the data for  $La_3TiSb_5$  which show two transitions at ~85 and 120 K. Although a variable temperature single crystal X-ray diffraction study did not give any evidence for a structural transition occurring at 120 K, it would be useful to collect neutron diffraction data, with a temperature range spanning both transitions. Furthermore, magnetism studies are vital as the electronic transitions may be of magnetic origin. However, before these studies can be carried out, single phase (or nearly so)



material needs to be synthesized, a task which so far has not been achieved. Given the considerable range of substitutional flexibility of the  $RE_3MSb_5$  series, an extensive study of the steric effects (largely due to the  $RE$  atom) and electronic effects (largely due to the  $M$  atom) on the physical properties can be undertaken. Moreover, preliminary results from doping experiments with alkaline-earth metals for the rare-earth metals seem promising, providing yet another route for tuning the properties.

The effect of the structural versatility exhibited by the  $RESn_xSb_2$  family of compounds on their physical properties should be further studied. For instance, if suitable single crystals can be prepared with diverse compositions, the electrical resistivity as a function of Sn content can be investigated. Further magnetic studies are required before any trend in magnetic properties can be concluded. The striking similarities between the structures of  $RESn_xSb_2$  and  $REIn_{1-x}Sb_2$  enable the formation of the solid solution  $RE(In,Sn)_xSb_2$ , and a structural study would yield at what composition the crossover from the  $RESn_xSb_2$  to  $REIn_{1-x}Sb_2$  structure types occurs.

The ternary rare-earth antimonide systems have continued to be a fruitful area of research, bearing new structures and compounds with interesting and exciting properties. Further investigations into the ternary, and even quaternary or higher, systems will expand our knowledge of antimony bonding patterns in low-dimensional networks and help us to develop coherent structure-property relationships, eventually providing us with the ability to rationally design new materials with specific, useful properties.



## REFERENCES

- (1) Bolloré, G.; Ferguson, M. J.; Hushagen, R. W.; Mar A. *Chem. Mater.* **1995**, 7, 2229
- (2) Ferguson, M. J.; Hushagen, R. W.; Mar, A. *J. Alloys Compd.* **1997**, 249, 191.
- (3) Brylak, M.; Jeitschko, W. *Z. Naturforsch. B: Chem. Sci.* **1995**, 50, 899.
- (4) Ferguson, M. J.; Ellenwood, R. E.; Mar, A. *Inorg. Chem.* **1999**, 38, 4503.
- (5) Ferguson, M. J.; Hushagen, R. W.; Mar, A. *Inorg. Chem.* **1996**, 35, 4505.
- (6) Sologub, O.; Noël, H.; Leithe-Jasper, A.; Rogl, P.; Bodak, O. I.; *J. Solid State Chem.* **1995**, 115, 441.
- (7) Brylak, M.; Möller, M. H.; Jeitschko, W. *J. Solid State Chem.* **1995**, 115, 305.
- (8) Sologub, O.; Hiebl, K.; Rogl, P.; Bodak, O. *J. Alloys Compd.* **1995**, 227, 40.
- (9) Sologub, O.; Hiebl, K.; Rogl, P.; Noël, H.; Bodak, O. *J. Alloys Compd.* **1994**, 210, 153.
- (10) Leithe-Jasper, A.; Rogl, P. *J. Alloys Compd.* **1994**, 203, 133.
- (11) Cordier, G.; Schäfer, H.; Woll, P. *Z. Naturforsch. B: Anorg. Chem., Org. Chem.* **1985**, 40, 1097.
- (12) Pankevich, Yu. V.; Pecharskii, V. K.; Bodak, O. I. *Izv. Akad. Nauk SSSR, Met.* **1983**, 227.
- (13) Mills, A. M.; Mar, A. Unpublished results.
- (14) Mulder, F. M.; Thiel, R. C.; Buschow, K. H. J. *J. Alloys Compd.* **1994**, 210, 335.
- (15) Hofmann, W. K.; Jeitschko, W. *J. Less-Common Met.* **1988**, 138, 313.
- (16) Hofmann, W. K.; Jeitschko, W. *Monatsh. Chem.* **1985**, 116, 569.





- (17) Pecharskii, V. K.; Pankevich, Yu. V.; Bodak, O. I. *Dopov. Akad. Nauk Ukr. RSR. Ser. B: Geol., Khim. Biol. Nauki* **1982**, 44.
- (18) Zwiener, G.; Neumann, H.; Schuster, H.-U. *Z. Naturforsch. B: Anorg. Chem., Org. Chem.* **1981**, 36, 1195.
- (19) Rühl, R.; Jeitschko, W. *Mater. Res. Bull.* **1979**, 14, 513.
- (20) Marchand, R.; Jeitschko, W. *J. Solid State Chem.* **1978**, 24, 351.
- (21) Gordon, R. A.; DiSalvo, F. J.; Pöttgen, R. *J. Alloys Compd.* **1995**, 228, 16.
- (22) Evers, C. B. H.; Jeitschko, W.; Boonk, L.; Braun, D. J.; Ebel, T.; Scholz, U. D. *J. Alloys Compd.* **1995**, 224, 184.
- (23) Braun, D. J.; Jeitschko, W. *J. Less-Common Met.* **1980**, 72, 147.
- (24) Patil, S.; Hossain, Z.; Paulose, P. L.; Nagarajan, R.; Gupta, L. C. *Solid State Commun.* **1996**, 99, 419.
- (25) Skolozdra, R. V.; Salamakha, P. S.; Ganzyuk, A. L.; Bodak, O. I. *Izv. Akad. Nauk SSSR, Neorg. Mater.* **1993**, 29, 25.
- (26) Kasaya, M.; Katoh, K.; Takegahara, K. *Solid State Commun.* **1991**, 78, 797.
- (27) Dwight, A. E. *Acta Crystallogr. Sect. B: Struct. Crystallogr. Cryst. Chem.* **1977**, 33, 1579.
- (28) Hartjes, K.; Jeitschko, W. *J. Alloys Compd.* **1995**, 226, 81.
- (29) Kasaya, M.; Suzuki, H.; Yamaguchi, T.; Katoh, K. *J. Phys. Soc. Jpn.* **1992**, 61, 4187.
- (30) Malik, S. K.; Adroja, D. T. *J. Magn. Magn. Mater.* **1991**, 102, 42.
- (31) Wenski, G.; Mewis, A. *Z. Anorg. Allg. Chem.* **1986**, 543, 49.



- (32) Pecharskii, V. K.; Pankevich, Yu. V.; Bodak, O. I. *Sov. Phys. Crystallogr. Engl. Transl.* **1983**, 28, 97.
- (33) Rossi, D.; Marazza, R.; Mazzone, D.; Ferro, R. *J. Less-Common Met.* **1981**, 78, P1.
- (34) Tomuschat, C.; Schuster, H.-U. *Z. Naturforsch. B: Anorg. Chem., Org. Chem.* **1981**, 36, 1193.
- (35) Marazza, R.; Rossi, D.; Ferro, R. *J. Less-Common Met.* **1980**, 75, P25.
- (36) Sologub, O.; Vybornov, M.; Rogl, P.; Hiebl, K. *J. Solid State Chem.* **1996**, 122, 266.
- (37) Gordon, R. A.; DiSalvo, F. J. *Z. Naturforsch. B: Chem. Sci.* **1996**, 51, 52.
- (38) Gordon, R. A.; DiSalvo, F. J.; Pöttgen, R.; Brese, N. *J. Chem. Soc., Faraday Trans.* **1996**, 92, 2167.
- (39) Lam, R.; Mar, A. Unpublished results.
- (40) Rehr, A.; Kauzlarich, S. *J. Alloys Compd.* **1994**, 207/208, 424.
- (41) Chan, J. Y.; Wang, M. E.; Rehr, A.; Kauzlarich, S. M. *Chem. Mater.* **1997**, 9, 2131.
- (42) Greenwood, N. N.; Earnshaw, A. *Chemistry of the Elements*; Pergamon Press: Oxford, U.K., 1994.
- (43) Hornbostel, M. D.; Hyer, E. J.; Thiel, J.; Johnson, D. C. *J. Am. Chem. Soc.* **1997**, 119, 2665.



## Appendix

**Table A-1.** Anisotropic Displacement Parameters <sup>a</sup> (Å<sup>2</sup>) for LaSn<sub>0.75</sub>Sb<sub>2</sub>

atom	$U_{11}$	$U_{22}$	$U_{33}$	$U_{12}$	$U_{13}$	$U_{23}$
La	0.0061(2)	0.0056(2)	0.0067(2)	0	0	0
Sb(1)	0.0074(2)	0.0065(2)	0.0075(2)	0	0	0
Sb(2)	0.0081(2)	0.0098(2)	0.0064(2)	0	0	0

<sup>a</sup> The form of the anisotropic displacement parameter is:  $\exp[-2\pi^2(h^2a^{*2}U_{11} + k^2b^{*2}U_{22} + l^2c^{*2}U_{33} + 2hka^*b^*U_{12} + 2hla^*c^*U_{13} + 2klb^*c^*U_{23})]$ .

**Table A-2.** Anisotropic Displacement Parameters <sup>a</sup> (Å<sup>2</sup>) for LaSn<sub>0.61</sub>Sb<sub>2</sub>

atom	$U_{11}$	$U_{22}$	$U_{33}$	$U_{12}$	$U_{13}$	$U_{23}$
La	0.0087(4)	0.0074(4)	0.0102(4)	0	0	0
Sb(1)	0.0102(5)	0.0082(5)	0.0116(5)	0	0	0
Sb(2)	0.0094(5)	0.0132(5)	0.0108(5)	0	0	0

<sup>a</sup> The form of the anisotropic displacement parameter is:  $\exp[-2\pi^2(h^2a^{*2}U_{11} + k^2b^{*2}U_{22} + l^2c^{*2}U_{33} + 2hka^*b^*U_{12} + 2hla^*c^*U_{13} + 2klb^*c^*U_{23})]$ .



**Table A-3.** Powder X-ray Diffraction Data for  $\text{LaIn}_{0.8}\text{Sb}_2$ 

$hkl$	$d_{obs}$ (Å)	$d_{calc}$ (Å)	$I/I_o^a$	$hkl$	$d_{obs}$ (Å)	$d_{calc}$ (Å)	$I/I_o^a$
1 0 $\bar{2}$	—	3.871	5	2 1 1	1.906	1.905	6
0 1 2	3.492	3.495	13	0 1 6	1.784	1.785	6
1 0 2	3.288	3.287	8	1 1 $\bar{6}$	1.754	1.752	7
1 1 $\bar{1}$	3.097	3.097	11	0 2 4	1.746	1.748	16
0 0 4	2.932	2.936	32	1 2 3	1.699	1.698	7
1 1 1	2.921	2.921	23	1 2 $\bar{4}$	1.684	1.685	5
1 1 $\bar{2}$	2.896	2.892	100	2 1 3	1.669	1.668	3
1 0 3	2.719	2.719	12	2 1 $\bar{5}$	1.640	1.639	5
1 0 $\bar{4}$	2.665	2.665	8	2 2 $\bar{1}$	1.566	1.565	9
1 1 2	2.622	2.623	55	2 2 0	1.553	1.554	7
1 1 $\bar{3}$	2.589	2.587	7	1 0 7	—	1.489	4
0 1 4	2.432	2.434	24	2 2 2	1.461	1.461	3
2 0 $\bar{1}$	2.254	2.254	12	0 2 6	1.457	1.455	5
2 0 0	2.220	2.222	9	2 2 $\bar{4}$	1.444	1.446	7
0 2 0	2.175	2.175	31	1 2 $\bar{6}$	1.435	1.437	6
2 0 1	2.120	2.119	4	2 1 5	1.413	1.413	10
2 0 $\bar{3}$	2.088	2.089	4	3 1 0	1.403	1.402	9
0 1 5	2.069	2.067	4	1 1 $\bar{8}$	1.392	1.392	9
1 1 4	2.017	2.019	5	3 1 $\bar{3}$	1.392	1.392	5
2 0 2	1.969	1.971	4	0 1 8	1.392	1.391	5
0 0 6	—	1.957	5	2 1 $\bar{7}$	1.386	1.386	5





**Table A-3.** Powder X-ray Diffraction Data for  $\text{LaIn}_{0.8}\text{Sb}_2$  (cont'd)

$2\ 0\ \bar{4}$	1.936	1.935	8	$3\ 1\ 1$	————	1.367	4
$1\ 0\ \bar{6}$	1.913	1.914	7	$1\ 3\ \bar{2}$	1.358	1.358	13

<sup>a</sup> The intensities were calculated from the crystal structure of  $\text{LaIn}_{0.8}\text{Sb}_2$  with the use of the program LAZY-PULVERIX (Yvon, K.; Jeitschko, W.; Parthé, E. *J. Appl. Crystallogr.* **1977**, *10*, 73-74.)



**Table A-4.** Powder X-ray Diffraction Data for CeIn<sub>0.8</sub>Sb<sub>2</sub>

<i>hkl</i>	<i>d</i> <sub>obs</sub> (Å)	<i>d</i> <sub>calc</sub> (Å)	<i>I</i> / <i>I</i> <sub>o</sub> <sup>a</sup>	<i>hkl</i>	<i>d</i> <sub>obs</sub> (Å)	<i>d</i> <sub>calc</sub> (Å)	<i>I</i> / <i>I</i> <sub>o</sub> <sup>a</sup>
1 0 $\bar{2}$	—	3.838	5	1 0 $\bar{6}$	—	1.895	7
0 1 2	3.468	3.470	13	2 1 1	—	1.893	6
1 0 2	3.261	3.264	8	0 1 6	1.770	1.769	6
1 1 $\bar{1}$	3.079	3.076	12	1 1 $\bar{6}$	1.733	1.736	7
0 0 4	2.913	2.908	32	0 2 4	1.733	1.735	16
1 1 1	2.898	2.903	23	1 2 3	1.689	1.687	7
1 1 $\bar{2}$	2.871	2.870	100	1 2 $\bar{4}$	1.671	1.672	5
1 0 3	2.699	2.699	12	2 1 $\bar{5}$	—	1.625	5
1 0 $\bar{4}$	2.635	2.639	8	2 2 $\bar{1}$	1.556	1.555	9
1 1 2	2.603	2.605	56	2 2 0	1.544	1.545	7
1 1 $\bar{3}$	2.572	2.566	7	0 2 6	1.443	1.443	5
0 1 4	2.414	2.413	24	2 2 $\bar{4}$	1.434	1.435	7
2 0 $\bar{1}$	2.240	2.238	12	1 2 $\bar{6}$	1.425	1.425	6
2 0 0	2.210	2.208	9	2 1 5	1.401	1.402	10
0 2 0	2.160	2.162	31	3 1 0	1.394	1.393	9
2 0 1	2.104	2.105	4	3 1 $\bar{3}$	1.383	1.382	5
0 1 5	2.049	2.048	4	1 1 $\bar{8}$	—	1.379	9
1 1 4	2.004	2.004	5	0 1 8	—	1.378	5
0 0 6	1.939	1.938	5	2 1 $\bar{7}$	1.374	1.374	5
2 0 $\bar{4}$	1.916	1.919	7	1 3 $\bar{2}$	1.350	1.349	13

<sup>a</sup> The intensities were calculated from the crystal structure of LaIn<sub>0.8</sub>Sb<sub>2</sub> with the use of the program LAZY-PULVERIX (Yvon, K.; Jeitschko, W.; Parthé, E. *J. Appl. Crystallogr.* **1977**, *10*, 73-74.)



**Table A-5.** Powder X-ray Diffraction Data for  $\text{PrIn}_{0.8}\text{Sb}_2$ 

$hkl$	$d_{obs}$ (Å)	$d_{calc}$ (Å)	$I/I_o^a$	$hkl$	$d_{obs}$ (Å)	$d_{calc}$ (Å)	$I/I_o^a$
$10\bar{2}$	——	3.828	5	$10\bar{6}$	1.884	1.887	7
$012$	3.451	3.452	14	$211$	1.884	1.885	6
$102$	3.249	3.247	8	$016$	1.759	1.759	6
$11\bar{1}$	3.068	3.065	12	$11\bar{6}$	1.725	1.728	7
$004$	2.894	2.891	32	$024$	1.725	1.726	16
$111$	2.894	2.890	23	$123$	1.680	1.679	7
$11\bar{2}$	2.854	2.860	100	$12\bar{4}$	1.667	1.665	5
$103$	2.683	2.683	13	$21\bar{5}$	1.621	1.620	5
$10\bar{4}$	2.633	2.629	8	$22\bar{1}$	1.549	1.549	9
$112$	2.591	2.592	56	$220$	1.538	1.538	7
$11\bar{3}$	2.562	2.557	8	$026$	1.438	1.436	5
$014$	2.402	2.400	24	$22\bar{4}$	1.432	1.430	7
$20\bar{1}$	2.232	2.232	12	$12\bar{6}$	1.418	1.419	7
$200$	2.200	2.200	9	$215$	1.395	1.395	10
$020$	2.149	2.152	31	$310$	1.388	1.388	9
$201$	2.097	2.097	4	$31\bar{3}$	1.377	1.379	5
$015$	2.038	2.037	4	$11\bar{8}$	1.371	1.372	9
$114$	1.990	1.993	5	$018$	1.368	1.370	5
$006$	1.931	1.927	5	$21\bar{7}$	1.368	1.369	5
$20\bar{4}$	1.916	1.914	7	$13\bar{2}$	1.342	1.343	13

<sup>a</sup> The intensities were calculated from the crystal structure of  $\text{LaIn}_{0.8}\text{Sb}_2$  with the use of the program LAZY-PULVERIX (Yvon, K.; Jeitschko, W.; Parthé, E. *J. Appl. Crystallogr.* **1977**, *10*, 73-74.)



**Table A-6.** Powder X-ray Diffraction Data for NdIn<sub>0.8</sub>Sb<sub>2</sub>

<i>hkl</i>	<i>d</i> <sub>obs</sub> (Å)	<i>d</i> <sub>calc</sub> (Å)	<i>I</i> / <i>I</i> <sub>o</sub> <sup>a</sup>	<i>hkl</i>	<i>d</i> <sub>obs</sub> (Å)	<i>d</i> <sub>calc</sub> (Å)	<i>I</i> / <i>I</i> <sub>o</sub> <sup>a</sup>
1 0 $\bar{2}$	—	3.800	5	2 0 $\bar{3}$	2.050	2.054	4
0 1 2	3.443	3.444	14	0 1 5	2.034	2.031	4
1 0 2	3.239	3.244	8	1 1 4	—	1.990	5
1 1 $\bar{1}$	3.066	3.054	12	0 0 6	1.923	1.920	5
1 1 1	2.887	2.885	23	2 0 $\bar{4}$	1.898	1.900	7
0 0 4	2.887	2.880	32	2 1 1	1.877	1.881	6
1 1 $\bar{2}$	2.855	2.847	100	1 0 $\bar{6}$	1.870	1.875	7
1 0 3	2.676	2.681	13	0 1 6	1.756	1.753	6
1 0 $\bar{4}$	2.604	2.610	8	0 2 4	1.719	1.722	16
1 1 2	2.586	2.589	57	1 1 $\bar{6}$	1.719	1.718	7
1 1 $\bar{3}$	—	2.543	8	1 2 3	1.678	1.677	7
0 1 4	2.395	2.393	24	1 2 $\bar{4}$	1.660	1.659	5
2 0 $\bar{1}$	2.229	2.222	12	2 1 $\bar{5}$	1.609	1.610	5
2 0 0	2.196	2.193	9	2 2 $\bar{1}$	1.546	1.544	9
0 2 0	2.144	2.149	31	2 2 0	1.532	1.535	7
2 0 1	2.093	2.093	4				

<sup>a</sup> The intensities were calculated from the crystal structure of LaIn<sub>0.8</sub>Sb<sub>2</sub> with the use of the program LAZY-PULVERIX (Yvon, K.; Jeitschko, W.; Parthé, E. *J. Appl. Crystallogr.* **1977**, *10*, 73-74.)





**Table A-7.** Anisotropic Displacement Parameters <sup>a</sup> (Å<sup>2</sup>) for LaIn<sub>0.8</sub>Sb<sub>2</sub>

atom	$U_{11}$	$U_{22}$	$U_{33}$	$U_{12}$	$U_{13}$	$U_{23}$
La	0.0127(10)	0.0068(6)	0.0100(8)	0	0.0024(6)	0
In	0.042(2)	0.0351(17)	0.0186(17)	0	-0.0131(13)	0
Sb(1)	0.0125(11)	0.0075(7)	0.0123(9)	0	0.0026(7)	0
Sb(2)	0.0121(11)	0.0080(7)	0.0102(9)	0	0.0018(7)	0

<sup>a</sup> The form of the anisotropic displacement parameter is:  $\exp[-2\pi^2(h^2a^{*2}U_{11} + k^2b^{*2}U_{22} + l^2c^{*2}U_{33} + 2hka^*b^*U_{12} + 2hla^*c^*U_{13} + 2klb^*c^*U_{23})]$ .



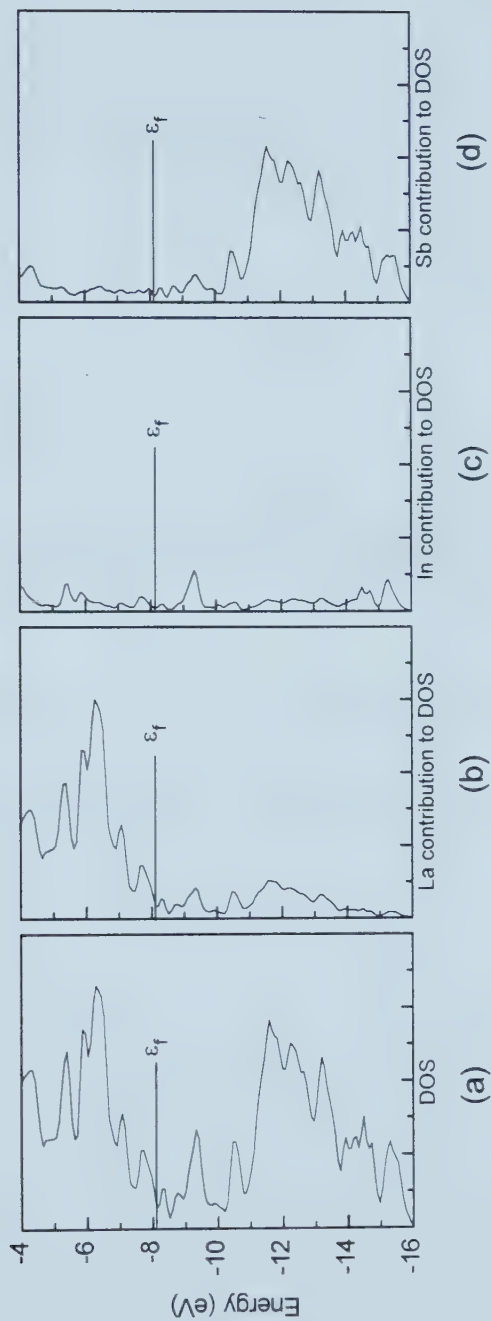


**Figure A-1.** (a) Total density of states for the ordered superstructure  $\text{LaIn}_{0.75}\text{Sb}_2$ . The individual atomic contributions (La, In, and Sb) to the density of states are shown in (b) – (d). The Fermi level ( $\epsilon_f = -8.06$  eV) is shown.



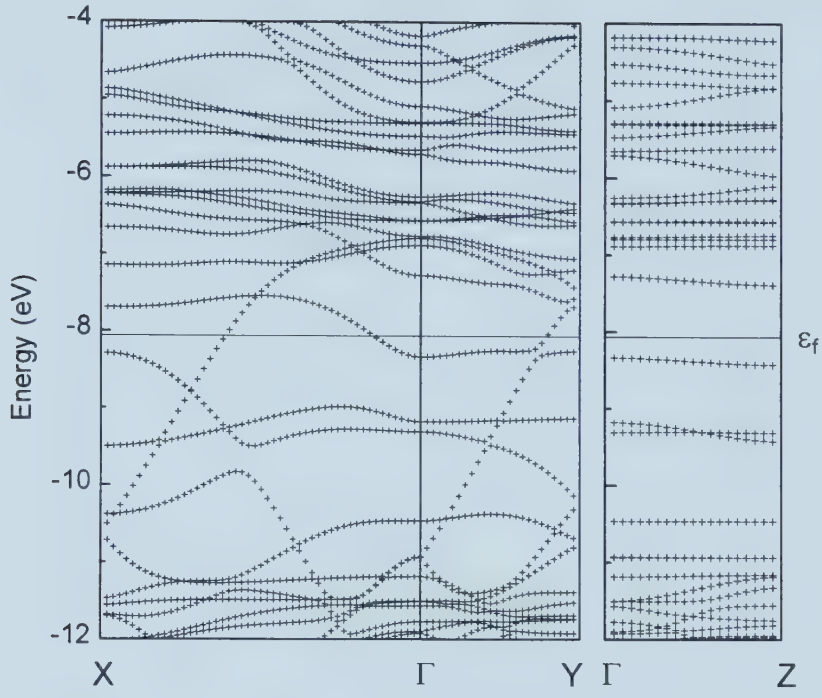


**Figure A-2.** Band dispersion curves for the ordered superstructure  $\text{LaIn}_{0.75}\text{Sb}_2$  along the special symmetry lines  $\Gamma\text{X}$ ,  $\Gamma\text{Y}$ , and  $\Gamma\text{Z}$ . The Fermi level ( $\epsilon_f = -8.06$  eV) is shown.



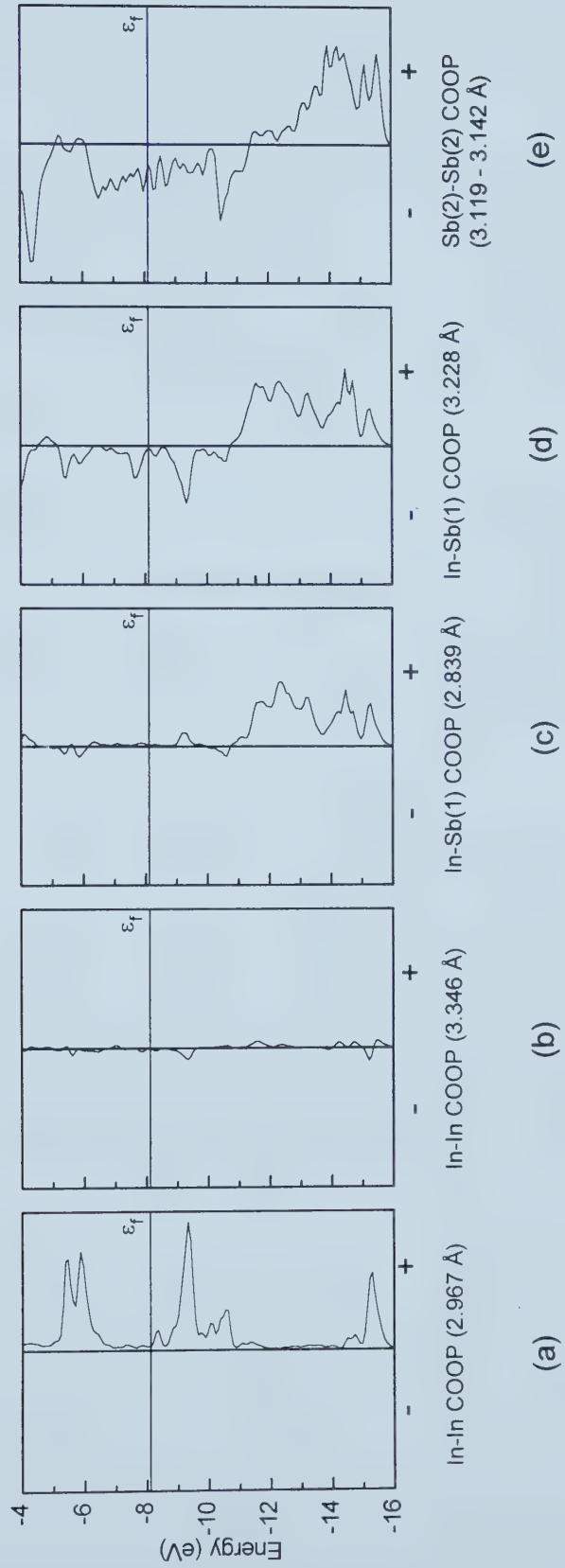


**Figure A-3.** Crystal orbital overlap population curves for In-In, In-Sb(1), and Sb(2)-Sb(2) interactions for the ordered superstructure  $\text{LaSn}_{0.75}\text{Sb}_2$ . The Fermi level ( $\epsilon_f = -8.06 \text{ eV}$ ) is shown.





**Table A-8.** Anisotropic Displacement Parameters <sup>a</sup> (Å<sup>2</sup>) for La<sub>3</sub>TiSb<sub>5</sub>, La<sub>3</sub>ZrSb<sub>5</sub>, and La<sub>3</sub>HfSb<sub>5</sub> for Data Collections at –60°C

atom	$U_{11}$	$U_{22}$	$U_{33}$	$U_{12}$	$U_{13}$	$U_{23}$
La <sub>3</sub> TiSb <sub>5</sub>						
La	0.0054(4)	0.0055(5)	0.0054(5)	0.0028(2)	0	0
Ti	0.0054(14)	0.0054(14)	0.009(2)	0.0027(7)	0	0
Sb(1)	0.0053(4)	0.0055(5)	0.0064(5)	0.0028(3)	0	0
Sb(2)	0.0050(4)	0.0050(4)	0.0070(6)	0.0025(2)	0	0
La <sub>3</sub> ZrSb <sub>5</sub>						
La	0.0058(5)	0.0080(6)	0.0103(7)	0.0040(3)	0	0
Zr	0.0047(8)	0.0047(8)	0.009(1)	0.0023(4)	0	0
Sb(1)	0.0049(5)	0.0066(6)	0.0107(8)	0.0033(3)	0	0
Sb(2)	0.0058(6)	0.0058(6)	0.015(1)	0.0029(3)	0	0
La <sub>3</sub> HfSb <sub>5</sub>						
La	0.0046(4)	0.0070(5)	0.0070(5)	0.0035(3)	0	0
Hf	0.0051(4)	0.0051(4)	0.0079(6)	0.0026(2)	0	0
Sb(1)	0.0039(4)	0.0055(5)	0.0075(6)	0.0027(2)	0	0
Sb(2)	0.0043(5)	0.0043(5)	0.0133(8)	0.0022(2)	0	0

<sup>a</sup> The form of the anisotropic displacement parameter is:  $\exp[-2\pi^2(h^2a^{*2}U_{11} + k^2b^{*2}U_{22} + l^2c^{*2}U_{33} + 2hka^*b^*U_{12} + 2hla^*c^*U_{13} + 2klb^*c^*U_{23})]$ .



**Table A-9.** Crystallographic Data for  $\text{La}_3\text{TiSb}_5$  for Data Collection at  $-170^\circ\text{C}$ 

Formula	$\text{La}_3\text{TiSb}_5$
Formula mass (amu)	1073.38
Space Group	$D_{6h}^3 - P6_3/mcm$
$a$ (Å)	$9.5198(13)^a$
$c$ (Å)	$6.2693(8)^a$
$V$ (Å <sup>3</sup> )	492.05(11)
$Z$	2
$T$ (°C)	$-170$
Diffractometer	Siemens P4RA/SMART 1000 CCD
$\rho_{\text{calc}}$ (g cm <sup>-3</sup> )	7.245
Crystal dimensions	Silver needle, $0.320 \times 0.060 \times 0.060$ mm <sup>3</sup>
Radiation	Graphite-monochromated $\text{MoK}\alpha$ , $\lambda = 0.71073$ Å
$\mu$ (cm <sup>-1</sup> )	268.9
Transmission factors <sup>b</sup>	0.084–0.284
Scan-type	mixture of $\phi$ rotations and $\omega$ scans
$2\theta$ limits	$5^\circ \leq 2\theta(\text{MoK}\alpha) \leq 64^\circ$
Data collected	$-14 \leq h \leq 13, -12 \leq k \leq 14, -9 \leq l \leq 9$
No. of data collected	4567
No. of unique data, including $F_o^2 < 0$	339 ( $R_{\text{int}} = 0.045$ )
No. of unique data, with $F_o^2 > 2\sigma(F_o^2)$	339
No. of variables	14
Extinction coefficient <sup>c</sup>	0.082(3)



**Table A-9.** Crystallographic Data for  $\text{La}_3\text{TiSb}_5$  for Data Collection at  $-170^\circ\text{C}$  (cont'd)

$R(F)$ for $F_o^2 > 2\sigma(F_o^2)^d$	0.020
$R_w(F_o^2)^e$	0.044
Goodness of fit <sup>f</sup>	1.31
$\Delta\rho_{\text{max}}, \Delta\rho_{\text{min}}$ ( $e \text{ \AA}^{-3}$ )	2.19, -1.02

<sup>a</sup> Obtained from a refinement constrained so that  $\alpha = \beta = 90^\circ$  and  $\gamma = 120^\circ$ .

<sup>b</sup> Face-indexed absorption corrections were applied, with the use of the programs in the SHELXTL package (Sheldrick, G. M. *SHELXTL* Version 5.0, Siemens Analytical X-ray Instruments, Inc.: Madison, WI, 1994).

<sup>c</sup> An extinction parameter  $x$  is refined, where  $F_c$  is multiplied by:  $k[1 + 0.001 * x * F_c^2 * \lambda^3 / \sin(2\theta)]^{-1/4}$ .

$$^d R(F) = \sum \|F_o| - |F_c\| / \sum |F_o|.$$

$$^e R_w(F_o^2) = [\sum [w(F_o^2 - F_c^2)^2] / \sum wF_o^4]^{1/2}; w^{-1} = [\sigma^2(F_o^2) + (0.0151P)^2 + 4.46P],$$

where  $P = [\max(F_o^2, 0) + 2F_c^2] / 3$ .

$$^f \text{Goof} = S = \left[ \sum [w(F_o^2 - F_c^2)^2] / (n - p) \right]^{1/2} \text{ where } n \text{ is the number of reflections and } p \text{ is the total number of parameters refined.}$$



**Table A-10.** Atomic Coordinates and Equivalent Displacement Parameters ( $\text{\AA}^2$ ) for  $\text{La}_3\text{TiSb}_5$  for Data Collection at  $-170^\circ\text{C}$ 

atom	Wyckoff position, site symmetry		$x$	$y$	$z$	$U_{\text{eq}}^a$
La	6g	$m2m$	0.61767(4)	0	$\frac{1}{4}$	0.00409(17)
Ti	2b	$\bar{3} . m$	0	0	0	0.0053(4)
Sb(1)	6g	$m2m$	0.25077(5)	0	$\frac{1}{4}$	0.00428(17)
Sb(2)	4d	$3 . 2$	$\frac{1}{3}$	$\frac{2}{3}$	0	0.00428(19)

<sup>a</sup>  $U_{\text{eq}}$  is defined as one-third the trace of the orthogonalized  $U_{ij}$  tensor.

**Table A-11.** Anisotropic Displacement Parameters <sup>a</sup> ( $\text{\AA}^2$ ) for  $\text{La}_3\text{TiSb}_5$  for Data Collection at  $-170^\circ\text{C}$ 

atom	$U_{11}$	$U_{22}$	$U_{33}$	$U_{12}$	$U_{13}$	$U_{23}$
La	0.0031(2)	0.0038(2)	0.0057(2)	0.00188(12)	0	0
Ti	0.0041(6)	0.0041(6)	0.0076(9)	0.0021(2)	0	0
Sb(1)	0.0032(2)	0.0034(3)	0.0064(3)	0.00168(12)	0	0
Sb(2)	0.0032(2)	0.0032(2)	0.0066(3)	0.00157(11)	0	0

<sup>a</sup> The form of the anisotropic displacement parameter is:  $\exp[-2\pi^2(h^2a^{*2}U_{11} + k^2b^{*2}U_{22} + l^2c^{*2}U_{33} + 2hka^*b^*U_{12} + 2hla^*c^*U_{13} + 2klb^*c^*U_{23})]$ .





**Table A-12.** Anisotropic Displacement Parameters <sup>a</sup> (Å<sup>2</sup>) for LaCrSb<sub>3</sub>

atom	$U_{11}$	$U_{22}$	$U_{33}$	$U_{12}$	$U_{13}$	$U_{23}$
La	0.0045(10)	0.0024(11)	0.0049(12)	-0.0003(7)	0	0
Cr	0.017(3)	0.004(2)	0.011(3)	0	0	0.003(2)
Sb(1)	0.0132(11)	0.0046(12)	0.0104(12)	0.0018(8)	0	0
Sb(2)	0.0086(12)	0.0042(12)	0.0061(12)	0.0024(7)	0	0
Sb(3)	0.0054(12)	0.0046(12)	0.0058(12)	0	0	-0.0007(6)

<sup>a</sup> The form of the anisotropic displacement parameter is:  $\exp[-2\pi^2(h^2a^{*2}U_{11} + k^2b^{*2}U_{22} + l^2c^{*2}U_{33} + 2hka^*b^*U_{12} + 2hla^*c^*U_{13} + 2klb^*c^*U_{23})]$ .















University of Alberta Library



0 1620 1250 7040

**B45365**